UNIVERSIDAD
DE GRANADA

ISOTOPE PRODUCTION IN DONES: Exhaustive analysis of different isotopes and preliminary design of their industrial production

---

TESIS DOCTORAL

María Elena López Melero

PROGRAMA DE DOCTORADO EN FÍSICA Y CIENCIAS DEL ESPACIO

Granada, Julio de 2025

ISOTOPE PRODUCTION IN DONES: Exhaustive analysis of different isotopes and preliminary design of their industrial production

REALIZADO POR:
María Elena López Melero

DIRIGIDO POR:
Antonio Javier Praena Rodríguez
Eduardo Romero Sanz

DEPARTAMENTO:
Departamento de Física Atómica, Molecular y Nuclear

UNIVERSIDAD DE GRANADA

PROGRAMA DE DOCTORADO EN FÍSICA Y CIENCIAS DEL ESPACIO

Granada, Julio de 2025

Editor: Universidad de Granada. Tesis Doctorales
Autor: María Elena López Melero
ISBN: 978-84-1195-898-1
URI: https://hdl.handle.net/10481/108333

A mis padres.

Acknowledgements

En este manuscrito se presenta el resultado del esfuerzo y la constancia de muchos años de dedicación, no solo referidos a mi formación, sino también a mis inquietudes y crecimiento personal. Un camino que no he recorrido sola y al que tengo mucho que agradecer.

En primer lugar, quiero dar las gracias a Javier, Ignacio y Fernando, quienes me dieron la oportunidad de trabajar con ellos hace ya unos pocos años y que, a día de hoy, siguen apostando por mí. Me permitieron descubrir una nueva senda llena de oportunidades, conocer a maravillosas personas y disfrutar de increíbles vivencias y experiencias.

Personas, como mis FAMNtásticos compañeros de departamento, la "ratonera que no me olvida" y a la que es y será difícil de olvidar: Alejandro, Álex, Álvaro, Ana María, Antònia, Araceli, Dani, Emilio, Fran, Garvi, Joaquín (y su piscina), Juan Manuel, Laura, Lidia, Matilde, Pedro y Víctor. Gracias por todos esos buenos momentos en el trabajo, paseos al Lidl, comidas en La Tuttoria, cafés y helados, pero, sobre todo, por saber escuchar, reír y disfrutar a mi lado.

Mis compañeros DONITOS, unidos por una misma causa: Andy, Antonio, Juan Antonio, Francisco, Mario, Pablo Araya y Pablo Canca. ¡¡Mis chicas DONITAS!! Gracias Cristina e Irene, sin lugar a duda, esta experiencia sin vosotras no hubiera sido igual. Tertulias largas, intercambio de dramas y todo el cariño compartido ha forjado una increíble amistad.

Vivencias, como conocer los entresijos, historias y leyendas del CIEMAT, de la mano de grandes compañeros, y ahora amigos. Gracias Eduardo, aunque no lo ubiques en el espacio-tiempo, he aprendido y aprenderé mucho a tu lado. Gracias Miguel Ángel por hacer posible esta unión UGR-CIEMAT, por tu disponibilidad y apoyo siempre; y por supuesto a todos los compañeros de la familia CIEMAT: Fernando, Lagares, Laura, Marta Ibáñez, Marta Oteo, Natalia Chamorro, Natalia Magro y Víctor. Espero que el "Luteci" y los nuevos proyectos nos sigan uniendo mucho tiempo más.

Experiences such as discovering the Loire from its source to its mouth, Orléans-Nantes. Thank you Conchi, Isidro and Férid, for your hospitality and the opportunity you have given me to make incredible stays and collaborations, allowing me to discover the world of experimentation unknown, until then, to me. Thank you Arnaud and Etienne for your supervision, help and knowledge of the "stacked-foil technique", you have been a great reference for me during my stay. And of course, I can't forget the beautiful group of

colleagues and friends I met at GIP ARRONAX: Alexandre, Gabriela, Laurine, Michele, Noor and Vanessa, thank you for the coffee times, laughs and picnics!

Por último, todo esto hubiera sido imposible sin el apoyo incondicional de mis padres, mis pilares fundamentales. Confiaron en mí desde el primer minuto en el que embarqué en la loca idea de estudiar física y espero que estén tan orgullosos de mí como yo de ellos.

This work has been carried out under the fellowship MCIN/AEI/10.13039/501100011033 from the EUROfusion Consortium, funded by the European Union via the Euratom Research and Training Programme (Grant Agreement No 101052200 — EUROfusion). Views and opinions expressed are, however, those of the author only and do not necessarily reflect those of the European Union or the European Commission. Neither the European Union nor the European Commission can be held responsible for them. Partially, this work was supported by Spanish Ministerio de Ciencia e Innovación (PID2020-117969RBI00), Junta de Andalucía (FEDER Andalucia 2014–2020) projects P20-00665 and B-FQM-156-UGR20, Empresarios Agrupados Internacional, S.A. with funding from Spanish CDTI (Misiones DONES-EVO) (Contrato UGR-OTRI 5270), Instituto Carlos III (ISCIII DTS22 /00147) and from France State aid managed by the Agence Nationale de la Recherche under the Programme d'Investissements d'Avenir (ANR-16-IDEX-0007) and financial support from the Pays de la Loire Region. Personally, I would like to thank the support from Junta de Andalucía, European Regional Development Fund (ERDF), Euratom Research, co-founded by the European Union, ENEN2Plus and Training Programme IRC TransForMed mobility grants. I would also like to acknowledge the support of the RYC-GIP ARRONAX tool.

Agradecer también la implicación y ayuda a Mabel Porras, Mari Carmen Ruíz del departamento de Biología Molecular III e Inmunología de la Universidad de Granada, Fernando Mota y Maribel Ortiz del Laboratorio Nacional de Fusión del CIEMAT. Finalmente, quiero hacer mención y agradecer la dedicación y el tiempo empleado por los revisores internacionales expertos que han aceptado la revisión externa del manuscrito.

¡Mil gracias!

Resumen

La Medicina Nuclear engloba una parte importante de las aplicaciones médicas de las radiaciones ionizantes, basándose en el uso de radioisótopos como fuentes de radiación y permitiendo el diagnóstico y tratamiento médico de las principales enfermedades con mayor impacto social.

Los radioisótopos utilizados en Medicina Nuclear son producidos mediante bombardeo de núcleos estables con partículas cargadas, fotones o neutrones, para inducir las reacciones nucleares deseadas, y tienen lugar en instalaciones nucleares como reactores de fisión o en aceleradores de partículas (linacs, sincrotrones, ciclotrones, etc.). Estas tecnologías, junto con los generadores de radionucleidos, son las principales vías de abastecimiento de radioisótopos médicos en los hospitales, y deben considerarse complementarias y no competitivas.

El acelerador lineal de alta intensidad y última generación, IFMIF-DONES, podrá acelerar deuterones hasta una energía de 40 MeV y una corriente de 125 mA. Estas partículas cargadas golpearán un blanco de litio líquido produciendo neutrones a través de la reacción nuclear de producción $D^+ + {}^7Li$, contenida dentro de la celda de prueba (*Test Cell*), produciendo un flujo de neutrones rápidos de 10^{14} n/cm^2/s con un pico amplio entre $14 - 20$ MeV en su espectro neutrónico. En el campo de la producción de radioisótopos, IFMIF-DONES facilitaría tanto las posibilidades de producción de radioisótopos mediante reacciones inducidas con haz de deuterones como con neutrones, gracias al flujo neutrónico residual dentro de la celda de prueba tras el módulo de alto flujo (*High Flux Test Module*).

En el contenido de esta tesis, se estudia de forma exhaustiva y detallada la viabilidad de producción de algunos de los radioisótopos más relevantes en la clínica actual ^{165}Er, ^{177}Lu y ^{99}Mo/^{99m}Tc, así como su adaptación realista de producción a la instalación, considerándose algunas modificaciones en el diseño actual del acelerador para la correcta implemen tación de esta aplicación complementaria relevante en el campo de la Medicina Nuclear.

Finalmente, se ha cerrado esta tesis con un caso práctico de aplicación en la campo de la Medicina Nuclear. Concretamente se ha evaluado un radiofármaco experimental radiomarcado con ^{177}Lu en modelo animal para definir sus posibilidades preclínicas ante una potencial investigación traslacional desde el ámbito de las terapias dirigidas con radionucleidos a otras estrategias terapéuticas.

Abstract

Nuclear Medicine covers an important part of the medical applications of ionising radiation, based on the use of radioisotopes as radiation sources and allowing the diagnosis and medical treatment of the main diseases with the greatest social impact.

Radioisotopes used in Nuclear Medicine are produced by bombarding stable nuclei with charged-particles, photons or neutrons, to induce the required nuclear reactions, and take place in nuclear facilities such as fission reactors or particle accelerators (Linacs, synchrotrons, cyclotrons, etc.). These technologies, together with radionuclide generators, are the main supply routes for medical radioisotopes in hospitals and should be seen as complementary and non-competitive.

The state-of-the-art, high-intensity linear accelerator, IFMIF-DONES, will be able to accelerate deuterons up to 40 MeV of energy and 125 mA of current. The charged-particle beam will strike a liquid lithium target producing neutrons through the nuclear production reaction $D^+ + {}^7Li$, contained inside the Test Cell, producing a fast neutron flux of 10^{14} n/cm^2/s with a broad peak between $14 - 20$ MeV in its neutron spectrum. In the framework of radioisotope production, IFMIF-DONES would allow radioisotope production by deuteron- induced and neutron-induced nuclear reactions, the latter thanks to the residual neutron flux inside the Test Cell behind the High Flux Test Module.

In the content of this thesis, the production feasibility of ^{165}Er, ^{177}Lu and ^{99}Mo/^{99m}Tc, some of the most relevant radioisotopes in the current clinic is analysed in an exhaustive and detailed study, as well as their realistic production within the facility, considering some updates in the design of the accelerator for the correct implementation of this relevant complementary application in the field of Nuclear Medicine.

Finally, this thesis has been closed with a practical case of application in the field of Nuclear Medicine. Specifically, an experimental radiopharmaceutical radiolabelled with ^{177}Lu has been evaluated in an animal model to define its preclinical possibilities for a potential translational research from the field of targeted radionuclides therapies to other therapeutic strategies.

Contents

Acronyms

AE Auger Electron

AUC Area Under the Curve

BFC Bifunctional Chelator

BNCT Boro Neutron Capture Therapy

CAD Computer-Aided Design

CT Computed Tomography

DT Dead Time

EC Electron Capture

ENDF Evaluated Nuclear Data File

EOB End Of Bombardment

EXFOR Experimental Nuclear Reaction Data

F4E Fusion for Energy

HFTM High Flux Test Module

HPGe High Purity Germanium

HPLC High Performance Liquid Chromatography

IAEA International Atomic Energy Agency

IC Internal Conversion

IFMIF-DONES International Fusion Materials Irradiation Facility - DEMO Oriented Neutron Source.

IP Isotopic Purity

IT Isomeric Transition

ITER International Thermonuclear Experimental Reactor

LET Linear Energy Transfer

LT Live Time

MCNP Monte Carlo N-Particle

NET Neuroendocrine Tumour

NSCLC Non-Small Cell Lung Cancer

PBS Phosphate Buffered Saline

PET Positron Emission Tomography

RF Radio Frequency

RIPD RadioIsotope Production Device

RNP Radionuclide Purity

RQP Radiochemical Purity

RT Real Time

RYC Radionuclide Yield Calculator

SA Specific Activity

SEM Standard Error of the Mean

SPECT Single Photon Emission Computed Tomography

SRIM Stopping and Range of Ions in Matter

SS Somatostatin

SSTR Somatostatin Transmembrane Receptors

SUV Standard Uptake Value

TC Test Cell

TENDL TALYS-based Evaluated Nuclear Data Library

TIAC Time-Integrated Activity Coefficient

TRNT Targeted RadioNuclide Therapy

TTY Thick Target Yield

List of Figures

List of Tables

Introduction

The International Fusion Materials Irradiation Facility - DEMO Oriented NEutron Source Facility (IFMIF-DONES)

The International Fusion Materials Irradiation Facility - Demo Oriented NEutron Source (IFMIF-DONES) will be a unique scientific infrastructure in the world where materials to be used in future fusion nuclear reactors will be tested, validated and qualified. In relation to this international project, in December 2017, Fusion for Energy (F4E) positively assessed the joint Spanish and Croatian proposal to locate IFMIF-DONES in Escúzar (Granada, Spain) [1].

IFMIF-DONES will be a facility for irradiating with fast neutrons key materials to be used inside of fusion reactors. It will simulate the conditions reached inside a fusion reactor as demonstration power plant prototype (DEMO) in terms of neutrons flux and high temperatures [2]. Together with the International Thermonuclear Experimental Reactor (ITER) facility, IFMIF-DONES is the key facility for designing DEMO. IFMIF facility consists of two linear accelerators delivering deuterons on the same neutron production

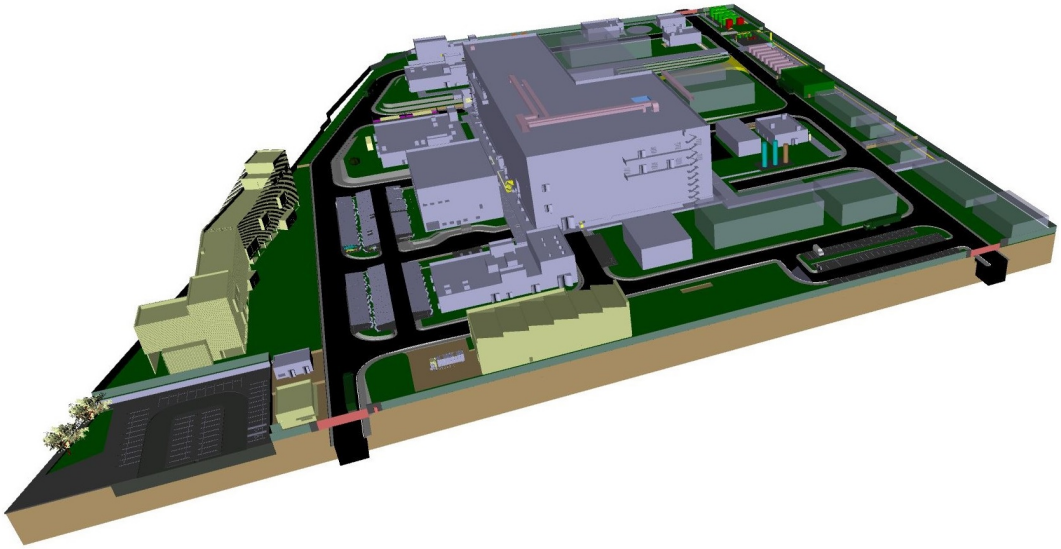

Figure 1: Artistic bird's eye view of the IFMIF-DONES facility. Image provided by IFMIF-DONES Spain Consortium.

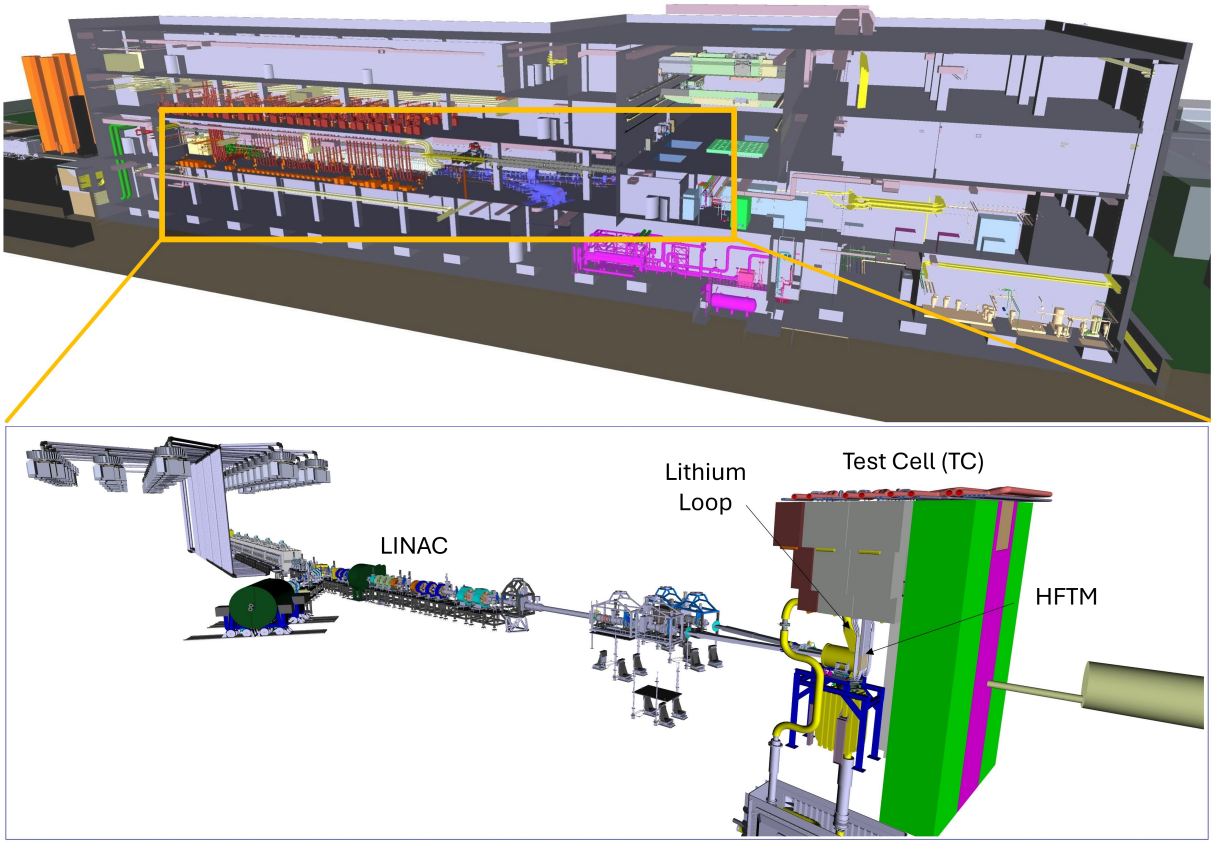

Figure 2: Side view of the IFMIF-DONES Linac. Images provided by IFMIF-DONES Spain Consortium.

target (lithium jet). However, in view of the urgent need of data on materials, the construction of DONES was decided. DONES will consist of a single linear accelerator (5 MW) delivering deuterons on the lithium jet target. Currently, the project is dealing with the construction phase [3].

The DONES high-intensity linear accelerator will be able to accelerate deuterons up to 40 MeV energy and 125 mA current. These charged-particles will strike a liquid lithium target producing neutrons through the $D^+ + {}^7Li$ stripping reaction, contained inside the Test Cell (TC) [4]. An expected fast neutron flux of 10^{14} n/cm^2/s will be generated with a broad peak between $14 - 20$ MeV The key materials for designing DEMO will be irradiated in the High Flux Test Module (HFTM) few centimetres far away from the neutron production lithium target.

IFMIF-DONES will be a relevant facility for the development of fusion as an energy source. However, the unique characteristics of IFMIF-DONES facility will also be very important in other areas of research and knowledge that will benefit from its technology, as medicine, particle physics, basic physics studies or industry, among others, developing complementary applications for fundamental and applied physics with a minimum impact of the normal functioning of the facility [5–7].

In the field of radioisotope production, IFMIF-DONES will enable the possibility to work with the deuteron beam and also with the neutron produced at the lithium target. For which, some improvements of the accelerator design are being studied for these complementary applications.

On one side, it would be possible to deflect 0.1 % of the initial deuteron beam to another experimental room (R026). Therefore, 40 MeV deuteron beam at 125 μA current would be available for other applications as radioisotope production via deuteron nuclear reactions. This would be the case for the production of ^{165}Er or ^{177}Lu radioisotope [8, 9]. On the other hand, a Radioisotope Production Device (RIPD) is planned after the HFTM (inside TC), where targets for radioisotope production will be placed to be irradiated under the residual neutron flux. This would be the case for the production of ^{99}Mo, the parent nucleus of ^{99m}Tc. The location of these complementary applications is shown in Figure 3.

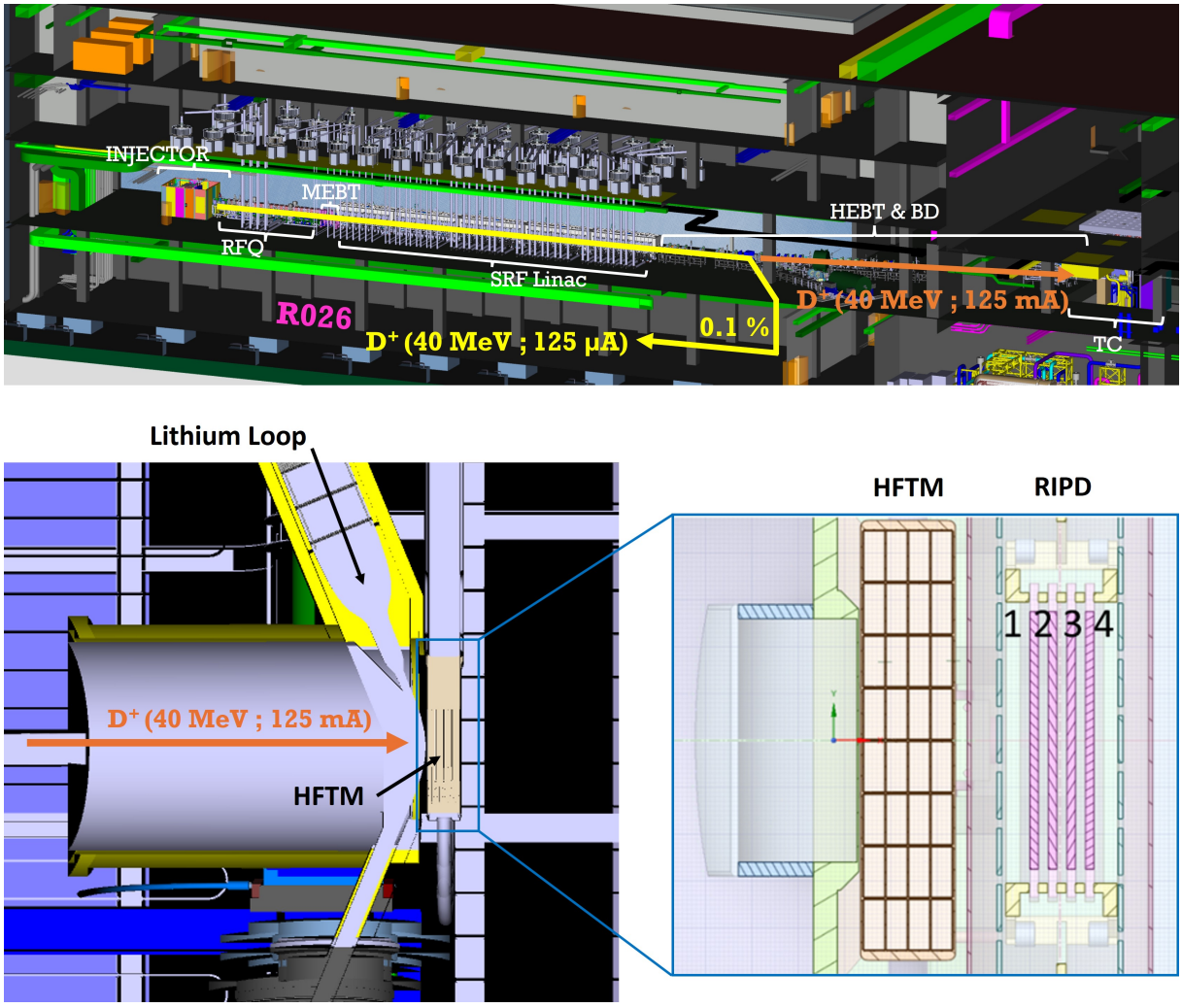

Figure 3: Radioisotope production locations. Up: R026 for deuteron radioisotope production. Down: RIPD, 8 cm behind HFTM for neutron radioisotope production (inside TC).

Chapter I

Radioisotopes in Nuclear Medicine

1 Radioactivity

Radiation has been part of the universe since its origin, however it was not until the end of the 19^{th} century, when in 1896 Henri Becquerel, Marie Curie and Pierre Curie (Nobel Prizes in physics in 1903) happened to witness and were able to explain the phenomenon of radioactivity.

With the discovery of radioactivity, the concept of the universe was modified, as a consequence of the new conception of one of its smallest components, the atom. The atom is made up of three types of particles: electrons in its shell and nucleons (protons and neutrons) in its nucleus, with an unladen radius ratio $R_{atom}/R_{nucleus} = 10^{-10}$ m$/10^{-14}$ m. The representation of a nucleus X can be written as ${}^{A}_{Z}X$ where Z is the atomic number equal to the number of protons and A is the mass number equal to the number of nucleons (protons + neutrons). Given the neutral nature of the atom, there will be Z electrons (electric charge -1) associated with a nucleus containing Z protons (electric charge +1). Nuclei with the same Z but different A are called isotopes and have the same chemical properties.

Nuclear instability can occur between nucleons of different isotopes as a result of an equilibrium between the electrostatic repulsive forces of the protons (electrically positive charges) and the very short-range, charge-independent nuclear forces of the nucleons. Radioactivity is the phenomenon that occurs spontaneously when the nucleons of unstable atoms (i.e. radioisotope or radionuclide) emit a large amount of energy in the form of particles or electromagnetic radiation in an attempt to seek the stability of the nucleus [10]. Radiation with sufficient energy to strip electrons from the atoms of matter is called ionizing radiation. Ionising radiation generated in radioactive decay can be of three types: alpha, beta or gamma decay.

The way a radionuclide decays to be stable depends mainly on the ratio of the number of neutrons/protons in its nucleus. The radionuclide chart is the representation of nuclei in terms of their number of protons and neutrons. Figure I.1 shows the number of

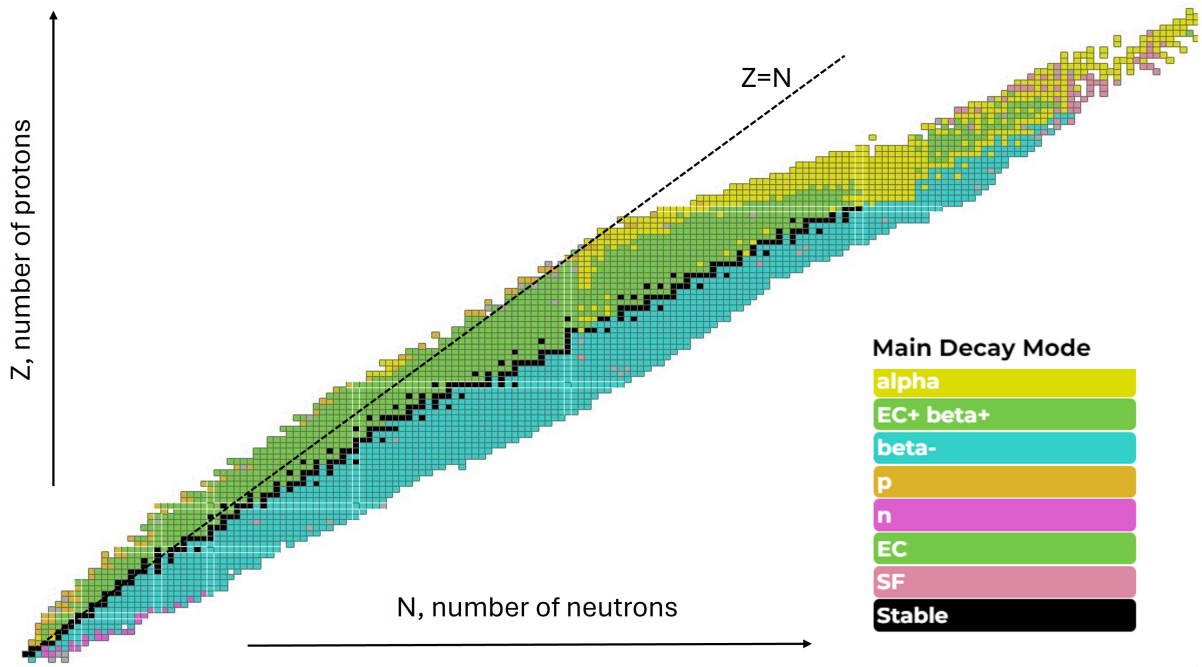

Figure I.1: Live chart of nuclides. The valley of stability is composed of the stable nuclei of the nuclide chart. All radionuclides plotted on the chart access the valley of stability by different decay chains [11].

protons on the abscissa axis and neutrons on the ordinate axis. Each square represents a nucleus. In black, the natural stable nuclei form the valley of stability, which corresponds approximately to $Z = N$ for light nuclei. The coloured nuclei are radioactive and will try to return to the valley of stability by decay. The colours define the dominant decay mode of the nucleus: green for β^+ decay/electron capture, blue for β^- decay, and yellow for α decay, mainly [12].

1.1 Alpha decay

This is a type of disintegration typical of heavy nuclei (A $>$ 140) and consists of the emission of a helium nucleus. This He^{2+} nucleus, composed of 2 protons and 2 neutrons, will deposit all its energy in a very short path, and it can be stopped in a sheet of paper or a few centimetres of air, so it is considered a low-penetrating radiation.

$$ {}^{A}_{Z}X \rightarrow {}^{A-4}_{Z-2}Y + {}^{4}_{2}He $$

Alpha particles are emitted with an energy of the order of several MeV. This high energy deposition over a short distance is capable of causing lethal cell damage. Ionising radiation might cause damage to a cell through direct or indirect mechanisms. Direct action occurs when radiation interacts directly with critical cell targets causing irreversible structural damage to the DNA of cell nuclei. This scenario is most likely in the case of

dense ionising radiation, such as alpha particles. However, indirect action can also occur. In this case, the radiation interacts with other parts of the cells. Since a cell is mainly composed of water (about 80 %), free radicals are normally generated by the radiolysis of water, which can diffuse and damage cellular DNA.

1.2 Beta decay and Electron Capture

Beta decay is a more penetrating type of radiation, depositing all its energy in a longer path. It would require a sheet of aluminium or several metres of air to stop it. It usually occurs in nuclei with an excess of neutrons (β^-) or protons (β^+) and is accompanied by gamma disintegration.

β^- decay:

It is the result of the disintegration of a neutron from the nucleus which transforms into a proton giving rise to the emission of an electron and an antineutrino. It occurs in neutron-rich nuclei, being below the valley of stability (see Figure I.1).

$$ {}^{A}_{Z}X \rightarrow {}^{A}_{Z+1}Y + e^- + \bar{\nu} $$

β^+ decay:

It is the result of the disintegration of a proton from the nucleus which transforms into a neutron giving rise to the emission of a positron and a neutrino. It occurs in proton-rich nuclei, being above the valley of stability (see Figure I.1).

$$ {}^{A}_{Z}X \rightarrow {}^{A}_{Z-1}Y + e^+ + \nu $$

The energy difference between the parent and the daughter nucleus is shared between the β-particle and the neutrino or antineutrino in form of kinetic energy. As the distribution varies from one decay to another, there will be a continuous energy distribution of the emitted electrons. The kinetic energy of the emitted electrons can vary from a few tens of keV to several MeV.

Electron Capture (EC):

Electron capture is a process by which an atomic electron, usually from the K-shell, combines with a proton from the nucleus to form a neutron and a neutrino. It is an alternative and competing process to β^- decay with positron emission for proton-rich nuclei.

$$ {}^{A}_{Z}X + e^- \rightarrow {}^{A}_{Z-1}Y + \nu $$

Although the resulting atom remains neutral, a vacancy remains in the inner K-shell. This vacancy is filled by upper-shell electrons through one or more atomic transitions with characteristic X-ray emission or Auger electrons.

β^+-emission and EC are two processes by which a proton-rich nucleus can transform to achieve greater stability. Both mechanisms convert a proton into a neutron but occur under different conditions. The relative likelihood of β^+ decay versus EC depends on the energy difference between the initial and final nuclear states. If this energy difference is less than 511 keV, β^+ decay is energetically forbidden, and only electron capture can occur [12]. EC is more likely to predominate in heavy nuclei, where the nucleus is larger and inner electron orbitals are closer to the nucleus.

1.3 Gamma decay

Gamma radiation emitted in the gamma decay is the most penetrating type of radiation and consists of a deexcitation process by gamma photon emission. The photon is an elementary corpuscle or quantum of energy associated with an electromagnetic wave, with energies above the keV order for gamma photons. Dense and heavy materials, such as lead or concrete, are required to absorb them.

$$ {}^{A}_{Z}X^{*} \rightarrow {}^{A}_{Z}X + \gamma $$

The energy spectrum of gamma emission is discrete, the energies and intensities are specific to each radionuclide. This allows qualitative and quantitative isotopic analysis in the determination of radionuclides in a radioactive sample.

1.4 Internal conversion

Internal Conversion (IC) is a competing mechanism to gamma decay, as it also consists of a nuclear deexcitation process, in which an excited nucleus interacts with one of the orbital electrons of an atom electromagnetically. This causes the electron to be ejected from the atom. Thus, in internal conversion a high-energy electron is emitted from the excited atom, but not from the nucleus.

$$ E_{e^-} = E_{\gamma} - E_{shell} \tag{I.1} $$

The vacancy left by the electron (usually K or L shell) is filled by another electron from a higher shell with the consequent emission of a characteristic X-ray or Auger electron.

1.4.1 Characteristics X-ray

Characteristic radiation occurs when an electron from an outermost shell falls to fill the vacancy created in the innermost shell, a photon is released whose energy corresponds to

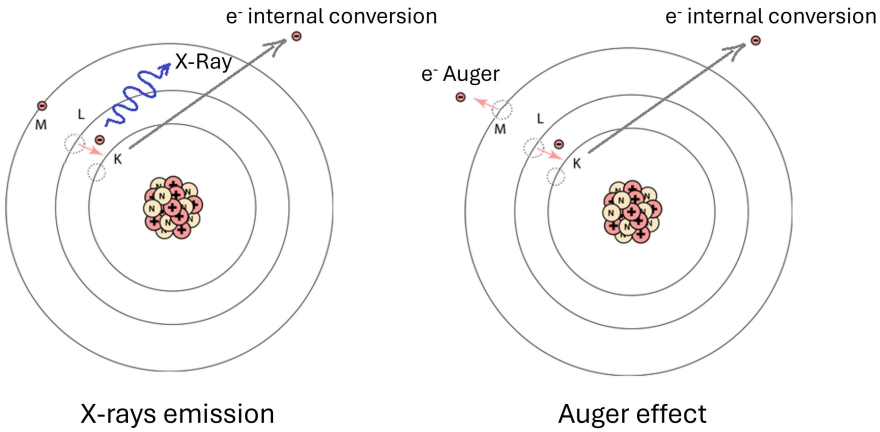

Figure I.2: Schematic diagram of the atom deexcitation by internal conversion, together with the possible emission of characteristic X-rays or Auger electrons.

the energy difference between the electron shells, therefore it is a characteristic energy of each atom. Energies range from one eV to several tens of keV for X-rays.

$$E_{R_X} = E_{Vacancy\ shell} - E_{Transition\ shell} \tag{I.2}$$

1.4.2 Auger Electron

The Auger Electron (AE) effect occurs when, during the emission of an X-ray photon, it transfers its energy to another electron in the shell, which is emitted from the atom [13]. The Auger electron energy corresponds to the difference between the primary electronic transition energy and the ionisation energy for the shell from which the Auger electron was emitted.

$$E_{AE} = (E_{Vacancy\ shell} - E_{Transition\ shell}) - E_{Auger\ shell} \tag{I.3}$$

2 Nuclear Medicine

Nuclear Medicine is the medical specialty that uses ionising radiation, based on the use of radiopharmaceuticals as radiation sources and allowing the diagnosis and medical treatment of diseases that usually have a great social impact [14]. In Nuclear Medicine a constant effort is devoted to produce new radiopharmaceuticals and molecular targets. This is to pioneer new treatment techniques, such as Targeted Radionuclide Therapies (TRNTs) and also to improve imaging for diagnostics with non- invasive methods. These techniques are typically applied for the diagnosis and treatment of cancer [15].

The effects of radiation depend on the amount of energy deposited per unit mass, the type of particles emitted and the organ or tissue affected. The Absorbed Dose (D) is the mean energy imparted (or expectation value of the energy imparted) ($\bar{\varepsilon}$) per unit mass to an infinitesimal volume [16]. The energy imparted (ε) by ionising radiation to the matter in a volume is the fundamental quantity of radiation dosimetry [16]. It is a stochastic quantity due to the random nature of both the emission of ionising particles from their sources and their interactions with matter [17].

2.1 Radiopharmaceuticals

As shown in Figure I.3, a radiopharmaceutical is a compound consisting of two main components: a carrier molecule and a radioactive atom. The carrier molecule, often referred to as the "vector molecule", directs the radiopharmaceutical to specific biological targets, such as organs or tissues, by exploiting metabolic or receptor mediated pathways. The radionuclide, known as the "information vector", emits radiation that can be detected for imaging purposes (γ-photons or β^+-particles for diagnostic applications) or used to deliver cytotoxic doses to the target tissue (α-, β^--particles or Auger electrons for therapeutic applications). Depending on the type of emitted radiation, the radiopharmaceutical is tailored for its intended clinical use [18].

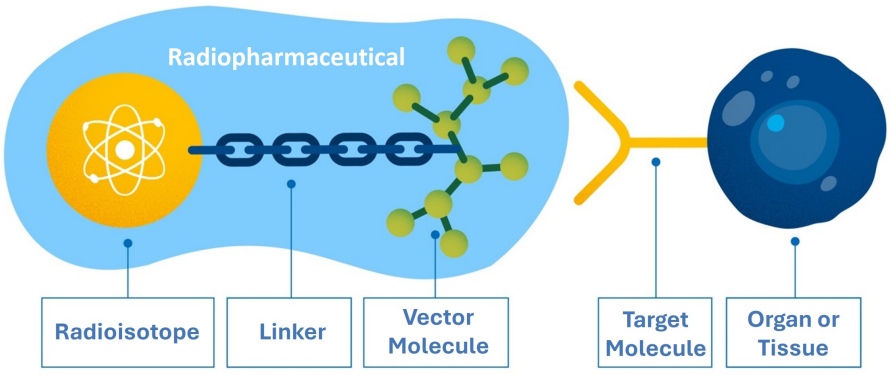

Figure I.3: Schematic diagram of a radiopharmaceutical. The vector molecule is able to recognise the target molecule overexpressed in organ or tissue [18].

The type of radiopharmaceutical to be used depends of each specific aim and tumour. Research into new molecular targets allows for more personalised and precision medicine, where the doses administered are safe and effective, with minimal toxicity to surrounding healthy tissue [19].

2.2 Radionuclides for nuclear imaging

Nuclear imaging is the technique used in Nuclear Medicine to perform diagnosis of human diseases. It is an ideal medical diagnostic tool: a non-invasive method to provide functional, morphological, three-dimensional, qualitative and quantitative information, simultaneously [19].

To obtain imaging of an internal organ or tissue, a radiopharmaceutical must be administrated to patients. The radiopharmaceutical must be optimised to reach the organ or tissue of interest and to distribute in suitable concentration in the structure that must be studied. A critical point for imaging techniques is the energy emission limit of radionuclides and the loss of sensitivity of detection systems with increasing emission energy. Currently, gamma camera, SPECT and PET are the main techniques for medical diagnosis with radioisotopes.

2.2.1 Single Photon Emission Computed Tomography (SPECT)

Single Photon Emission Computed Tomography (SPECT) technique is based on imaging by measuring the spatial distribution and concentration of the radioisotope in the body using scintillation cameras and gamma detectors [20]. The SPECT images provided are two-dimensional projections. To obtain a three-dimensional SPECT image, several two-dimensional images, acquired in different views around the patient, are combined following appropriate image reconstruction methods. The radiopharmaceutical radioactive component, should preferably be a pure γ-emitter with an emission energy between $100 - 400$ keV, the optimum energy for current SPECT detection systems [19].

^{99m}Tc as imaging radionuclide

The most common used radionuclide in SPECT diagnostics is ^{99m}Tc. It is estimated to be used in almost 85 % of the SPECT imaging diagnostics, which corresponds to about 40 million patient studies per year [21].

The ^{99m}Tc is a short half-life ($T_{1/2}$ = 6.01 h) pure gamma emitter at an energy of 140 KeV (89.0 % relative intensity) [22]. The energy of the emitted photon is high enough to exit from the organ or tissue of interest and be detected with external radiation. However, it does not cause damage to the biological tissues, and it does not generate image noise. Its energy is optimal for the efficiency of SPECT detectors (gamma cameras with crystals such as NaI(Tl)). In addition, its great advantage and what enhances its

high demand for clinical use is its easy availability, as it is obtained from the ^{99}Mo decay ($T_{1/2} = 65.92$ h) via ^{99}Mo/^{99m}Tc generator. This makes ^{99m}Tc available in hospitals on a daily basis, without the need for more comprehensive infrastructures such as cyclotrons.

2.2.2 Positron Emission Tomography (PET)

Another diagnostic imaging technique is the so-called Positron Emission Tomography (PET). This technique requires radioisotopes emitting β^+-particles. The emitted positron undergoes an annihilation process with an electron in the body within milliseconds after its emission, releasing two back-to-back γ-photons (511 keV) moving in opposite directions. The two photons generated by annihilation process are detected in coincidence during PET imaging. The detectors in PET scanners are scintillation crystals in the form of a circular ring coupled to photomultiplier tubes [23]. The patient is placed in a PET scanner to image the spatial and temporal evolution of the molecule labelled by the radioisotope.

Some of the main PET radioisotopes used in Nuclear Medicine are ^{18}F ($T_{1/2} = 109.77$ min), ^{11}C ($T_{1/2} = 20.36$ min), ^{13}N ($T_{1/2} = 9.96$ min) and ^{15}O ($T_{1/2} = 2.04$ min), all characterised by short half-lives where the most widely used is ^{18}F [11, 19]. The half-life of the radionuclide used in diagnostic imaging must be long enough to be produced, radiolabelled and transported to the medical facility, but it must also be short enough to reduce unnecessary doses to the patient and to allow relatively fast measurement processes. Typically, PET imaging centres require radioisotope production and purification facilities close to the hospital, such as low-energy proton cyclotrons and radiopharmacies.

Highly sensitive Nuclear Medicine techniques (SPECT and PET) can be combined with high-resolution techniques such as Computed Tomography (CT) to provide greater potential for precision diagnosis [24].

2.3 Radionuclides for therapy

The use of radionuclides for the treatment of diseases is based both on their favourable chemical properties to bind to molecules with affinity to organs or tissues, and their physical properties by which radiation doses are delivered selectively to target tissues through non-invasive systemic mechanisms, e.g. TRNTs [19]. In the case of oncological diseases, this radiation is used to cause direct or indirect damage to the DNA nucleus of tumour cells, aiming at cell death.

Radioisotope therapy procedures are performed with short range ionising particles, α-particles, β^--particles, Auger electrons or internal conversion electrons. The radiopharmaceutical is injected into the patient and transported by the vector molecule to the target organs or tissues. The radionuclide decays and emits particles that deposit their energy along the path. The way each particle deposit energy as a function of the distance in tissue is described by LET [25].

^{165}Er as therapeutic Auger electron radionuclide

^{165}Er is a pure radioisotope emitting Auger electrons and characteristic X-rays, without gamma radiation. Although its AEs can have maximal energies of tens of kiloelectron volts, 36.8 − 55.6 keV (4.8 %), most of the emitted AEs have very low energies 3.8 − 9.4 keV (65.4 %) [26]. These energies are deposited in less than 500 nm in tissues, because of their high LET, i.e. about 4 − 26 keV/μm of energy deposition per unit length [27]. This results in little or no damage to surrounding healthy tissues, when the radiopharmaceutical has internalised in the target organ or tissue.

Moreover, its half-life ($T_{1/2}$= 10.36 h) makes it suitable for convenient preparation and administration of the radiopharmaceutical, and it can be produced by direct production or by a ^{165}Tm/^{165}Er generator. Being a member of the lanthanide family, it has chemical properties similar to those of other elements used in therapy (e.g. ^{166}Ho), which facilitates its labelling chemistry.

Currently, ^{165}Er is a preclinical radioisotope and proof-of-concept radiolabelling studies have already been successfully performed by synthesising [^{165}Er]-Er-PSMA-617, which will be used *in vitro* and *in vivo* to understand the role of AEs in PSMA-targeted radionuclide therapy of prostate cancer [28, 29].

2.4 Theranostics

The concept of theranostics refers to the use of radiopharmaceuticals for diagnostic and therapeutic purposes in a minimum number of procedures.

This approach requires the administration of radionuclides, both to assess the location and extent of the tumour by diagnostic imaging, and for therapeutic effect (usually β^--emitters). For this purpose, different combinations of theranostic strategies can be used. One of them is to use the same vector molecule with two isotopic radioisotopes, such as ^{44}Sc/^{47}Sc or ^{123}I/^{131}I, in the same procedure. An alternative strategy would be to use a pair of radioisotopes with similar chemical properties such as ^{68}Ga/^{177}Lu (diagnostic PET/β^--particle therapy). In this case, two procedures are required.

However, there is the exception of theranostic radiopharmaceuticals that might be radiolabelled with a unique radioisotope capable of performing both functions, these kinds of radioisotopes are the so-called "theranostic radioisotopes" [30]. This is the particular case of the emerging radioisotope ^{177}Lu (diagnostic SPECT/β^--particle therapy).

Today, the concept of "theranostics" is already being implemented in clinical practice. It allows a more comprehensive approach to disease management, as nuclear imaging can offer several simultaneous functions. In addition, this therapy combines the high cytotoxic potential of β^--particles with the specificity of molecules directed at molecular targets, offering a promising therapeutic option in cases where other treatments have failed. Therefore, this area has a potentially high social impact. A necessary step for an extensive use of this strategy is to establish a reliable production network to ensure a

worldwide supply of theranostic agents to meet the growing demand for diagnostic and therapeutic radionuclides.

^{177}Lu as theranostic radionuclide

^{177}Lu ($T_{1/2}$ = 6.65 d) is one of the most promising theranostic radioisotopes used in Nuclear Medicine. What makes it special is the possibility to develop radiopharmaceuticals that combine diagnosis and therapy in a single procedure, owing to its ideal physical properties. It is a γ-emitter with peaks at 112.95 keV (6.23 %) and 208.37 keV (10.41 %) which makes it detectable by SPECT imaging. On the other hand, thanks to its 100 % emission of β^--particle ($\sim$ 496.8 keV) with short range is ideal for electron therapy [31].

It is currently being implemented in the clinic with the vector molecules DOTA-TATE and PSMA, which are aimed at the treatment and diagnosis of neuroendocrine tumours and prostate cancer, respectively [32, 33].

3 Radioisotope Production

Artificial radioisotopes used in Nuclear Medicine are obtained by bombarding stable nuclides with particles to produce nuclear reactions, whether in nuclear fission reactors or in accelerators (linears, synchrotrons, cyclotrons, etc). These technologies, together with generators, are the main ways of medical radionuclide supply today, and should be considered complementary.

3.1 Nuclear fission reactors

In 2023, there were a total of 413 reactors in operation worldwide. According to the latest information from the International Atomic Energy Agency (IAEA), as of June 2021, there were a total of 223 reactors employed for radionuclide production, scientific research and training, with 11 more under construction and 16 more planned. These reactors are distributed in more than 50 countries [34].

Neutrons are very effective in the production of radionuclides because they have no electrical charge. Therefore, they do not experience repulsion from the nucleus. The energies of neutrons produced in nuclear reactors vary widely (from cold, thermal, epithermal, fast and to ultrafast, depending on their speed and energy). In the production of radionuclides in the nuclear reactor, several aspects have to be considered: the nuclear reaction, the target nuclei, the irradiation conditions and the chemical treatment of the irradiated target.

However, the main advantage of nuclear reactor production is that the production cross-section of the radioisotopes of interest are usually very high. Therefore, large samples can be irradiated for a reasonably long time to obtain very high yields. There are several nuclear processes that can be triggered by the interaction of neutrons with the target material as a means of radioisotope production in nuclear reactors:

1. **(n,γ) Reactions:**
   This reaction takes place with thermal neutrons at energies close to 0.025 eV and velocities of $2.2{\cdot}10^5$ cm/s.

   $$ {}^{A}_{Z}X + {}^{1}_{0}n \rightarrow {}^{A+1}_{Z}X + \gamma $$

   The radionuclide produced is an isotope of the target nuclide, so it is not possible to separate it chemically. In order to obtain significant specific activities, it is necessary to use enriched targets with a high cross-section. This is the case of production ^{177}Lu at nuclear reactor using ^{176}Lu enriched or ^{99}Mo using enriched ^{98}Mo targets.

2. **(n,γ) Reactions followed by decay:**
   This reaction is one of the most frequent in the production of radionuclides. Target

nuclei with a mass number one unit higher decay by emission of β^--particles in the radioisotope of interest. This kind of reactions takes place with thermal neutrons.

$$ {}^{A}_{Z}X + {}^{1}_{0}n \rightarrow {}^{A+1}_{Z}X \rightarrow {}^{A+1}_{Z+1}Y + e^- + \bar{\nu} $$

In this case the final radionuclide is not an isotope of the target nucleus. Therefore, the final product will be free of isotopic impurities and a high specific activity will be obtained. This is the case of production of ^{177}Lu at nuclear reactor using ^{176}Yb enriched targets.

3. **(n,p) or (n,α) Reactions:**
(n,p) or (n,α) reactions take place with fast neutrons ($1-20$ MeV and $\sim 10^9$ cm/s). The radioisotope produced is not an isotope of the target, so it has a high specific activity. However, the final radioisotope yield after irradiation is much lower than that achieved in (n,γ) reactions, since only a small part of the neutron flux in the reactors reaches high energies and the cross-section values for this type of nuclear reactions sometimes have threshold energies of the order of MeV.

$$ {}^{A}_{Z}X + {}^{1}_{0}n \rightarrow {}^{A}_{Z-1}Y + {}^{1}_{1}H $$
$$ {}^{A}_{Z}X + {}^{1}_{0}n \rightarrow {}^{A-3}_{Z-2}Y + {}^{4}_{2}He $$

Therefore, conventional nuclear reactors would not be the ideal facilities to enhance pathways for the production of radionuclides by such nuclear reactions.

4. **(n,2n) or (n,xn) Reactions:**
(n,2n) or (n,xn) reactions take place with fast neutrons. In this case, radioisotopes produced are the same element that the target isotope, so the use of enriched target is essential to achieve high specific activity. However, these reaction routes (above 1 MeV energy threshold) are not usual in conventional nuclear reactors.

$$ {}^{A}_{Z}X + {}^{1}_{0}n \rightarrow {}^{A-(x-1)}_{Z}X + x({}^{1}_{0}n) $$

This would be an alternative production route of production ^{99}Mo/^{99m}Tc using enriched target via ^{100}Mo(n,2n) nuclear reaction.

5. **Fission reactions:**
The most common neutron bombardment is of ^{235}U and ^{239}Pu targets which fission lead to a huge variety of radionuclides, some of which have characteristics suitable for use in *in vivo* studies. Among the most commercial radionuclides produced in a nuclear fission process are the following: ^{99}Mo, ^{89}Sr, ^{90}Y, ^{131}I, ^{132}Te, ^{133}Xe, mainly.

3.2 Generator systems

Certain radionuclides give rise to another nuclide as a consequence of their decay. The former isotope is called "parent nuclide", while the latter isotope is called "daughter nuclide".

Therefore, a generator can be defined as any system incorporating a radioactive nuclide parent which, in its disintegration, gives rise to a daughter radionuclide, which will be used as an integral part of a radiopharmaceutical. The most typical case, commercially available, is the ^{99}Mo/^{99m}Tc generator [37].

The separation of radionuclides in a generator system is based on the difference in chemical properties of the parent-daughter pair, since in any natural nuclear decay, the parent and daughter isotopes have different atomic numbers (Z) and therefore different chemistry, with the exception of the isomeric transition[1] (IT), where both nuclei are the same chemical element. Among the different techniques developed for the separation of the daughter nuclide, we can highlight the column chromatography [38]. This technique is universally adopted due to its low complexity, high elution yields and its ability to be incorporated into a closed system.

Chromatographic generators are based on the separation of the parent nuclei from the daughter nuclei due to their interaction between the mobile and the stationary phases. The adsorbent material (also called stationary phase) is placed in a glass chromatographic column. This stationary phase usually consists of porous micro-spheres of varying diameter and internal surface area, which allow the eluent (mobile phase) to pass through.

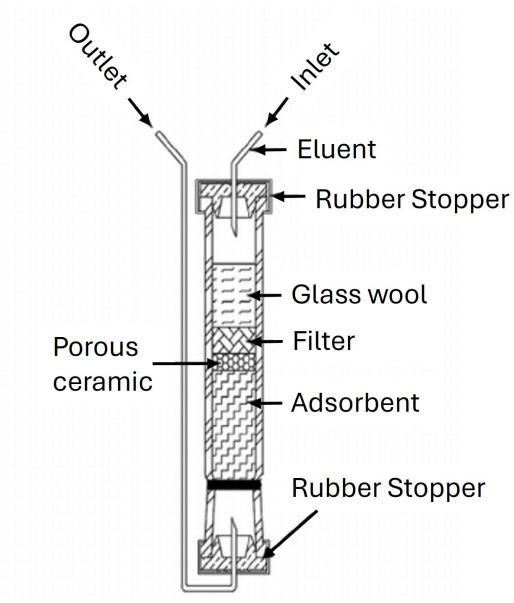

Figure I.4: Schematic diagram of a chromatographic generator systems.

[1] An isomeric transition or internal transition (IT) is the decay of a nuclear isomer to a lower-energy nuclear state. The process has two modes: γ-ray emission or internal conversion (IC)

The mobile phase, which can be aqueous or organic, moves the sample through the column, and the selective radiochemical separation and elution rate depend on their relative affinity for both phases [38]. Because the daughter radionuclide has a different affinity for the mobile phase than the parent radionuclide, it is the daughter nucleus that dissolves in the mobile phase and is carried off the column, while the parent nucleus remains attached to the stationary phase.

3.3 Cyclotrons

In 2024, there were 1269 cyclotrons around the world, located in 95 countries. Most of them are fully or partially used for radioisotope production [35].

Accelerators were constructed to respond to the need of particle beams with controlled direction, intensity and energy, since much of the knowledge of nuclear physics has arisen from experiments in which the nucleus has been bombarded with high-energy particles. Thus, devices such as cyclotrons, betatrons, Van der Graff generators, linear particle accelerators have been developed.

An important group of accelerators are those in which charged-particles follow circular trajectories, receiving additional cumulative energy at each revolution, giving them high velocities after a suitable number of them. The most commonly used positive ions in nuclear experiments are protons, deuterons and helium nuclei (α-particles).

Figure I.5 shows the schematic plant of a cyclotron. The cyclotron is the fundamental accelerator in the production of radionuclides. It was devised by Lawrence and Livigston (1931) to produce high-energy particles. It consists essentially of two semicircular flat metal chambers called "D" because of their similarity to the letter D. These "Ds" are located inside a metal cylinder between the poles of an electromagnet, so that the magnetic field is perpendicular to the base of the cylinder and parallel to the axis. At the centre of "Ds" tens of kV will be applied as an initial voltage.

The "Ds" are isolated from each other and kept under vacuum. They are connected to a high-frequency oscillator which creates an electric field between them and causes the sign of the voltage to change about 10^7 times per second. A filament is placed between the plates which, when it becomes incandescent, emits electrons. These electrons are made to flow over a gas, previously placed in the vacuum chamber, dissociating and ionising its molecules and giving rise to protons, deuterons or alpha particles. Most modern accelerators now use external ECR sources.

When a charged-particle leaves the source, it is accelerated within the "Ds" in one direction or the other by the action of the electric field set up by the oscillator. The circular trajectory of the particle is given by the action of the magnetic force experienced, as described in Equation (I.5). The frequency of the oscillator and the strength of the magnetic field are adjusted so that when the particle reaches the edge of the "D", the electric field changes, giving the particle an acceleration and causing it to jump and circle around the "D" opposite, increasing its velocity and travelling along a path of increased

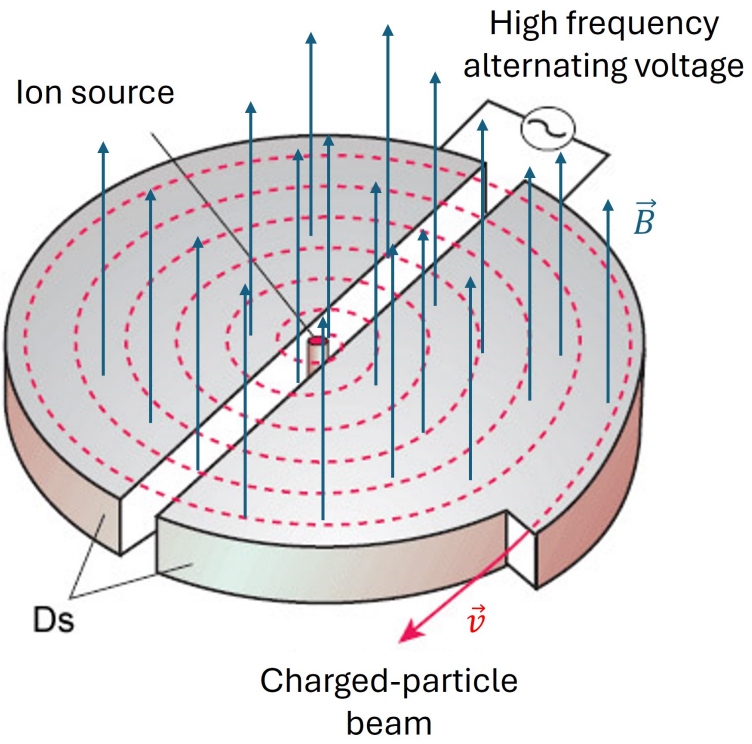

Figure I.5: Schematic diagram of a cyclotron plant [36].

radius. The process is repeated successively when the particle reaches the edge of the "D" again.

$$\overrightarrow{F} = q\,(\overrightarrow{E} + \overrightarrow{v} \times \overrightarrow{B}) \tag{I.4}$$

$$r = \frac{m \cdot v}{|q| \cdot B} \tag{I.5}$$

The charged-particles can be extracted at different points during their acceleration, redirecting them to an experimental room where they will interact with the target sample to produce a nuclear reaction.

The main advantage of low energy cyclotrons is the possibility to easily produce short half-life radionuclides, such as the β^+ emitters, specifically ^{11}C, ^{13}N, ^{15}O and ^{18}F, which are widely used for diagnostic by PET imaging. Moreover, due to their more compact size and lower complexity, they can be built close to hospital sites. The most common clinical radioisotope production is by proton beam, but deuteron beams, tritons or α-particles can also be used, although less frequently.

3.4 Linear accelerators

In 2022, according to the latest information from the International Atomic Energy Agency (IAEA), there were about 1000 medical linear accelerators (Linacs) in worldwide [39].

In recent years, in addition to the use of nuclear reactors and cyclotrons, Linacs have been proposed as an alternative method for radionuclide production. Unlike cyclotrons, Linacs do not deflect the particle trajectory in a circular path by means of a magnetic field. Radio Frequency Linacs are devices that use high-frequency electromagnetic waves to accelerate charged-particles in a straight line, which can be a few metres or several kilometres long.

RF Linacs can be a valid alternative to nuclear reactors or cyclotrons for radioisotope production. For example, at Brookhaven National Laboratory (Upton, NY, USA) [40], a proton beam of up to 200 MeV energy and 165 μA of current is generated by the Linac and it is used both for medical radionuclide production and fundamental physics research, or PULSAR-7 [41], developed by ACCSys (Pleasanton, CA, USA), characterised by 7 MeV accelerated protons and over 150 μA of current.

The main advantage of RF Linacs over cyclotrons is that the complex and heavy magnet system is not needed and high-current particle beams can be achieved. They are mainly used in industrial applications and, to a lesser extent, in radioisotope production. RF Linacs are devices designed to accelerate charged-particles of a single type, such as electrons or protons, to high energy and with a single beam output. This means that the RF Linac is designed for the specific production of a radioisotope.

The DONES high-intensity linear accelerator offers a unique opportunity for more versatile radioisotope production. It will deliver a 40 MeV deuteron beam with a current of 125 mA. Furthermore, the spallation process will generate a high neutron flux, enabling the simultaneous irradiation of multiple samples after de HFTM. The following chapters explore in detail several clinically relevant radioisotopes, including ^{165}Er, ^{177}Lu and ^{99}Mo/^{99m}Tc, which could potentially be produced at the IFMIF-DONES facility.

Chapter II

Nuclear Radioisotope Production Data

The International Atomic Energy Agency (IAEA) is proposing to explore new routes for radioisotope production and to increase the number of facilities working for medical applications, as an alternative to traditional nuclear reactor, which suffer continuous supply shortages due to their ageing and maintenance operations [42]. These new facilities shall have the capacity to generate radioisotopes relevant to Nuclear Medicine. MEDICIS at Isolde (CERN) [43] represents an excellent example of this new model, or the future International Fusion Materials Irradiation Facility-DEMO Oriented Neutron Source, which will also be an ideal setting for it.

However, for the production of new and/or conventional radioisotopes by alternative production routes, a thorough knowledge of the nuclear data of the nuclear reactions involved in these production pathways is essential for a robust feasibility assessment.

In this chapter, the stacked-foil technique for the measurement of nuclear reaction cross-sections for radionuclides produced by charged-particle beams, mainly deuterons, will be developed in detail. In addition, the experience and results obtained during two international collaborations on nuclear data experiments of deuteron-induced nuclear reaction cross-sections are presented. The motivation for these experimental measurements was the lack of nuclear data in certain energy regions which made it difficult to precisely define the nuclear evaluation of the cross-section up to 40 MeV, or the lack of nuclear data for certain metastable impurities relevant to the study.

The first colaboration took place at the *Conditions Extrêmes et Matériaux: Haute Température et Irradiation* (CEMHTI) of the *Centre National de la Recherche Scientifique* (CNRS) (Orleans, France) [44] and involved the measurement of the cross-section of the reaction ^{nat}Ho(d,2n)^{165}Er and its main impurities ^{nat}Ho(d,p)^{166g}Ho,^{166m}Ho up to 17.5 MeV deuteron energy. The second collaboration involved the measurement of the nuclear reaction ^{nat}Yb(d,x)^{177cum}Lu, plus numerous impurities, as well as, the upper limit of its isotopic impurity ^{177m}Lu, and took place at the GIP ARRONAX cyclotron (Saint-Herblain, France) [45] up to 33 MeV deuteron energy.

1 Charged-particles cross-section

In nuclear physics, the cross-section is the physical quantity that expresses the probability of interaction between an incident particle and a target nucleus for a nuclear reaction to take place. The cross-section is a measure of the "effective" area and it depends on the energy of the incident particle. It is denoted by the letter *sigma*, σ, and measured in units of area in barn, where 1 barn equals 10^{-24} cm^2 [46].

A solid knowledge of nuclear cross-section data is essential for the estimation of radionuclide production rates. In this framework, it will be crucial for feasibility studies of alternative routes of radioisotope production for Nuclear Medicine by deuteron-induced nuclear reactions, one of the two types of particles available in the future IFMIF-DONES facility.

A comprehensive study of radioisotope production will make it possible to assess in advance the feasibility of producing certain radioisotopes in terms of reaction yield, purity and quality of the proposed final product by new alternative routes. The main data that could be extracted from charged-particle-induced nuclear reaction cross-section measurements for the optimisation of radioisotope production are:

- Ideal production energy range, which maximises the production of the radioisotope of interest but minimises the production of unwanted radioisotopic impurities in the final irradiated product.

- Expected Thick Target Yield (TTY) of radioisotopes produced as a function of the irradiation time. The particle flux varies as a function of target depth, so for the use of thick targets, the value of the final activity of a particular radioisotope can be calculated without difficulty by numerical integration of the production rate as a function of energy, if the value of the excitation function is well known.

The excitation functions represent the energy-dependent cross-section function. Experimental values of the cross-section at certain energies are measured using thin targets (a few tens of micrometres), where the energy loss of the particles due to their interaction with matter is negligibly small, so that the particle flux per target depth remains constant throughout the thickness of the foil. This consideration is preferable in order to simplify measurement calculations. In addition, the experimental measurement of cross-sections is performed with cheaper thin samples of natural isotopic composition. As a result, multiple radioisotopes may be produced alongside the isotope of interest, providing a more complete study in terms of impurities.

On the other hand, for the production of radioisotopes for medical purposes, thick and highly enriched samples are irradiated to increase the activity produced but at the same time minimising the co-production of impurities. The presence of radioactive impurities in the final product only increases an unwanted dose to the patient without any clinical

benefit. Therefore, the objective will be to maximize the radionuclide purity, isotopic purity and specific activity of the radioisotope of interest in the final product. These control quantities regulate the quality of the final product for clinical use, as explained below.

- Radionuclide purity (RNP). It is defined as the activity ratio of the radionuclide of interest and the total activity produced in the sample, expressed as a percentage. When these radionuclides are radioisotopes of the same element, the radionuclide purity coincides with the radioisotope purity.
- Isotopic purity (IP). It is the ratio of the number of atoms of the radioisotope of interest and the total number of atoms of isotopes produced in the sample, both radioactive and not, expressed as a percentage.
- Specific activity (SA). This is the activity of a radioisotope divided by the mass of the target to which both the stable and unstable nuclei contained contribute. It is usually expressed in units of Bq/g and should be as high as possible, which means that there will be no competition between atoms in some chemical processes such as labelling processes [47].

It is important to note that all three quantities are time-dependent. For this reason, both sample irradiation times and post-irradiation cooling times up to the synthesis of the radiopharmaceutical and administration to the patient will be relevant.

1.1 Physical formalism

A nuclear reaction is denoted as $A(x,y)B$, where the target nucleus, A, is bombarded by an incident particle or projectile, x, producing a residual nucleus, B, and the emission of light particles, y. The residual nucleus production rate, R_B [atm/s], is the product of the number of incident particles and the probability of particle-nucleus reactions along the target thickness. Assuming a thick target, it must be integrated in energy, being the integration limits the energy of the incoming particles and their residual energy as they exit the target [48]:

$$R_B = \int_{E_{in}}^{E_{out}} \chi \cdot n_A \cdot \phi(E) \cdot \sigma(E) \cdot R(E)\ dE \tag{II.1}$$

where, χ is the isotopic and chemical purity of the target, n_A is the target nucleus density [atm/cm^3], $\phi(E)$ is the beam intensity of the incident particles [s^{-1}], $\sigma(E)$ is the cross-section [cm^2] and $R(E)$ is the range of projectile in the target [cm].

For heavy charged-particles, the range corresponds to the length of their trajectory, since it is practically rectilinear. This quantity is inversely proportional to the stopping

power. When a charged-particle interacts with matter, it loses its energy in successive interactions. An important quantity in the quantitative description of energy loss is the stopping power, $S(E)$, which is defined as the particle energy loss per unit length,

$$S(E) = -\frac{dE}{dx} \tag{II.2}$$

Therefore, the range can be redefined in terms of the stopping power and the energy of the heavy charged-particle as:

$$R(E) = \int_0^R dx = \int_{E_{in}}^{E_{out}} -\frac{dE}{S(E)} \tag{II.3}$$

The stopping power depends on the properties of projectile, such as its velocity, charge and mass and the properties of the material. However, in order to tabulate the stopping power as a function of the energy and type of particle in a given medium (Z), an artifice is used that avoids the dependence on density (otherwise it has to be tabulated for each density of the same Z). This mathematical artifice involves working with the mass stopping power, i.e. the energy loss per unit mass thickness, defining the mass thickness as the product of the geometric thickness and the density of the medium, $\tau = n_A \cdot x$ [atm/cm^2]:

$$S(E) = \left(-\frac{dE}{d\tau}\right) = -\frac{1}{n_A}\left(\frac{dE}{dx}\right) \tag{II.4}$$

Writing the production rate for thick targets as,

$$R_B = \chi \int_{E_{out}}^{E_{in}} \frac{\phi(E) \cdot \sigma(E)}{S(E)}\, dE \tag{II.5}$$

where E_{in} and E_{out} are the energies of the charged-particle at the inlet and outlet in matter.

Whereas, assuming a thin target, the production rate can be estimated as:

$$R_B = \chi \cdot \tau \cdot \phi(E) \cdot \sigma(E) \tag{II.6}$$

where, τ is the mass target thickness, $\phi(E)$ and $\sigma(E)$ are the average flux and cross-section in the target, respectively.

Therefore, the number of atoms produced at the end of the irradiation of a thin target can be expressed as a function of the production rate as follows:

$$N_{B_0} = R_B \cdot \frac{(1 - e^{-\lambda_B \cdot t_{irr}})}{\lambda_B} = \chi \cdot \tau \cdot \phi(E) \cdot \sigma(E) \cdot \frac{(1 - e^{-\lambda_B \cdot t_{irr}})}{\lambda_B} \tag{II.7}$$

where λ_B is the decay constant of the nucleus produced [s^{-1}] and t_{irr} is the irradiation

time [s]. N_{B_0} is the number of atoms produced during the irradiation. From now on, the instant of the End of the Bombardment (EOB) will be denoted as "time zero". The development of this formula is detailed in the Appendix A.

Experimentally, the number of activated atoms can be measured by the activity of the sample ($A = \lambda \cdot N$). Taking all this into account, the cross-section as a function of the energy, can be calculated as follows:

$$\sigma(E) = \frac{A_{B_0}}{\chi \cdot \tau \cdot \phi(E) \cdot (1 - e^{-\lambda_B \cdot t_{irr}})} \tag{II.8}$$

The cross-section uncertainty can be estimated in the standard way. Independent relative errors of the linearly contributing processes are summed quadratically and the square root of the sum is taken. The uncertainties considered in the cross-section measurements in each case are as follows: residual nucleus activity, sample thickness and the incident number of particles per time unit, while the uncertainties in the target density or the decay constant are small compared to the above and can be negligible. Since the parameters in Equation (II.8) are independent, the uncertainty can be written as follows:

$$(\Delta\sigma)^2 = (\Delta A_{B_0})^2 + (\Delta\tau)^2 + (\Delta\phi)^2 \tag{II.9}$$

1.2 Activation method: Stacked-foil technique

The stacked-foil technique is an activation method that involves stacking a series of thin foils one behind the other to make several cross-section measurements at different energies [49]. The method is convenient because the cross-sections vary continuously depending on the slowing down of the charged-particles in the irradiated material. The use of thin foils means that the energy loss of the charged-particles due to its interaction with matter is negligibly small in the thickness of the foil, therefore the energy and flux of particles per depth of the thin foil remains almost constant inside it.

The thickness of the thin target foils used in the stacked-foil technique is in the order of a few tens of micrometres. The stack is a set of several identical patterns, each consisting of a target foil and several monitor foils, separated by a thick foil, which acts as a degrader, allowing us to study differentiated energy sets between the different foil patterns in the stack. Figure II.1 shows a diagram of a stack on which a beam of charged-particles impinges, represented by the black dashed arrow. The target foils of interest, where the nuclear reaction under study takes place, are depicted in blue. Next foils, in green, are the monitor foils used to determine the particle flux. Moreover, it is possible that, after a nuclear reaction, the nucleus formed has enough energy to leave the foil. These nuclei are called recoil nuclei[1] and, if not correctly quantified, will lead to an error in the cross-section

[1]Atomic recoil is the result of the interaction of an atom with an energetic elementary particle. As a consequence of the linear momentum conservation of the system, the momentum of the interacting particle is transferred to the atom, causing the nucleus to be displaced from its normal position.

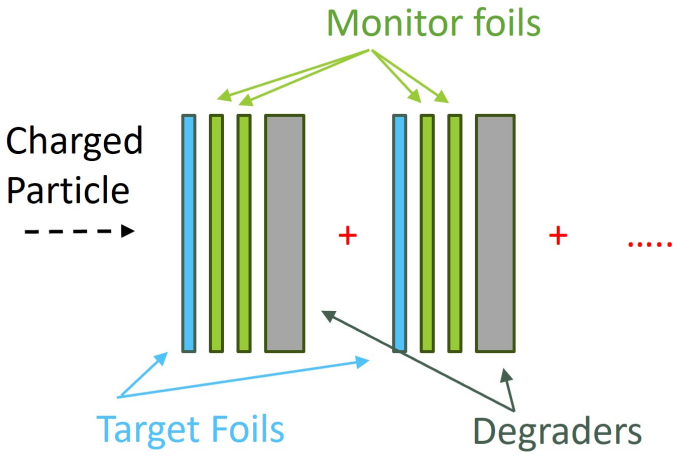

Figure II.1: Schematic diagram of the stacked-foil activation method.

measurement. Therefore, monitor foils will have a second function, to retrieve possible recoil nuclei from the target or from the first monitor foil. Finally, between each pattern, in grey, a thick foil of variable thickness called degrader is placed to reduce the beam energy for the next pattern, allowing measurement in equispaced energies.

The stacked-foil technique allows the calculation of the cross-section by a relative method. This consists of an initial determination of the particle beam flux from the monitor foils. These foils, strategically located in the stack, will produce several nuclear reactions, for which cross-sections are well known. The International Atomic Energy Agency (IAEA) provides reference nuclear reaction cross-sections for different projectiles over a wide range of energies [51]. One of the main advantages of this relative method for beam flux calculation is its easy implementation during irradiation experiments. As well as, the versatility in the placement of the monitoring foils or the number of them to perform the beam flux measurements within the stack.

From the reactions occurring in the monitor foils, the particle beam flux through the stack is determined using the formula for activated nuclei for thin targets described in Equation (II.7). The parameters concerning the monitoring foils are indicated with an apostrophe.

$$\phi'(E') = \frac{A'_{B_0}}{\chi' \cdot n'_A \cdot \tau' \cdot \sigma'(E') \cdot (1 - e^{-\lambda'_B \cdot t_{irr}})} \tag{II.10}$$

Since the experiments performed during this thesis use a juxtaposed target and monitor foils, each a few tens of micrometres thick, we can assume that the beam flux through the target foil is the same as that through its juxtaposed monitor foil, hence $\phi(E) = \phi'(E')$.

The average energy of particles crossing the monitor foil or reaction foil and its uncertainty can be estimated by means of Monte Carlo simulation programmes for the study of particle transport in matter, such as Stopping and Range of Ions in Matter

(SRIM) 2003 software [50]. The energy uncertainty of the beam in each irradiated foil may be estimated including cumulative effects such as uncertainty in the primary beam energy, stopping estimation influenced by target thickness and beam straggling, all of which can also be estimated by Monte Carlo simulation.

Finally, the activity determination in the activated foils, for the correct implementation of the method, will be carried out experimentally by means of a High Purity Germanium detector (HPGe), which will be described in depth in the following section.

1.3 High purity germanium detector (HPGe) spectrometry

After foil activation, using the stacked-foil technique, a suitable system will be required to measure the activation energy spectra of the individual foils. In the case of X-ray characteristic and γ-radiation spectrometry, the most suitable energy resolution is achieved by crystal counters such as High-Purity Germanium (HPGe) semiconductor detectors, coupled to a multi-channel analyser, which allow photons to be discriminated by their energy.

When ionising radiation passes through a semiconductor such as a HPGe crystal, it generates abundant electron-hole pairs. A hole consists of a missing electron in the interatomic bonds of the crystal structure, which can move through the crystal volume, and its properties resemble a positive ion. The energy resolution of a germanium detector depends on the fluctuations on the number of charges [12].

Due to the high nuclear charge, Z, of germanium, ionising particles lose all their energy in a very short time. Thus, β-particles that can travel several metres in air, are completely absorbed in a few millimetres of germanium. Therefore, a high detection efficiency per unit volume of the detector can be achieved. On the other hand, germanium has a band gap of 0.7 eV, giving rise to a large bulk leakage current caused by thermal electron-hole pair creation in the depletion region. This current gives rise to an unacceptable noise and therefore germanium detectors must be used at reduced temperature, usually liquid nitrogen ($\sim$ 77 K).

In order to calculate the activity of a radioisotope detected with this n-type of detectors, it is necessary to know both the number of pulses or counts (area of the photopeaks) that have been detected at a certain energy, and the efficiency or detection performance (number of events recorded by the detector/ number of events emitted by the sample) at that energy. However, the detector efficiency depends on both the radiation energy and the sample-detector geometry. Therefore, to calculate the activity of the irradiated sample, not only an energy calibration of the detector must be performed, but also an efficiency calibration, where the relationship between detector efficiency and energy is well known.

The energy and efficiency calibration procedure required for an HPGe detector will be detailed below, as well as an interpretation of a detected spectrum profile according to the mechanisms of interaction of photons with matter.

1.3.1 Energy calibration

A photon-emitting radionuclide is characterised by the following properties, which can be found in databases such as, Livechart of Nuclides developed by International Atomic Energy Agency (IAEA) [11] or NuDat (3.0) developed by the National Nuclear Data Center (NNDC) [52].

a) Energy and relative intensity of gamma lines (E_γ and I_γ).

b) Radionuclide half-life ($T_{1/2}$).

The aim of the energy calibration is to obtain the relationship between the spectrometer channel number where the detected pulses are collected and the associated energy value. Energy calibration sources such as ^{152}Eu, ^{133}Ba or ^{241}Am, whose energies and intensities associated with the emitted γ-photons are well known, are used to relate the spectrometer channels to an energy value, allowing the identification of any other photon-emitting radionuclides.

The ^{152}Eu source has two branches: EC, 72.08 %, and β^-, 27.92 %, emitting gamma energy ranging from 120 keV up to 1.4 MeV. The ^{133}Ba source decays by EC, 100 %, emitting gamma energy ranging from 80 keV up to 360 keV. While the ^{241}Am source decays α mode, 100 %, and emits a single gamma at 59.5 keV energy. For the energy calibration measurements, the gamma peaks used are summarized in Table II.1, which correspond to their most intense γ-rays.

Source	Half-life, $T_{1/2}$ (year)	Energy, E_γ (keV)	Intensity, I_γ (%)
^{152}Eu	13.517	121.8	28.6
		244.7	7.6
		344.3	26.5
		411.1	2.2
		778.9	12.9
		867.4	4.2
		964.0	14.6
		1085.8	10.2
		1112.1	13.6
		1212.9	1.4
		1299.1	1.6
		1408.0	21.0
^{133}Ba	10.551	81.0	32.9
		302.9	18.3
		356.0	62.1
^{241}Am	432.6	59.5	35.9

Table II.1: Most intense γ-peaks of the ^{154}Eu, ^{133}Ba and ^{241}Am radioactive sources.

For X-ray characteristic or γ-ray spectroscopy, linear representation between the energy of each photopeak with the corresponding channel from the acquisition system is adequate for calibration in energy:

$$E(c) = a_1 + a_2 \cdot c \tag{II.11}$$

The coefficients a_1 and a_2 are the linear fit parameters of the energy calibration.

1.3.2 Efficiency calibration

The aim of an efficiency calibration is to correlate the number of pulses or counts accumulated in the photopeak of the spectrum to the activity in disintegrations per second of the photon-emitting radionuclide corresponding to that energy.

Therefore, the efficiency calibration consists of obtaining the empirical function that relates the counting efficiency of the detector as a function of energy for the geometrical sample-detector distance used. Its definition is the ratio between the number of counts per second at each detected photopeak, and the number of γ-rays emitted from the target, which are calculated as the product between the activity of the sample and the relative intensity of each emitted γ-line.

$$\varepsilon(E_\gamma) = \frac{C_{peak}(E_\gamma)}{LT \cdot A \cdot I(E_\gamma)} \tag{II.12}$$

where, $\varepsilon(E_\gamma)$ is the detector efficiency as a function of photon-energy, C_{peak} are the net counts of the photopeak, LT is the Live Time of the measurement [s], A is the activity of the sample [s^{-1}] and $I(E_\gamma)$ is the intensity of the energy photon-emission.

Two correction factors must be taken into account as a consequence of the time elapsed between the EOB and the end of measurement at the HPGe:

- Natural activity decay as a function of time, where t_c is the cooling time EOB and the beginning of activation measurement.

$$A(t = t_c) = A_0 \cdot e^{-\lambda \cdot t_c} \tag{II.13}$$

- Decay factor of the nuclei during the measurement time. During the measurement time or Real Time[2], the activity of the sample is not constant, but decreases. To correct for this effect, the average activity during the measurement is considered:

$$< A(t = RT) >= \frac{1}{RT} \int_0^{RT} A_0 \cdot e^{-\lambda \cdot t_c} \cdot e^{-\lambda \cdot t} dt \tag{II.14}$$

[2]Real Time (RT) is given by the sum of Live Time (LT) and the Dead Time (DT) of the detector. Each recorded event inhibits the measurement capability of the detector for a period of dead time, producing a mismatch between the number of observed and real events.

$$< A(t = RT) >= A_0 \cdot e^{-\lambda \cdot t_c} \cdot \frac{(1 - e^{-\lambda \cdot RT})}{\lambda \cdot RT} \tag{II.15}$$

It follows that the efficiency calibration will be given by:

$$\varepsilon(E_\gamma) = \frac{C_{peak}(E_\gamma)}{LT \cdot A_0 \cdot I(E_\gamma)} \cdot e^{\lambda \cdot t_c} \cdot \frac{\lambda \cdot RT}{(1 - e^{-\lambda \cdot RT})} \tag{II.16}$$

The semi-empirical formula between efficiency calibration and energy can be approximated to a typical relationship of the type form:

$$\varepsilon(E) = \sum_{i=0}^{5} b_i \cdot ln(E)^i \tag{II.17}$$

where the coefficients b_i are the fit parameters of the efficiency calibration. The energy and efficiency calibration of the detectors used in the context of this thesis are exemplified and detailed in Appendix B.

Radionuclides emitting γ-rays at different energies will produce total absorption peaks in the spectrum at each of these energies. It will then be possible to calculate the activity from all these peaks. The activity associated with each γ-peak is calculated using the following relation:

$$A_0^{(E_\gamma)} = \frac{C_\gamma}{LT \cdot \varepsilon_\gamma \cdot I_\gamma} \cdot e^{\lambda \cdot t_c} \cdot \frac{\lambda \cdot RT}{(1 - e^{-\lambda \cdot RT})} \tag{II.18}$$

where the uncertainties considered in the activity measurements in each peak are as follows: net counting of the peak gamma areas, detector efficiency and γ-ray intensity, while the uncertainties in the Live Time, Real Time or the decay constant are small compared to the above and can be negligible. Since the parameters in Equation (II.18) are independent, the uncertainty can be written as follows:

$$\left(\Delta A_0^{(E_\gamma)}\right)^2 = (\Delta C_\gamma)^2 + (\Delta \varepsilon_\gamma)^2 + (\Delta I_\gamma)^2 \tag{II.19}$$

Finally, the activity of the radionuclide is derived by taking an uncertainty-weighted average.

$$< A_{B_0} >= \frac{\sum_{E_\gamma} \left(A_0^{(E_\gamma)} / (\Delta A_0^{(E_\gamma)})^2\right)}{\sum_{E_\gamma} \left(1/(\Delta A_0^{(E_\gamma)})^2\right)} \tag{II.20}$$

$$(\Delta < A_{B_0} >)^2 = \frac{1}{\sum_{E_\gamma} \left(1/(\Delta A_0^{(E_\gamma)})^2\right)} \tag{II.21}$$

1.3.3 Interaction of photons with matter: γ-ray spectrum profile

Electromagnetic radiation differs markedly from its interaction with matter, with respect to charged-particles. For charged-particles, the energy is gradually lost with each collision until they are slowed down and absorbed. However, when a beam of electromagnetic radiation strikes a thin absorber, each photon lost by the beam results from a single process (absorption or scattering), called attenuation of the radiation.

The internal mechanism of attenuation of a photon beam is complex as it results from the superposition of several independent processes of which the most likely are the photoelectric effect, Compton scattering and pair production [12]. The superposition of the above-mentioned effects can be identified in Figure II.2, a scheme common to all γ-spectra profile as shown, which is important when analysing the data from an HPGe in order to take all these phenomena into account.

Due to the photoelectric effect, the gamma emitted by the activated foil will transmit all its energy to an electron in the medium. This collected electron will deposit its energy in the detector, leading to the formation of the total absorption peak (photopeak) at the energy of the incident gamma photon.

Because of Compton scattering, the photon emitted by the activated foil will transmit part of its energy to an electron in the medium which will deposit its energy in the detector, while the photon will be able to escape from the detector without depositing its residual energy. Therefore, the detector will collect less energy than the incident photon. In addition, as the scattering angle of the Compton effect is variable, the energy collected varies from one photon to another. This will result in the creation of a background in the spectrum called the Compton Background together with its characteristic edge.

Finally, as a consequence of the pair production mechanism, the annihilation of an electron-positron pair results in the emission of two 511 keV γ-photons, emitted in opposite directions. When one or both of the 511 keV photons escape from the detector

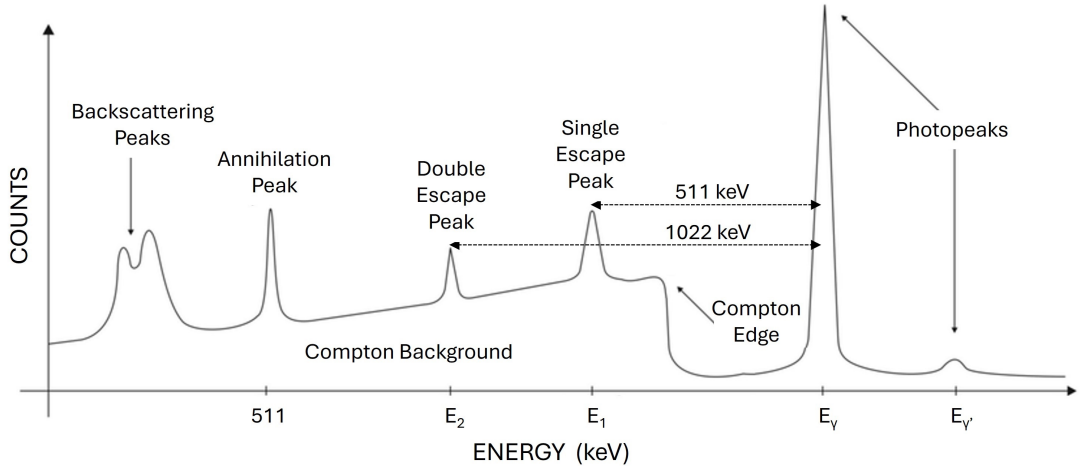

Figure II.2: Base scheme of a γ-spectrum profile recorded by an HPGe detector.

without depositing their energy in it, the escape peaks appear. Their positions will be at the corresponding energy of the main γ-photon which would be detected as a photopeak minus 511 keV or 1022 keV, for the single or double escape peak, respectively.

Another interesting effect is backscattering, producing lower energy peaks, typically below 200 keV for common γ-ray sources. Backscattering in gamma spectra occurs when a γ-ray interacts with the materials near the detector or its surroundings (detector walls, the detector itself or the shielding) and is scattered backwards, losing some of its energy before being detected.

1.4 Thick Target Yields

Physical Thick Target Yields (TTYs) represent the production efficiency in a process of irradiation. The TTY can be calculated using the measured cross-sections and the mass stopping power of the charged-particles in the target in an energy range between the input and output energy of the particle in the sample [53], as shown the following formula:

$$TTY(E) = \chi \cdot \lambda \int_{E_{out}}^{E_{in}} \left(-\frac{1}{n_A} \frac{dE}{dx} \right)^{-1} \frac{\sigma(E)}{Ze} \, dE \tag{II.22}$$

where χ is the isotopic and chemical purity of the target, λ is the decay constant of the radionuclide of interest [s^{-1}], E_{in} and E_{out} is the beam energy at the entrance and exit of the sample, respectively [MeV], $(-1/n_A \; dE/dx)$ is the mass stopping power for the target material [MeV/(10^{21}atm/cm^2)], $\sigma(E)$ the excitation function as a function of the charged-particle kinetic energy [cm^2], Z the charge number ($Z = 1$ for protons and deuterons), and e the projectile charge [C]. The TTY calculation gives the activity of the radionuclide produced commonly expressed in units of MBq·μA^{-1}·h^{-1}. The energy integration limits are chosen as a function of cross-section to optimise the yield and production of the radioisotope of interest and minimise possible impurities produced in the final product, as will be detailed further in Chapter III.

In this chapter, the tool used to estimate the thick target yield is the programme "Radionuclide Yield Calculator" (RYC) [54] that has been developed by Mateusz Sitarz at GIP ARRONAX to calculate the yield curve from a given cross-section. The development of the tool is described in detail in Appendix C.

The stacked-foil technique carried out for the calculation of experimental cross-sections measurements and TTY estimations for both studies on the production of therapeutic radionuclides ^{165}Er and ^{177}Lu, using high energy deuteron beams, will now be put into practice. The motivation for these experiments was the lack of high-energy experimental data in the nuclear databases, which are needed to improve the production estimates available so far for two of the most promising radioisotopes in therapy.

2 Deuteron-induced cross-section measurements for ^{165}Er up to 17.5 MeV

The ^{165}Er rare-earth element is considered a great candidate for Auger-electron targeted radionuclide therapy due to their typical emission of low-energy Auger electrons, $3.8 - 9.4$ keV (65.4 %) and $36.8 - 55.6$ keV (4.8 %) in a extremely short range (on the order of nanocrometres). AE radionuclides leads to radiotoxicity resulting from high LET, i.e. about $4 - 26$ keV/μm energy deposition per unit length [55]. The internalisation of ^{165}Er-labelled radiocompounds in specific subcellular targets means high radiotoxicity in the form of complex molecular modifications, including complex DNA lesions, possibly driving the high tumour cell killing efficiency and corresponding high radiobiological efficacy, with low toxicity to surrounding healthy tissues [56].

As shown in Figure II.3, the radioisotope ^{165}Er ($T_{1/2}$ = 10.36 h) decays by Electron Capture (EC) to ^{165}Ho stable state, accompanied by characteristic low-energy X-rays without gamma radiation, thus avoiding possible additional doses to patients [26].

The ^{165}Er pure Auger-electron emitter might be produced by several routes in reactors or cyclotrons but only in the latter type of facilities can assure the required high specific activity needed for labeling of radiopharmaceuticals [57]. Using charged-particle-induced nuclear reactions the main direct or indirect production routes for ^{165}Er are listed in Table II.2. The experimental maximal cross-section value correspond to the nuclear reaction ^{165}Ho(p,n)^{165}Er measured by Tárkányi *et al.* [57], while other routes show the theoretical maximal cross-section calculated by TALYS-1.2 code [58].

In view of the data, the highest cross-sections correspond to the indirect production routes ^{166}Er(d,3n)^{165}Tm $\rightarrow$ ^{165}Er and ^{166}Er(p,2n)^{165}Tm $\rightarrow$ ^{165}Er via generator, which require deuteron beam energies in the range of $20 - 25$ MeV. Unfortunately, the use of high-energy cyclotrons is not widespread in clinical use worldwide. Optimal energy range

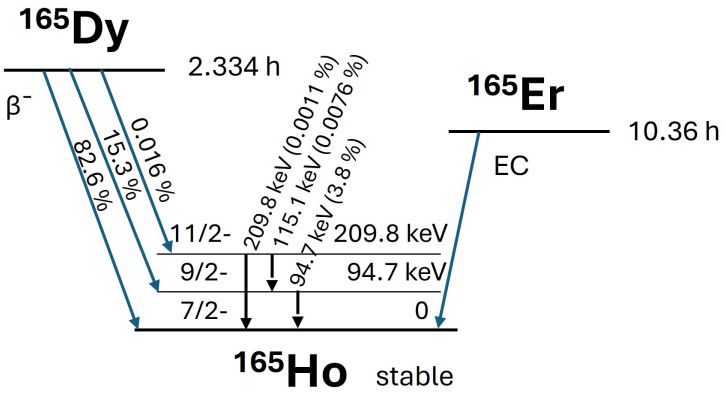

Figure II.3: Decay scheme of ^{165}Er (CE, 100 %) and ^{165}Dy (β^-, 100 %) at ^{165}Ho.

Particle	Direct/Indirect production route	Maximal cross-section (mbarn)	Energy of the maximal cross-section (MeV)
Proton (p)	^{165}Ho(p,n)^{165}Er	172 ± 19	9.5 ± 0.6
	^{166}Er(p,2n)^{165}Tm → ^{165}Er	1263.3	21
Deuteron (d)	^{165}Ho(d,2n)^{165}Er	753.6	13
	^{164}Er(d,n)^{165}Tm → ^{165}Er	120.4	10
	^{166}Er(d,3n)^{165}Tm → ^{165}Er	1523.9	25

Table II.2: ^{165}Er production routes using charged-particle-induced reactions [55].

when using small medical cyclotrons is less than 18 MeV [35]. On the other hand, for indirect production routes, ^{166}Er or ^{164}Er enriched target are required, as their natural abundances are 33.50 % and 1.60 %, respectively. Therefore, taking this into account, by using natural targets, indirect routes become less favourable in terms of efficiency and production costs.

Another production way is through the direct route ^{165}Ho(d,2n)^{165}Er, which is the most suitable option, not only due to the required energy available in cyclotrons (around 13 MeV), but also because the natural abundance of ^{165}Ho is 100 %, thus the targets are more affordable. In addition, ^{165}Ho(d,2n)^{165}Er reaction achieves a higher maximal cross-section value than the conventional ^{165}Ho(p,n)^{165}Er reaction which reaches a maximum cross-section of 172 ± 19 mbarn at 9.5 ± 0.6 MeV proton energy [57].

In this section, we present the experimental cross-section measurement of the nuclear reaction ^{165}Ho(d,2n)^{165}Er, as well as the study of its generated impurities, as an alternative method for production in more easily accessible accelerators, due to the increase in the number of them and their development in recent years. A meaningful possibility is the latest generation of high-intensity linear particle accelerators, such as IFMIF-DONES, able to accelerate deuterons up to 40 MeV energy and 125 μA current for complementary applications.

2.1 Target preparation and irradiation at CEMHTI

The measurement cross-section of the ^{165}Ho(d,2n)^{165}Er nuclear reaction was determined using a well-established stacked-foil technique combined with HPGe γ-ray spectrometry, as described in Chapter II Section 1.

The fundamental element to carry out the experimental measurement of cross-section by the stacked-foil technique is undoubtedly the use of thin foils as target, where the radionuclide of interest and its impurities, are produced by nuclear reactions. In our case, it would be ^{nat}Ho, whose natural abundance corresponds to ^{165}Ho (100 %). The foils must be thin enough not to degrade the energy of the projectile but, at the same time, they must be thick enough to produce considerable activity to give good statistics. By means of Monte Carlos simulations, it is considered that the optimum thicknesses for

this purpose are a few tens of micrometers. Therefore, the thicknesses of the ^{nat}Ho foils ranged between $25 - 50$ μm with a 25 x 25 mm^2 surface area, both with purity greater than 99.9 % and purchased from Goodfellow Cambridge Ltd (UK) [59].

In order to apply the stacked-foil activation method, it is necessary to use additional monitoring foils, which were ^{nat}Cu (25 μm), ^{nat}Ti (25 μm) and ^{nat}Fe (10 μm), according to IAEA cross-section recommendations in the whole energy range studied: ^{nat}Cu(d,x)^{65}Zn, ^{nat}Ti(d,x)^{48}V,^{46}Sc, ^{nat}Fe(d,x)^{56}Co [51]. Their cross-section data are reported in Figure II.4 and Figure II.5. All foils had the same surface area 25 x 25 mm^2 and were also purchased from Goodfellow Cambridge Ltd (UK). The natural composition and isotopic abundances for the monitor foils are reported in Table II.3.

Monitor foils were inserted between consecutive ^{nat}Ho samples throughout the whole stack. All monitor and target foils were cut circularly with the help of an electric lathe to present a diameter of 12.70 $\pm$ 0.01 mm, ensuring equal areas for all foils that were aligned

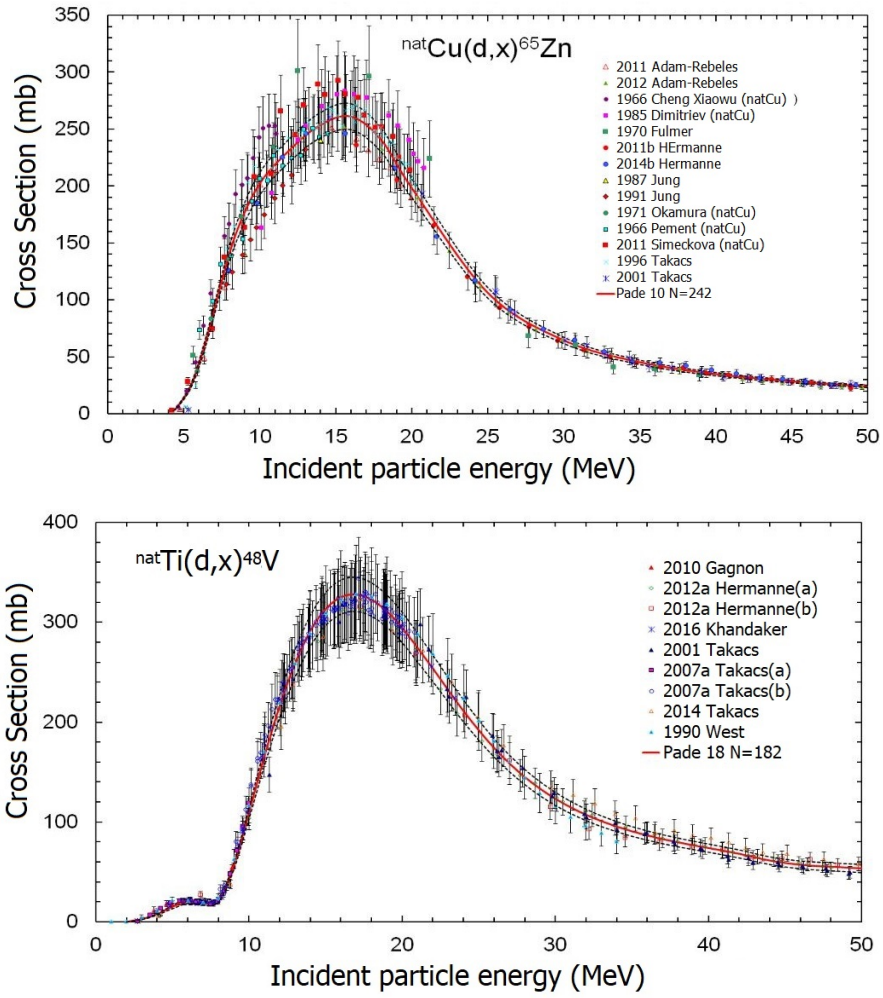

Figure II.4: IAEA monitor reaction cross-section used to estimate the beam flux across the stack. Up: ^{nat}Cu(d,x)^{65}Zn. Down: ^{nat}Ti(d,x)^{48}V [51].

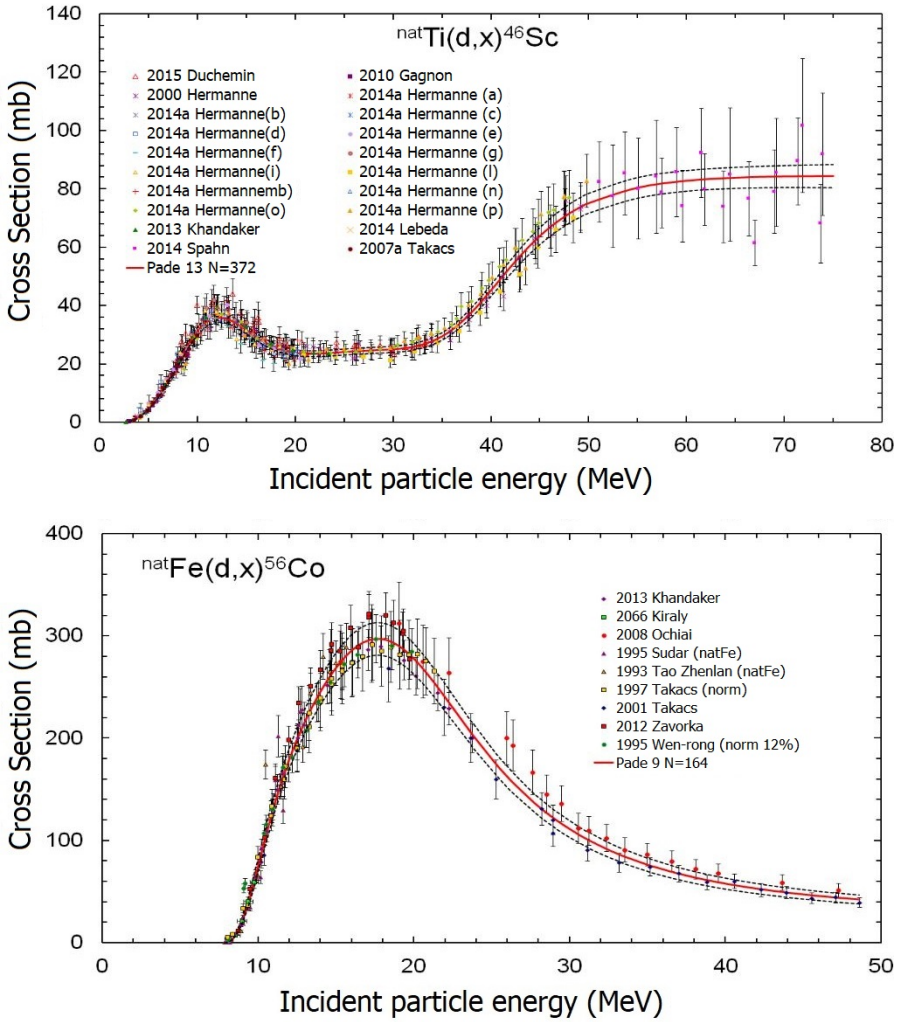

Figure II.5: IAEA monitor reaction cross-section used to estimate the beam flux across the stack. Up: ^{nat}Ti(d,x)^{46}Sc. Down: ^{nat}Fe(d,x)^{56}Co [51].

Isotope	Abundance	Isotope	Abundance	Isotope	Abundance
^{63}Cu	69.15 %	^{46}Ti	8.25 %	^{54}Fe	5.85 %
^{65}Cu	30.85 %	^{47}Ti	7.44 %	^{56}Fe	91.75 %
		^{48}Ti	73.72 %	^{57}Fe	2.12 %
		^{49}Ti	5.41 %	^{58}Fe	0.28 %
		^{50}Ti	5.18 %		

Table II.3: Natural composition and isotopic abundances for natural copper, titanium and iron monitor foils.

with the beam. Knowing the area, density and mass, the thickness of each foil was determined with an uncertainty lower than that indicated by the manufacturers of 25 %. The beam was collimated to 10 mm diameter. The irradiations were carried out in two days, each day using the same stack structure but different thickness of ^{nat}Ho target and

Irradiation Day/Time (dd/mm/yy hh:mm)	Deuteron Energy (MeV)	Time (min)	Current (nA)	Stack Configuration (x 4 times)
10/10/22 11:14 10/10/22 13:07	13.0 ± 0.5	30	490 ± 10	^{nat}Ho - ^{nat}Cu/Ti/Fe ^{nat}Cu - ^{nat}Ti
11/10/22 11:53 11/10/22 14:27	17.5 ± 0.5	30	510 ± 15	^{nat}Ho - ^{nat}Cu/Ti/Fe ^{nat}Cu - ^{nat}Ti

Table II.4: Irradiation parameters set for irradiations in the cyclotron laboratory at CEMHTI.

irradiation energy. The first irradiated stack consisted of a sequence of ^{nat}Ho (25 μm), ^{nat}Cu (25 μm), ^{nat}Ho (25 μm), ^{nat}Ti (25 μm), ^{nat}Ho (25 μm), ^{nat}Fe (10 μm), ^{nat}Ho (25 μm), ^{nat}Cu (25 μm) that was irradiated up to 13 MeV, while the second stack was irradiated up to 17.5 MeV. The holmium foils for the second irradiation were 50 μm thickness. In addition, one more configuration was irradiated each day with the same energy and flux parameters. The configuration of these stacks consisted of a sequence of ^{nat}Cu-^{nat}Ti foils repeated 4 times to have a second test for the beam current intensity. The beam current was also "live" measured during the irradiation by a Faraday cup.

After assembly, the targets were bombarded with deuterons of different energies to induce nuclear reactions to produce ^{165}Er and its contaminants in ^{nat}Ho foils, as well as the monitoring radioisotopes in the corresponding ^{nat}Cu/Ti/Fe foils. The irradiation of the targets was performed under vacuum and with a chilled water system for the target. The excitation functions were measured between $8 - 17.5$ MeV deuteron energy by bombarding the stacks with low intensity deuteron beams, up to 500 nA for 30 min at the cyclotron of the laboratory CEMHTI. This cyclotron is able to provide also proton and α-beams, not used in the context of this thesis work. A peculiarity of the irradiation, which must be taken into account, is that the cyclotron output in the experimental area where the experiment was carried out, has an inclination of 30º with the normal axis, so all the foil thicknesses were corrected by this factor when the corresponding calculations were made.

Table II.4 shows the irradiations performed during the experiment and the energy, time and intensity parameters set for each of them. Finally, all the steps described from the acquisition of the foils to their irradiation, as well as the preparation of the stack are shown in Figure II.6.

2.2 Data acquisition

After the irradiation, an adequate cooling time was allowed to decrease the activity of the short half-life impurities. The samples were placed in a lead shield. The following day, the samples were removed from the target holder, and the radioactivity of each sample and monitor foil was assessed non-destructively by using a high resolution coaxial HPGe γ-spectrometry (model GC1319, Serial No. b93081, 13 % relative efficiency) couple to

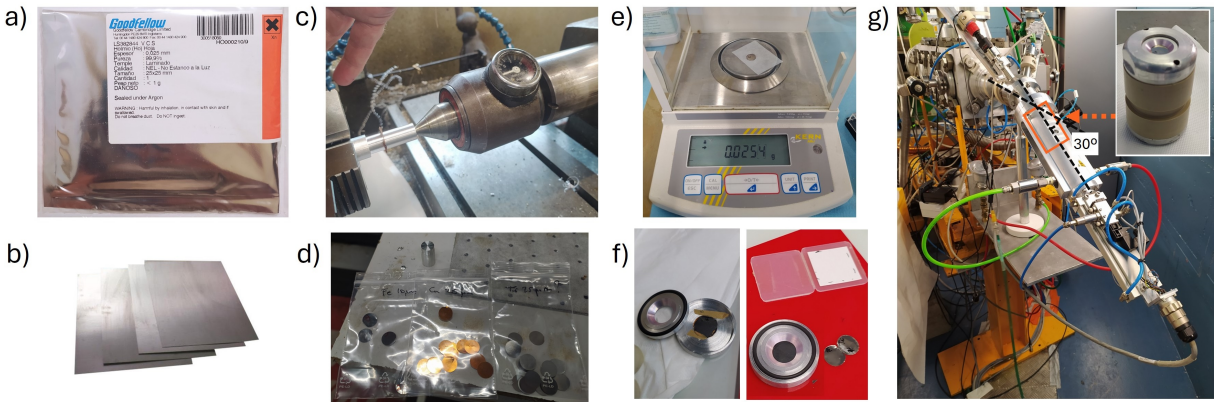

Figure II.6: Photographs of the target preparation before the irradiation process. a) Acquisition of the target foils. b) ^{nat}Ho foils of 25 x 25 mm^2, $25 - 50$ μm thickness and 99.9 % purity. c) Cutting process of the foils with an electric lathe. d) Cut monitoring foils organized in bags and the metal piece showing the lathe cut. e) Balance for weighing the different foils. Sensitivity 0.0001 g. f) Assembly of the stacked-foils on the support. g) Stacked-foils setup introduction into the vacuum tube at the outlet of the cyclotron (30º inclination).

a multi-channel analyser. The spectrum analysis was performed with the GENIE-2000 software package [60] using the correction algorithm implemented in the software, LIVE TIME (corrected real time as a function of detector dead time) and with a peak area uncertainty of 2 sigma, value corresponding to a confidence percentage of 95.45 %. In addition, the spectra were corrected by background subtraction. The detector energy calibration was performed using standard calibration sources, ^{152}Eu (120-1400 keV) and ^{133}Ba (80-360 keV), whose gamma energy peaks are well known, while the efficiency calibration as a function of the gamma energy were determined at the counting distance of 5 cm from the end-cap of the detector. The corresponding energy and efficiency calibration was carried out by the maintenance operators of the facility equipment, which justifies the lack of this information in Appendix B.

The first counting series started one day after the EOB and repeated $6 - 8$ times on subsequent days to follow the decay of the radionuclides. Due to the large number of foils and only one detector available, the first counting time was restricted to 10 minutes for each side, increasing in subsequent days. Typical dead times ranged from 3 % for the first series of measurements to less than 1 % for the last measurements. For the long-lived radionuclide, the measurements were repeated after a cooling time of one year, when short-lived radionuclides had disappeared. For these measurements, the HPGe used corresponds to a more up-to-date model (GC2020, serial number b12310, 20 % relative efficiency).

Figure II.7 shows a subsequence of photographs from the recovery of the irradiated setup with the stacked-foils to the analysis of the foil activities with the help of the GENIE-2000 analytical software.

The radioactivity measured is a consequence of the radioisotopes produced, which

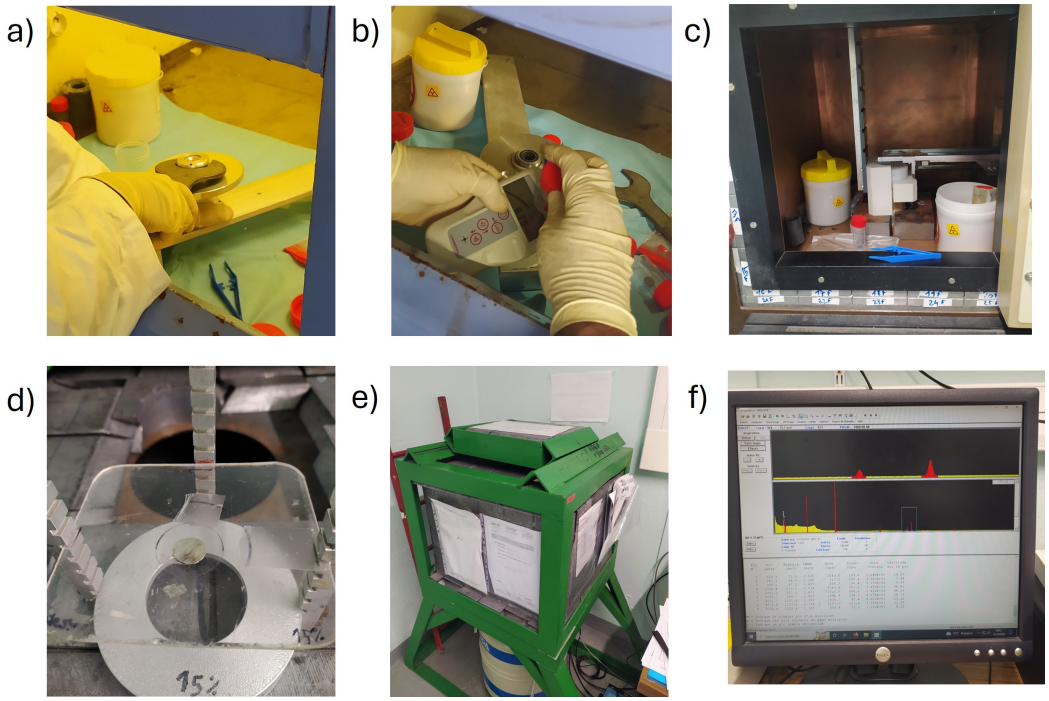

Figure II.7: Photographs of the handling of the samples after irradiation. a) Recovery and opening of the setup with the stacked-foils. b) Separation of the individual foils into bottles and measurement of their activity separately. c) Activated foils inside the lead shield. d) Measurement of the foils in the HPGe at a distance of 5 cm from the end-cap. e) HPGe γ-spectrometry (model GC1319, Serial No. b93081, 13 % relative efficiency). f) Open view of the screen of the GENIE-2000 software analyser.

almost always undergo β-decay, with some exceptions. The β-decay, regardless of the type (β^-, β^+) or Electron Capture (EC), usually leaves the daughter nucleus in an excited state, whose deexcitation might cause γ-emission. According to the Radionuclide Chart shown in Figure I.1 and the displacement caused by deuteron-induced nuclear reactions resulting from bombardment at 17.5 MeV energy, only radioisotopes that are peripherally in contact with the target nucleus are allowed to be produced, as shown in Figure II.8. Therefore, by deuteron beams on ^{165}Ho targets, only the production of the radioisotopes ^{165,166,167}Er, ^{164,166}Ho and ^{163,164,165}Dy is possible.

The radioisotopes ^{166,167}Er and ^{163,164}Dy are stable and therefore not detectable by activity measurement techniques. On the other hand, as a consequence of the cooling day after the EOB, it is not possible to detect ^{165}Dy, whose half-life is 2.33 h (after 24 h of cooling, 10 half-lives are exceeded, the conventional time for a radioisotope to be considered fully decayed). The waiting time between the EOB and the first foil measurement was carefully established, with two objectives: first, to clean the spectrum from short-lived radionuclides that are not relevant for this study. Secondly, and even more importantly, because the ^{165}Dy has the same characteristics X-ray as the ^{165}Er, and it is the only way to be sure that the identified signals came 100 % from the ^{165}Er (see

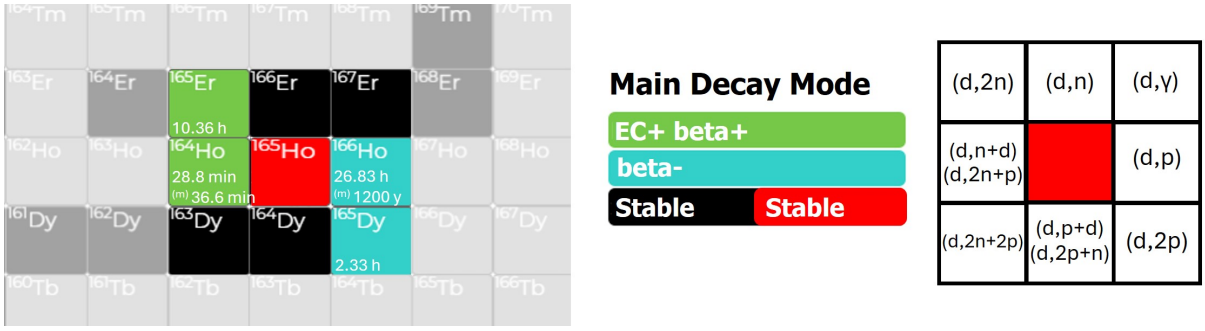

Figure II.8: Main displacement caused by deuteron-induced nuclear reactions on ^{nat}Ho at 17.5 MeV energy, radioisotope produced, half-lives and decay modes.

Figure II.3). For this waiting time, the possibility of detecting ^{164g}Ho ($T_{1/2}$ = 28.8 min) and ^{164m}Ho ($T_{1/2}$ = 36.6 min) is also null.

The decay data and mode of radioisotopes detected after one day EOB onward, both from natural Ho targets and from natural Cu, Ti and Fe monitoring foils, expressed by the half-life ($T_{1/2}$), the γ-ray energy (E_γ) and the γ-ray emission probability (I_γ) used in the determination of the investigated radionuclides are summarized in Table II.5. The threshold energies are also presented. It is important to note that, as previously mentioned, the decay of the Auger-electron emitting ^{165}Er, was only accompanied by characteristic X-rays, which have also been included in Table II.5, as this will be the only way to be able to identify it by spectrometry.

Figure II.9 shows an HPGe spectrum acquired two days after the EOB. The peaks identified correspond to the main characteristic X-ray emitted by ^{165}Er and ^{166g}Ho (listed in Table II.5), as well as, the γ-peak of ^{166g}Ho at 80.57 keV. From the number of counts, the relative intensity and the detector efficiency for each characteristic radionuclide photopeak, the analyser will provide an average activity value with its uncertainty for each of the radioisotopes identified corrected for the cooling time from the EOB.

2.3 Determination of foil energies and beam intensity

For the determination of the beam intensity, cross-section data for the monitoring reactions taken from the IAEA recommendations [51], have been used (shown in Figure II.4 and Figure II.5).

The cross-section data must be associated with an energy value. The deuteron energy degradation along the stacked-foils was calculated by the Monte Carlo code SRIM 2003 [50]. Knowing the initial beam energy and the thickness of the different stacked-foils, the average energy loss of the incoming beam in the middle of each irradiated foil can be simulated, as shown in the graphical description of the simulation in Figure II.10.

The uncertainty of the energy as estimated includes cumulative effects such as initial energy uncertainty of the cyclotron (± 0.5 MeV private communication), stopping estima-

Produced Nuclei	Half-life, $T_{1/2}$	Decay mode, Branch (%)	Energy, $E_{X/\gamma}$ (keV)	Intensity, $I_{X/\gamma}$ (%)	Contributing reactions	Threshold (MeV)
^{166g}Ho	26.83 h	β^- (100)	48.2 49.1 55.5-57.4 57.1 80.6 1379.4	2.95 5.24 2.15 0.44 6.56 0.92	^{165}Ho(d,p)	0
^{166m}Ho	1200 y	β^- (100)	184.4 711.7 810.3	72.0 54.1 56.9	^{165}Ho(d,p)	0
^{165}Er	10.36 h	EC (100)	46.7 47.6 53.7-55.5	21.40 38.10 15.52	^{165}Ho(d,2n)	3.42
^{65}Zn	243.93 d	EC, β^+ (100)	1115.5	50.0	^{nat}Cu(d,x)	0
^{56}Co	77.24 d	EC, β^+ (100)	846.8	99.94	^{nat}Fe(d,x)	0
^{48}V	15.97 d	EC, β^+ (100)	983.5 1312.1	99.98 98.20	^{nat}Ti(d,x)	0
^{48}Sc	43.71 h	β^- (100)	983.5 1312.1	100.00 100.00		
^{46}Sc	83.79 d	β^- (100)	889.3 1120.5	99.98 99.98		

Table II.5: Decay data and the important contributing reactions of the detected radionuclides with their threshold energies.

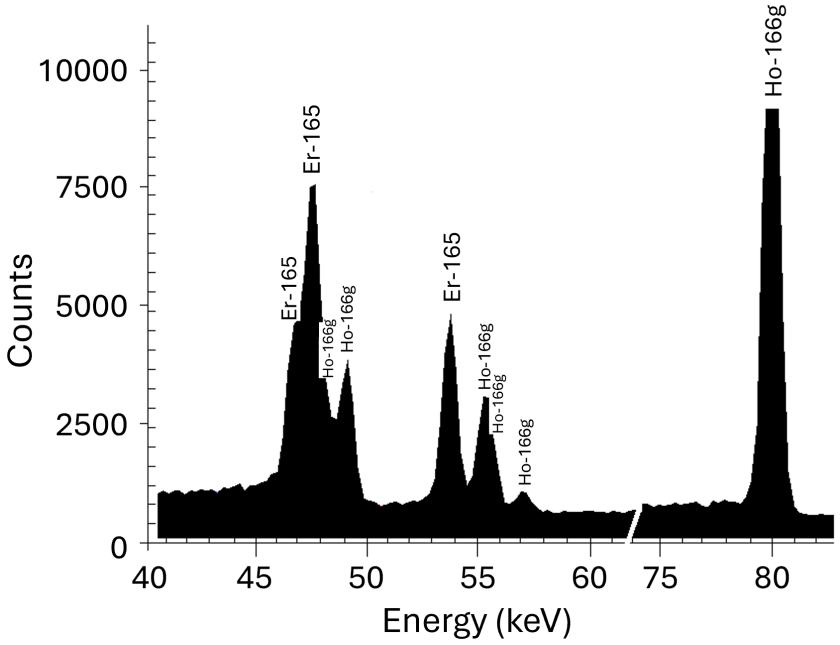

Figure II.9: HPGe spectrum acquired 2 days after EOB of a irradiated ^{nat}Ho foil.

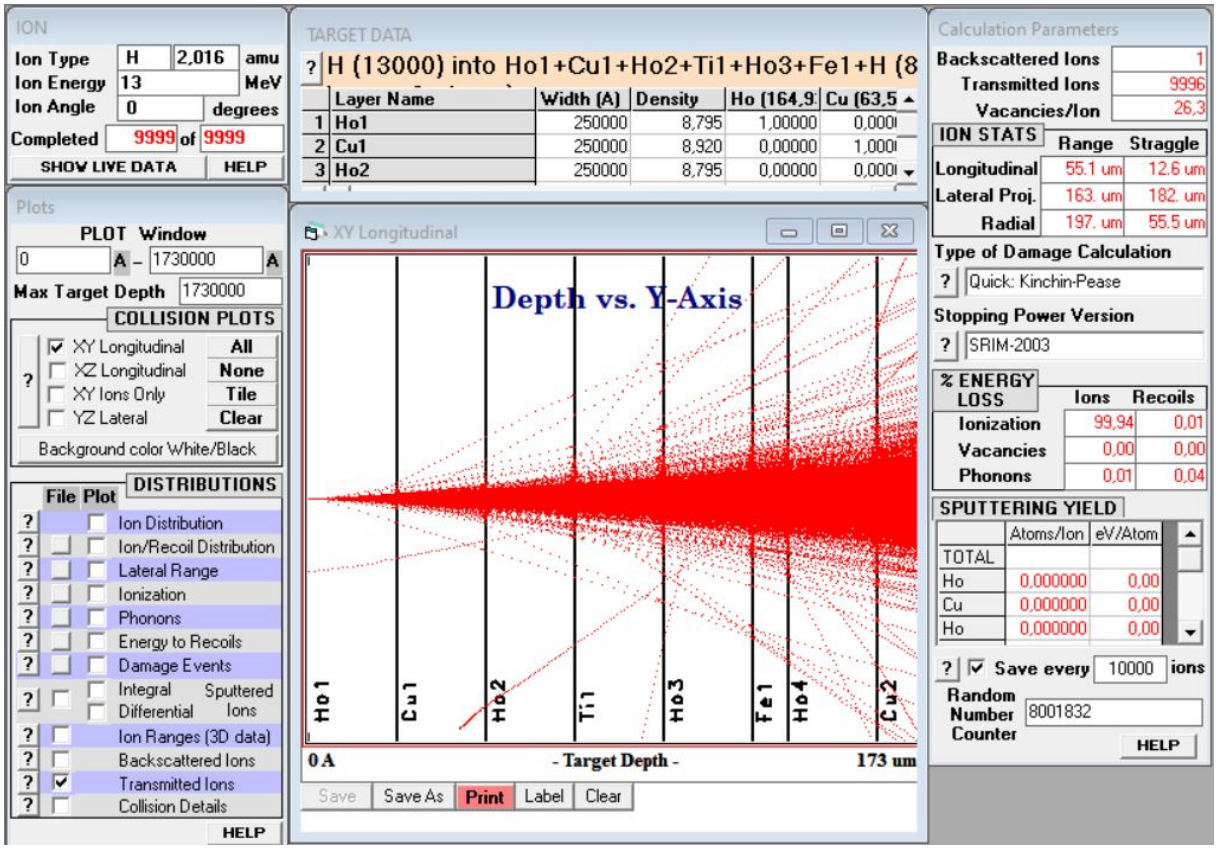

Figure II.10: SRIM 2003 transmitted ion simulation to evaluate the deuteron beam energy loss and straggling through the stacked-foils. Energy output file will be generated. This simulation exemplifies the last measurement of the copper monitor foil of the stack irradiated at 13 MeV.

tion influenced by target thickness and beam straggling. This estimate results in an overall uncertainty of 8 %, which corresponds to an uncertainty in the energy between $\pm$ 0.5 – 0.7 MeV (see Table II.6).

The values corresponding to the beam energy in monitor foils were used for the deter-

Initial Beam Energy (MeV)	$Foil_{stack-pos}$	Thickness (μm)	Energy (MeV)	Intensity (nA)
13.0 $\pm$ 0.5	Ho_1	25.48 $\pm$ 0.01	12.7 $\pm$ 0.6	490 $\pm$ 10
	Ho_2	22.79 $\pm$ 0.01	11.1 $\pm$ 0.7	512 $\pm$ 12
	Ho_3	22.87 $\pm$ 0.01	9.7 $\pm$ 0.7	490 $\pm$ 8
	Ho_4	24.55 $\pm$ 0.01	8.4 $\pm$ 0.7	486 $\pm$ 9
17.5 $\pm$ 0.5	Ho_1	59.19 $\pm$ 0.01	16.8 $\pm$ 0.5	510 $\pm$ 15
	Ho_2	50.14 $\pm$ 0.01	14.8 $\pm$ 0.6	512 $\pm$ 10
	Ho_3	55.46 $\pm$ 0.01	13.0 $\pm$ 0.6	494 $\pm$ 8
	Ho_4	57.21 $\pm$ 0.01	11.2 $\pm$ 0.7	490 $\pm$ 7

Table II.6: Holmium reaction foil calculated thicknesses values, particle energies and beam intensities for the two irradiations performed at cyclotron laboratory in CEMHTI.

mination of their cross-sections, according to the IAEA recommendations [51]. These values together with the measured monitor foil activities were used to calculate the average beam intensity in each monitor foil. For the determination of the average beam intensity in each holmium foil, the beam intensity across the juxtaposed foils is considered to be the same, i.e., $\phi(E) = \phi'(E')$. Beam intensity values carry an uncertainty around 10 %, that takes into account the uncertainties of the measured monitor foil activity, the monitor foil cross-section and the average energy in this monitor foil. The average energy and beam intensity in each holmium reaction foil are summarised in Table II.6.

2.4 Experimental cross-section measurements

This study was undertaken to accurately measure the values of the cross-section around its maximum for the Auger-electron emitting therapeutic radioisotope produced via the alternative route, ^{165}Ho(d,2n)^{165}Er. This short-lived radionuclide ($T_{1/2}$ = 10.36 h) was identified with low uncertainty the first day after EOB. As a consequence of irradiation with deuterons up to 17.5 MeV energy on ^{nat}Ho, the main impurity obtained in the by-product was ^{166}Ho, both in its metastable and ground states.

This impurity is considered non-isotopic, since it belongs to a different element and therefore has different chemical properties, which make its chemical separation possible. The radionuclide ^{166}Ho has a ground state ($T_{1/2}$ = 26.83 h) and a very long-lived metastable state ($T_{1/2}$ = 1200 y) which does not contribute to formation of the ground state ^{166g}Ho because it decays by β^- to stable ^{166}Er. To measure the metastable state cross-section, ^{166m}Ho ($T_{1/2}$ = 1200 y), it was necessary to measure again the foils twelve months after the EOB, when the activity of the targets was low and with long measurement times it was possible to identify ^{166m}Ho γ-emission peaks.

The experimental cross-section data for the reactions ^{nat}Ho(d,2n)^{165}Er and ^{nat}Ho(d,p)^{166g,m}Ho up to 17.5 MeV are given in Table II.7, as well as, are plotted in Figure II.11 to Figure II.13, together with the experimental values measured by F. Tárkányi *et al.* [57] and H. Hermanne *et al.* [61] available from Experimental Nuclear Reaction Data (EXFOR) [62] database and theoretical data from TALYS-based Evaluated Nuclear Data Library-2023 (TENDL-2023) [63].

2.4.1 ^{nat}Ho(d,2n)^{165}Er cross-section

Figure II.11 shows the ^{nat}Ho(d,2n)^{165}Er cross-section in comparison with the results of earlier studies by F. Tárkányi *et al.* [57] up to 20 MeV and A. Hermanne *et al.* [61] up to 42 MeV. Our results of cross-section agree well with them in the energy region up to 17 MeV. Moreover, theoretical calculations obtained from TENDL-2023 database [63] of the ^{nat}Ho(d,2n)^{165}Er nuclear reaction is also compared up to 50 MeV.

Our new experimental results confirm the trend defined at the maximum cross-section peak, reducing the uncertainties of previous measurements. Moreover, these data can

Energy (MeV)	Cross-section (mbarn)		
	^{165}Er	^{166g}Ho	^{166m}Ho
8.4 ± 0.7	15 ± 1	104 ± 2	
9.7 ± 0.7	316 ± 9	143 ± 3	
11.1 ± 0.7	540 ± 15	158 ± 3	
11.2 ± 0.7	462 ± 16	144 ± 4	50 ± 6
12.7 ± 0.6	664 ± 18	158 ± 3	67 ± 5
13.0 ± 0.6	629 ± 22	155 ± 4	60 ± 6
14.8 ± 0.6	594 ± 19	147 ± 4	60 ± 6
16.8 ± 0.5	372 ± 12	109 ± 3	48 ± 6

Table II.7: Experimental cross-section (mbarn) values for the production of ^{165}Er and ^{166g,m}Ho by deuteron-induced reactions at the cyclotron of the laboratory CEMHTI.

improve the theoretical estimates above the maximum energy peak, beyond which the trend curve does not fully reproduce the behaviour measured by the experimental data.

2.4.2 ^{nat}Ho(d,p)^{166g}Ho cross-section

A good agreement with the earlier experimental data can be seen in Figure II.12. Our present data above 17.5 MeV are in the overlapping region with the data measured by F. Tárkányi *et al.* [57] and A. Hermanne *et al.* [61] whereas the theoretical results from TENDL-2023 database [63] strongly underestimate these trends. This indicates that there is a lack of nuclear parameterisation of the models used for the evaluation of these nuclear data.

In addition, the peak of the maximum energy is shifted to the left, underestimating the final yield of the radioisotope and not correctly assessing the energy range of maximisation of the production rate.

2.4.3 ^{nat}Ho(d,p)^{166m}Ho cross-section

Finally, no experimental cross-section values are available in the literature for the nuclear reaction ^{nat}Ho(d,p)^{166m}Ho. Therefore, Figure II.13 has been compared with the theoretical data estimated by TENDL-2023 database [63], which is in agreement in terms of the curve shape. However, it clearly shows a shift of the peak of the maximum cross-section, as also seen in Figure II.12, which shows the estimate of the nuclear reaction cross-section of ^{nat}Ho(d,p)^{166}Ho.

A good knowledge of the ^{166m}Ho metastable state cross-section is relevant for two main reasons. The first one is a consequence of the β^- decay of ^{166m}Ho into the stable isotope ^{166}Er, whose growth by this additive route would reduce the gross value of the specific activity of the final product of interest, ^{165}Er. To avoid this drawback, early chemical separation of the two elements would be necessary.

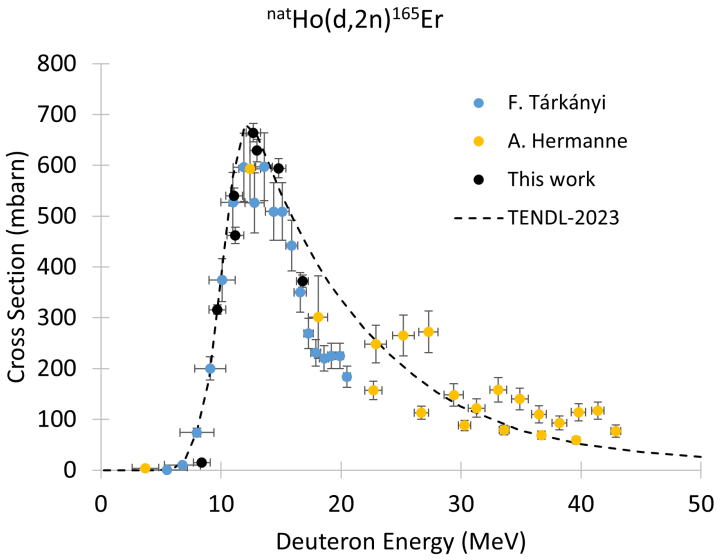

Figure II.11: Cross-section of the nuclear reaction ^{nat}Ho(d,2n)^{165}Er.

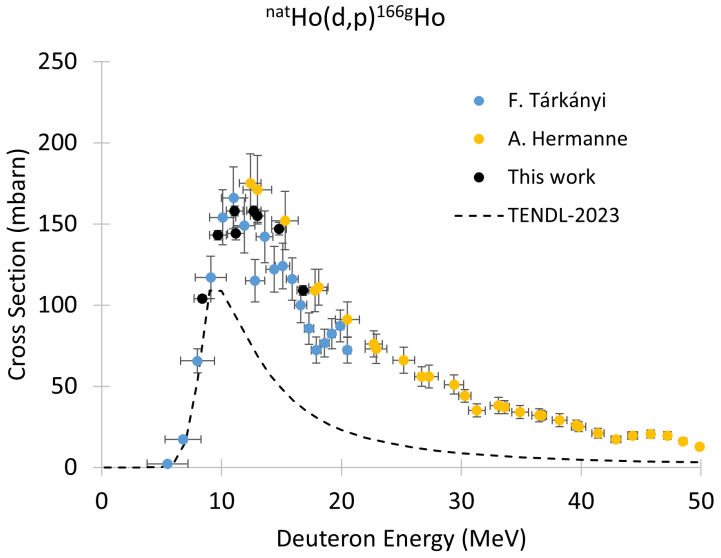

Figure II.12: Cross-section of the nuclear reaction ^{nat}Ho(d,p)^{166g}Ho.

On the other hand, the present work allows the study of the excitation function of the ^{nat}Ho(d,p)^{166g}Ho, another emerging therapeutic agent. The β^--emitting ^{166g}Ho ($T_{1/2}$ = 26.83 h) has favorable radiation characteristics (β^- energies: 1.85 MeV (48.8 %) and 1.77 MeV (49.9 %) [64]) and it seems to be a suitable choice among others for endovascular radionuclide therapy and hepatocellular carcinoma [65]. Usually, ^{166g}Ho is produced with high yield at nuclear reactors via ^{nat}Ho(n,γ) route resulting in a carrier-added product. At high flux reactors a no-carrier-added product can be obtained via

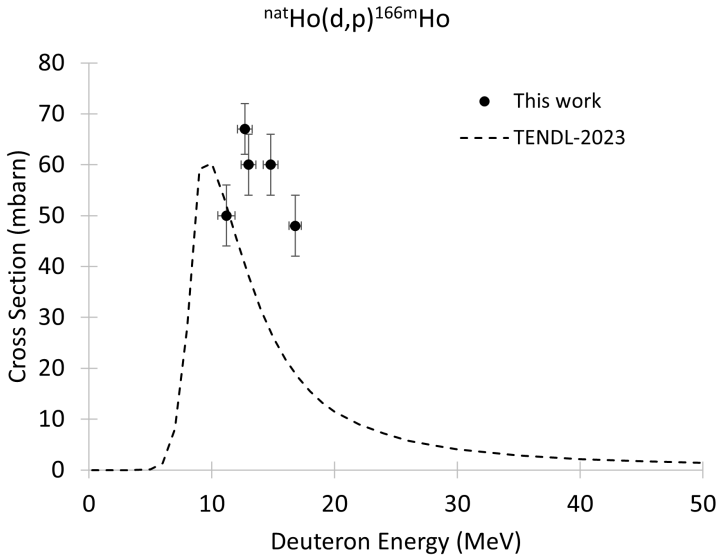

Figure II.13: Cross-section of the nuclear reaction ^{nat}Ho(d,p)^{166m}Ho.

double neutron capture (^{164}Dy(n,γ)^{165}Dy(n,γ)^{166}Dy(β^-) $\rightarrow$ ^{166}Ho) [66]. We are aware that the ^{165}Ho(d,p)^{166g}Ho route investigated here cannot compete with the reactor method if only the yield is considered. However, we can obtain ^{166g}Ho by a complementary route as a final by-product of our reaction of interest. For this, the estimation of its isotopic impurity ^{166m}Ho is essential, as it would only provide unwanted dose. It should be noted that it could not be chemically separated or removed by natural decay due to its half-life longer than the ground state. The ratio between activities detected of ^{166m}Ho and ^{166g}Ho is less than $1/10^6$ at the EOB, for 30 minutes of irradiation. Therefore, contamination by ^{166m}Ho is considered negligible.

2.5 Calculated physical Thick Target Yields (TTYs)

The studied route ^{nat}Ho(d,2n)^{165}Er is an ideal direct pathway for production of ^{165}Er. As shown in Figure II.14, compared to the conventional ^{nat}Ho(p,n)^{165}Er production route measured by G.J. Beyer *et al.* [67]. At 18 MeV particle incident energy the yield of the nuclear reaction ^{nat}Ho(d,2n)^{165}Er is above 250 MBq/μA·h, which is about three times more than the TTY for the proton-induced reaction on ^{165}Ho at the same particle energy.

Compared to the experimental integral TTY data found in the literature for deuteron-induced nuclear reaction, P. Dmitriev *et al.* [68] reported radioactive thick target nuclide yields measured at 22 MeV incident deuteron energy for ^{166g}Ho. The yield is 34.5 $\pm$ 5.5 MBq/μA·h, in good approximation with our calculated yield for this radionuclide.

A. Hermanne *et al.* [61] reported his results for physical yields of the radionuclides of interest, ^{166g}Ho and ^{165}Er. Their deduced yield curves shown very similar to ours up to 17.5 MeV. The similarity at high energies depends on the excitation function quality

fitting due to the lack of experimental values for us. TTYs shown in Figure II.14 have been calculated with the RYC tool from the data of the cross-sections measured in this work and those available in EXFOR database [62].

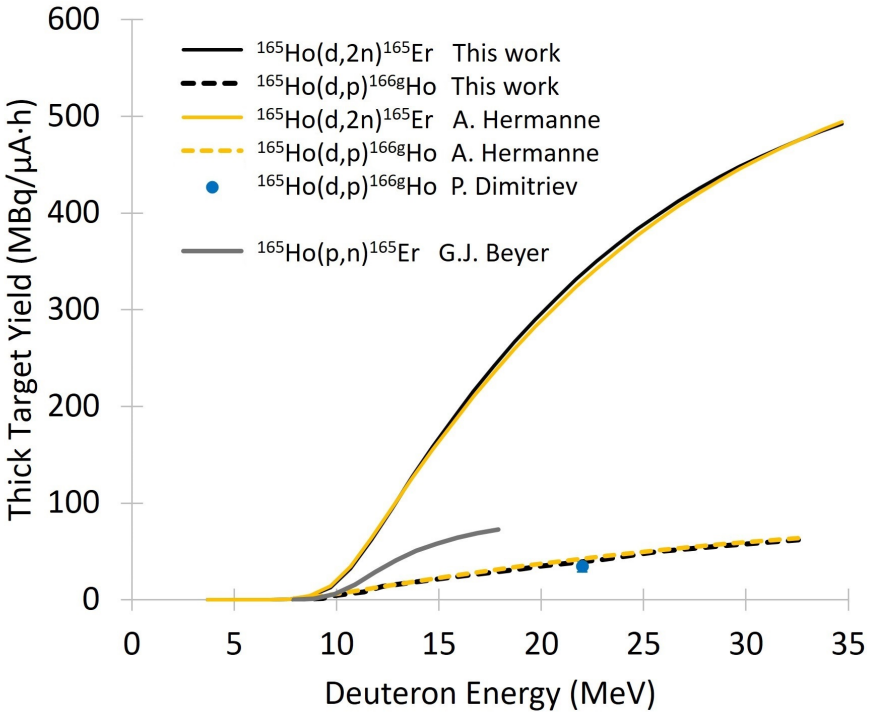

Figure II.14: Physical TTYs for production of ^{165}Er and ^{166g}Ho by deuteron and proton irradiations of natural ^{165}Ho targets, compared with values available in EXFOR database.

3 Deuteron-induced cross-section measurement for ^{177}Lu up to 33.0 MeV

The pure β^--emitting radioisotope ^{177g}Lu ($T_{1/2} = 6.65$ d; $E^{max}_{\beta^-} = 496.8$ keV, $I^{total}_{\beta^-} = 100$ %; $E_\gamma = 208.37$ keV, $I_\gamma = 10.41$ % [31]) is used for theranostic applications thanks to its low energy electrons, which makes it ideal in targeted radiotherapy applications, as well as, its single gamma emission, because it is detectable with imaging techniques such as SPECT.

Currently, ^{177g}Lu is produced by neutron-capture on ^{176}Lu(n,γ)$^{177(g+m)}$Lu, known as carrier-added (c.a) route, or on ^{176}Yb(n,γ)^{177}Yb $\rightarrow$ ^{177g}Lu, no-carrier-added (n.c.a) route, at nuclear reactors [69]. The most common production route is c.a, due to the fact that ytterbium is non-monoisotopic element and its purification process is complex. However, n.c.a is preferable used because it has a higher specific activity after purification, so higher radiolabelling efficiency than ^{177}Lu c.a. [70]. In addition, the n.c.a route does not produce ^{177m}Lu ($T_{1/2} = 160.4$ d; $E^{max}_{\beta^-} = 1466.98$ keV, $I^{total}_{\beta^-} = 77.30$ %; $E^{max}_{I.T} = 970.18$ keV, $I^{total}_{I.T} = 22.70$ % [31]) which delivers an unwanted dose to the patient. This metastable state of ^{177}Lu decays directly to ^{177}Hf via β^- decay and Isomeric Transition[3] (IT).

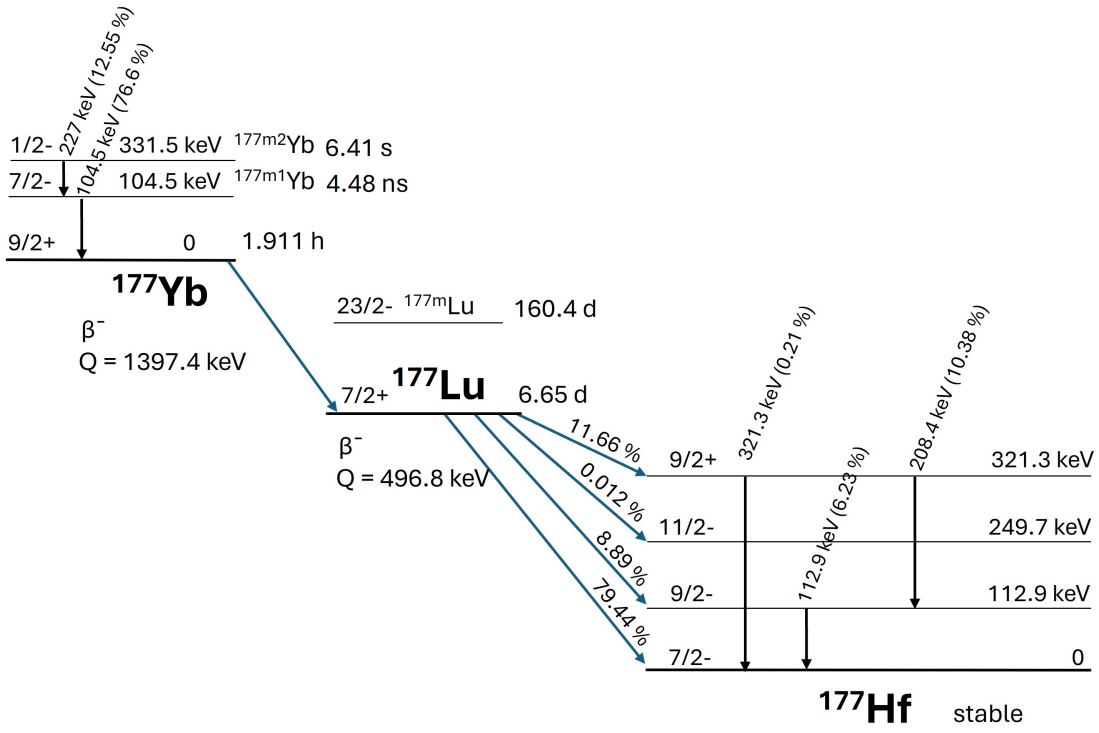

Figure II.15: Decay scheme of ^{177}Yb and ^{177}Lu to ^{177}Hf.

[3] An isomeric transition or internal transition (IT) is the decay of a nuclear isomer to a lower-energy nuclear state or ground state. The process has two types of decay mode: γ-emission or internal conversion electrons.

An alternative ^{177g}Lu production route could be achieved by charged-particles as deuteron-induced nuclear reactions on enriched ^{176}Yb targets by the following reactions: the direct production route, ^{176}Yb(d,n)$^{177(m+g)}$Lu, and the indirect route, ^{176}Yb(d,p)^{177}Yb $\rightarrow$ ^{177g}Lu. In terms of production of the impurity ^{177m}Lu, the first route, can be compared to the carrier-added route as the conventional neutron capture reaction method, while the second route will be a no-carrier-added route (see the decay scheme in Figure II.15).

In this subsection, the experimental cross-section values of the deuteron-induced nuclear reactions on ^{nat}Yb targets are presented, in order to measure ^{177g}Lu, and to assess the proportion of ^{177m}Lu produced. The experiment was carried out at the GIP ARRONAX cyclotron. The results are compared with early experimental data available from EXFOR database. Data sets define cross-sections up to 24 MeV measured by A. Hermanne *et al.* [71], S. Manenti *et al.* [72] and M.U. Khandaker *et al.* [73]. At higher energies, there is only one data set by F. Tárkányi *et al.* [74], which does not seem to be in complete agreement with the other low-energy data. Therefore, these new measures are aimed at building consensus among all of them.

3.1 Targets preparation and irradiation at GIP ARRONAX

The method used for the measurement of the deuteron-induced cross-sections has been a well-established stacked-foil technique [72, 75] combined with HPGe γ-ray spectrometry, as described in Chapter II Section 1.

As already mentioned in the previous section, the fundamental element of the experimental measurement of cross-section is the use of thin foils as target, where the nuclear reactions take place. In this case under study, ^{176}Yb(d,n)$^{177(m+g)}$Lu, and ^{176}Yb(d,p)^{177}Yb. Natural ytterbium has an isotopic composition consisting of 7 isotopes with different abundances. However, by applying a proportionality correction factor, it would be possible to use natural foils to perform cross-section measurements. This considerably reduces the cost of the material used and is the usual method of work in cross-section measurement experiments. By contract, in the industrial radioisotope productions for medical use, highly enriched thick targets are undoubtedly used. For the case of clinical lutetium, $^{176}Yb_2O_3$ thick targets with 99.43 % enrichment are used [76].

In this study, 99.0 % high purity natural ytterbium foils were used as targets. The dimensions were 25 μm nominal thickness and 25 x 25 mm^2 surface area, purchased from Goodfellow Cambridge Ltd (UK) [77]. Subsequently, positioned after a ^{nat}Yb foils, high purity natural titanium (99.9% purity; 10 μm thickness; Goodfellow UK) and nickel (99.9% purity; $15 - 20$ μm thickness; Goodfellow UK) were used as monitoring foils. As shown in Figure II.16 and Figure II.17, the IAEA recommended monitor reactions are ^{nat}Ti(d,x)^{48}V,^{46}Sc and ^{nat}Ni(d,x)^{58,56}Co, for deuteron-induced nuclear reactions in the whole energy range studied [51]. Thin natural aluminium foils (99.9% purity; 10 μm thickness; ^{27}Al 100 %; Goodfellow UK) were included to collect the produced ^{58,56}Co recoil nuclei whose kinetic energy could allow their displacement from the ^{nat}Ni foil to the

subsequent foil, losing part of the quantification of those produced nuclei. Finally, the different patterns were separated by thick natural aluminium foils (around $200 - 300$ μm) used as beam energy degraders. Natural aluminium foils are ^{27}Al 100 %, whereas isotopic abundances of the other natural foils are listed in Table II.8.

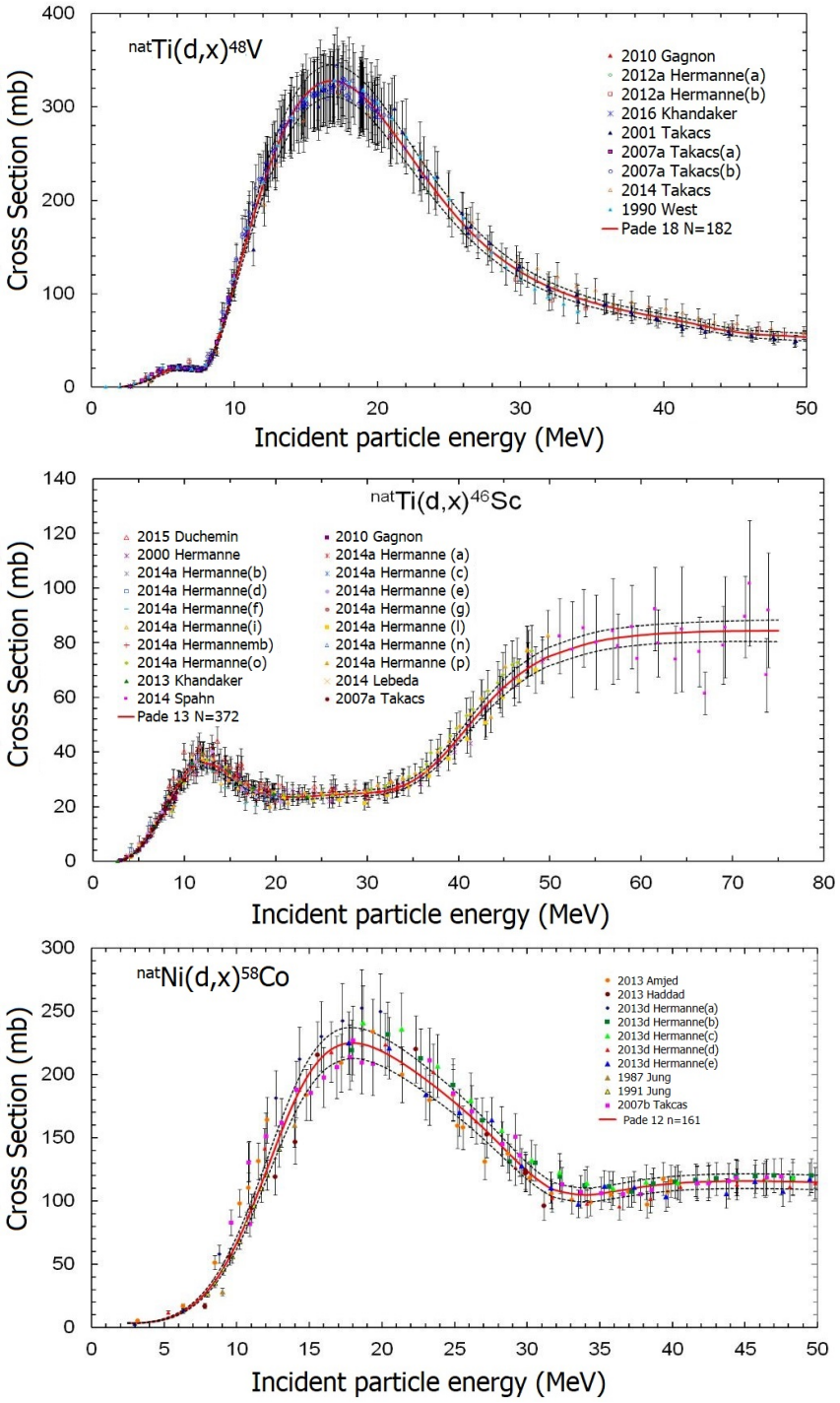

Figure II.16: IAEA monitor reaction cross-section used to estimate the beam flux across the stack. Up: ^{nat}Ti(d,x)^{48}V. Middle: ^{nat}Ti(d,x)^{46}Sc. Down: ^{nat}Ni(d,x)^{58}Co [51].

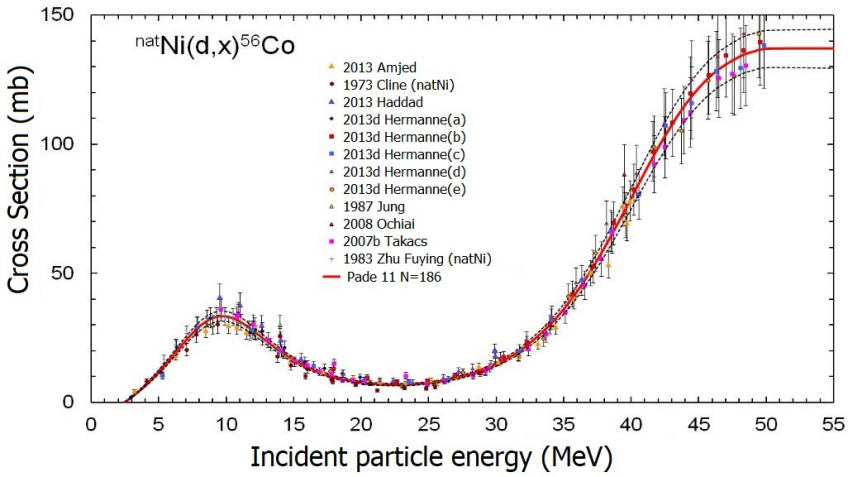

Figure II.17: IAEA ^{nat}Ni(d,x)^{56}Co monitor reaction cross-section used to estimate the beam flux across the stack [51].

Isotope	Abundance	Isotope	Abundance	Isotope	Abundance
^{168}Yb	0.123 %	^{46}Ti	8.25 %	^{58}Ni	68.08 %
^{170}Yb	2.982 %	^{47}Ti	7.44 %	^{60}Ni	26.22 %
^{171}Yb	14.086 %	^{48}Ti	73.72 %	^{61}Ni	1.14 %
^{172}Yb	21.686 %	^{49}Ti	5.41 %	^{62}Ni	3.63 %
^{173}Yb	16.103 %	^{50}Ti	5.18 %	^{64}Ni	0.93 %
^{174}Yb	32.025 %				
^{176}Yb	12.995 %				

Table II.8: Composition and isotopic abundances for natural ytterbium, titanium and nickel foils.

All foils have the same surface area of 25 × 25 mm^2. The stack structure consisted of a sequence of ^{nat}Yb, ^{nat}Ti, ^{nat}Ni, ^{nat}Al and thick ^{nat}Al degrader was repeated between three to four times, depending of the number of ^{nat}Yb foils per irradiation. Figure II.18 shows how the foils were numbered and arranged concentrically in the stack. The stack was located in a stainless steel capsule, which was aligned and centered at the exit of the cyclotron for irradiation. Before the stack overlay, the mass and thickness of each foil were accurately measured. The foils were weighed with a 0.0001 g sensitivity scale and the thicknesses were calculated using a scanning technique to determine the surface area, since the mass and density of the material are known. The uncertainty of the thickness of each foil was less than the 25 % indicated by the manufacturers.

As can be seen in Figure II.18 f), the irradiations were performed in air. Specifically, between the 50 μm kapton foil (which delimited the exit of the cyclotron) and the first foil of the stack, there was 6 cm of air. To ensure that the entire assembly was perfectly aligned and centered with the charged-particle beam, a system of lasers and level metres was used. In addition, an alumina foil was inserted in place of the target as a pre-irradiation test.

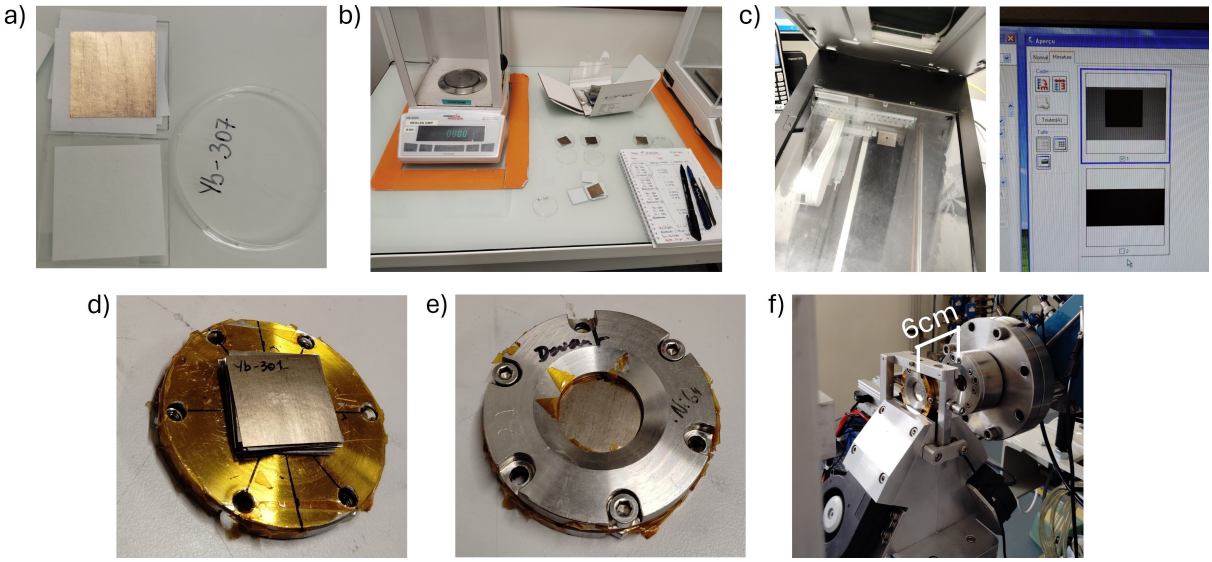

Figure II.18: Photographs of the preparation of the target before the irradiation process. a) Enumeration and identification of the foils. b) Balance to determine the mass of the different foils. Sensitivity 0.0001 g. c) Scanner to determine the accurate area of the foils. d) Stacking foils in their corresponding sequencing order. e) Encapsulation of the stacked-foils in the irradiation setup. f) Positioning of the setup in front of the cyclotron output.

In this way, it was possible to visualise the collimated beam profile shape at 10 mm diameter on the alumina foil, which emits fluorescence when the charged-particles hit on it. This effect was observed remotely with the help of cameras previously installed inside the irradiation area, from an external control room. The image of the pre-testing beam observed from the control room during the assembly is shown in Figure II.19.

After target assembly and beam control, three irradiations of deuterons with an average current intensity around 100 nA were performed using the C70 XP cyclotron at GIP ARRONAX. This cyclotron is able to provide also proton and α-beams, not used in the context of this work. Each irradiation had similar stack structure but was irradiated

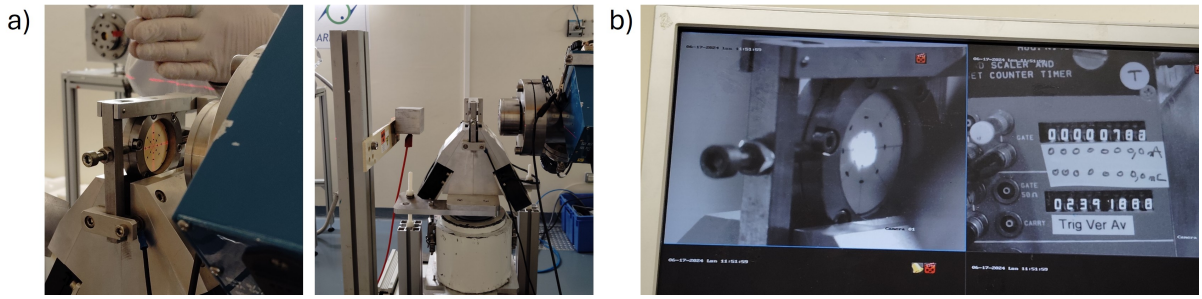

Figure II.19: Photograph of the placement of the target before the irradiation process. a) Laser system used to align the beam, the target and the beam stop. b) Photograph of the beam profile shape on the alumina as seen from a room outside the cyclotron, as well as a current control recorded at the beam stop.

Irradiation Day/Time (dd/mm/yy hh:mm)	Deuteron Energy (MeV)	Time (min)	Current (nA)	Stack Configuration (x nº times)
14/05/24 09:17	25.8 ± 0.5	60	110 ± 7	^{nat}Yb-Ti-Ni-Al-Degrader (x3)
03/06/24 19:20	33.0 ± 0.5	20	110 ± 7	^{nat}Yb-Ti-Ni-Al-Degrader (x3)
17/06/24 13:24	32.5 ± 0.5	20	120 ± 5	^{nat}Yb-Ti-Ni-Degrader (x4)

Table II.9: Irradiation parameters set in the irradiation runs at GIP ARRONAX cyclotron.

with different initial deuteron energy. The first stack consists of three ytterbium foils, it was irradiated at 25.8 MeV for 60 minutes. The second stack, made up of three more foils at 33 MeV for 20 minutes, and finally, four foils in the third stack at 32.5 MeV deuteron energy for 20 minutes. Table II.9 summarised the irradiations performed during the experiment together with the energy and intensity parameters set for each irradiation.

3.2 Data acquisition

At the end of each irradiation, an adequate cooling time was allowed to decrease the activity and replace the air in the bunker. Then, the stacked-foil target was recovered and disassembled. The thicker Al foils used as beam energy degraders were stored in a lead shield as they were not to be measured. The thin ^{nat}Yb and ^{nat}Ti foils were prepared for a first batch of measurements of the short half-life radioisotopes, such as ^{177}Yb in the ^{nat}Yb foil or nuclei injected in ^{nat}Ti, while the remaining ^{nat}Ni or ^{nat}Al foils were kept for future measurements in the coming days.

Figure II.20: View of the HPGe Detector called Recherche. The samples were placed at a distance of 19 cm from the detector head.

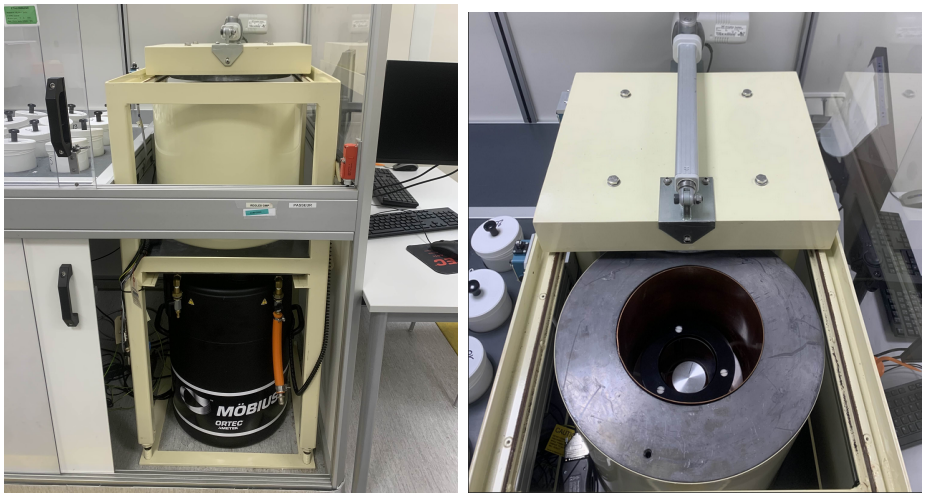

Figure II.21: View of the HPGe Detector called Passeur. The samples were placed at a distance of 20 cm from the detector head.

The radioactivity of each foil was measured non-destructively by two CANBERRA High-Purity Germanium γ-detectors (HPGe) cooled by liquid nitrogen. Two reference sources, with the same geometry as the samples, were used for energy and efficiency calibrations: ^{152}Eu (120-1400 keV) and ^{241}Am (59.5 keV) at a distance of 19 cm from the detector head shown in Figure II.20 and 20 cm from the second detector head shown in Figure II.21. Data were analysed using FitzPeaks Gamma Analysis [78] with a peak area uncertainty sigma value of 1.645 corresponding to a 90 % of confidence percentage and with background subtraction. The use of the detectors for the different foil measurements was indifferent, as the updated calibration files were available for each of them. Energy and efficiency calibration process for detectors are detailed in Appendix B.

Because natural ytterbium has 7 stable isotopes, the production of non-isotopic and isotopic impurities in the final product was unavoidable. For this reason, the measurements of the foil batches were repeated over time, considering the half-lives of the produced radioisotopes, in order to quantify most of them.

The first counting batch was started one hour after EOB and was repeated during the subsequent days, weeks and months to follow the decay of all produced radionuclides in function of their half-lives. The first counting time was about 20 minutes for each ^{nat}Yb foils. In the following days, the counting duration was between 8 h and 17 h, increasing from two to four days for the foils measured in the following weeks. Typical dead times ranged from $11 - 13$ % for the first series of measurement (few hours after EOB) to less than 1 % for the last measurements. For long-lived radionuclides the measurement was repeated after a cooling time of more than six months, when short half-life radionuclides had disappeared. Figure II.22 shows a HPGe spectrum in energy, measured one hour after EOB. A multitude of γ-peaks can be observed, in particular in the added zoom, the main peaks of interest coming from ^{177}Yb and ^{177g}Lu.

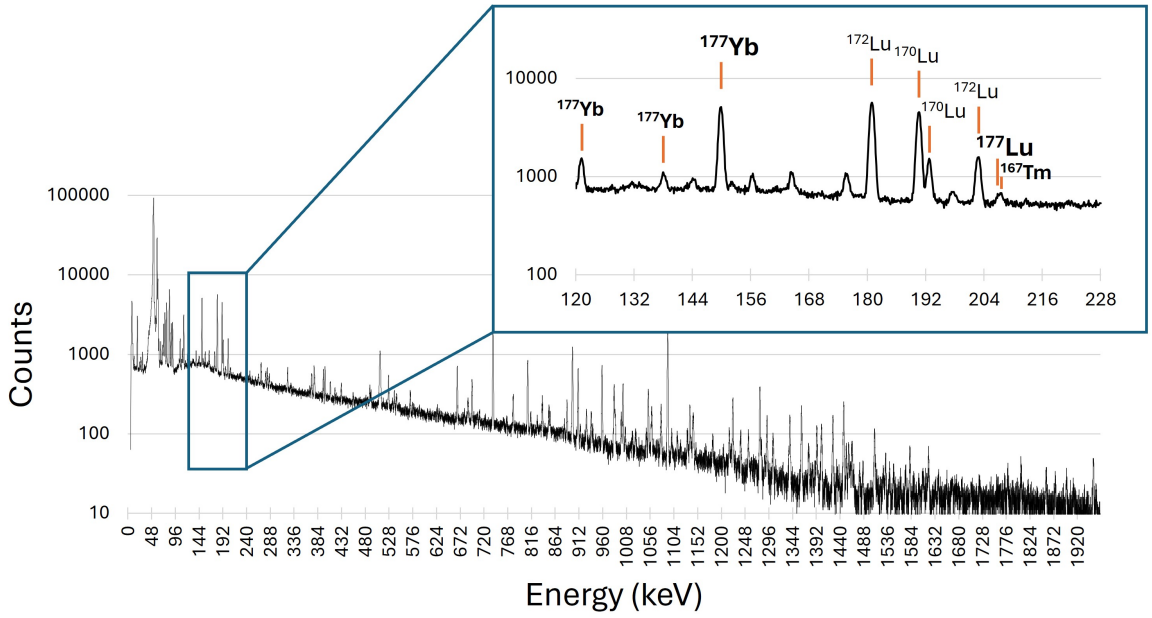

Figure II.22: HPGe spectrum as a function of energy measured 1 hour EOB, for 20 minutes. Zoom: Main γ-lines of ^{177}Yb and ^{177}Lu, together with other impurities detected.

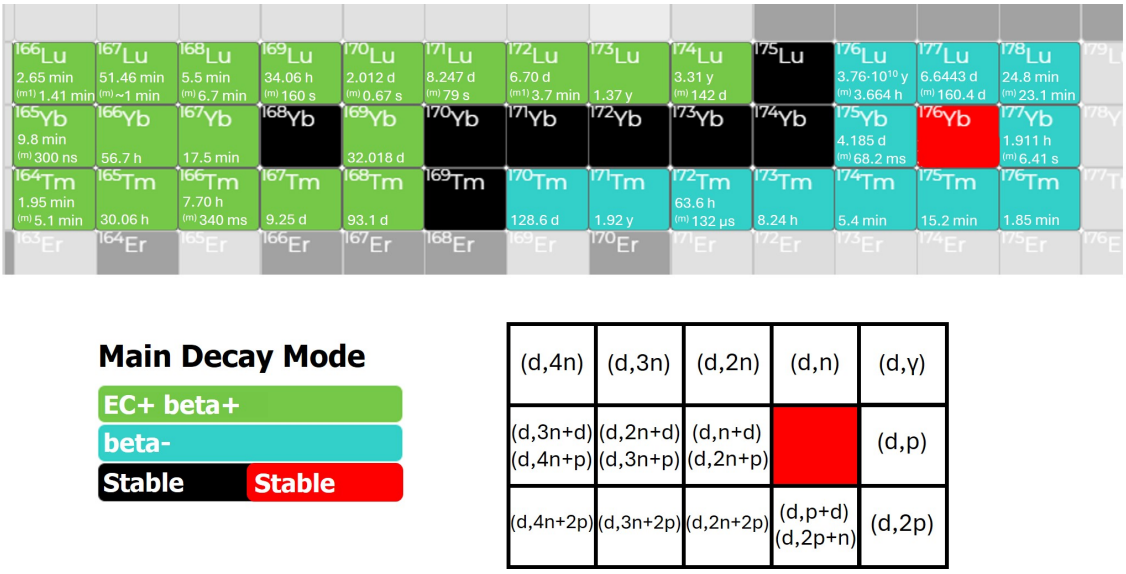

Figure II.23: Main displacement caused by deuteron-induced nuclear reactions on ^{nat}Yb at 33.0 MeV energy, radioisotope produced, half-lives and decay mode.

According to the Radionuclide Chart shown in Figure I.1 and the displacement caused by deuteron-induced nuclear reactions resulting from bombardment at 33.0 MeV energy, as shown in Figure II.23, radioisotopes that are peripherally in contact with the target nucleus are allowed to be produced. Furthermore, because of the high irradiation energies, channels such as (d,3n+x) or (d,4n+x) are energetically possible.

However, not all of them have been detected due to several reasons, such as having a very short half-life or shorter than the minimum cooling time of 1 hour after EOB, which leads us to discard radioisotopes like ^{166,168}Lu, ^{165}Yb and ^{164,174,175,176}Tm. Another reason is because they have γ-peaks with very low intensities, as would be the case with ^{170,171,172}Tm, or because they have high energy threshold or their production cross section values are very low, e.g. ^{166}Yb. Table II.10 and Table II.11 list the radioisotopes identified in the HPGe spectrum after irradiation, summarizing the half-life values ($T_{1/2}$), γ-ray energies (E_γ), γ-ray emission probabilities (I_γ), main production pathways and threshold energies for the radionuclides detected.

Produced Nuclei	$T_{1/2}$	Branch (%)	E_γ (keV)	I_γ (%)	Contributing reactions	Threshold (MeV)
^{177}Yb	1.91 h	β^- (100)	150.4 1080.2	18.01 5.13	^{176}Yb(d,p)	0
^{175}Yb	4.19 d	β^- (100)	396.3 282.5	13.20 6.13	^{174}Yb(d,p) ^{176}Yb(d,n+d) ^{176}Yb(d,2n+p) ^{175}Tm β^- decay	0 6.9 9.2
^{169}Yb	32.03 d	EC (100)	177.2 130.5 307.7	22.28 11.38 10.05	^{168}Yb(d,p) ^{170}Yb(d,n+d) ^{170}Yb(d,2n+p) ^{171}Yb(d,2n+d) ^{171}Yb(d,3n+p) ^{169}Lu β^+ decay	0 8.5 10.8 15.2 17.5
^{168}Tm	93.1 d	β^+ (99.9) β^- (0.01)	447.5 720.4 816.0	24.0 12.2 51.0	^{168}Yb(d,2p) ^{170}Yb(d,2n+2p) ^{171}Yb(d,3n+2p) ^{172}Yb(d,4n+2p)	1.7 17.2 23.9 32.0
^{167}Tm	9.25 d	EC (100)	207.8	41.30	^{168}Yb(d,n+2p) ^{170}Yb(d,3n+2p) ^{171}Yb(d,4n+2p) ^{167}Lu β^+ decay ^{167}Yb β^+ decay	8.6 24.1 30.8
^{48}V	15.97 d	EC, β^+ (100)	983.5 1312.1	99.98 98.20	^{nat}Ti(d,x)	0
^{46}Sc	83.79 d	β^- (100)	889.3 1120.5	99.98 99.98		
^{58}Co	70.86 d	EC, β^+ (100)	810.8	99.45	^{nat}Ni(d,x)	0
^{56}Co	77.24 d	EC, β^+ (100)	846.8	99.94		

Table II.10: Decay data, main contributing reactions and the gamma emissions used for the analysis of the produced ytterbium, thulium, ^{48}V, ^{46}Sc, ^{58}Co and ^{56}Co radionuclides with their threshold energies.

Produced Nuclei	$T_{1/2}$	Branch (%)	E_γ (keV)	I_γ (%)	Contributing reactions	Threshold (MeV)
^{177g}Lu	6.65 d	β^- (100)	208.4	10.38	^{176}Yb(d,n) ^{177}Yb β^- decay ^{177m}Lu $\rightarrow$ ^{177g}Lu	0
^{177m}Lu	160.4 d	β^- (77.3) IT (22.7)	208.4 228.5 378.5 418.5 413.7 319.0	55.40 36.96 29.40 21.72 17.62 10.51	^{176}Yb(d,n)	0
^{176m}Lu	3.66 h	β^- (99.9) EC (0.01)	88.4	8.90	^{176}Yb(d,2n)	3.1
^{174g}Lu	3.31 y	β^+ (100)	74.5 1241.8	5.90 5.14	^{173}Yb(d,n) ^{174}Yb(d,2n) ^{176}Yb(d,4n) ^{174m}Lu $\rightarrow$ ^{174g}Lu	0 4.4 17.2
^{174m}Lu	142.0 d	IT (99.38) EC (0.62)	44.7 67.1	12.40 7.25	^{173}Yb(d,n) ^{174}Yb(d,2n) ^{176}Yb(d,4n)	0 4.4 17.2
^{173}Lu	1.37 y	EC (100)	272.1 100.7	21.20 5.24	^{172}Yb(d,n) ^{173}Yb(d,2n) ^{174}Yb(d,3n)	0 3.7 11.3
^{172}Lu	6.70 d	β^+ (100)	900.7 810.1 912.2 78.7 697.3 1002.7	29.80 16.60 15.30 10.60 6.01 5.25	^{171}Yb(d,n) ^{172}Yb(d,2n) ^{173}Yb(d,3n) ^{174}Yb(d,4n)	0 5.6 12.0 19.6
^{171}Lu	8.25 d	β^+ (100)	739.8 667.4 75.9 780.7	48.70 11.20 6.19 4.44	^{170}Yb(d,n) ^{171}Yb(d,2n) ^{172}Yb(d,3n) ^{173}Yb(d,4n)	0 4.5 12.6 12.6
^{170}Lu	2.01 d	β^+ (100)	84.3 1280.3 985.1 1054.3	8.70 7.90 5.40 4.60	^{170}Yb(d,2n) ^{171}Yb(d,3n) ^{172}Yb(d,4n)	6.5 6.0 21.3
^{169}Lu	34.06 h	β^+ (100)	960.6 191.2	21.20 18.70	^{168}Yb(d,n) ^{170}Yb(d,3n) ^{171}Yb(d,4n)	0 13.9 20.6
^{167}Lu	51.46 min	EC, β^+ (100)	239.2 1267.3	18.20 4.30	^{168}Yb(d,3n)	1.5

Table II.11: Decay data, main contributing reactions and the gamma emissions used for the analysis of the produced lutetium radionuclides with their threshold energies.

3.3 Determination of foil energies and beam intensity

The deuteron beam intensity was calculated for each ^{nat}Yb foil in the stack using the IAEA recommended monitor foil cross-section reference data for deuteron particles in the studied energy range [51]. Specifically, making use of the reactions ^{nat}Ti(d,x)^{48}V,^{46}Sc on titanium foils located just behind the ytterbium foils in the stack. While the reactions ^{nat}Ni(d,x)^{58}Co,^{56}Co were used for a double check of the beam intensity.

The energy values associated with each cross-section value were simulated with the Monte Carlo code SRIM 2003 [50]. As shown in Figure II.24, knowing the initial beam energy, the thickness of the kapton foil (50 μm) that closes the beam output, the air distance to the stack (6 cm) and the thickness and material of all the stacked-foils, the beam energy loss through the setup is simulated. SRIM simulations were also used to estimate the uncertainty in the beam energy in each irradiated foil, which was estimated by including cumulative effects such as uncertainty in the primary beam energy ($\pm$ 0.5 MeV private communication), stopping estimation influenced by target thickness and beam straggling. The energy uncertainties ranged between $1.6 - 3.4$ %.

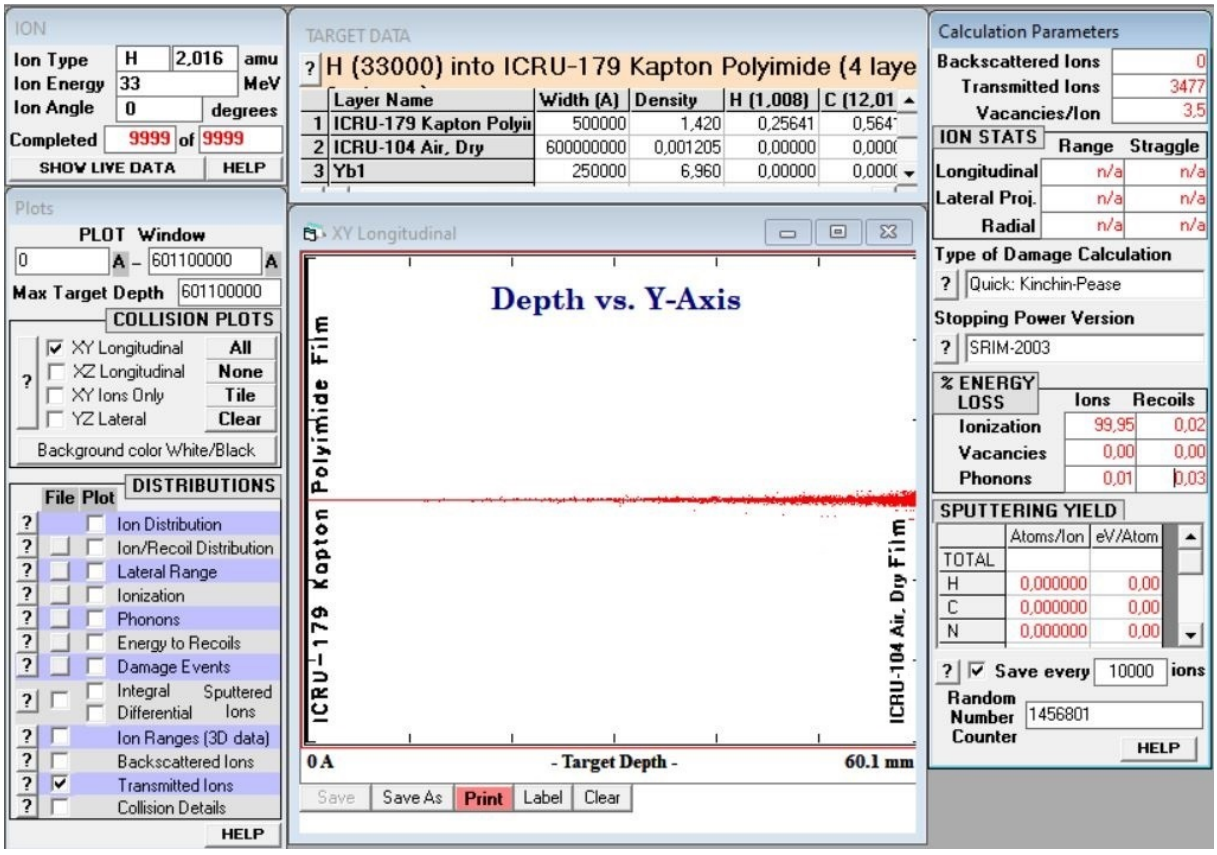

Figure II.24: SRIM 2003 transmitted ion simulation to evaluate the deuteron beam energy loss and straggling through the target. Energy output file will be generated. This simulation exemplifies the energy loss of a 33.0 MeV deuteron beam in an ytterbium foil after passing through 50 μm of kapton and 6 cm of air.

Initial Beam Energy (MeV)	Foil$_{n^o\ pos}$	Thickness (μm)	Energy (MeV)	Intensity (nA)
25.8 ± 0.5	Yb_1	28.91 ± 0.10	25.1 ± 0.5	105 ± 7
	Yb_2	25.88 ± 0.09	21.9 ± 0.6	112 ± 6
	Yb_3	26.35 ± 0.09	19.1 ± 0.6	110 ± 6
30.0 ± 0.5	Yb_1	25.81 ± 0.09	32.5 ± 0.5	110 ± 6
	Yb_2	28.74 ± 0.10	29.8 ± 0.5	116 ± 6
	Yb_3	24.19 ± 0.09	26.9 ± 0.6	106 ± 6
32.5 ± 0.5	Yb_1	27.78 ± 0.10	32.0 ± 0.5	122 ± 5
	Yb_2	26.07 ± 0.09	28.5 ± 0.6	120 ± 5
	Yb_3	23.96 ± 0.08	26.3 ± 0.6	115 ± 5
	Yb_4	22.39 ± 0.08	23.1 ± 0.7	119 ± 5

Table II.12: Calculated values of ytterbium reaction foil thickness, particle energies and beam intensity through each foil for the three irradiations performed at GIP ARRONAX cyclotron.

For the determination of the average beam intensity in each ytterbium foil, the beam intensity is assumed to be constant between juxtaposed monitor foils and corresponds to the average intensity calculated for the monitor foil, i.e. $\phi(E) = \phi'(E')$. Beam intensity values carry an uncertainty around 6 %, that takes into account the uncertainties of the measured monitor foil activity, the monitor foil cross-section and the average energy in this monitor foil. The average energy and beam intensity in each ytterbium reaction foil are shown in Table II.12.

3.4 Experimental cross-section measurements

The experimental cross-section measurements of the ^{177cum}Lu, ^{177}Yb and the rest of radionuclides produced (listed in Table II.10 and Table II.11) during the irradiation at the GIP ARRONAX cyclotron between the energy range of $19 - 33$ MeV are presented below.

Natural ytterbium isotopic abundances are used to determine the experimental cross-sections, which have been compared with the experimental data from EXFOR [62] database measured by A. Hermanne *et al.* [71], S. Manenti *et al.* [72], F. Tárkányi *et al.* [74] and M.U Khandaker *et al.* [73], as well as, with evaluated data from TENDL-2023 library [63]. The experimental measured cross-section data are presented in Table II.13.

Energy (MeV)	Cross-section (mbarn)					
	^{177cum}Lu	^{176m}Lu	$^{174(g+m)}$Lu	^{174m}Lu	^{174g}Lu	^{173}Lu
19.1 ± 0.6	143 ± 10	73 ± 6	63 ± 11	13 ± 1	63 ± 19	387 ± 37
21.9 ± 0.6	143 ± 10	59 ± 5	86 ± 11	25 ± 2	86 ± 12	397 ± 32
23.1 ± 0.7	130 ± 14	67 ± 9	93 ± 30	27 ± 11	93 ± 50	404 ± 35
25.1 ± 0.5	109 ± 8	49 ± 4	113 ± 12	41 ± 2	112 ± 9	283 ± 28
26.3 ± 0.6	93 ± 17	45 ± 7	122 ± 47	43 ± 17	121 ± 54	278 ± 25
26.9 ± 0.6	93 ± 12	40 ± 6	124 ± 44	46 ± 18	123 ± 53	275 ± 27
28.5 ± 0.6	69 ± 9	40 ± 6	146 ± 30	45 ± 17	145 ± 43	197 ± 17
29.8 ± 0.5	58 ± 15	45 ± 6	115 ± 39	44 ± 18	124 ± 46	168 ± 16
32.0 ± 0.5	72 ± 10	27 ± 5	125 ± 25	44 ± 17	114 ± 52	185 ± 16
32.5 ± 0.5	52 ± 24	43 ± 5	125 ± 27	43 ± 21	124 ± 53	185 ± 17

Energy (MeV)	Cross-section (mbarn)				
	$^{172(g+m)}$Lu	$^{171(g+m)}$Lu	$^{170(g+m)}$Lu	$^{169(g+m)}$Lu	^{167}Lu
19.1 ± 0.6	232 ± 17	267 ± 20	156 ± 12	22 ± 2	291 ± 147
21.9 ± 0.6	259 ± 16	320 ± 21	176 ± 16	30 ± 5	749 ± 269
23.1 ± 0.7	262 ± 14	322 ± 18	182 ± 10	32 ± 2	739 ± 336
25.1 ± 0.5	345 ± 22	363 ± 24	220 ± 15	69 ± 5	975 ± 336
26.3 ± 0.6	355 ± 20	364 ± 22	220 ± 13	69 ± 5	834 ± 348
26.9 ± 0.6	361 ± 25	364 ± 26	211 ± 16	74 ± 6	1045 ± 310
28.5 ± 0.6	394 ± 19	338 ± 18	254 ± 14	107 ± 7	901 ± 315
29.8 ± 0.5	383 ± 27	309 ± 23	241 ± 18	108 ± 9	962 ± 201
32.0 ± 0.5	420 ± 21	327 ± 18	300 ± 16	139 ± 9	595 ± 301
32.5 ± 0.5	423 ± 27	330 ± 22	300 ± 21	148 ± 11	902 ± 328

Energy (MeV)	Cross-section (mbarn)				
	$^{177(g+m)}$Yb	^{175cum}Yb	^{169cum}Yb	^{167}Tm	^{168}Tm
19.1 ± 0.6	117 ± 13	47 ± 3	23 ± 2	0.64 ± 0.04	0.7 ± 0.2
21.9 ± 0.6	92 ± 10	48 ± 3	39 ± 2	1.7 ± 0.2	1.1 ± 0.2
23.1 ± 0.7	93 ± 10	50 ± 3	39 ± 2	1.8 ± 0.3	-
25.1 ± 0.5	75 ± 9	53 ± 3	74 ± 4	3.6 ± 0.2	1.6 ± 0.1
26.3 ± 0.6	66 ± 8	52 ± 6	85 ± 5	2.6 ± 0.4	-
26.9 ± 0.6	73 ± 8	55 ± 4	88 ± 6	4.0 ± 0.5	-
28.5 ± 0.6	62 ± 7	57 ± 4	129 ± 6	4.0 ± 0.3	2.1 ± 0.5
29.8 ± 0.5	55 ± 6	54 ± 4	135 ± 9	3.8 ± 0.4	2.4 ± 0.4
32.0 ± 0.5	46 ± 5	58 ± 4	175 ± 8	4.1 ± 0.3	3.1 ± 0.7
32.5 ± 0.5	50 ± 6	62 ± 4	180 ± 11	4.1 ± 0.6	3.6 ± 0.5

Table II.13: Experimental cross-section (mbarn) values of ^{177}Lu and its main impurities produced by deuteron-induced nuclear reactions on ^{nat}Yb targets.

3.4.1 ^{176}Yb(d,x)^{177cum}Lu cross-section

The novel theranostic radioisotope ^{177g}Lu ($7/2^+$) can be produced by direct deuteron-induced reaction ^{176}Yb(d,n)$^{177(g+m)}$Lu or indirectly by decay of its parent ^{177}Yb ($9/2^+$). The production of metastable ^{177m}Lu ($23/2^-$) by ^{177}Yb decay is forbidden due to parity and angular momentum selection rules.

The ^{177g}Lu ($T_{1/2} = 6.65$ d) production has been measured taking into account the total decay of its parent ^{177}Yb ($T_{1/2} = 1.91$ h). As shown in Table II.11 the most abundant gamma emission of ^{177g}Lu is 208.4 keV (10.38 %). Unfortunately, this γ-ray overlaps with the 207.8 keV (41.3 %) gamma emission of ^{167}Tm ($T_{1/2} = 9.25$ d). Both radioisotopes have very similar half-lives, making it impossible to separate their signal exploiting a longer cooling time. Thus, to separate the two contributions around $\sim$ 208 keV energy peak a bi-gaussian fit method was applied to determine the net count area under the photopeaks, as shown in Figure II.25. The net area, once both contributions are separated, allowed us to determine the activity of ^{177g}Lu produced during irradiation, using Equation (II.18). Moreover, this gamma emission 208.4 keV is also a characteristic γ-line of its isomer ^{177m}Lu ($T_{1/2} = 160.4$ d). However, as concluded below, this γ-line is not contaminated by ^{177m}Lu.

The ^{177cum}Lu cumulative[4] cross-section measured in this study is shown in Figure II.26. A. Hermanne *et al.* [71], S. Manenti *et al.* [72] and M.U. Khandaker *et al.* [73] present agreement for the low-energy region, whereas F. Tárkányi *et al.* [74] cross-section data above 20 MeV shows discrepancies and are affected by large uncertainties due to the separation process of the 208 keV γ-line of ^{177g}Lu overlapping with the similar ^{167}Tm γ-line [74]. Our values are in good agreement with the early measurements up to 24 MeV, which is not the case with F. Tárkányi *et al.* [74] up to 30 MeV. Our points fit into the continuity of the curve and join those of F. Tárkányi *et al.* [74] after 30 MeV. Moreover, our points describe a shoulder on the curve, as the points of M.U. Khandaker *et al.* [73]

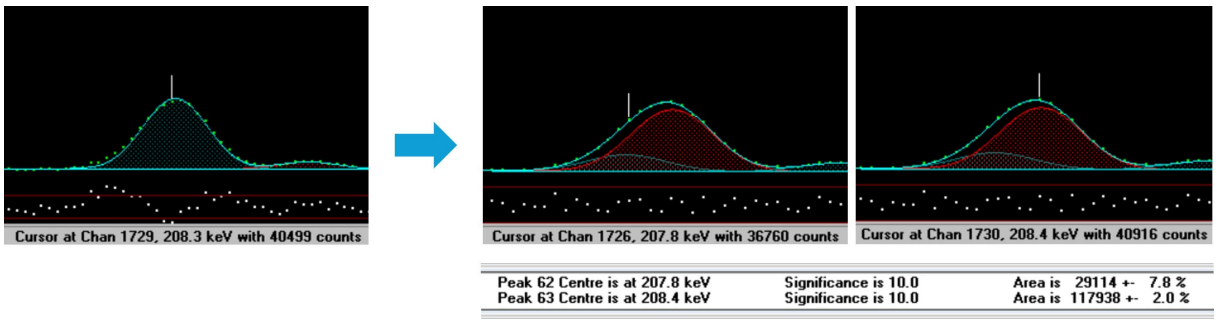

Figure II.25: Bi-Gaussian fitting method applied in FitzPeaks software to separate two γ-peaks identified as one. Uncertainty peak fits per channel is included.

[4]It is considered a cumulative measurement when the number of radioactive atoms used for the determination of the cross-section values includes those produced directly during irradiation, as well as those produced by the decay of a parent radionuclide.

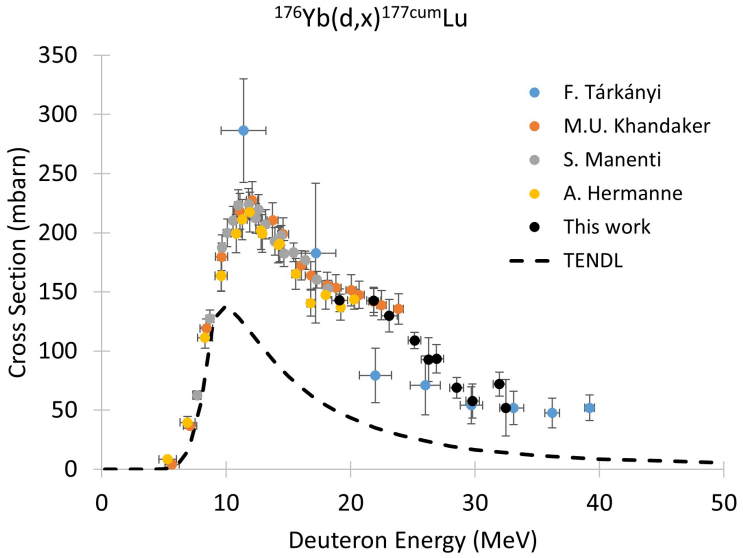

Figure II.26: Cross-section of the nuclear reaction ^{176}Yb(d,x)^{177cum}Lu.

seemed to show. Therefore, it has been possible to accurately discern the continuity of the curve based on the measurements available to date. On the other hand, TENDL-2023 [63] estimation does not accurately reproduce the experimental results.

3.4.2 ^{176}Yb(d,2n)^{176m}Lu cross-section

^{176}Lu has two states, a long-lived ground state ^{176g}Lu ($T_{1/2} = 3.76 \cdot 10^{10}$ y) and a relatively short-lived isomeric state ^{176m}Lu ($T_{1/2} = 3.664$ h). The ^{176g}Lu state could not be detected due to its long half-life, whereas the ^{176m}Lu cross-section, produced only by the ^{176}Yb(d,2n) deuteron-induced reaction, is shown in Figure II.27.

This work data is in a good agreement with the previous studies by M.U. Khandaker *et al.* [73] and S. Manenti *et al.* [72], whereas the estimation of the TENDL-2023 library [63] can only reproduce the low energy region up to 13 MeV well.

3.4.3 ^{nat}Yb(d,x)^{174g,174m}Lu cross-sections

The radioisotope ^{174}Lu has both a long-lived ground state ($T_{1/2} = 3.31$ y) and an isomeric state ($T_{1/2} = 142$ d). Measurements of cross-sections were performed four months after EOB, when the γ-peak signals of the long half-life radioisotopes were the only ones predominant in the gamma spectrum. The main contributions to their formation are the ^{174}Yb(d,2n) and ^{176}Yb(d,4n) nuclear reactions.

Due to the long half-life of both states, $^{174(g+m)}$Lu and ^{174m}Lu cross-sections have been measured simultaneously, as shown in Figure II.28 and Figure II.29. The behaviour of both trends is in agreement with that measured by M.U. Khandaker *et al.* [73] at higher energies. However, the estimated values of TENDL-2023 [63] are higher than

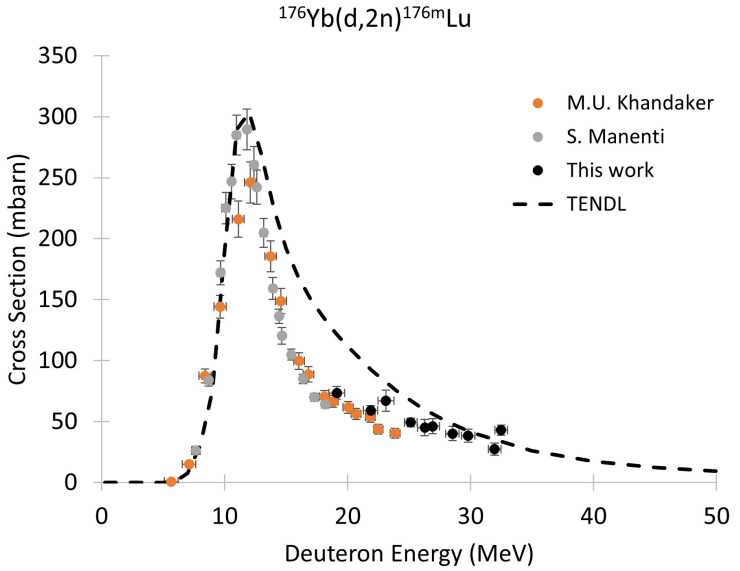

Figure II.27: Cross-section of the nuclear reaction ^{176}Yb(d,2n)^{176m}Lu.

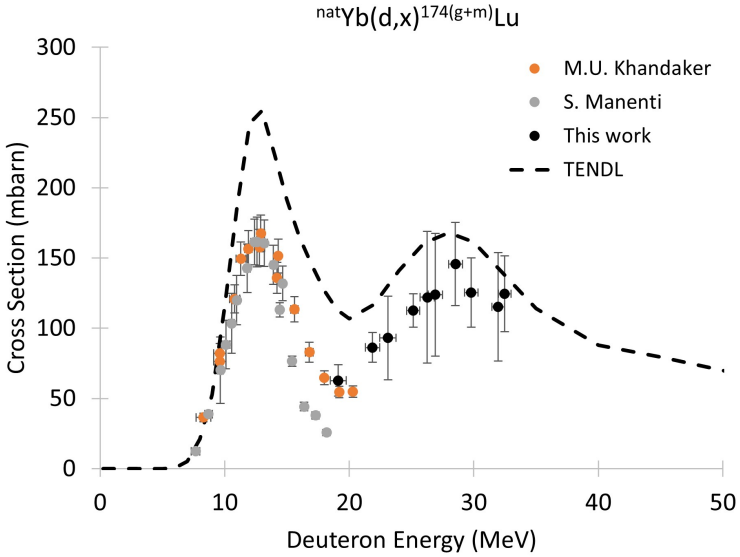

Figure II.28: Cross-section of the nuclear reaction ^{nat}Yb(d,x)$^{174(g+m)}$Lu.

the experimental ones, while maintaining the shape of the trend. Our values for the second and third irradiation compared to the values for the first irradiation show large uncertainties due to the reduction of the irradiation time by a factor of three, which has led to difficulties in measuring the activity produced.

Using the Bateman Equation (A.24) described in Appendix A, the single production of the ^{174g}Lu state might be obtained, as shown in Figure II.30. Good agreement is observed with the previous experimental data measured by A. Hermanne *et al.* [71] and S. Manenti *et al.* [72], as well as the trend estimated by TENDL-2023 [63] being quite accurate.

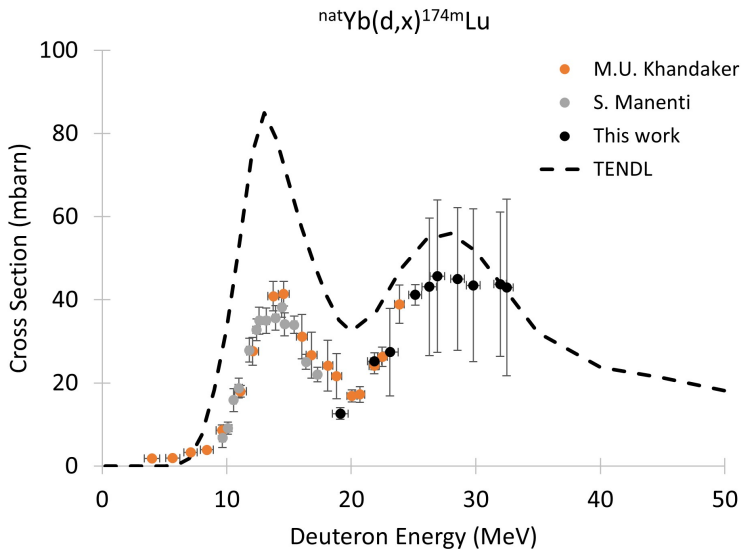

Figure II.29: Cross-section of the nuclear reaction ^{nat}Yb(d,x)^{174m}Lu.

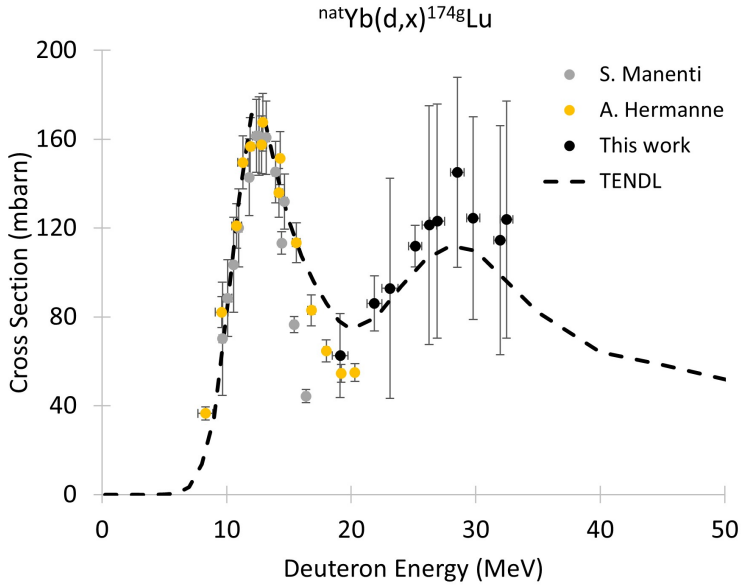

Figure II.30: Cross-section of the nuclear reaction ^{nat}Yb(d,x)^{174g}Lu.

3.4.4 ^{nat}Yb(d,x)^{173}Lu cross-section

Figure II.31 shows the total cross-section of ^{173}Lu ($T_{1/2}$ = 1.37 y) achieved from the contribution of four nuclear reactions of different stable isotopes of ytterbium. The predominant contribution of the first maximum corresponds to the deuteron-induced nuclear reaction ^{174}Yb(d,3n).

The good agreement with the previous experimental data by A. Hermanne *et al.* [71], S. Manenti *et al.* [72] and M.U. Khandaker *et al.* [73] shows the good continuity of the curve

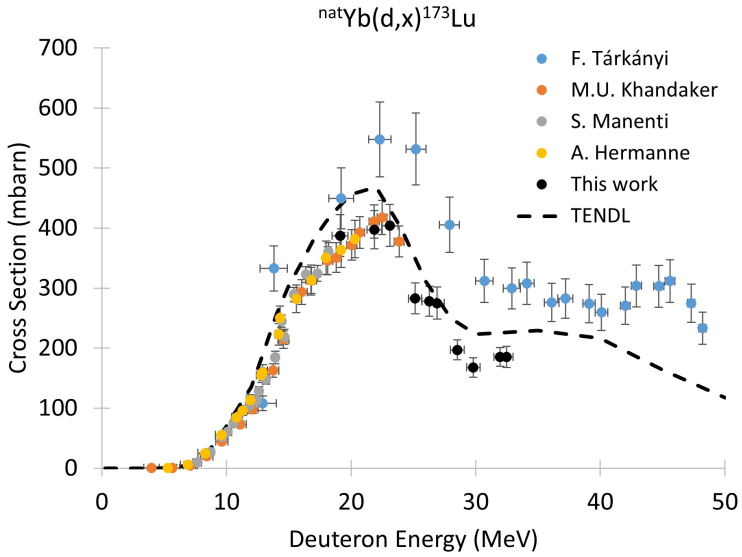

Figure II.31: Cross-section of the nuclear reaction ^{nat}Yb(d,x)^{173}Lu.

and reassures us that our experiments are running correctly despite the discrepancy with the F. Tárkányi *et al.* [74] data. However, the overall trend predicted by TENDL-2023 [63] for high energies is much closer to our results, but it estimates slightly higher values than the experimental ones.

3.4.5 ^{nat}Yb(d,x)$^{172(g+m_1+m_2)}$Lu cross-section

The radioisotope ^{172}Lu has three states, a ground state ^{172g}Lu ($T_{1/2}$ = 6.70 d), a first short-lived metastable state ^{172m_1}Lu ($T_{1/2}$ = 3.7 min) and a second isomeric state ^{172m_2}Lu ($T_{1/2}$ = 440 μs), both decaying to the ground state. The measurements of this radioisotope were carried out several days after the EOB. For this reason, the cross-section shown in the Figure II.32, corresponds to $^{172(g+m_1+m_2)}$Lu radioisotopes.

The excitation function is a contribution of three stable states of ytterbium. The dominant deuteron-induced reactions are both ^{172}Yb(d,2n) and ^{173}Yb(d,3n) up to 20 MeV, while ^{174}Yb(d,4n) for high energies. Our values are in good agreement with other authors by reducing the uncertainty of the measurements performed so far for high energies. The evaluated TENDL-2023 [63] curve shows a slightly higher description than the experimental results in the studied energy domain.

3.4.6 ^{nat}Yb(d,x)$^{171(g+m)}$Lu cross-section

Figure II.33 shows the cross-section of ^{171g}Lu ($T_{1/2}$ = 8.247 d) produced by five deuteron-induced nuclear reactions (listed in Table II.11) in different stable states of ytterbium, together with, the IT decay of its short-lived isomer ^{171m}Lu ($T_{1/2}$ = 79 s), which measurement was not possible due to the short decay time.

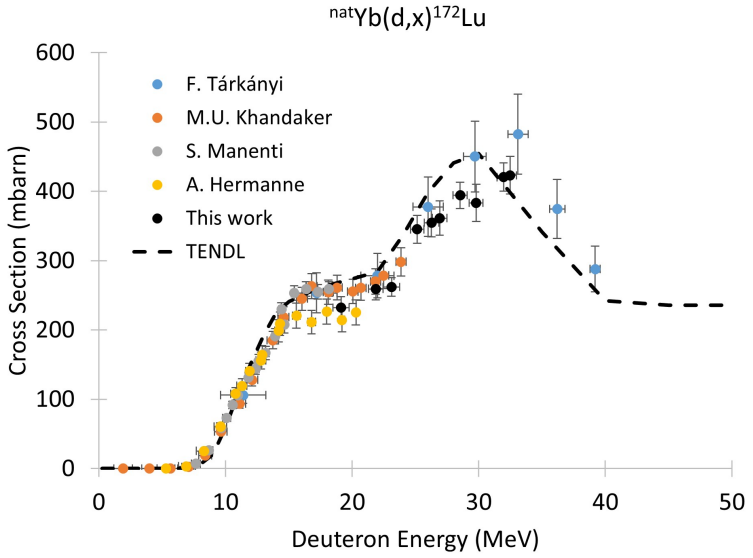

Figure II.32: Cross-section of the nuclear reaction ^{nat}Yb(d,x)$^{172(g+m_1+m_2)}$Lu.

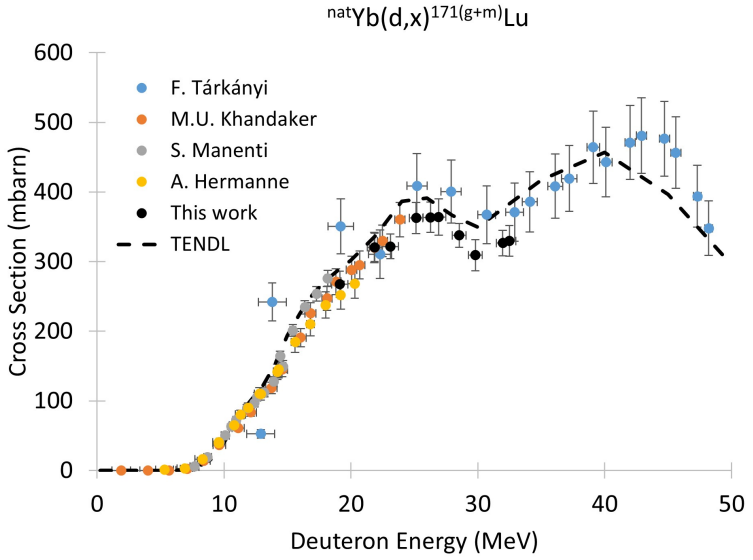

Figure II.33: Cross-section of the nuclear reaction ^{nat}Yb(d,x)$^{171(g+m)}$Lu.

Comparing with the experimental values measured by other authors we can claim a good overlap and prolongation of the trend, finding only some discrepancies with the overestimated values of F. Tárkányi *et al.* [74]. Anyway, the trend found is good, being reproduced quite well by the evaluated values of TENDL-2023 [63].

3.4.7 ^{nat}Yb(d,x)$^{170(g+m)}$Lu cross-section

Figure II.34 presents the cross-section of ^{170g}Lu ($T_{1/2}$ = 2.012 d) and its short-lived isomer ^{170m}Lu ($T_{1/2}$ = 0.67 s). The $^{170(g+m)}$Lu cross-section data align well with previous studies

and TENDL-2023 [63] curve runs in good description with all the experimental results measured by different authors up to 35 MeV.

3.4.8 ^{nat}Yb(d,x)$^{169(g+m)}$Lu cross-section

The measurements for the determination of the ^{169g}Lu ($T_{1/2}$ = 34.06 h) cross-section were carried out 2-3 days after EOB. It was produced by the routes described in Table II.11 and a complete IT decay of the short-lived isomer, ^{169m}Lu ($T_{1/2}$ = 160 s).

Figure II.35 shows a great consistency with the previous works, whereas TENDL-2023 [63] shows a larger production cross-section than the experimental values, specifically in the region between 22 MeV to 32 MeV where the main contribution corresponds to the direct production route ^{171}Yb(d,4n). The agreement of all experimental data will help to improve the theoretical estimates.

3.4.9 ^{168}Yb(d,3n)$^{167(g+m)}$Lu cross-section

No previous experimental data were present for ^{167g}Lu ($T_{1/2}$ = 51.46 min) production cross-sections. Its measurement was carried out only 1-2 hours after EOB, and once the IT decay of its very short half-life isomeric state ^{167m}Lu ($T_{1/2}$ = $\sim$ 1 min) was completed. As a consequence, the dead time of the measurement was high, between 11 – 13 %.

That fact, together with the low abundance of ^{168}Yb (0.123 %) in our natural ytterbium samples, makes the uncertainties associated with the measurement of the cross-section high, as can be observed in Figure II.36. TENDL-2023 [63] values seem to reproduce the experimental results. However, due to the high uncertainty, it is not possible to confirm an accurate shape.

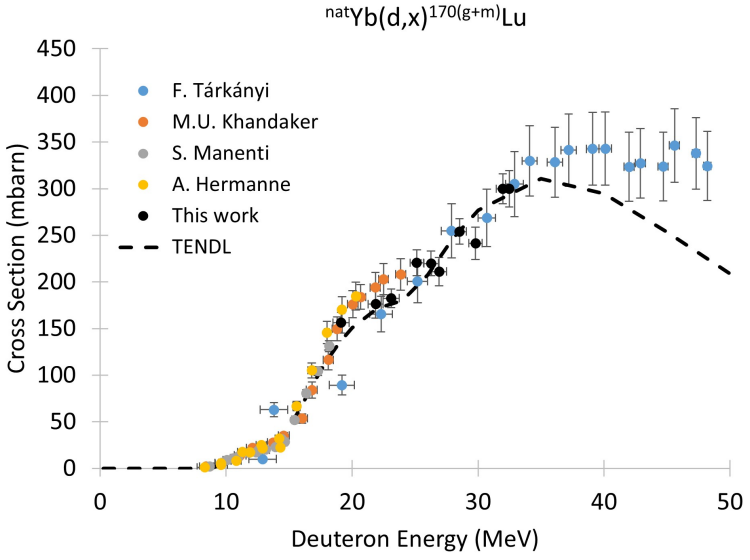

Figure II.34: Cross-section of the nuclear reaction^{nat}Yb(d,x)$^{170(g+m)}$Lu.

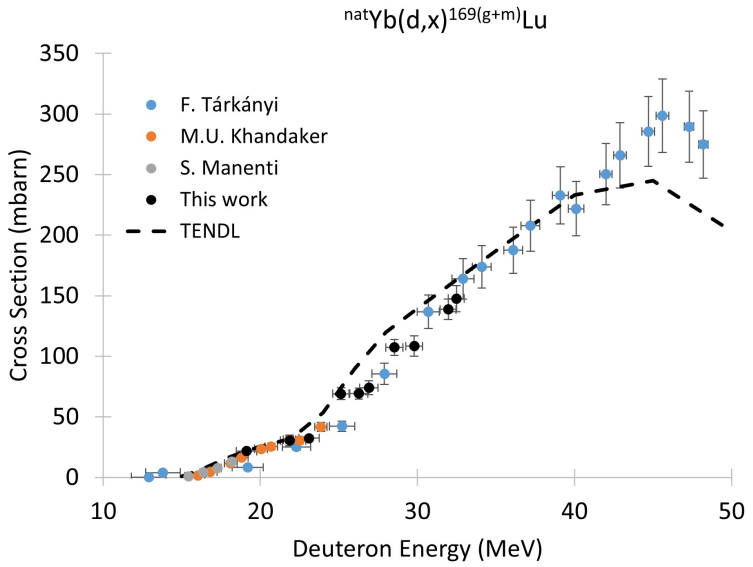

Figure II.35: Cross-section of the nuclear reaction ^{nat}Yb(d,x)$^{169(g+m)}$Lu.

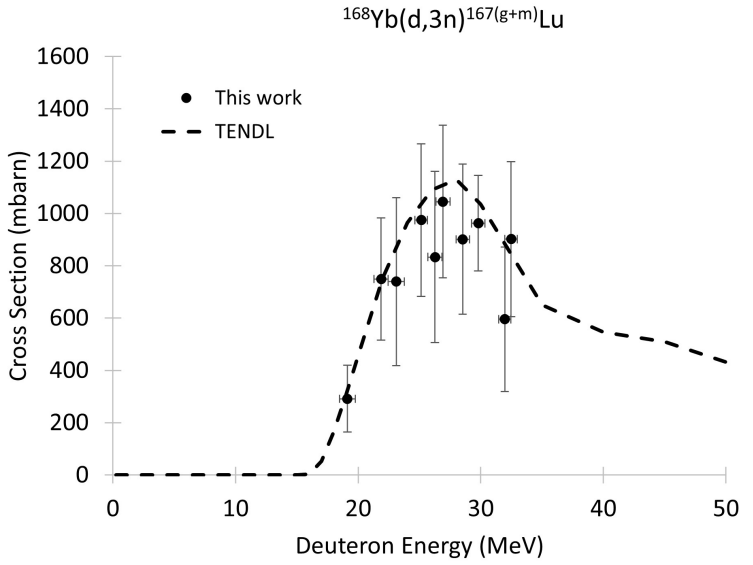

Figure II.36: Cross-section of the nuclear reaction ^{178}Yb(d,3n)$^{167(g+m)}$Lu.

3.4.10 ^{176}Yb(d,p)$^{177(g+m)}$Yb cross-section

The $^{177(g+m)}$Yb cross-section was another measurement performed only 1-2 hours after the EOB, due to the short half-life of it radioisotope ^{177g}Yb ($T_{1/2}$ = 1.911 h) and its isomeric state ^{177m}Yb ($T_{1/2}$ = 6.41 s), which decays via IT to the ground state.

This radioisotope is of great interest in our study because it is the parent nucleus of ^{177g}Lu, and also the main n.c.a production route of the theranostic radioisotope ^{177g}Lu via β^- decay. The comparison between the available experimental data and our results shows

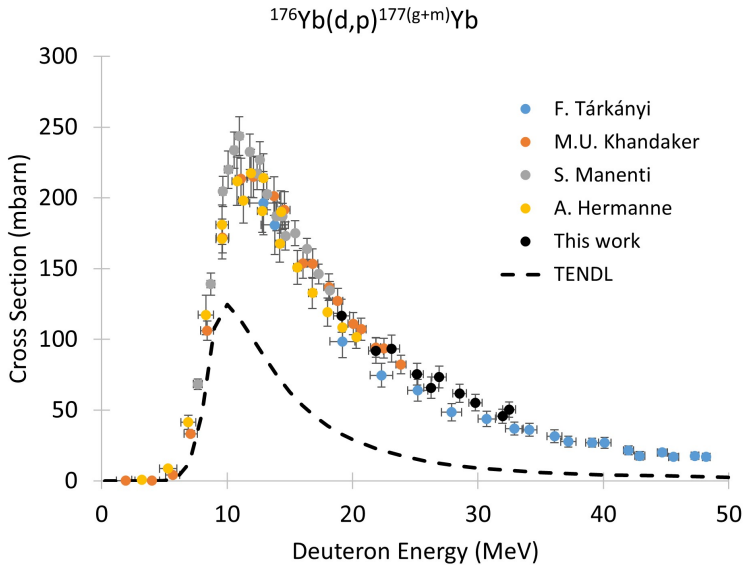

Figure II.37: Cross-section of the nuclear reaction ^{176}Yb(d,p)$^{177(g+m)}$Yb.

a great agreement, but this is not the case if we compare with TENDL-2023 [63] values, where a remarkable underestimation of the cross-section is observed (Figure II.37). All the experimental data so far will help to improve the theoretical parameterisations, which are clearly insufficient.

3.4.11 ^{nat}Yb(d,x)^{175cum}Yb cross-section

The measurement of the cumulative cross-section of ^{175}Yb ($T_{1/2}$ = 4.185 d) was performed $2-3$ days after the EOB, and is the result of different contributions, e.g. the direct production by nuclear reactions ^{174}Yb(d,p), ^{176}Yb(d,n+d) and ^{176}Yb(d,2n+p), causing the first and second maximum, respectively, and the β^- decay of ^{175}Tm ($T_{1/2}$ = 15.02 min). The excitation function is shown in Figure II.38.

Comparing with the results of other authors, we can observe a good trend according to the data of A. Hermanne *et al.* [71], S. Manenti *et al.* [72] and M.U. Khandaker *et al.* [73], whereas F. Tárkányi *et al.* [74] shows slightly higher values. However, TENDL-2023 [63] data are not able to adequately reproduce the expected trend as the direct ^{174}Yb(d,p) reaction, which is strongly underestimated.

3.4.12 ^{nat}Yb(d,x)^{169cum}Yb cross-section

Cross-section measurements for the determination of ^{169}Yb ($T_{1/2}$ = 32.018 d) cumulative excitation function were carried out 15 days after EOB, to allow for full decay of ^{169}Lu ($T_{1/2}$ = 34.06 h). This indirect production gives the main contribution at energies higher than 15 MeV.

We found a good agreement with both the early measurements by A. Hermanne *et al.* [71], S. Manenti *et al.* [72] and M.U. Khandaker *et al.* [73] in the overlapping energy domain and with the estimations of the TENDL-2023 library [63] in both the shape and the trend of the measured cross-section as shown in Figure II.39.

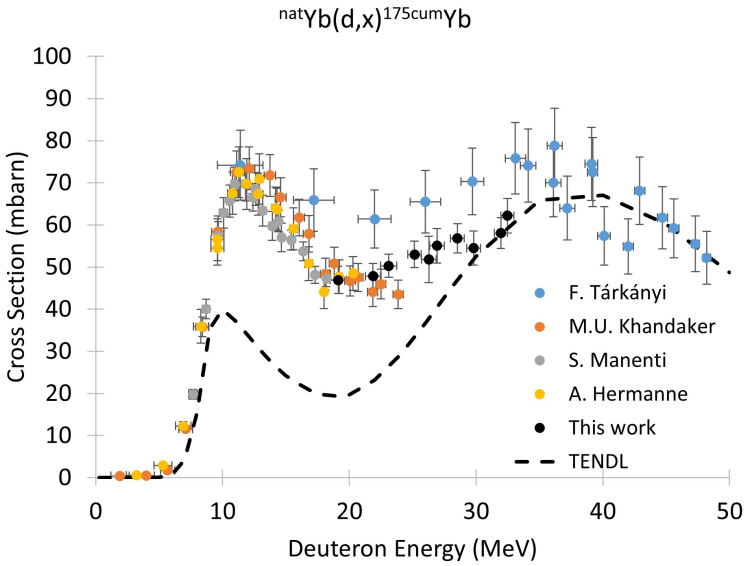

Figure II.38: Cross-section of the nuclear reaction^{nat}Yb(d,x)^{175cum}Yb.

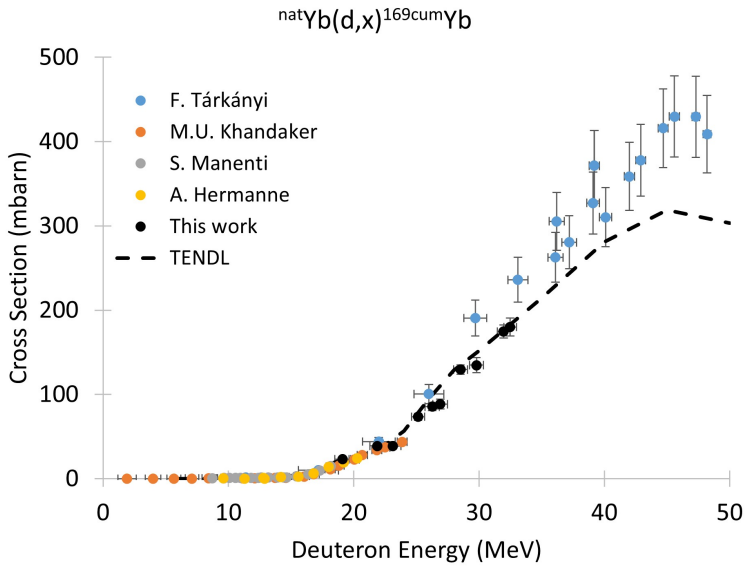

Figure II.39: Cross-section of the nuclear reaction ^{nat}Yb(d,x)^{169cum}Yb.

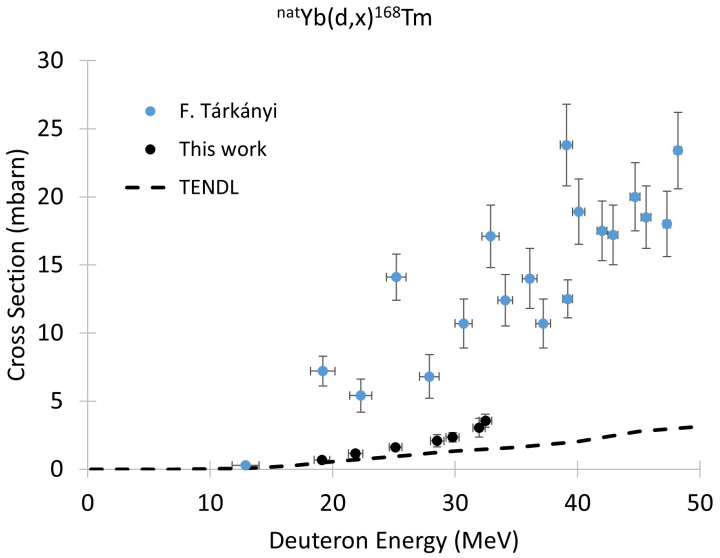

Figure II.40: Cross-section of the nuclear reaction ^{nat}Yb(d,x)^{168}Tm.

3.4.13 ^{nat}Yb(d,x)^{168}Tm cross-section

The measured cross-sections of ^{168}Tm ($T_{1/2}$ = 93.1 d) is shown in Figure II.40. Its gamma energy 198.3 keV (54.49 %) can be contaminated by the 197.9 keV γ-line (35.93 %) of ^{169}Yb ($T_{1/2}$ = 32.018 d). For that reason, neither of these two energies have been used to identify the corresponding radioisotopes, since a clear differentiation in the spectrum was not available as in the case of ^{177g}Lu.

TENDL-2023 [63] calculations closely reproduce the shape of the trend of our values, although underestimating the results. Nevertheless, large discrepancies are shown with respect to F. Tárkányi *et al.* [74] the only experimental values available, possibly due to contamination by radioisotope ^{169}Yb, whose energies mentioned above are used for the determination of both radioisotopes.

3.4.14 ^{nat}Yb(d,x)^{167cum}Tm cross-section

The radioisotope ^{167}Tm ($T_{1/2}$ = 9.25 d) is produced by the direct routes described in Table II.10 and from the EC and β^+ decay of its short-lived parent ^{167}Yb ($T_{1/2}$ = 17.5 min). In order to identify its cross-section it is necessary to separate its peak energy of 207.8 keV (41.3 %) from the nearest contribution of 208.4 keV (10.38 %) corresponding to ^{177g}Lu γ-ray and calculate the radionuclide activity by Equation (II.18).

For this reaction there is little experimental data to compare. F. Tárkányi *et al.* [74] admit that as a consequence of the overlapping of the ^{177g}Lu and ^{167}Tm γ-lines and the impossibility to separate both peaks due to the lack of energy resolution of the detector used, ^{167}Tm cross-section data have been acquired identifying the second ^{167}Tm γ-peak at 532 keV (1.61 %), presenting low count rate and large scattering. On the other hand,

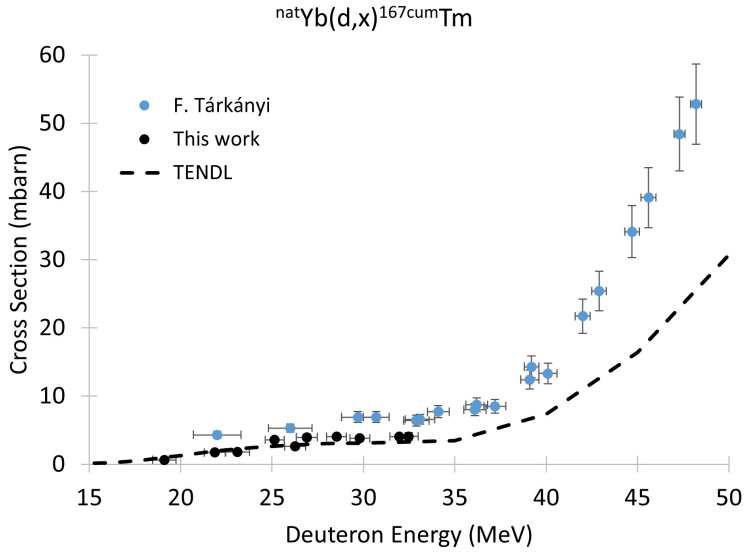

Figure II.41: Cross-section of the nuclear reaction ^{nat}Yb(d,x)^{167cum}Tm.

estimated data from TENDL-2023 [63] is in good agreement with our experimental values.

3.4.15 Estimation ^{177m}Lu contribution

^{177m}Lu ($T_{1/2}$ = 160.4 d) is a long-lived isotopic impurity of ^{177g}Lu. By deuteron-induced nuclear reaction, it can only be produced via direct production route ^{176}Yb(d,n)^{177m}Lu, that then decays β^- (77.3%) to ^{177}Hf and IT (22.7%) to ^{177g}Lu.

The irradiated natural ytterbium foils were measured again six months after the EOB, verifying that the long-lived metastable state, ^{177m}Lu, was below the detection limit of the gamma detector. Figure II.42 shows the γ-spectrum of thirteen days of measurement, acquired six months after EOB. The marked areas indicate the regions corresponding to the main ^{177m}Lu γ-peaks: 208.4 keV (55.4 %), 228.5 keV (36.96 %) and 378.5 keV (29.4 %). Confirmed by the fact that no signal peaks are observed, in the worst case, the long-lived impurity ^{177m}Lu activity values will correspond to the detection limit of γ-spectrometer.

The definitions of the detection limit concepts are a basic aspect of spectrometry and they have been taken from literature by authors such as L.A. Currie [79]. Three specific levels were defined: "Decision limit" (L_C) the net signal level (instrument response) above which an observed signal may be reliably recognized as "detected"; The "Detection limit" (L_D) is the minimum "true" net signal level at which an analytical procedure can reliably produce a response; and "Determination limit"(L_Q) the level at which the measurement precision will be satisfactory for quantitative determination [79]. According to the FitzPeaks Software manual [78], the formula to estimate the "Detection limit", L_D, at which a priori detection can be expected to occur is:

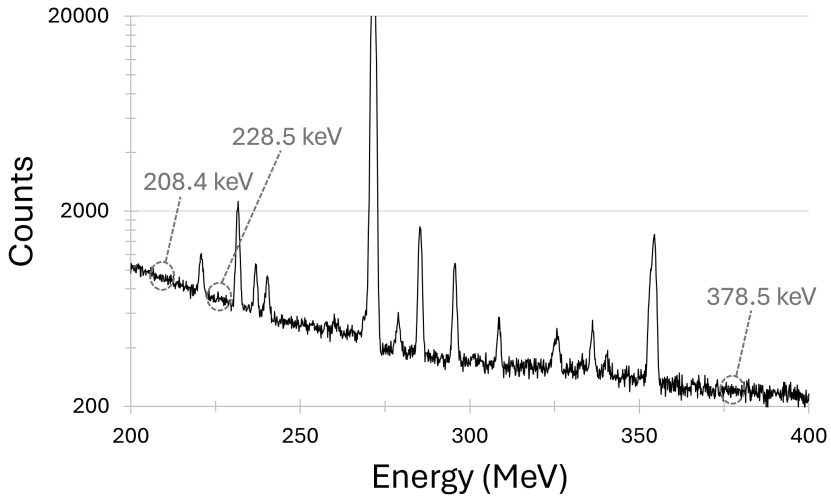

Figure II.42: HPGe spectrum with the most relevant ^{177m}Lu γ-lines for a thirteen days measurement performed six months after EOB.

$$L_D = 2L_C = 2\sigma\sqrt{(1 + n/2m) \cdot Bkg} \tag{II.23}$$

where the constant σ takes the value 1.645 (90 % percentage confidence value); n is the width of the region, in channels, where the peak would be found and is defined as 2.55 times the expected FWHM at that energy; m is the number of channels each side of the peak that would be used to determine the integral of the counts when fitting a peak; and Bkg is the background number of counts in the continuum in that region. The Equation (II.23) give a result in counts which is converted to activity by dividing by the product of the emission probability, the efficiency and the Live Time.

Under our irradiation conditions and according to Currie's criterion [79], the detection limit for ^{177m}Lu is L_D = 3.3 Bq (calculated for the energy value corresponding to the maximum of the cross-section for ^{177m}Lu, under the assumption that the two cross-sections, ^{177g}Lu and ^{177m}Lu by direct route, have the similar shape and slope. This consideration holds for an energy close to 20 MeV). More precisely, it is possible to calculate an upper limit for ^{177m}Lu using the yield ratio between the detection limit of ^{177m}Lu and ^{177g}Lu activity at EOB for an irradiation energy around 20 MeV. This value is estimated as 0.0005 % and it can be compared to 0.0045 % calculated by S. Manenti *et al.* [72] or less than 0.01 % estimated by Nagari *et al.* [80], in contrast to 0.010 − 0.015 % [81] and 0.02 % [82] reported for common ^{177}Lu production at nuclear reactors.

3.5 Calculated Physical Thick Target Yields (TTYs)

Based on the excitation functions of the cross-section fits, the physical thick target yields were calculated for all lutetium, ytterbium and thulium radioisotopes produced in the

irradiation processes limited to the energy region below 33 MeV. The ^{177cum}Lu, ^{176m}Lu and ^{177}Yb yields are estimated for 100 % enriched ^{176}Yb target, while for the rest yields have been estimated with total energy absorption of ^{nat}Yb. This is because in the production of ^{177g}Lu for clinical use, highly enriched targets are always used.

These experimental yields in MBq/μA·h are shown in Figure II.43 and Figure II.44, as well as, the experimental value 0.13 ± 0.02 MBq/μA·h for the yield of ^{173}Lu and 0.018 ± 0.003 MBq/μA·h for ^{174g}Lu at 22 MeV reports by P. Dmitriev *et al.* [68]. Comparing the ^{177cum}Lu and ^{177}Yb TTYs, it is possible to observe that up to 33 MeV the radioisotopes of interest can be produced with no or low co-production of the other radioactive impurities, with the exception of one of them, ^{176m}Lu ($T_{1/2}$ = 3.664 h) which, due to its short half-life, can be allowed to decay before using the ^{177g}Lu. Two days of cooling time would be sufficient.

TTYs shown in Figure II.43 and Figure II.44 have been calculated with the RYC tool from the data of the cross-sections measured in this work and those available in EXFOR database [62].

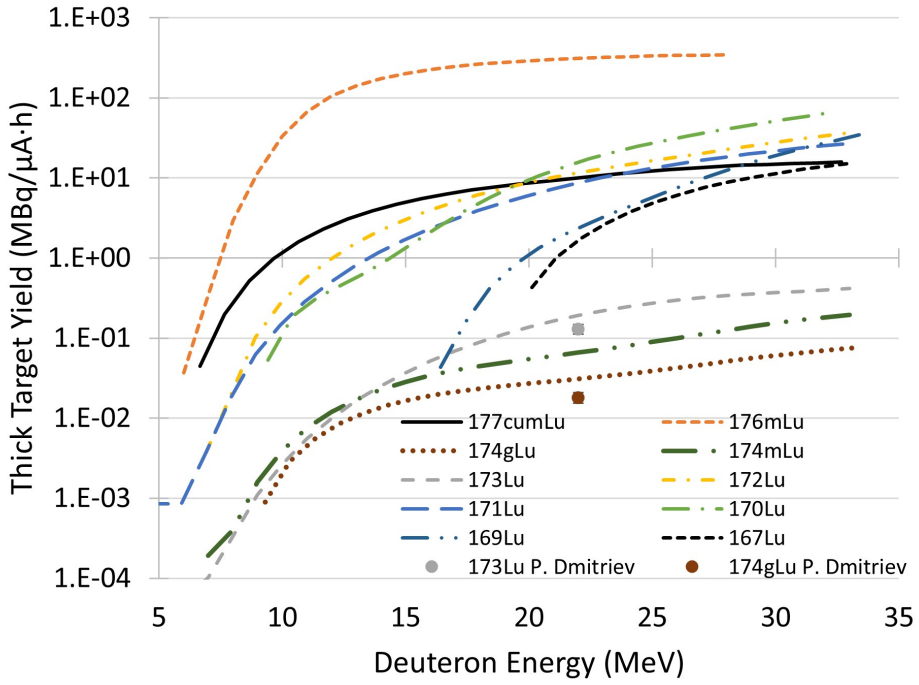

Figure II.43: Calculated physical thick target yields for the lutetium radionuclides with total energy absorption for ^{nat}Yb target. The presented yields of ^{177cum}Lu and ^{176m}Lu are estimated for the 100 % enriched ^{176}Yb target.

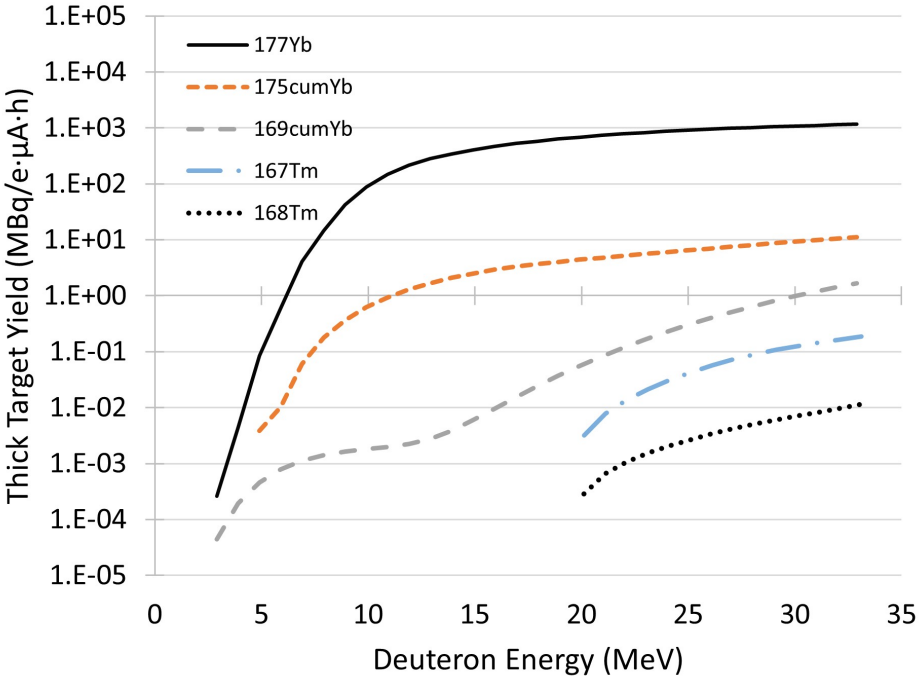

Figure II.44: Calculated physical thick target yields for the ytterbium and thulium radionuclides with total energy absorption for ^{nat}Yb target. The ^{177}Yb presented yield is estimated for the 100 % enriched ^{176}Yb target.

4 Chapter conclusions

Experimental determination of thick target yields and excitation functions constitute the main step in the the development of new and alternative production routes to conventional methods that can guarantee large-scale radioisotope production in novel facilities, such as the future international IFMIF-DONES facility. For this purpose, solid knowledge of nuclear data such as the deuteron-induced cross-sections of nuclear reactions is essential.

In this chapter, the concept of cross-section has been introduced and the main results obtained in experimental work among two international collaborations have been presented. Work concerned the measurement of the cross-sections of two of the radioisotopes of major clinical interest: ^{165}Er and ^{177}Lu. The new nuclear data can be used to optimize the production of the radionuclides of interest and minimize the production of their contaminants produced simultaneously during the irradiation process. In addition, the physical background and the methodology of stacked-foil and gamma spectrometry techniques required to obtain all the parameters involved in the measurement, as well as in the calculation of the cross-sections, have been discussed in detail. All the tools used to obtain the final results have been detailed in this chapter or in the Appendix A to Appendix C.

The measurement of the cross-section of the deuteron-induced reaction on ^{nat}Ho has allowed to redefine the maximum cross-section peak reducing the uncertainties of previous measurements. In addition, this new experiment has allowed measurement of the first time the isomeric state of the ^{166m}Ho produced as a non-isotopic impurity during the irradiation process, providing new nuclear data for this reaction, which until now has not been available in the experimental databases.

On the other hand, the nuclear measurements performed for the reaction induced by deuterons on ^{nat}Yb are of high scientific interest, as so far, nuclear measurements at high energies available in databases differ from each other without defining a clear excitation function. The new measurements are now a turning point that allows an improvement in the estimation of the production of these radionuclides, bringing new results to the scientific community. In addition, it has been possible to assess an upper limit of the metastable impurity ^{177m}Lu, which is very important for the approval of the final product of ^{177}Lu for clinical use.

In the following chapter, using the measured nuclear data, a detail study and implementation of the production of these potential radioisotopes of high clinical interest, ^{165}Er and ^{177}Lu, will be developed, in accordance with the particular characteristics of the future international IFMIF-DONES facility. In addition, a much more detailed study of the possible isotopic or non-isotopic impurities generated together with the radioisotopes of interest will also be carried out. Production estimations adapted to IFMIF-DONES will be performed using highly enriched realistic targets, such as those used in the clinic and commercially available.

Chapter III

Radioisotopes at IFMIF-DONES

The International Fusion Materials Irradiation Facility - Demo Oriented NEutron Source (IFMIF-DONES) will be an infrastructure to test new materials under high neutron flux and temperatures, to be used in the future DEMO fusion reactor. IFMIF-DONES will generate neutrons by hitting a high power deuteron beam (5 MW) on a liquid lithium target. A major effort is being made to take advantage of the facility unique neutron and deuteron characteristics. Within this framework, a complementary program is being developed, where the production of radioisotopes for Nuclear Medicine is one of the main complementary applications proposed in the project.

This chapter analyses the feasibility of the complementary application of radioisotope production within the facility. For this purpose, the calculation of the radioisotope production yield and the estimation of the specific activity of the final product is studied in comparison with conventional methods, with special emphasis on the isotopic impurities generated together with the final product of interest. Finally, realistic production device designs adapted to the conditions and preliminary plans of the planned facility are proposed, carrying out thermal, structural and mechanical simulations of the devices, as well as, flow and dose control simulations in critical areas.

By means of deuteron-induced nuclear reactions, the possibility of producing the radioisotopes already mentioned in Chapter II is studied, for which exhaustive work has been carried out to analyse their production yields, as well as isotopic and radionuclide purities in the final product. The radioisotopes studied are the Auger-electron emitting therapy ^{165}Er, and the novel theranostic radioisotope ^{177}Lu.

Using neutron-induced nuclear reactions, the alternative production route of ^{99}Mo, precursor and parent nucleus of the most widely used radioisotope for SPECT diagnostic imaging ^{99m}Tc, is studied. Furthermore, the goal was to optimize its production for large scalability.

1 Radioisotope production with deuterons

The high-intensity linear deuteron accelerator (40 MeV and 125 mA) that will produce a high-intensity neutron flux (10^{14} cm^{-2}s^{-1}) in the IFMIF-DONES core has exceptional neutron and deuteron characteristics that have prompted complementary applications in the field of radioisotope production for Nuclear Medicine [5, 83].

Some upgrades of the accelerator design are being studied for these complementary applications. In particular, the possibility exists of diverting 1 pulse per 1000, which would be 0.1 % intensity current of the initial deuteron beam, to an experimental room (R026) under the Linac hall. Therefore, a 40 MeV deuteron energy beam at 125 μA current intensity would be available for other deuteron applications.

To produce radioisotopes through deuteron-induced nuclear reactions (as explored in the description of activation experiments in Chapter II), a device holding the production targets that can be also coupled to the beamline output is necessary. All this, inside a bunker room that will remain closed during irradiation operations.

Therefore, an important part of the work has been the design of a realistic deuteron beam radioisotope production device able to dissipate the heat generated in the sample, and thermally and structurally support the irradiation process. On the other hand, from the excitation functions obtained in the previous chapter, the maximum specific activities of the ^{165}Er and ^{177}Lu radioisotopes produced with deuterons at IFMIF-DONES have been estimated and optimised, including a detailed study of the impurities generated and isotopic, radionuclide purities and specific activities estimations. For this purpose, Simpson's composite rule is used as a numerical integration method, which is developed to calculate the production rates and activities of radioisotopes induced by charged-particle nuclear reactions, as detailed in Appendix D.

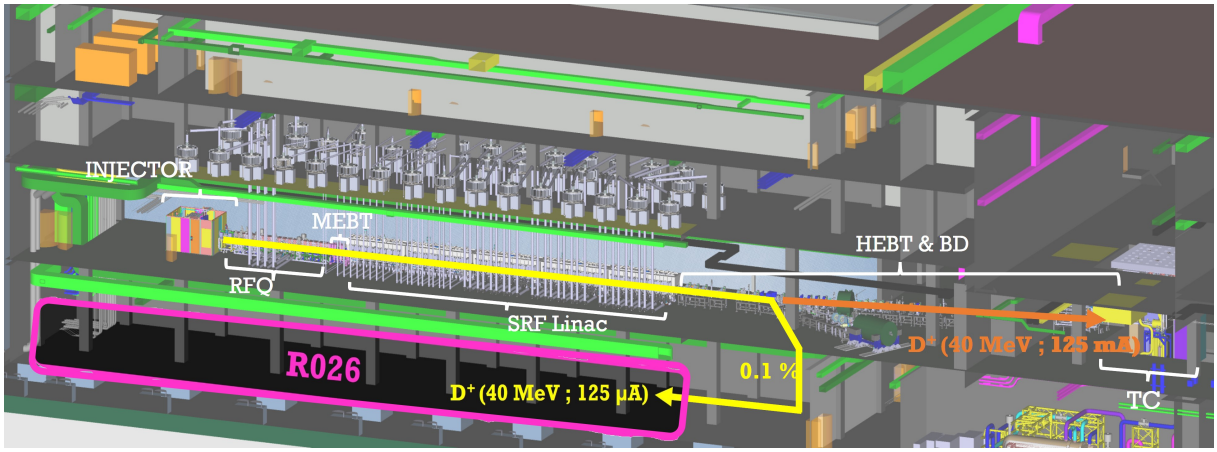

Figure III.1: Deflection of 0.1 % of the initial deuteron beam to the experimental room R026, enabled for complementary applications with deuterons at IFMIF-DONES.

1.1 Realistic design of a radioisotope production device

When using charged-particle beams for the production of radionuclides, special considerations have to be taken into account, such as the loss of energy of these particles in matter and the consequent generation of heat. Considering that the samples will be irradiated with deuterons up to 40 MeV energy at 125 μA intensity, the power dissipated in the sample is an issue. Therefore, it is necessary to design a cooled backing device for the samples. The design is based on a previous copper device that hosted a lithium target for the purpose of neutron production designed by P. Mastinu *et al.* [84]. The device was perforated by vertical channels and horizontal millichannels to circulate a fluid, as a cooling system. Figure III.2 shows some images of the original device. Experimental tests performed with proton beams dissipated 3 kW/cm^2 by keeping the device below 180 ^{o}C [85].

As already published in previous works related to radioisotope production at IFMIF-DONES [8,9], the modification of the device consists of a double cooling system embedding the target in a "sandwich" configuration. This configuration has the advantage that the total irradiated material remains always encapsulated, thus avoiding problems of toxicity or loss of material.

Figure III.3 shows the drawings of the designed device, a 7 mm thick backing with 45 mm width and height. It is perforated with 31 millichannels of 1 mm diameter each, with 1.5 mm of separation between them. The target is located between the double cooling system, with 0.5 mm distance between the target and the millichannels. The dimensions of the target holder are 20 mm diameter and 450 μm thickness. The backing material is copper and the cooling fluid is water which flows through the millichannels introduced by means of an external chiller at 3.5 l/min and 273 K.

A realistic design of the device was carried out using the graphic Computer-Aided Design (CAD) 3D and structural analysis programme SolidWorks [86]. The adaptation of the real model to the SolidWorks simulation is done by assembling different parts, previously designed individually. To couple the device to the outlet accelerator beamline,

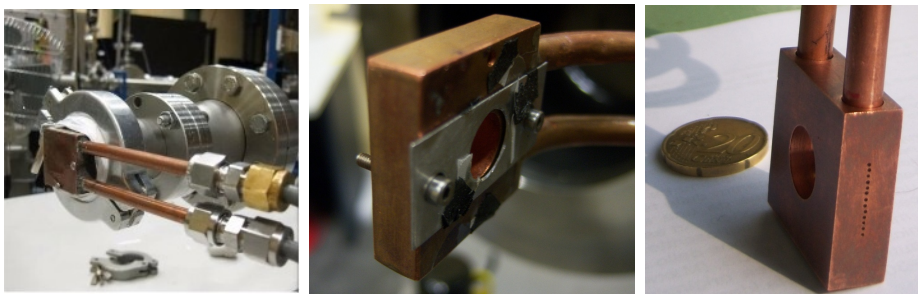

Figure III.2: Original copper device designed for the production of neutrons when a proton beam is incident on a lithium target. The device is cooled by a water system. Image courtesy of J. Praena.

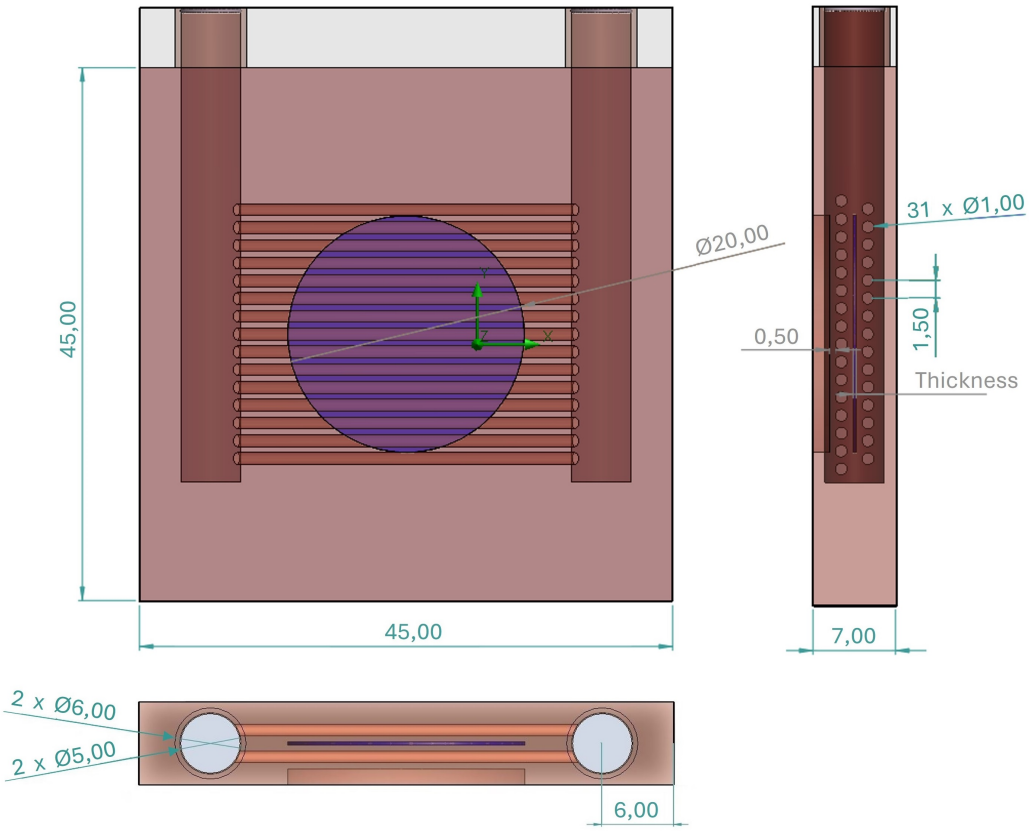

Figure III.3: Sketch of the copper backing with double water cooling system and sample holder.

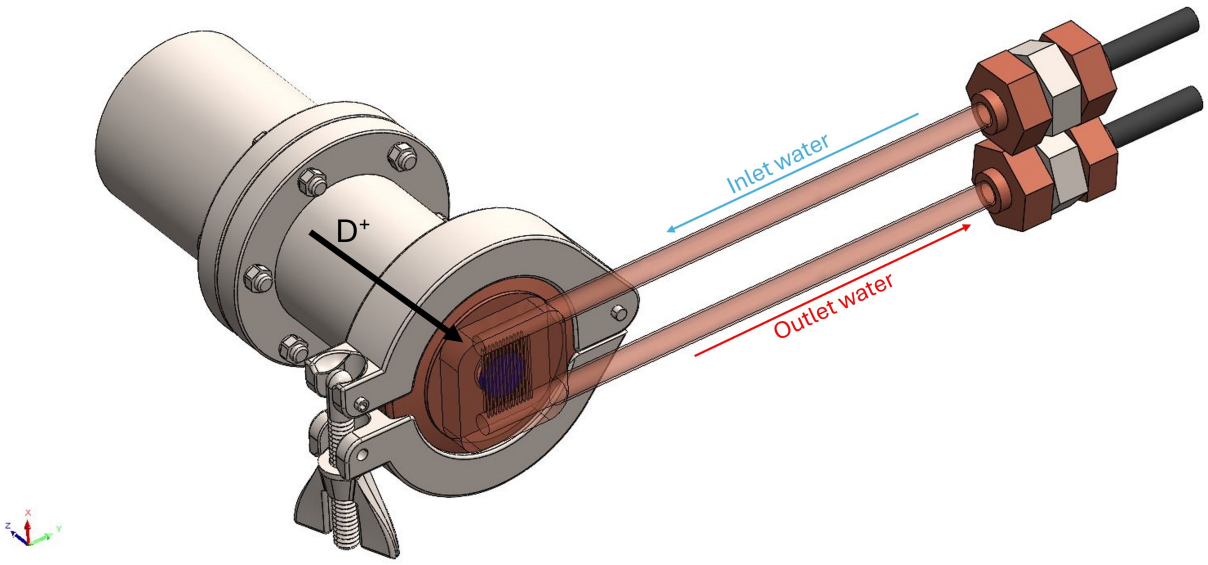

Figure III.4: CAD 3D SolidWorks design of the cooled radioisotope production device coupled to the deuteron beam output.

standardised mechanical parts are used as reference, such as O-rings, clamps, flanges or nipples of dimension KF40, available on Ideal Vacuum Products website [87]. The final result of the design and assembly process with SolidWorks is shown in Figure III.4.

SolidWorks software [88] has a computational fluid dynamics tool that allows heat transfer studies and flow simulations in complex systems, as well as estimating temperature, stress and strain distributions in the different assembly parts. Steady-state flow, thermal and structural simulations can be performed with the help of this tool. Assessing the dissipation of heat supplied to the device during the irradiation process to avoid structural damage to the sample or support.

The power dissipated by the copper backing as a function of the energy of the deuterons that pass through it to reach the sample can be estimated using the SRIM 2003 code [50]. For this purpose, the millichannel geometry of the device is simulated using a copper and water layer approximation through which 40 MeV deuterons are transported through, and their output energy is analysed, as shown in Figure III.5. The result of this simulation shows that the energy of the deuterons coming out of the backing that reach the target sample have an average energy of 18 MeV. Simulations assume that the initial beam is parallel and homogeneous, therefore, 33 % of the deuterons will lose all their initial energy when travelling through copper layers. Whereas, 67 % of the initial parallel beam crossing the copper and water layer configuration of the millichannels is not completely stopped, emerging towards the target with 18 MeV of average energy.

The power dissipated by the sample will depend on the deuteron energy deposited on it, therefore, it will depend on the thickness of the sample. The optimization of the target

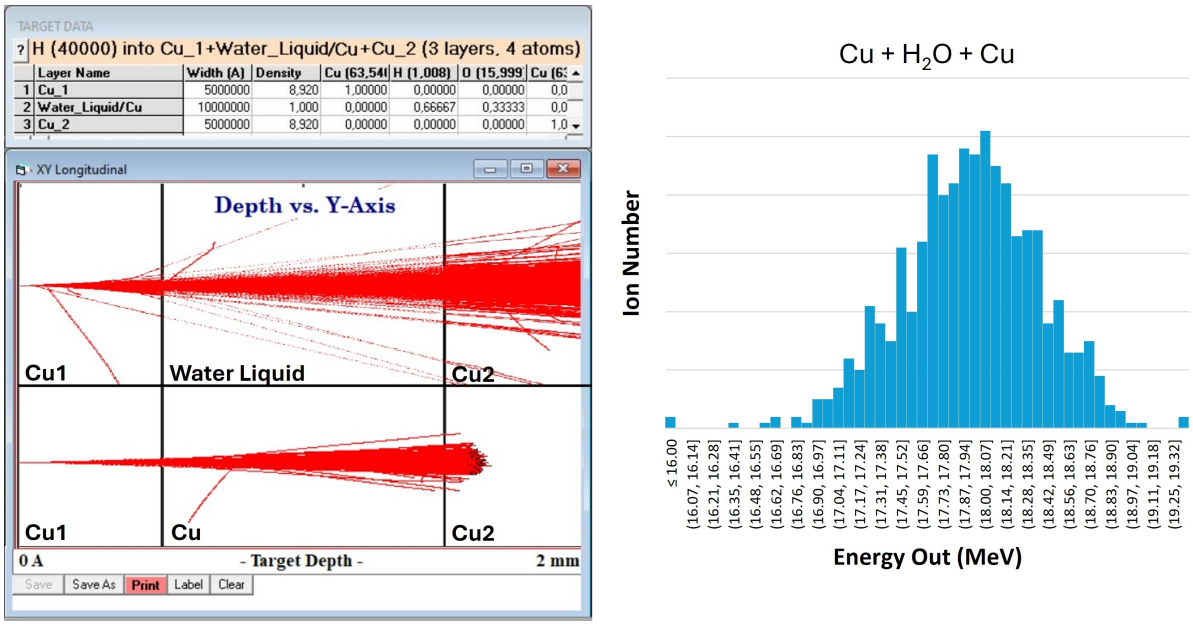

Figure III.5: SRIM 2003 simulation of the possible tracks followed by the 40 MeV energy beam deuterons (homogeneous and parallel) inside the copper backing cooled with water millichannels.

thickness will be given by the optimization of the production rate of the radionuclide of interest. Therefore, production studies are key in the process of estimating and planning the feasibility of the device designed.

1.2 ^{165}Er production study

The objective of this chapter is to study the viability of production of certain radioisotopes at IFMIF-DONES facility. Specifically, this subsection works on the estimation of ^{165}Er production from natural holmium targets with abundance in nature is 100 % ^{165}Ho.

As discussed in detail in Chapter II Section 2, the radionuclide of interest ^{165}Er produced through deuteron-induced nuclear reactions on ^{nat}Ho targets is only produced via the direct route (d,2n). Therefore, the number of ^{165}Er atoms after the irradiation process, obtained from the differential Equation (A.6), taking into account the production rate for thick targets from Equation (II.5), is

$$N_{^{165}Er}(t) = \chi \cdot \frac{I}{q} \cdot \frac{(1 - e^{-\lambda_{^{165}Er} \cdot t_{irr}})}{\lambda_{^{165}Er}} \cdot e^{-\lambda_{^{165}Er} \cdot t} \int_{E_{out}}^{E_{in}} \frac{\sigma_{(d,2n)}(E)}{S_d^{Ho}(E)} \, dE \tag{III.1}$$

where χ is the percentage purity of the material available on the market, metal holmium disk 99.0 % [59], I is the intensity current [A], in this case corresponding to 0.1 % of the deflected deuteron beam, q is the deuteron charge [C], $\lambda_{^{165}Er}$ is the decay constant [s^{-1}], t_{irr} is the irradiation time [s], t is the cooling time after EOB [s], $\sigma(E)$ is the excitation function of the ^{165}Ho(d,2n)^{165}Er nuclear reaction [cm^2] and $S_d^{Ho}(E)$ the stopping power of the deuterons inside the natural holmium target [eV/10^{15}atm·cm^2]. This value is available by SRIM 2003 code [50] and is shown together with the excitation function of the nuclear reaction ^{165}Ho(d,2n)^{165}Er in Figure III.6. The fit parameters for both functions are given in Appendix D. The integration limits are set according to the energy loss of the incoming deuterons in the target, estimated with the SRIM code and as a function of the sample thickness. It is important to remember that the incoming deuterons in the sample have an average energy of 18 MeV and account for 67 % of the initial particle flux.

1.2.1 Specific activity estimation using integrative method

The specific activity of ^{165}Er can be calculated from the activity and mass produced,

$$SA_{^{165}Er}(t) = \frac{A_{^{165}Er}(t)}{m_{Er}(t)} = \frac{\lambda_{^{165}Er} \cdot N_{^{165}Er}(t)}{m_{Er}(t)} \tag{III.2}$$

where m_{Er} is the total mass of erbium produced directly during the irradiation process and indirectly from decay processes as a function of time.

According to the displacement caused by deuteron-induced nuclear reactions on ^{nat}Ho shown in Figure II.8, the isotopes ^{166}Er and ^{167}Er were produced by the nuclear reactions

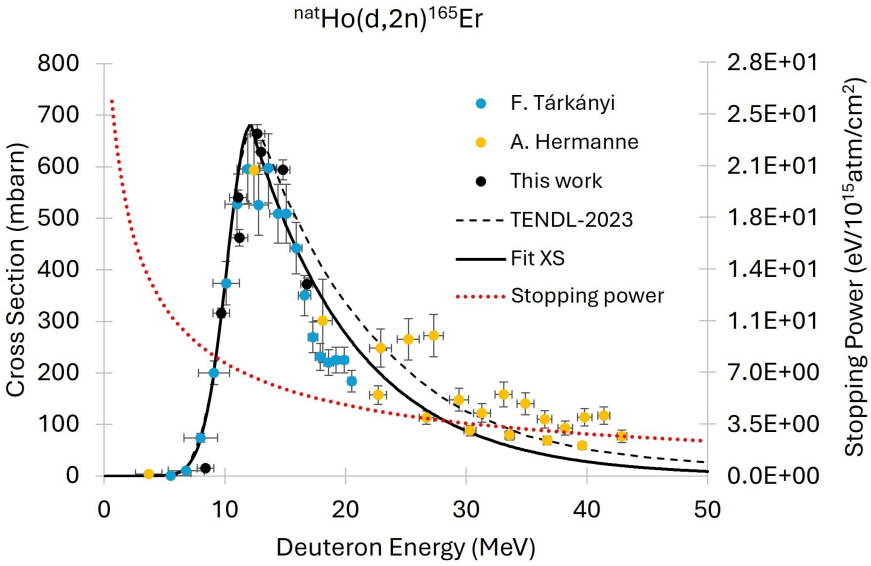

Figure III.6: Double-entry plot. Left: Experimental cross-section measurements by different authors, TENDL-2023 estimation and excitation function fitted to the experimental values. Right: Stopping power as a function of deuteron energy on a ^{165}Ho target obtained by SRIM 2003 code [50].

^{165}Ho(d,n) and ^{165}Ho(d,γ), respectively. Since these are stable isotopes, it was not possible to detect and measure their cross-sections using the stacked-foil activation method described in Chapter II. This would have required some other technique, such as mass spectrometry, which could not be carried out in this work.

Therefore, considering that the estimated TENDL-2023 cross-section for the case of the ^{165}Er radioisotope did not differ significantly from the experimental measurements, thus the TENDL-2023 database [63] was employed for the calculation of the production of the stable isotopes ^{166}Er and ^{167}Er. The TENDL-2023 tabular residual cross-sections are shown in Figure III.7.

On the other hand, two radioisotopes are also produced as a consequence of the reaction ^{nat}Ho(d,p), which are the short half-life radioisotope ^{166g}Ho ($T_{1/2}$ = 26.824 h) that decays β^- 100 % to the stable isotope ^{166}Er, increasing its number of atoms, as well as, the long half-life radioisotope ^{166m}Ho ($T_{1/2}$ = 1200 y), which also decays β^- 100 % to the stable isotope ^{166}Er, although its contribution is smaller due to the lower measured yield. The estimation of their contributions to the final number of ^{166}Er atoms will depend on the production of ^{166g}Ho and ^{166m}Ho at the EOB and the subsequent cooling time until chemical separation of the erbium from the holmium sample. The excitation functions for the reactions ^{nat}Ho(d,p)^{166g,166m}Ho have been obtained by fitting the experimental values of the cross-sections available so far, as shown in Figure III.8. The fit parameters for all the above functions are given in Appendix D.

The total mass of erbium produced after the irradiation process was calculated as the

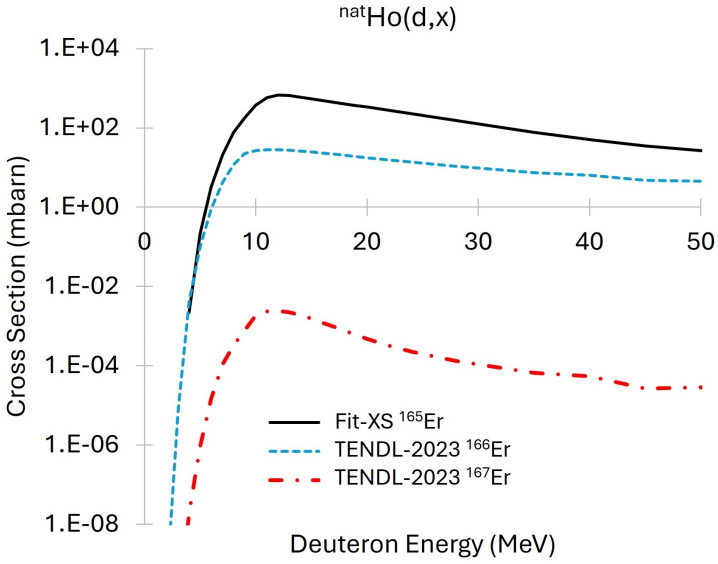

Figure III.7: TENDL-2023 tabular residual cross-sections [63] of the deuteron-induced nuclear reaction ^{165}Ho(d,n)^{166}Er and ^{165}Ho(d,γ)^{167}Er together with the excitation function fit of the experimental ^{165}Ho(d,2n)^{165}Er cross-section values.

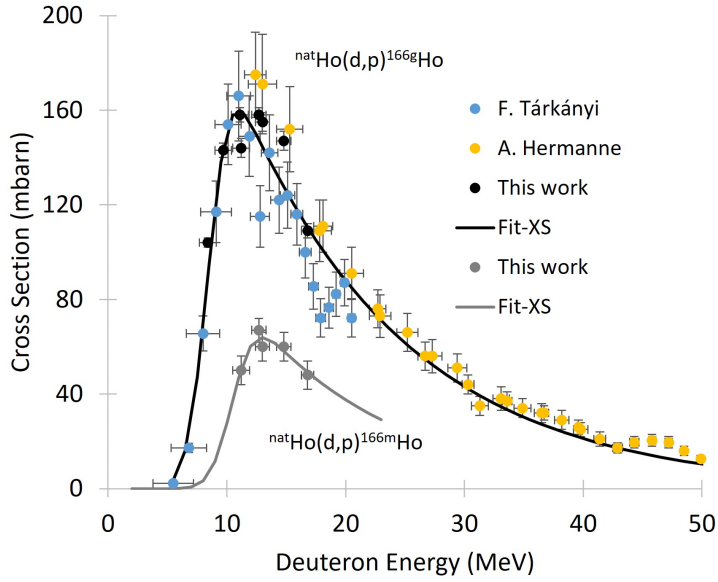

Figure III.8: Cross-section experimental measurements and excitation function fits of the deuteron-induced nuclear reaction ^{165}Ho(d,p)^{166g,166m}Ho.

sum of the atoms produced from radioisotopes ^{165}Er, ^{166cum}Er and ^{167}Er, as a function of time, taking into account that for stable isotopes the number of atoms is that produced at EOB, while for the radioisotopes the number of atoms follows the exponential decay.

$$m_{Er}(t) = \frac{M_{at_{Er}}}{N_A}\left(N_{^{165}Er}(t) + N_{^{166cum}Er}(t) + N_{^{167}Er}(EOB)\right) \quad \text{(III.3)}$$

To optimize the production of the radioisotope of interest by maximizing its specific activity (SA) and isotopic level (IP), different sample thicknesses have been used for production estimation. Knowing the thickness, the energy range of the particles inside the sample has been simulated with SRIM 2003 code. The estimated number of atoms produced for the different impurities, as well as the number of atoms, activity, SA and IP of ^{165}Er are shown in Table III.1 and Table III.2. Calculations have been performed for an irradiation time of 30 h corresponding to 3 half-lives of the radioisotope of interest, which would represent 87.5 % of produced fraction of the ^{165}Er radionuclide.

The Equation (III.1) has been solved using the numerical integration method described by Simpson's composite rule, which is developed in the Appendix D. The excitation functions fit used, as well as the stopping power function of the deuterons in metallic holmium targets, are also detailed in Appendix D. The systematic uncertainties in the calculation were estimated following the standard way, i.e. independent relative errors of linear contributions summed quadratically, considering the errors associated to the step of the integrative method, the uncertainty of the experimental cross-section data and the uncertainty parameters that were used in the excitation function fits.

Thickness (μm)	Energy (MeV)	Produced Nuclei (atm) ^{166}Er	^{167}Er	^{166g}Ho
200	18.0 - 14.0	$8.07{\cdot}10^{14}$ (3.12)	$4.53{\cdot}10^{10}$ (7.59)	$2.93{\cdot}10^{15}$ (3.24)
250	18.0 - 12.9	$1.04{\cdot}10^{15}$ (3.12)	$6.21{\cdot}10^{10}$ (7.59)	$3.79{\cdot}10^{15}$ (3.24)
300	18.0 - 11.7	$1.29{\cdot}10^{15}$ (3.12)	$6.07{\cdot}10^{10}$ (7.59)	$4.57{\cdot}10^{15}$ (3.24)
350	18.0 - 10.5	$2.54{\cdot}10^{15}$ (11.52)	$1.04{\cdot}10^{11}$ (10.80)	$5.74{\cdot}10^{15}$ (12.93)
400	18.0 - 9.1	$1.77{\cdot}10^{15}$ (11.55)	$1.17{\cdot}10^{11}$ (10.80)	$6.60{\cdot}10^{15}$ (12.93)
450	18.0 - 7.6	$1.91{\cdot}10^{15}$ (11.52)	$1.22{\cdot}10^{11}$ (10.80)	$7.17{\cdot}10^{15}$ (12.93)

Table III.1: Estimated number of atoms produced at EOB of the sample impurities for different target thicknesses. In brackets, systematic uncertainties in percentage.

Thickness (μm)	Energy (MeV)	Nuclei ^{165}Er (atom)	Activity ^{165}Er (GBq)	SA (GBq/mg)	IP (%)
200	18.0 - 14.0	$6.78{\cdot}10^{15}$ (1.56)	$1.27{\cdot}10^{2}$ (1.56)	$6.03{\cdot}10^{4}$ (8.50)	89.4 (8.50)
250	18.0 - 12.9	$9.01{\cdot}10^{15}$ (1.56)	$1.67{\cdot}10^{2}$ (1.56)	$6.05{\cdot}10^{4}$ (8.50)	89.7 (8.50)
300	18.0 - 11.7	$2.15{\cdot}10^{16}$ (1.75)	$2.15{\cdot}10^{2}$ (1.75)	$\mathbf{6.07{\cdot}10^{4}}$ (8.50)	**90.0** (8.50)
350	18.0 - 10.5	$1.37{\cdot}10^{16}$ (1.75)	$2.55{\cdot}10^{2}$ (1.75)	$6.06{\cdot}10^{4}$ (16.0)	89.9 (16.0)
400	18.0 - 9.1	$1.45{\cdot}10^{16}$ (1.75)	$2.69{\cdot}10^{2}$ (1.75)	$6.01{\cdot}10^{4}$ (16.0)	89.1 (16.0)
450	18.0 - 7.6	$1.55{\cdot}10^{16}$ (1.75)	$2.88{\cdot}10^{2}$ (1.75)	$6.00{\cdot}10^{4}$ (16.0)	89.0 (16.0)

Table III.2: EOB activity, specific activity and isotopic purity of ^{165}Er for different target thicknesses. In brackets, systematic uncertainties in percentage .

Systematic uncertainties range between $1.56 - 1.75$ % for ^{165}Er, $3.12 - 11.52$ % for ^{166}Er, $7.59 - 10.80$ % for ^{167}Er and $3.24 - 12.93$% for ^{166g}Ho atoms.

The different simulated target thicknesses are compatible with the gap dimensions of the irradiation device. An optimal thickness is around 300 μm, although all the values obtained, both for specific activity and isotopic impurity, are very promising, even without long exposure times.

Finally, the specific activity, radionuclide purity and isotopic purity quantities are influenced by the time after EOB. The number of ^{166}Er atoms will increase, due to the decay of the ^{166g}Ho and ^{166m}Ho impurities. This contribution and corresponding growth curve have been calculated following the Bateman Equation (A.24). On the other hand, there will be a significant decay of the radioisotope of interest itself, ^{165}Er, decreasing both its specific activity and its isotopic purity. Both of the above facts are observed in Figure III.9. Therefore, it is advisable to perform chemical separation and radiopharmaceutical dose administration before 10 hours after EOB [28], ensuring that more than 71.5 ± 7.6 % of the erbium nuclei correspond to ^{165}Er with high specific activity. The indirect production of ^{166}Er atoms from the decay of ^{166g,m}Ho stops after chemical separation. After chemical separation, the decrease of the ^{165}Er isotopic impurity will only be influenced by the natural decay of the radioisotope of interest.

Regarding the radionuclidic purity (RNP) of the sample, it is guaranteed to be higher than 99 %, as after isotopic separation ^{165}Er is the only radioactive erbium isotope in the final product.

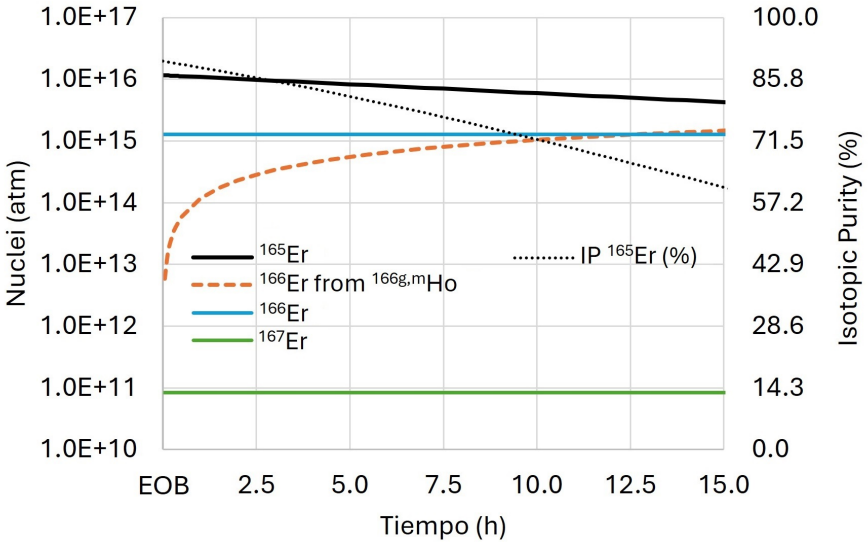

Figure III.9: Double-entry plot. Left: Number of atoms as a function of time after EOB. Right: Isotopic Purity of ^{165}Er as a function of time. Systematic uncertainties in the calculation for the energy range corresponding to 300 μm thickness were evaluated to be 1.75 % for ^{165}Er atoms, 3.12 % for ^{166}Er atoms, 7.59 % for ^{167}Er atoms, 3.24 % for ^{166g}Ho atoms and 5.29 % for ^{166m}Ho atoms, while 10.6 % for ^{165}Er isotopic impurity.

1.2.2 Comparison with other production routes

In this study, the alternative ^{165}Er production route by deuteron-induced nuclear reactions has been studied according to the particle flux available in IFMIF-DONES. Its estimated thick target yield is higher than that described by the conventional method of production by proton-induced reactions. As seen in Chapter II Section 2, there are other conventional indirect production routes of ^{165}Er via generators, which require to use expensive enriched targets and target recovery processes.

Table III.3 shows the results of activity produced with deuteron-induced reactions compared to conventional cyclotron-based ^{165}Er production routes [89, 91]. For direct route, ^{nat}Ho(p,n)^{165}Er reaction in conventional cyclotrons is studied by F. Tárkányi *et al.* [89] and N. Gracheva *et al.* [90]. In case of indirect routes, ^{nat}Er(p,xn)^{165}Tm→^{165}Er, is the reaction with the highest production yield of ^{165}Er [91].

The production of ^{165}Er at low current, 1 μA, and short irradiation times is very promising in IFMIF-DONES compared to conventional direct routes based on proton production in cyclotrons, thanks to the high specific molar activity[1] produced. The calculated specific molar activities are of the same order as conventional indirect production routes. However, the energy range needed for this, in the case of deuterons, is much smaller. Low energy ranges eliminate the opening of many energetically possible channels, which generate impurities and unnecessary activation on the target, maximising the isotopic purity.

Regarding the molar or specific activity required for radionuclide therapy with peptides, such as ^{165}Er-DOTA-compound there is no consensus, and an optimal value has to be de-

Route	ΔE (MeV)	I (μA)	t_i (h)	t_c (h)	Activity (MBq)	SA (TBq/mmol)
^{nat}Ho(p,n)^{165}Er	16 - 7 13.4 - 8.6	1 10	1 10	10	$3.91{\cdot}10^{1}$ $1.60{\cdot}10^{3}$	5 – 20
^{nat}Er(p,xn)^{165}Tm → ^{165}Er	30 - 14 70 - 14	1	30	1 - 24	$3.59{\cdot}10^{3}$ $1.24{\cdot}10^{4}$	$3.50{\cdot}10^{3}$ $4.22{\cdot}10^{3}$
^{nat}Ho(d,2n)^{165}Er (This work)	18 - 11.7	1 1 125	1 30 30	10	$6.60{\cdot}10^{1}$ $8.81{\cdot}10^{2}$ $1.10{\cdot}10^{5}$	$9.23{\cdot}10^{3}$ $8.04{\cdot}10^{3}$ $8.04{\cdot}10^{3}$

Table III.3: Comparison between the activity and specific molar activity obtained by different experimental ^{165}Er production routes. ΔE indicates the optimal energy range of charged-particles, I is its current, t_i is the irradiation time and t_c is the cooling decay time. Systematic uncertainties for the calculated ^{165}Er activity and specific molar activity are 1.75 % and 10.6 %, respectively.

[1]Specific molar activity is the ratio between the amount of radioactivity and the sum of the quantity of the radioactive and stable atoms. The unit is typically MBq/nmol. (1 MBq/nmol = 1 GBq/μmol = 1 TBq/mmol = 1 Ci/μmol)

fined experimentally, which could be, for example, a compromise between sufficient radioactivity per drug molecule without saturating the tumour receptors with inactive material [92]. Some publications show values of molar activities around $37 - 130$ GBq/μmol [28, 92, 93]. Similarly, typical administered masses are often in the 2.5–25 nmol range, where the activity injected in a single session with ^{169}Er citrate does not exceed 750 MBq (20 mCi) [93]. Although, other studies of peptide receptor radionuclide therapy such as ^{177}Lu-DOTA-TATE is well tolerated up to 29 GBq of cumulative activity (7.4 GBq (200 mCi)/cycle over 4 cycles) [32]. In this case, higher molar activities are required.

The mentioned values would be successfully achieved according to the molar activity quantities estimated in this study of ^{165}Er alternative production route based on deuteron-induced nuclear reactions. Therefore, it can be concluded that the activities achieved in IFMIF-DONES would allow clinical procedures with ^{165}Er.

1.2.3 Thermal and structural simulations with SolidWorks

The ^{165}Er production results are very promising, even at relative short exposure times and with an average sample thickness of 300 μm . However, complementary studies have been simulated with SolidWorks for the production of ^{165}Er at the 125 μA current limit to assess the resistance of the device housing the sample to dissipate the high heat power generated inside it.

In order to carry out the thermal and flow study in SolidWorks, it is necessary to include the boundary conditions of power dissipated by the backing and sample in the simulation, as well as the characterisation parameters of the heat transfer fluid. For simplification and calculation time saving, the simulations only include the critical parts of the assembly, being the copper backing and the holmium sample inserted inside it. The simulation model together with the boundary conditions set on the corresponding part faces are shown in Figure III.10. While Table III.4 shows the values for the boundary conditions. The particle energy losses for the calculation of the power dissipated by the device in the backing and sample were calculated with the SRIM 2003 code.

Flow simulations shows the temperature reached by the sample and backing in steady-state remains below the melting point of metallic holmium (1747 K) and copper (1358 K). Figure III.11 shows the solid and fluid temperature distribution in a side view and frontal plot of the device. Water cooling system helps to dissipate the heat generated.

On the other hand, based on the results of the pressure distribution obtained in the flow simulation through the millichannels, the study has been complemented with a structural analysis of thermo-mechanical stresses, shown in Figure III.12. As can be seen, the Von Mises parameter that evaluates the mechanical stresses of the system, fluid stresses and pressures, is within the limits of the maximum value of the tensile strength of copper (210 MPa). Structural simulations with SolidWorks give us a preliminary idea under non-ideal conditions that try to reproduce as closely as possible the system environment, however, in terms of power dissipation it strongly depends on the boundary conditions

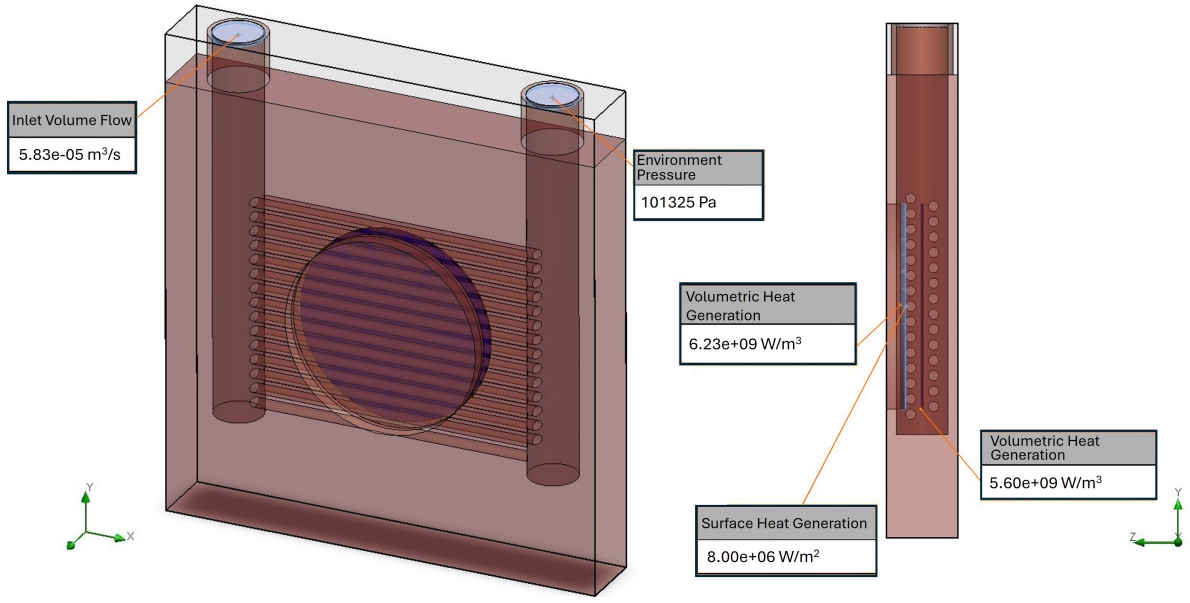

Figure III.10: SolidWorks simulation model together with the boundary conditions set on the corresponding faces.

Cooling System	
Inlet Volume Flow	3.5 l/min = $5.83{\cdot}10^{-5}$ m^3/s
Environment Pressure	1 atm = 101325 Pa
Fluid Temperature	273 K
Power Dissipation ($P = \Delta E \cdot I$)	
Volumetric Heat Generation Rate (100 % Cu_1)	$6.23{\cdot}10^9$ W/m^3
Surface Heat Generation Rate (67 % Water Liquid + Cu_2 / 33 % Cu + Cu_2)	$8.00{\cdot}10^6$ W/m^2
Volumetric Heat Generation Rate (67 % Sample)	$5.60{\cdot}10^9$ W/m^3
Wall Thermal Condition	
Outer Wall condition	Adiabatic wall
Inter Wall roughness	0.015 μm
Thermal Contact Resistance Interface Cu/Cu	0 $K{\cdot}m^2/W$
Thermal Contact Resistance Interface Cu/Ho/Cu	$4{\cdot}10^{-7}$ $K{\cdot}m^2/W$ [94]

Table III.4: Values of boundary condition parameters for thermal and fluid simulations. Dissipated power is calculated from the particle energy deposition.

related to the heat transfer inside the device and the contact resistances between the interfaces of different materials. Therefore, the previous proofs of concept already tested by P. Mastinu *et al.* [85] for a device less cooled than this one and capable of dissipating 3 kW/cm^2 not be disregarded. It is noted that the value of power dissipated by our system is lower, so the operation of the presented device can be considered workable.

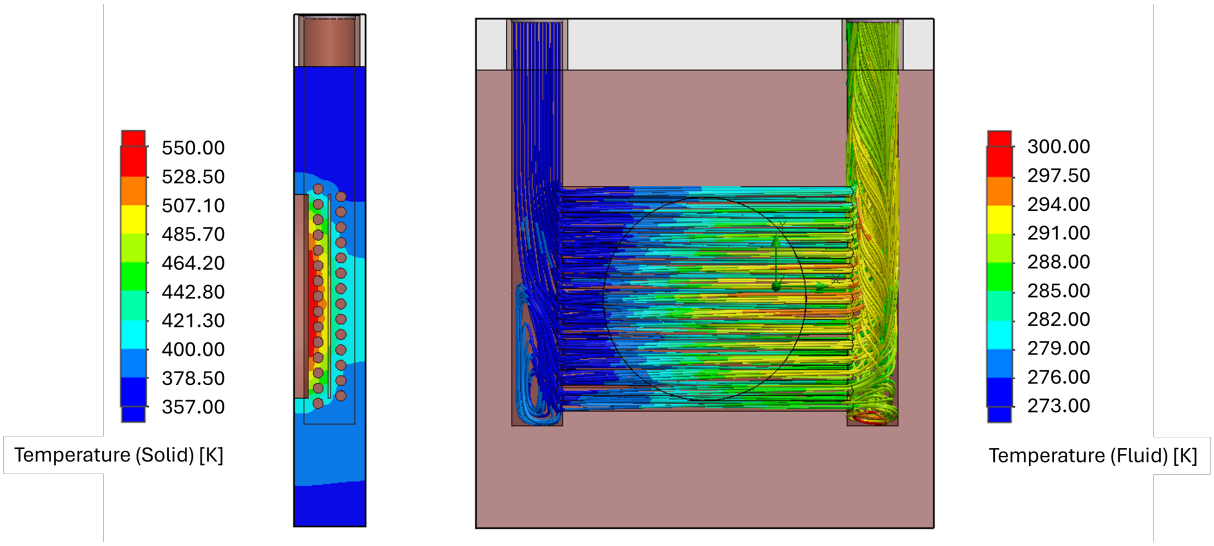

Figure III.11: Left: Device side view of temperature distribution in sample and backing. Right: Fluid temperature distribution on device front face.

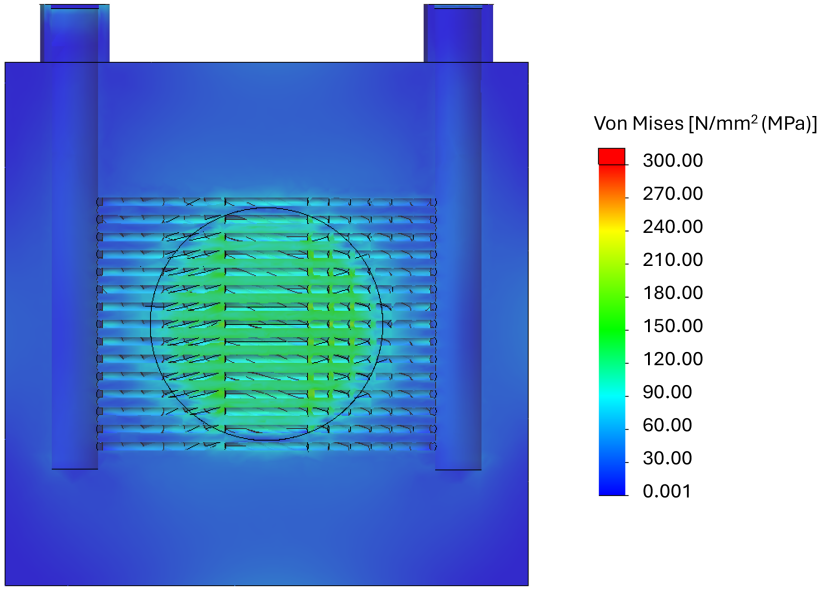

Figure III.12: Static analysis of Von Mises stresses. Cutaway plot of the from view of the device at the position of maximum detected stress.

1.3 ^{177}Lu production study

In this subsection, the estimation of ^{177}Lu produced from 99.588 % enriched ^{176}Yb targets in the form of oxide $^{176}Yb_2O_3$ marketed by Isoflex USA [95] is studied. The isotopic distribution of this enriched target is listed in Table III.5.

Isotope	^{168}Yb	^{170}Yb	^{171}Yb	^{172}Yb	^{173}Yb	^{174}Yb	^{176}Yb
Content (%)	0.0001	0.0035	0.0216	0.0487	0.0594	0.2782	99.588

Table III.5: Isotopic composition of the enriched oxide $^{176}Yb_2O_3$ target.

The radionuclide of interest ^{177}Lu produced through deuteron-induced reactions on enriched ^{176}Yb targets can be produced via the direct route ^{176}Yb(d,n) and indirect route ^{176}Yb(d,p) by the ^{177}Yb decay, as discussed in detail in Chapter II Section 3. The ^{177cum}Lu cumulative excitation function measured takes into account the total decay of its parent nuclei. Therefore, the number of ^{177g}Lu atoms after the irradiation process, obtained from the differential Equation (A.6) and for thick targets, according to the production rate defined in Equation (II.5) is,

$$N_{^{177cum}Lu}(t) = \chi \cdot \frac{I}{q} \cdot \frac{(1 - e^{-\lambda_{^{177g}Lu} \cdot t_{irr}})}{\lambda_{^{177g}Lu}} \cdot e^{-\lambda_{^{177g}Lu} \cdot t} \int_{E_{out}}^{E_{in}} \frac{\sigma_{(d,x)}(E)}{S_d^{^{176}Yb_2O_3}(E)}\, dE \qquad \text{(III.4)}$$

where χ is the percentage purity of the material available on the market, powder of ^{176}Yb enriched 99.588 % [95] multiplied by mass proportions 2(Yb):3(O), equivalent to 40 %, I is the intensity current [A], in this case corresponding to 0.1 % of the deflected deuteron beam, q is the deuteron charge [C], $\lambda_{^{177g}Lu}$ is the decay constant [s^{-1}], t_{irr} is the irradiation time [s], t is the time after EOB [s], $\sigma(E)$ is the cumulative excitation function of the ^{176}Yb(d,x)^{177cum}Lu nuclear reaction [cm^2] and $S_d^{^{176}Yb_2O_3}(E)$ the stopping power of the deuterons inside the enriched oxide ytterbium target [eV/10^{15}atm·cm^2]. This value is available en SRIM 2003 code [50] and is shown together with the excitation function fitted to the cross-sections of the nuclear reaction ^{176}Yb(d,x)^{177cum}Lu in Figure III.13. The fit parameters used are detailed in Appendix D. The integration limits are set according to the energy loss of the incoming deuterons in the target, estimated with the SRIM 2003 and as a function of the sample thickness. The incoming deuterons in the sample have an average energy of 18 MeV and account for 67 % of the initial particle flux.

1.3.1 Specific activity estimation using integrative method

The specific activity of ^{177g}Lu can be calculated from the activity and mass produced,

$$SA_{^{177cum}Lu}(t) = \frac{A_{^{177cum}Lu}(t)}{m_{Lu}(t)} = \frac{\lambda_{^{177g}Lu} \cdot N_{^{177cum}Lu}(t)}{m_{Lu}(t)} \qquad \text{(III.5)}$$

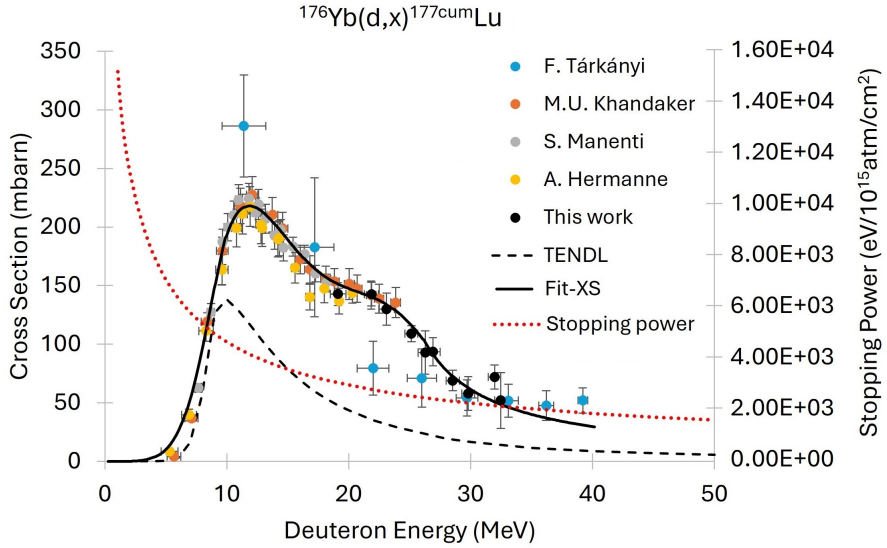

Figure III.13: Double-entry plot. Left: Experimental cross-section measurements by different authors, TENDL-2023 estimation and excitation function fitted to the experimental values. Right: Stopping power as a function of deuteron energy on a $^{176}Yb_2O_3$ target obtained from SRIM 2003 [50].

where m_{Lu} is the total mass of lutetium produced directly during the irradiation process and indirectly from decay processes as a function of time.

According to the displacement caused by deuteron-induced nuclear reactions on ^{176}Yb shown in Figure II.23, the isotopes ^{178}Lu, ^{177g,m}Lu, ^{176g,m}Lu and ^{175}Lu are simultaneously produced, in addition to ^{177}Yb, which decays β^- 100 % to ^{177g}Lu and ^{175}Yb, which decays β^- 100 % to ^{175}Lu. Although the sample is highly enriched, there is 0.2782 % of ^{174}Yb and 0.0594 % of ^{173}Yb, thus other Lu radioisotopes would also be produced. However, most of them are radioactive with short half-lives, which rapidly decay into other elements that can be chemically separated from lutetium, as in the case of hafnium.

Based on the information gathered from the IAEA database [11], lutetium radioisotopes that can compete in mass with the ^{177g}Lu produced have been listed. Table III.6 shows the possible lutetium radioisotopes produced by deuterons on ^{176}Yb, ^{174}Yb and ^{173}Yb, their production routes, decay mode, half-life and daughter nucleus. The main isotopic impurity influencing the calculation of the ^{177g}Lu mass activity is the stable radioisotope ^{175}Lu produced by direct route ^{176}Yb(d,2n) and by ^{175}Yb decay, as well as, the long half-life radioisotopes ^{176g}Lu, ^{174m}Lu, ^{174g}Lu and ^{173}Lu. Moreover, it is also important to quantify the contamination by the isomeric state, ^{177m}Lu. For the short half-life radioisotopes, it would be necessary to wait a cooling time of at least 2 days after EOB to ensure their decay, especially ^{177}Yb which decays to ^{177g}Lu and ^{176m}Lu to ^{176}Hf.

Figure III.14 shows the excitation function fits for the impurities to be taken into account in the ^{177}Lu production process, which are ^{176m}Lu, ^{174g,m}Lu, ^{173}Lu, ^{175}Yb. For these fits, all the contributing reactions have been taken into account. Only the excitation

Target	Reaction	Isotope	Decay Mode	$T_{1/2}$	Daughter
^{176}Yb (99.588 %)	(d,γ)	^{178}Lu	β^- 100 %	28.4 min	^{178}Hf
	(d,p)	^{177}Yb	β^- 100 %	1.911 h	^{177g}Lu
	(d,n)	^{177m}Lu	β^- 77.30 %	160.4 d	^{177}Hf
			IT 22.70 %		^{177g}Lu
	(d,n)	^{177g}Lu	β^- 100 %	6.6443 d	^{177}Hf
	(d,2n)	^{176m}Lu	β^- 100 %	3.664 h	^{176}Hf
	(d,2n)	^{176g}Lu	β^- 100 %	$3.76{\cdot}10^{10}$ y	^{176}Hf
	(d,n+d), (d,2n+p)	^{175}Yb	β^- 100 %	4.185 d	^{175}Lu
	(d,3n)	^{175}Lu	stable		
^{174}Yb (0.2782 %)	(d,γ)	^{176m}Lu	β^- 100 %	3.664 h	^{176}Hf
	(d,γ)	^{176g}Lu	β^- 100 %	$3.76{\cdot}10^{10}$ y	^{176}Hf
	(d,p)	^{175}Yb	β^- 100 %	4.185 d	^{175}Lu
	(d,n)	^{175}Lu	stable		
	(d,2n)	^{174m}Lu	IT 99.38 %	142 d	^{174}Lu
	(d,2n)	^{174g}Lu	EC, β^+ 100 %	3.31 y	^{174}Yb
	(d,3n)	^{173}Lu	EC 100 %	1.37 y	^{173}Yb
^{173}Yb (0.0594 %)	(d,n)	^{174m}Lu	IT 99.38 %	142 d	^{174}Lu
	(d,n)	^{174g}Lu	EC, β^+ 100 %	3.31 y	^{174}Yb
	(d,2n)	^{173}Lu	EC 100 %	1.37 y	^{173}Yb

Table III.6: Lutetium radioisotopes produced by deuterons on enriched $^{176}Yb_2O_3$ target, their production routes, decay mode, half-life and daughter nucleus.

functions for the production of the radioisotopes ^{175}Lu and ^{176g}Lu were not measured by the stacked-foils activation study of Chapter II, so their tabular residual cross-sections were taken from the TENDL-2023 database [63] and are shown in Figure III.15.

Therefore, the total mass of lutetium as a function of time includes the direct or indirect production of the following nuclides and their subsequent decay from the EOB to the chemical separation of the final product:

$$m_{Lu}(t) = \frac{M_{at_{Lu}}}{N_A}\left(N_{^{177cum}Lu}(t) + N_{^{176g}Lu}(t) + N_{^{175cum}Lu}(t) + N_{^{174g,m}Lu}(t) + N_{^{173}Lu}(t)\right) \tag{III.6}$$

To optimize the production of the radioisotope of interest by maximising its specific activity (SA) and isotopic purity (IP), different sample thicknesses, compatible with the gap dimensions of the irradiation device have been used for production estimation. Knowing the thickness, the energy range of the particles inside the sample has been simulated with SRIM 2003 code [50]. The values of activity, specific activity, number of atoms produced and isotopic purity from ^{177}Lu, as well as, from its isotopic impurities are shown in Table III.7 and Table III.8. Calculations have been performed after 7 days of irradiation and 2 days of cooling time. The irradiation time corresponds to one half-life of the ^{177}Lu radioisotope, which would represent 50 % of its produced fraction.

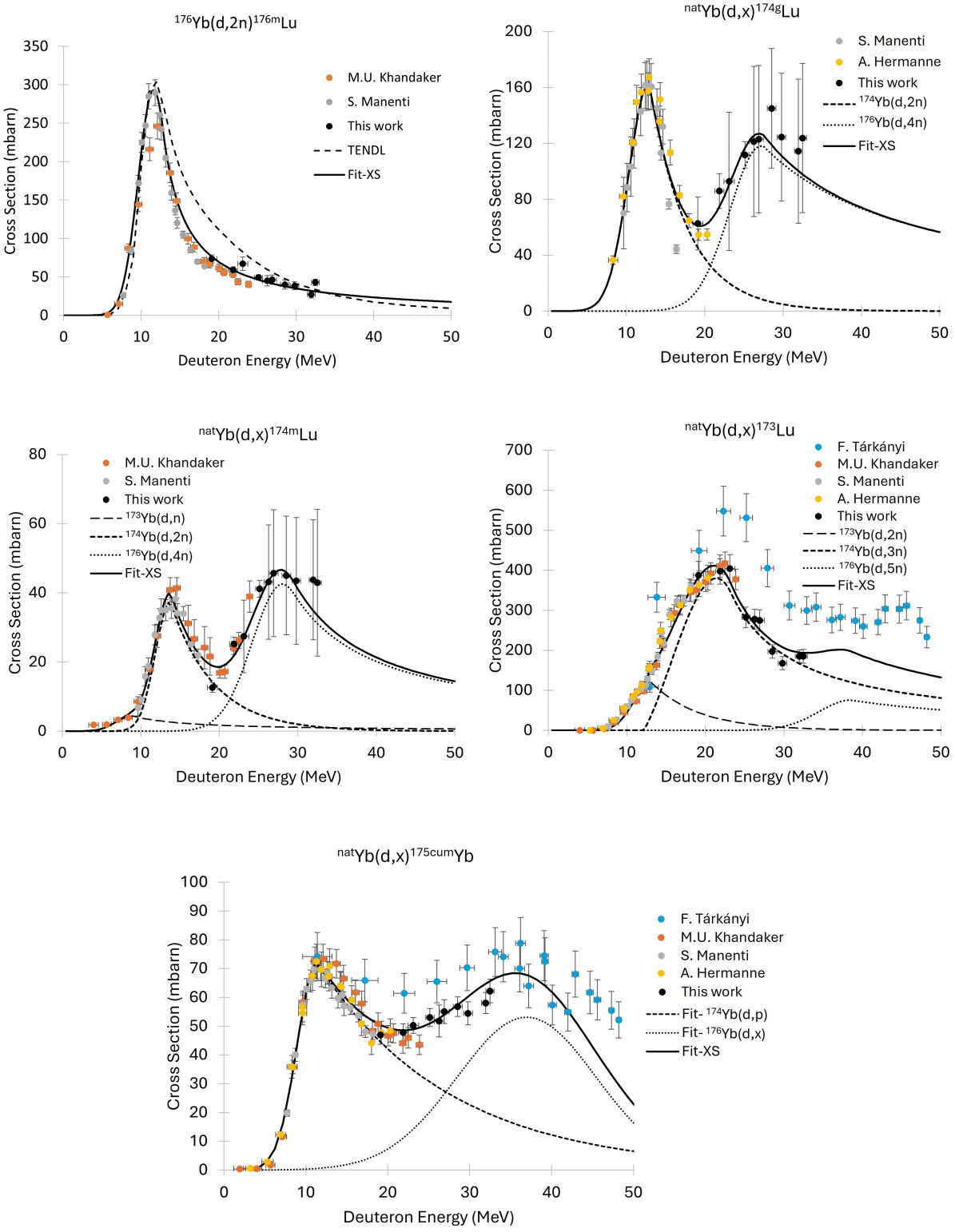

Figure III.14: Cross-section experimental measurements and excitation function fits of the deuteron-induced nuclear reactions ^{176}Yb(d,2n)^{176m}Lu and ^{nat}Yb(d,x) ^{174g,174m,173}Lu,^{175cum}Yb.

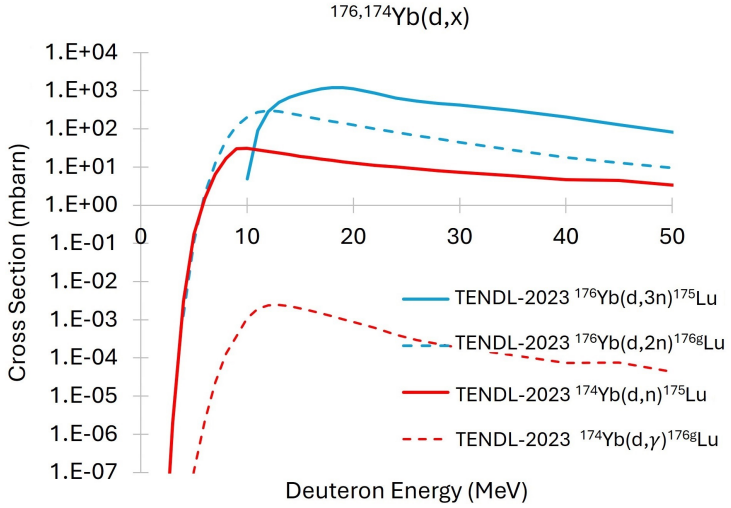

Figure III.15: TENDL-2023 tabular residual cross-sections of deuteron-induced nuclear reactions ^{176}Yb(d,x)^{175,176g}Lu and ^{174}Yb(d,x)^{175,176g}Lu [63].

The equation (III.4) has been solved using the numerical integration method described by Simpson's composite rule, which is developed in the Appendix D. In addition, the excitation functions fit used, as well as the stopping power function of the deuterons in enriched oxide ytterbium, are also listed in Appendix D. Systematic uncertainties in the calculation are evaluated considering errors associated with the step of the integrative method, uncertainty of the experimental cross-section data and uncertainty parameters that were used in the fits, listed in Appendix D. These are 5.2−12.2 % for ^{177}Lu, 2.4−6.3 % for ^{176g}Lu, 4.7 − 6.7 % for ^{175}Lu, 10.8 − 14.7 % for ^{174g}Lu, 9.7 − 15.2 % for ^{174m}Lu and 2.7 − 6.2 % for ^{173}Lu.

As discussed above, the main impurity in the production is from the nuclear reaction ^{176}Yb(d,2n)^{175}Lu, which considerably reduces the isotopic purity of the final product of

Thickness (μm)	Energy (MeV)	Nuclei ^{177}Lu (atm)	Isotopic Purity, ^{B}Lu/^{T}Lu (%)				
			^{177}Lu	^{176g}Lu	^{175}Lu	^{174g,m}Lu	^{173}Lu
200	18.0 - 13.4	$1.80{\cdot}10^{16}$ (5.2)	8.28 (24.8)	16.25	**75.41**	0.027	0.048
250	18.0 - 12.1	$2.34{\cdot}10^{16}$ (5.2)	9.28 (24.8)	18.79	71.87	0.032	0.045
300	18.0 - 10.7	$2.85{\cdot}10^{16}$ (5.2)	10.26 (25.0)	21.31	68.37	0.036	0.042
350	18.0 - 9.1	$3.36{\cdot}10^{16}$ (12.2)	11.33 (27.3)	22.96	65.64	0.037	0.040
400	18.0 - 7.3	$3.65{\cdot}10^{16}$ (12.2)	12.02 (27.3)	23.34	64.58	0.038	0.039
200	15.0 - 9.5	$2.09{\cdot}10^{16}$ (5.2)	15.65 (25.0)	33.35	50.92	0.057	0.020
250	15.0 - 7.9	$2.42{\cdot}10^{16}$ (12.2)	16.97 (27.3)	33.91	49.05	0.057	0.019
200	12.0 - 5.0	$1.39{\cdot}10^{16}$ (11.0)	**26.73** (28.2)	45.05	28.15	0.067	0.011

Table III.7: Estimated number of atoms and isotopic purity produced for the different lutetium isotopes, target thicknesses and energy ranges. In brackets, systematic uncertainty percentages.

Thickness (μm)	Energy (MeV)	Activity ^{177}Lu (GBq)	SA ^{177}Lu (GBq/mg)	Activity ratio, ^{B}Lu/^{177}Lu (%)		
				^{176g}Lu	^{174g,m}Lu	^{173}Lu
200	18.0 - 13.4	$2.17{\cdot}10^{1}$ (5.2)	$3.40{\cdot}10^{2}$ (24.8)	<0.0001	0.0047	0.0070
250	18.0 - 12.1	$2.82{\cdot}10^{1}$ (5.2)	$3.81{\cdot}10^{2}$ (24.8)	<0.0001	0.0048	0.0057
300	18.0 - 10.7	$3.44{\cdot}10^{1}$ (5.2)	$4.21{\cdot}10^{2}$ (25.0)	<0.0001	0.0046	0.0048
350	18.0 - 9.1	$4.06{\cdot}10^{1}$ (12.2)	$4.66{\cdot}10^{2}$ (27.3)	<0.0001	0.0042	0.041
400	18.0 - 7.3	$4.40{\cdot}10^{1}$ (12.2)	$4.94{\cdot}10^{2}$ (27.3)	<0.0001	0.0039	0.038
200	15.0 - 9.5	$2.52{\cdot}10^{1}$ (5.2)	$6.43{\cdot}10^{2}$ (25.0)	<0.0001	0.0043	0.017
250	15.0 - 7.9	$2.93{\cdot}10^{1}$ (12.2)	$6.97{\cdot}10^{2}$ (27.3)	<0.0001	0.0039	0.015
200	12.0 - 5.0	$1.68{\cdot}10^{1}$ (11.0)	$\mathbf{1.10{\cdot}10^{3}}$ (28.2)	<0.0001	0.0021	0.0006

Table III.8: Estimated activity and specific activity of ^{177}Lu and activity ratio for the different lutetium isotopes produced for different target thicknesses and energy ranges. In brackets, systematic uncertainties in percentage.

^{177g}Lu. To try to minimise this isotopic impurity contribution, it is necessary to reduce the irradiation energy to 12 MeV. For this purpose, a copper degrader of variable thickness between 100 - 200 μm is inserted in front of the $^{176}Yb_2O_3$ sample. This technique is close to the concept of stacked-foils, which for the production of ^{177g}Lu has already been proposed in other works for higher energies, as L. Shao *et al.* [96].

The optimal configuration is 200 μm copper degrader and 200 μm $^{176}Yb_2O_3$ sample, irradiated up to 12 MeV deuterons, obtaining a specific activity of 1100 $\pm$ 330 GBq/mg of ^{177}Lu produced, with a isotopic purity around 27 $\pm$ 8 %, after 7 days of irradiation and 2 days of cooling where the radioisotopes ^{177}Yb and ^{176m}Lu have totally decayed and ^{175}Yb partially decayed. This time is also necessary to perform the chemical separation of the lutetium from the irradiated sample.

1.3.2 Radionuclidic purity control

The radionuclide purity is defined as the ratio, in percentage, between the activity of the radionuclide of interest and the total activity of all the radionuclides produced. The radionuclide purity of the product ^{177}Lu for radiolabelling is regulated by European Directorate for the Quality of Medicines & HealthCare [97].

According to the European Pharmacopoeai [98], the main impurities to be considered are ^{177m}Lu and ^{175}Yb being the set levels:

- **Lutetium-177**: minimun 99.9 per cent of the total radioactivity.
- The total radioactivity due to **ytterbium-175** lower than 0.1 per cent.
- The total radioactivity due to **lutetium-177m** lower than 0.07 per cent.
- The total radioactivity due to **other radionuclidic impurities** lower than 0.01 per cent.

Thickness (μm)	Energy (MeV)	Radionuclidic purity, ^{B}Lu/^{T}Lu (%)		
		^{177g}Lu	$^{176g+174g,m+173}$Lu	^{177m}Lu
200	18.0 - 13.4	99.9882	0.0118	0.0005
250	18.0 - 12.1	99.9893	0.0106	
300	18.0 - 10.7	99.9905	0.0095	
350	18.0 - 9.1	99.9916	0.0084	
400	18.0 - 7.3	99.9922	0.0078	
200	15.0 - 9.5	99.9939	0.0061	0.0005
250	15.0 - 7.9	99.9946	0.0055	
200	12.0 - 5.0	99.9972	0.0028	0.0005

Table III.9: Radionuclidic purity of the Lu radioisotopes generated in the sample after 7 days of irradiation and 2 days of cooling.

Most of the cases studied fulfill the radionuclide purity requirements, as shown in Table III.9. The radioactivity of ^{175}Yb after 2 days EOB is about 0.1 %, however it would be relevant to evaluate the purity after the Yb-Lu separation process and check that it is less than 0.1 per cent. The impurity limit of ^{177m}Lu is taken from the study shown in Chapter II Section 3.4.15, and is less than 0.0005 % up to 20 MeV, the energy range studied.

1.3.3 Comparison with other production routes

In this study, the alternative route of ^{177}Lu production by deuteron-induced reactions has been studied. ^{177g}Lu is currently produced in reactors either by the direct ^{176}Lu(n,γ) $^{177(g+m)}$Lu reaction or by the indirect ^{176}Yb(n,γ)^{177}Yb $\rightarrow$ ^{177g}Lu reaction [99, 100].

The direct route carrier-added (c.a) has a high thermal neutron capture cross-section of ^{176}Lu, reaching up to 2090 barn [99]. However, a drawback of the direct route is the production of ^{177m}Lu as an impurity of concern, around 0.010$-$0.015 % [81] and 0.02 % [82] radionuclide purity reported for common ^{177}Lu production at nuclear reactors. Currently, the average specific activity of the direct route in nuclear reactor is approximately 740 - 1100 GBq/mg, with an ^{177g}Lu/^{T}Lu isotopic purity ratio around 20 %, after 2 days EOB [96, 101], which requires further improvements.

On the other hand, the indirect production route (n.c.a) offers the advantage of producing a high specific activity, approximately 2960 GBq/mg, with an isotopic purity of ^{177g}Lu/^{T}Lu higher than 70 %. Moreover it does not generate ^{177m}Lu as an impurity [96]. However, there are some disadvantages associated with the indirect production route. It has low production yields due to the low cross-section of ^{176}Yb, which is only 2.5 barns. In addition, the chemical properties of Yb and Lu are very similar, making it difficult to separate them [69]. Finally, the whole process is generally more expensive compared to the c.a. route. Table III.10 provides a summary of the typical specific activities of ^{177}Lu from different current suppliers [69].

Suppliers	Specific Activity (GBq/mg)	^{177m}Lu Route
Perkin Elmer, USA	∼740	c.a
ORNL, USA	1850 - 2960	n.c.a
MURR, USA	925	c.a
MDS Nordion, Canada	1665	n.c.a
ITG, Garching, Germany	2960	n.c.a
IDB Holland BV	∼740	c.a
This work	∼1100	c.a

Table III.10: Specific activity ranges of ^{177}Lu commercially available at reactors [69].

Therefore, if our study is compared to these values, in terms of specific activity and isotopic impurity, it would be at the level of the carrier-added production route developed in current nuclear reactors. However, in terms of yield, the production is lower due to the low operating energy range (up to 12 MeV) to avoid a high contribution of isotopic impurities. At low energies, the cross-section area available is very small, as the reaction peak ^{176}Yb(d,x)^{177cum}Lu is lost. In order to improve the results in terms of specific activity and isotopic purity, important for the synthesis of radiopharmaceuticals, an alternative two-step production procedure is proposed.

1.3.4 ^{177}Lu two-step production

^{177}Lu two-step production arises from the need to limit or minimize the contribution of isotopic impurities generated from lutetium. The idea for its production in two steps, or in two chemical separations involves a first chemical separation just after irradiation, recovering ^{177}Yb from the isotopic lutetium impurities generated directly during the irradiation, ^{176g}Lu, ^{175}Lu, ^{174g,m}Lu and ^{173}Lu, in addition to ^{177g,m}Lu. The suppression of ^{177g}Lu produced by the direct route ^{176}Yb(d,n)^{177g,m}Lu is a drawback in terms of total activity produced.

After this first chemical separation, a second chemical separation will be performed approximately 12 hours after EOB to ensure that the ^{177g}Lu produced by the decay of ^{177}Yb is maximised. An advantage of this two-step separation is that the ^{177}Lu produced is guaranteed to be free of the metastable impurity ^{177m}Lu and that the specific activity of the final product will be higher due to the removal of isotopic impurities.

With the first chemical separation, the ^{175}Yb produced during the irradiation process has also been recovered, which decays into the stable isotopic impurity ^{175}Lu. It is therefore the only isotopic impurity to be taken into account after the second chemical separation in the final product.

Therefore, the number of ^{177g}Lu atoms produced as a function of time, is obtained from the Bateman Equation (A.24):

$$N_{^{177g}Lu}(t) = \frac{\lambda_{^{177}Yb}}{\lambda_{^{177g}Lu} - \lambda_{^{177}Yb}} \cdot N_{^{177}Yb}(0) \cdot \left(e^{-\lambda_{^{177}Yb} \cdot t} - e^{-\lambda_{^{177g}Lu} \cdot t}\right) \tag{III.7}$$

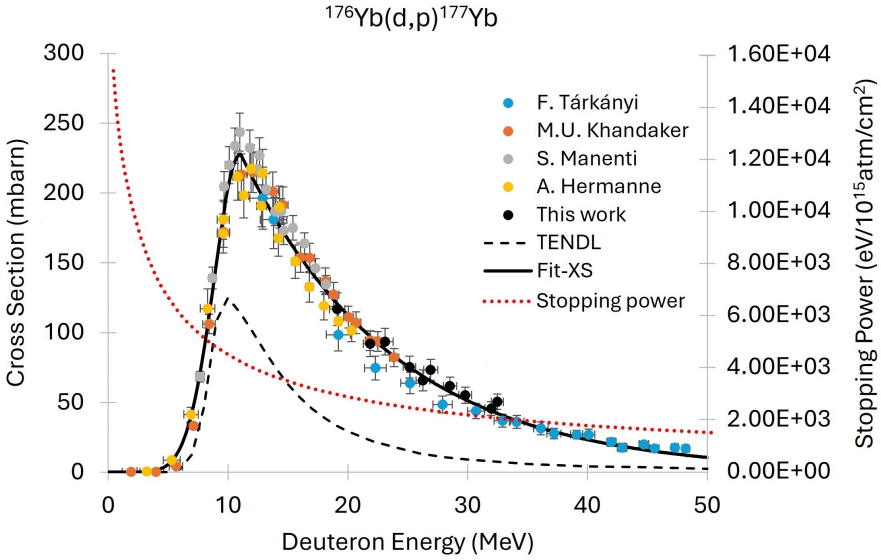

Figure III.16: Cross-section experimental measurements and excitation function fit to the deuteron-induced nuclear reaction ^{176}Yb(d,p)^{177}Yb.

On the other hand, the specific activity only takes into account the mass of ^{177g}Lu and ^{175}Lu produced indirectly from decay processes as a function of time.

$$SA_{^{177g}Lu}(t) = \frac{A_{^{177g}Lu}(t)}{m_{Lu}(t)} = \frac{\lambda_{^{177g}Lu} \cdot N_{^{177g}Lu}(t)}{m_{Lu}(t)} \tag{III.8}$$

Direct EOB production of the number of ^{177}Yb and ^{175}Yb atoms has been calculated using the numerical integration method already described in Appendix D. The fits of the excitation function ^{176}Yb(d,p)^{177}Yb and the stopping power are shown in Figure III.16 and listed in Appendix D. Table III.11 and Table III.12 list the values of atoms, activity, isotopic impurity and specific activity obtained for the production of ^{177}Lu by this two-step method. The quantification of the single isotopic impurity ^{175}Lu generated indirectly, is also included. The irradiation time is 6 h (corresponding to 3 half-lives of the radioisotope of interest, it represents an 87.5 % of produced fraction of the ^{177}Yb radionuclide) while the cooling time is 12 h. Systematic uncertainties in the calculation are evaluated to be 12 % for ^{177g}Lu and 15 % for ^{175}Lu.

Thickness (μm)	Energy (MeV)	Nuclei (atm)		Isotopic Purity (%)	
		^{177}Lu	^{175}Lu	^{177}Lu/^{T}Lu	^{175}Lu/^{T}Lu
400	18.0 - 7.3	$1.23{\cdot}10^{15}$	$2.08{\cdot}10^{12}$	99.83	0.17
400	17.0 - 5.0	$1.12{\cdot}10^{15}$	$1.78{\cdot}10^{12}$		

Table III.11: Estimated number of atoms and isotopic purity produced for ^{177g,175}Lu.

Thickness (μm)	Energy (MeV)	Activity ^{177}Lu (GBq)	SA ^{177}Lu (GBq/mg)	Radionuclidic purity (%) ^{177}Lu/^{T}Lu
400	18.0 - 7.3	$1.49{\cdot}10^{0}$	$4.10{\cdot}10^{3}$	> 99
400	17.0 - 5.0	$1.35{\cdot}10^{0}$		

Table III.12: Estimated number of atoms, activity, isotopic purity and specific activity produced for ^{177g,175}Lu.

As a consequence of this double chemical separation, the isotopic purity percentage is high, as only one isotopic impurity is produced, which is generated by the decay of its parent nucleus ^{175}Yb with a longer half-life compared to ^{177}Yb. Therefore, quick chemical separation ensures a high isotopic purity of the recovered ^{177}Lu after the second chemical separation, approximately 12 hours after EOB where the indirect production of ^{177}Lu is maximised, as shown in Figure III.17. Regarding the radionuclide impurity, as ^{175}Lu is a stable nucleus, there is no contribution in activity that competes with that of ^{177}Lu, and there is no ^{177m}Lu either, as we are working with a no-carrier-added production route, therefore a radionuclide impurity higher than 99 % is estimated.

Finally, if we compare these values obtained with those estimated by the European Pharmacopoeai [98], the established limits are guaranteed for the clinic use of ^{177}Lu produced. Moreover, comparing with Table III.10 of productions in conventional reactors, this work presents specific activity values and isotopic impurities levels of the order of the n.c.a reactions comparable at nuclear reactors (SA $>$ 3000 GBq/mg and IP $>$ 70 %), but far from the yields achieved in these facilities.

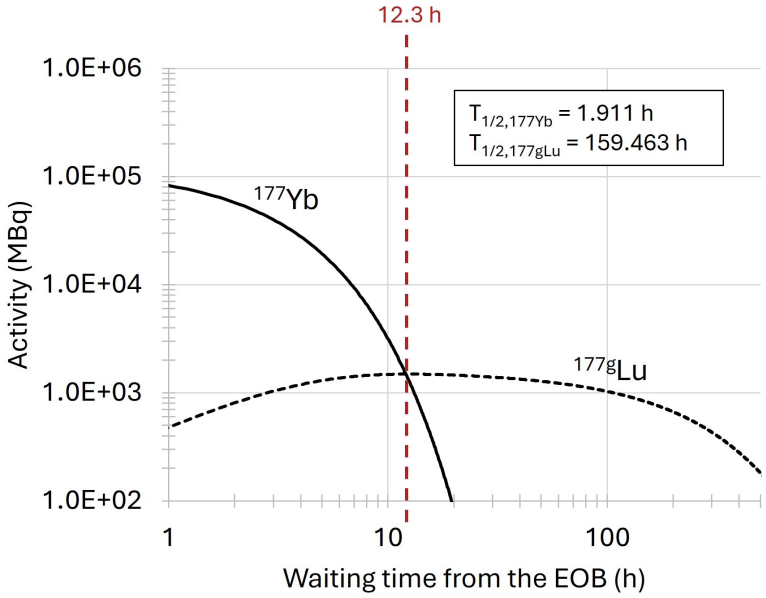

Figure III.17: Decay curve of ^{177}Yb and the growing and decay curve of ^{177g}Lu obtained from the Bateman Equation.

Therefore, optimising SA and IP by the two-step production method is detrimental to the net EOB activity produced. By eliminating the direct route of ^{177}Lu production, the maximum activity achieved per irradiated sample would not allow commercial production at clinical level competitive with current production nuclear reactors. However, these results must be assessed in terms of the possibility of having a domestic preclinical production that would allow the development of a research network for the use of pharmaceuticals radiolabelled with ^{177}Lu.

1.3.5 Thermal and structural simulations with SolidWorks

Following the theoretical development of ^{177}Lu production at two-step, the optimal configuration for the radioisotope of interest consists of a 400 μm $^{176}Yb_2O_3$ sample.

The production at 125 μA of current, has been studied with SolidWorks to assess both the resistance of the device and the sample to the dissipated power. The simulations is carried out in the same way as described above. The boundary conditions of the system, in terms of heat transfer fluid flow rate and thermal contact conditions between surfaces remain the same, however, the power dissipated is adapted to the new model and materials. The values of the boundary conditions are listed in Table III.13. The dissipated power is calculated from the particle energy deposition on the backing and sample using the SRIM 2003 code. Figure III.18 shows the simulation model together with the boundary conditions set on the faces of the corresponding parts.

Flow simulations show that the temperature reached by the sample and backing in steady-state remains well below the melting point of ytterbium oxide (2628 K) and copper (1358 K). Figure III.19 shows the solid and fluid temperature distribution in a side view

Cooling System	
Inlet Volume Flow	3.5 l/min = $5.83{\cdot}10^{-5}$ m^3/s
Environment Pressure	1 atm = 101325 Pa
Fluid Temperature	273 K
Power Dissipation ($P = \Delta E \cdot I$)	
Volumetric Heat Generation Rate (100 % Cu 1)	$6.23{\cdot}10^9$ W/m^3
Surface Heat Generation Rate (67 % Water Liquid + Cu 2 / 33 % Cu + Cu 2)	$8.00{\cdot}10^6$ W/m^2
Volumetric Heat Generation Rate (67 % Sample)	$7.13{\cdot}10^9$ W/m^3
Wall Thermal Condition	
Outer Wall condition	Adiabatic wall
Inter Wall roughness	0.015 μm
Thermal Contact Resistance Interface Cu/Cu	0 K·m^2/W
Thermal Contact Resistance Interface Cu/Ho/Cu	$4{\cdot}10^{-7}$ K·m^2/W [94]

Table III.13: Values of boundary condition parameters for thermal and fluid simulations.

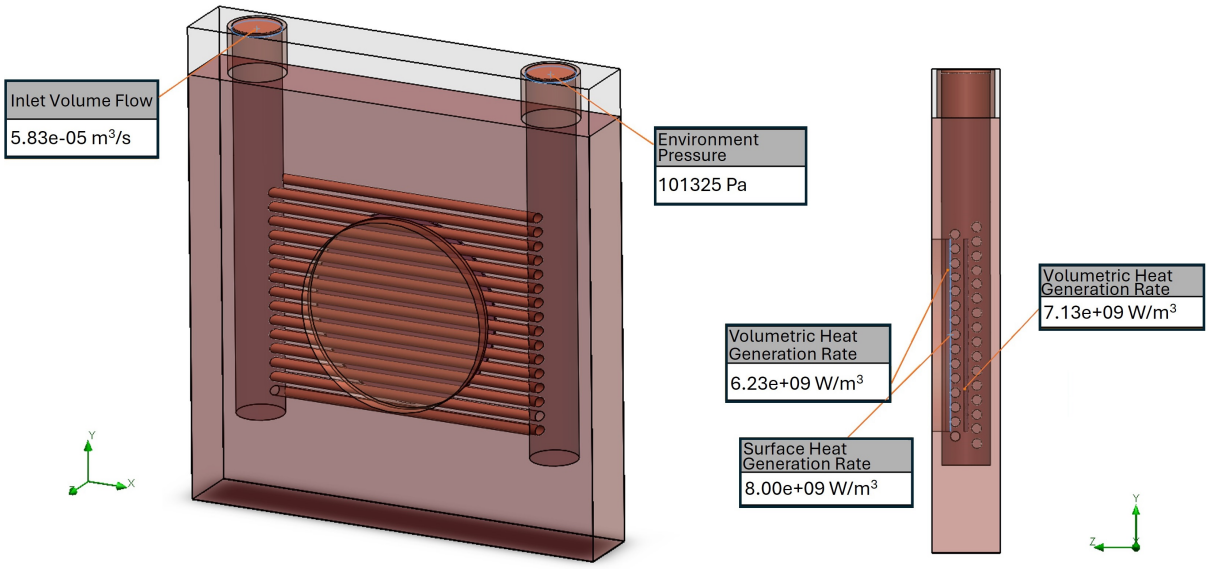

Figure III.18: SolidWorks simulation model together with the boundary conditions set.

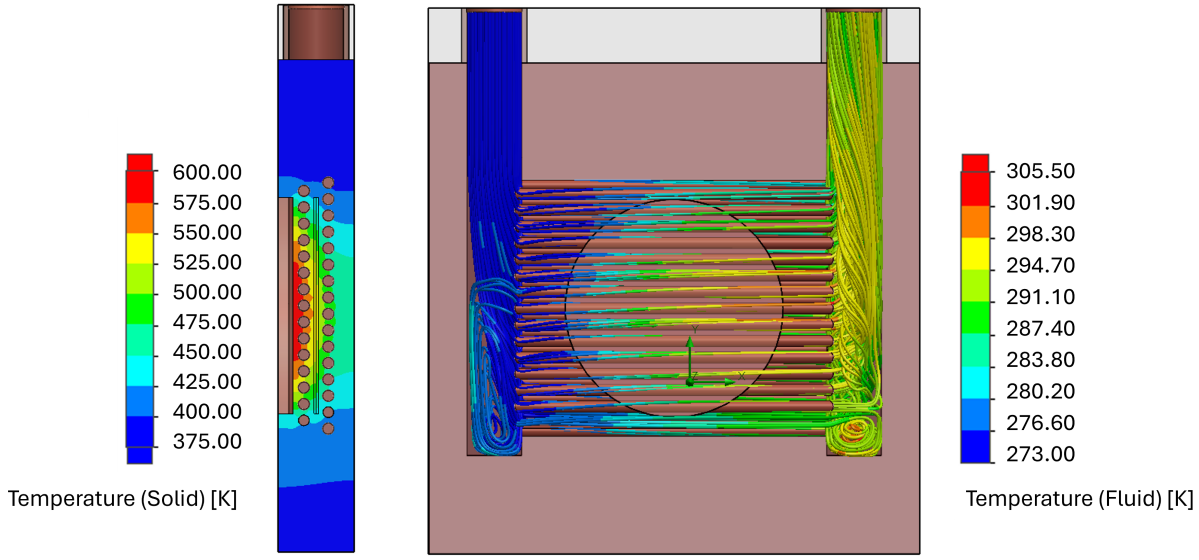

Figure III.19: Left: Side view of the backing and oxide $^{176}Yb_2O_3$ sample temperature distribution. Right: Fluid temperature distribution on the device front face.

and frontal plot of the device. Water cooling system helps to dissipate the heat generated in the sample and backing. The results of temperature and pressure distributions have been used to carry out a complementary study of mechanical stresses inside the device. Figure III.20 shows the values of the Von Mises stress parameter for the evaluation of the mechanical stresses of the system. The simulated results predict stress values higher than the theoretical upper limit of the estimated tensile strength for copper (210 MPa).

These simulations aim to predict the behaviour of the device under demanding boundary conditions. They model the heat transfer of the initial 40 MeV deuteron beam as it passes

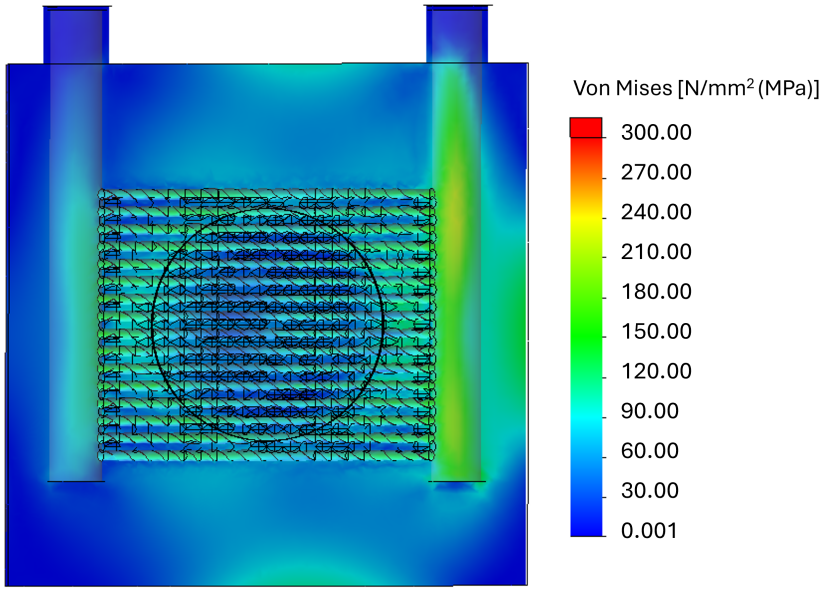

Figure III.20: Static analysis of Von Mises stresses. Cut plot of the side view of the device.

through successive copper layers, gradually depositing its energy. However, the conditions imposed in the model do not always accurately reflect reality. In some cases, the dissipated powers are introduced as surface sources (per unit area) instead of volumetric (per unit volume), due to the complexity of the simulated geometries, particularly in the critical area of the millichannels. Additionally, the contact resistance values between materials are not precisely known, introducing further uncertainty into the model.

Therefore, having proofs of concept or tests to support the feasibility of the device will always play a positive role in establishing the simulations as reliable. Our device should dissipate around 1.6 kW/cm^2, while previous studies of the copper device with less cooling demonstrated heat dissipation capacities of up to 3 kW/cm^2 [85].

2 Radioisotope production with neutrons

Currently, the supply of some of the radionuclides essential for Nuclear Medicine is largely dependent on a limited and ageing number of nuclear reactors located in Europe, North America, South Africa and the Asia-Pacific region [102]. Many of the primary production reactors are nearing the end of their operational life, being almost 50 years old.

This is the case of ^{99m}Tc, the most widely radioisotope used in clinical trials, for approximately 85 % of SPECT diagnostic imaging studies for cancer [102]. Its supply is conditioned by the 100 % operability of the few reactors that produce it worldwide, with serious shortages in hospitals when one of these reactors closes due to maintenance or operational failure [103].

Ensuring the supply of this and other radioisotopes is essential for the national health systems. The International Fusion Materials Irradiation Facility Demo Oriented NEutron Source (IFMIF-DONES) could be a complementary facility for the supply of medical radioisotopes produced by neutron-induced nuclear reactions.

IFMIF-DONES will consist of a 40 MeV deuteron accelerator at 125 mA. The deuteron beam will hit on a lithium liquid target to produce the neutron source based on a stripping reaction $D^+ + {}^7Li$ [4]. The objective of this facility will be to test new materials under similar neutron irradiation conditions as expected in nuclear fusion reactors [2, 104]. Samples of these materials will be irradiated in the core of this facility, the High Flux Test Module (HFTM), just behind the lithium jet, all within the Test Cell (TC). In parallel to the irradiation of materials, the facility will be available for complementary experiments using the residual neutron flux in the Test Cell [5].

Figure III.21 shows a CAD layout of the IFMIF-DONES facility that will host the different modules of the high-current linear accelerator up to the Test Cell. The deuterons of 40 MeV energy and 125 mA current will strike the liquid lithium loop at an inclination of 9^{o} to produce the spallation reaction. The neutron production will take place inside the TC which is heavily shielded with concrete blocks. Making a section in the XY-Plane (indicated in red) of the CAD geometrical design, the HFTM section can be seen just behind the lithium loop. This position is the one where the neutron flux is higher. Figure III.21 includes the simulated average neutron fluence rates in $1 \times 1 \times 1$ cm^3 cells at different positions inside the TC, 8 cm behind the HFTM and at the entrance of the duct towards the experimental room R160. The distance between the two locations is 160 cm and a neutron fluence rate drop of two orders of magnitude is observed.

In this subsection, the feasibility of the production of ^{99}Mo, the parent nuclei of ^{99m}Tc, by neutron-induced nuclear reactions is studied, taking into account the characteristics of the residual neutron flux available within the TC. In addition, a design of a Radioisotope Production Device (RIPD) coupled to the TC geometry is developed and studied in colaboration with the National Fusion Laboratory of the Centre for Energy, Environmental and Technological Research (CIEMAT) in Madrid (Spain).

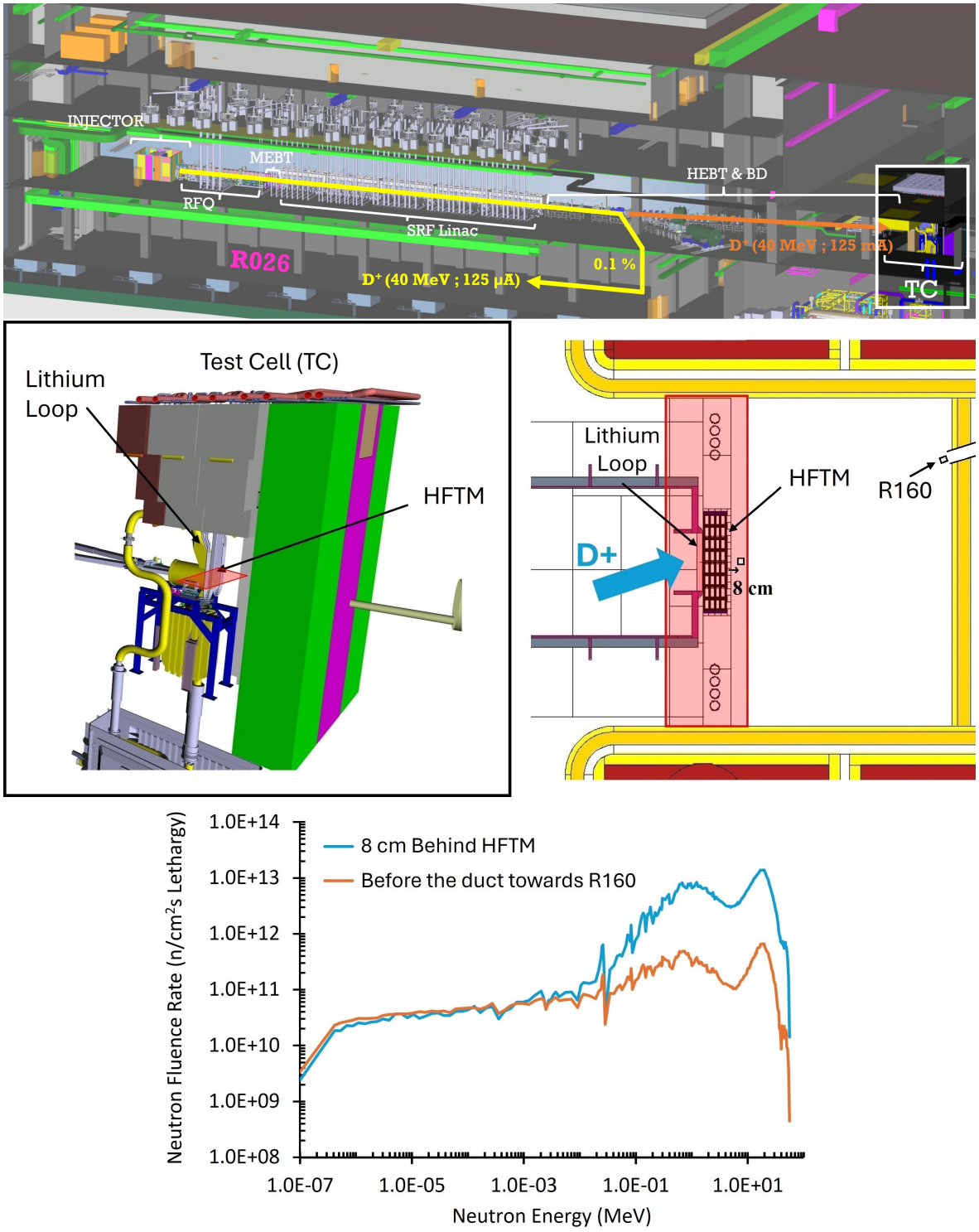

Figure III.21: Up: CAD of IFMIF-DONES facility and Test Cell. Middle: Additional sectional view of the HFTM after the lithium loop inside the TC. Down: Neutron fluence rate expected at two different positions inside the TC [7].

2.1 ^{99}Mo/^{99m}Tc production study

One of the most significant radioisotopes for "in vivo" diagnosis is ^{99m}Tc. This isotope offers physical properties that minimise the radiation dose to the patient, primarily due to its short half-life ($T_{1/2} = 6$ h) and its low pure gamma emission energy. The gamma photon emitted at 140 keV, with an 89 % yield, is sufficiently energetic to exit the body without substantial attenuation [22], enabling SPECT diagnostic imaging. ^{99m}Tc is employed in over 85 % of nuclear medicine studies worldwide [21, 102]. Typically, this radioisotope is produced via a generator through de decay of its "parent nucleus", ^{99}Mo, which has a half-life of approximately 66 hours and undergoes β^- decay with a maximum energy of 1.36 MeV. The decay scheme is shown in Figure III.22.

The most common ^{99}Mo production route involves uranium-aluminum mini-plates irradiations in nuclear reactors, in which there is a constant neutron flux. Among the various fission products, approximately 6.1 % of fission events result in the formation of ^{99}Mo [102]. Simultaneously, other medically relevant radioisotopes, such as ^{131}I (around 3 %), are also produced. Subsequently, these radioisotopes must be separated from the other elements produced during the irradiation process that have no clinical relevance.

To guarantee the supply of ^{99}Mo/^{99m}Tc, in view of the ageing of nuclear facilities and their continuous supply shutdowns, new production routes are being analysed. Neutron irradiation of molybdenum samples is one such alternatives. This process has drawbacks since the ^{99}Mo produced by this process has a lower specific activity than the ^{99}Mo produced by neutron fission, whereas it has the advantage of generating less radioactive waste [105]. Neutron irradiation is therefore only practical for reactors specifically designed for this type of production or state-of-the-art high-intensity linear accelerators capable of producing a very high neutron flux, such as IFMIF-DONES facility.

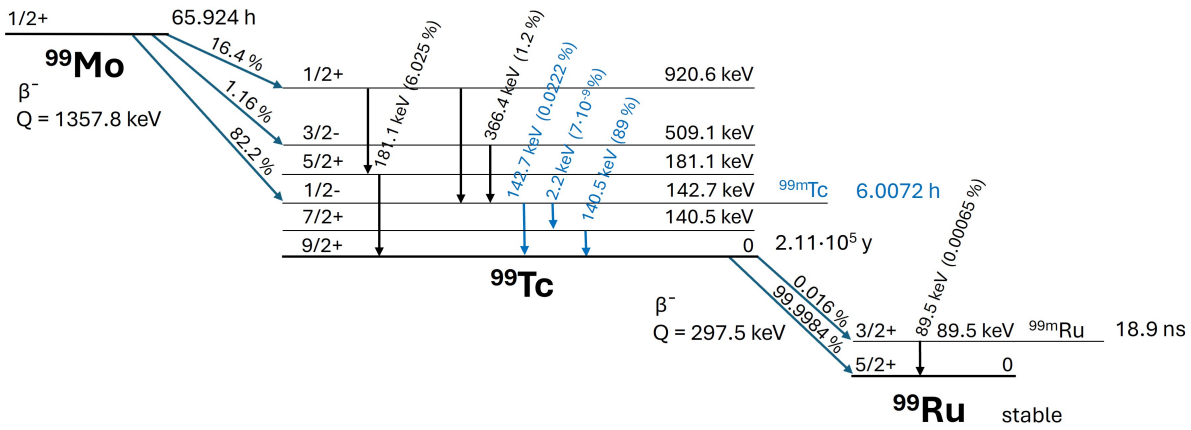

Figure III.22: Decay scheme of ^{99}Mo and ^{99m}Tc to ^{99}Ru stable state.

2.1.1 ^{100}Mo(n,2n)^{99}Mo Production route.

According to the main displacement caused by neutron-induced nuclear reactions, ^{99}Mo can be produced by two direct nuclear reactions, ^{98}Mo(n,γ) and ^{100}Mo(n,2n), as shown in Figure III.23. The most efficient production route for ^{99}Mo using molybdenum targets in nuclear reactors is the ^{98}Mo(n,γ) reaction with thermal neutrons, whereas, due to the characteristics of the IFMIF-DONES fast neutron flux, the most efficient and alternative production route is the ^{100}Mo(n,2n) reaction. Cross-sections are plotted in Figure III.24, which also compares the IFMIF-DONES fluence rate with a conventional radioisotope production reactor, the Japan Research Reactor-3 (JRR-3) [106]. The direct reaction ^{98}Mo(n,γ) is common in nuclear reactors with thermal neutrons, while ^{100}Mo(n,2n) is the alternative production direct route with fast neutrons. Moreover, a third production route exists indirectly via the decay of ^{99}Nb, produced through the ^{100}Mo(n,n+p) reaction. The

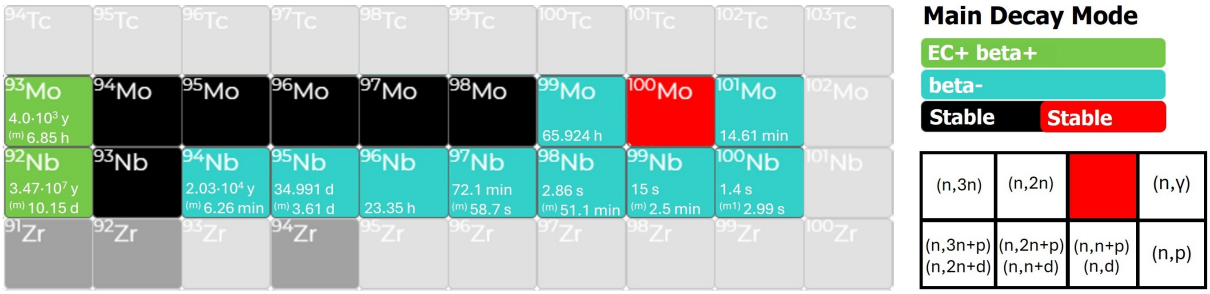

Figure III.23: Main displacement caused by neutron-induced nuclear reactions on Mo targets, radioisotopes produced, their decay mode and half-lives.

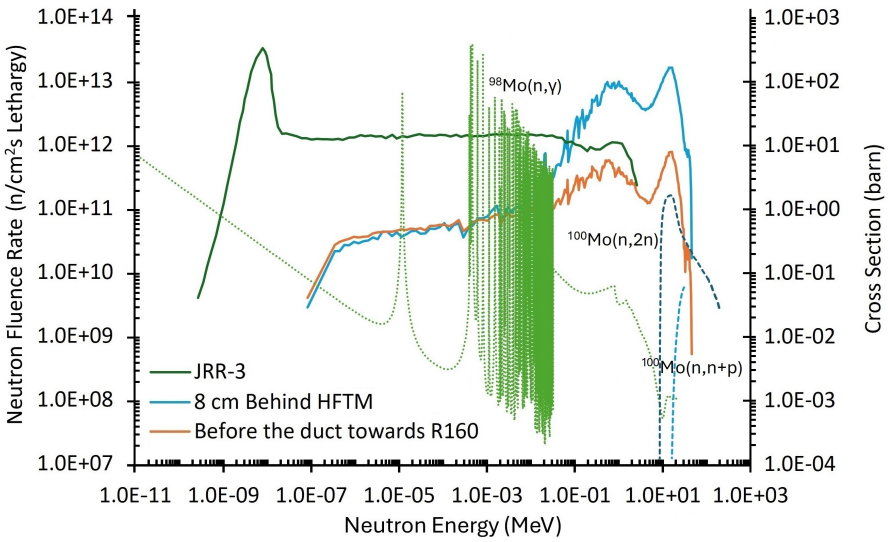

Figure III.24: Double-entry graph. Left: Neutron fluence rate expected at two positions inside the TC, compared to the typical nuclear reactor neutron fluence rate, as the JRR-3 reactor [106]. Right: Different ^{99}Mo production cross-sections: ^{98}Mo(n,γ), ^{100}Mo(n,2n) and ^{100}Mo(n,n+p).

^{98}Mo(n,γ)^{99}Mo cross-section is taken from ENDF/B VIII.0 evaluation database [113] and exhibits large resonances from 12 eV to 10 keV energy region. The ^{100}Mo(n,2n)^{99}Mo and ^{100}Mo(n,n+p)$^{99(g+m)}$Mo reactions, are from TENDL-2023 nuclear database [63] with a threshold energy value above 8.4 MeV and 11.2 MeV, respectively.

On the other hand, despite the use of enriched targets, due to the existence of traces of different stable molybdenum isotopes, it must be considered that stable molybdenum isotopes are formed as a consequence of the Mo(n,γ) and Mo(n,xn) reactions. Furthermore, numerous niobium radioisotopes are also produced, which decay β^- to stable isotopes of molybdenum. Radioisotopes above the valley of stability such as ^{93}Mo or ^{92}Nb, which decay β^+ to stable isotopes of molybdenum and zirconium, will also be produced. However, all these mentioned radioisotopes do not interfere neither in the production of ^{99}Mo nor in possible technetium isotopes that would be carried over after the ^{99}Mo/^{99m}Tc chemical separation, with the exception of the two following reactions.

^{100}Mo(n,γ)^{101}Mo reaction, whose half-life is 14.61 minutes and decays β^- 100 % to the radioisotope ^{101}Tc ($T_{1/2}$=14.2 min), which in turn decays again β^- 100 % to the stable isotope ^{101}Ru. Due to the short half-lives of these isotopic impurities, a time of at least 5 hours after EOB is necessary to ensure their removal in the final sample.

The second impurity reaction is ^{100}Mo(n,n+p)$^{99(g+m)}$Nb, whose ground stable and metastable state decay β^- in a few minutes to ^{99}Mo. This production route is therefore simultaneous with the ^{100}Mo(n,2n) route, although its cross-section and production yield is much smaller, as shown in Figure III.24.

Considering the fluxes available in IFMIF-DONES with a fast neutron broad peak up to 20 MeV and in order to reduce the impurities, the optimal targets for ^{99}Mo production are ^{100}Mo highly enriched oxide targets ($^{100}MoO_3$), as already published in previous research on the feasibility of ^{99}Mo production at the IFMIF-DONES via the novel ^{100}Mo(n,2n)^{99}Mo activation route [7], not accessible in conventional nuclear reactors due to their threshold energy.

In the following subsection, the specific activity of ^{99}Mo produced using realistic samples in IFMIF-DONES is estimated at the position of highest available neutron flux inside the Test Cell. For this purpose, different calculation methods carried out with the Monte Carlo Neutron-Particle Transport code (MCNP) [107] are used. A more detailed explanation of the different methods implemented is found in Appendix E.

2.1.2 Specific activity estimation using MCNP simulations.

For neutron-induced nuclear reactions $A(n,y)B$, and following the definition given for thick targets of the Equation (II.1), the radionuclide production rate can be rewritten as,

$$R_B = \chi \cdot n_A \cdot \int_E \phi(E) \cdot f(E)\, dE \tag{III.9}$$

where, χ is the isotopic and chemical purity of the target, n_A is the target nucleus density [atm/cm^3], $\phi(E)$ is the neutron energy-dependent flux [s^{-1}] and $f(E)$ is a response function of the neutron interactions with matter and takes into account both the track length of particles and the cross-section of the nuclear reactions [105].

Therefore, according to the specific activity equation, we can determine it directly as,

$$SA_B(t) = \frac{\lambda_B \cdot N_B(t)}{m} = \frac{R_B}{m} \cdot (1 - e^{-\lambda_B \cdot t}) \tag{III.10}$$

$$SA_B(t) = \frac{\chi \cdot n_A}{m} \int_E \phi(E) \cdot f(E)\ dE\ \cdot (1 - e^{-\lambda_B \cdot t}) \tag{III.11}$$

Monte Carlo N-Particle (MCNP) is a computational simulation code that uses the Monte Carlo method to model the interaction of particles with matter, especially neutrons. It relies on statistical simulations to track the trajectory of individual particles as they interact with user-defined materials and media. The results of these interactions and calculations are recorded in computational tools called tallies, which provide specific physical quantities, such as particle fluxes, reaction rates, angular distributions, deposited energies, among others, across a surface, in a cell or at a detection point. All these MCNP tallies are normalised per source particles unless a different normalisation is specified. In fact, any quantity of the form,

$$q = \int_E \phi(E) \cdot f(E)\ dE \tag{III.12}$$

can be tallied, where $\phi(E)$ is the energy-dependent fluence rate and $f(E)$ is any product or summation of the quantities in the cross-section libraries or a response function provided by the user.

Therefore, the calculation of the specific activity can be summarized as follows,

$$SA_B(t) = C \cdot I \cdot q \cdot (1 - e^{-\lambda_B \cdot t}) \tag{III.13}$$

where the factor C is a scalar quantity of mass [g^{-1}], I is the total source neutron flux [s^{-1}] (tallies are normalised per source particles) and q is the result of the activated atom tally obtained by Monte Carlo simulation [atm].

The production rate simulated with MCNP can be performed by different methods, i.e. using different types of tallies accompanied by specific calculation cards. It also requires the definition of a geometry and materials, the definition of a neutron source and the physics mode, mainly consisting in enabling the particles and reactions of interest in our problem. The MCNP code version used in the development of this thesis is MCNP.6.2 [108]. The detailed calculation process of the C- and q-factors for the radionuclide production rate simulation, together with the discussion of the different MCNP calculation methods developed in this work, is described in the Appendix E. In addition, a detailed tally exemplification for each method is included.

MCNP simulation

To set up and simulate an irradiation system based on a $^{100}MoO_3$ highly enriched pellet, MCNP allows the modelling of three-dimensional geometries using surfaces and bodies, as well as the definition of radiation sources. For our simplified case, it is sufficient to detail the geometry and material of the sample to be irradiated, and to place in front of it a neutron source with defined dimensions and a characteristic neutron fluence rate, as shown Figure III.25.

^{100}Mo is a non-stable radioisotope with such a very long half-life ($T_{1/2}$=7.01·10^{18} y) that it can be considered observably stable and it abundance in nature is 9.75 %. A realistic target to simulate the production of ^{99}Mo by the ^{100}Mo(n,2n) neutron-induced nuclear reaction, is a spark plasma sintered pellet from 95 % enriched molybdenum oxide powder, $^{100}MoO_3$ [110]. After the sintering process, the density of the pellet is around 80 − 85 % of the theoretical, 4.70 g/cm^3, and the isotopic composition of the enriched $^{100}MoO_3$ target is ^{92}Mo (0.81 %), ^{94}Mo (0.52 %), ^{95}Mo (0.89 %), ^{96}Mo (0.92 %), ^{97}Mo (0.53 %), ^{98}Mo (1.33 %) and ^{100}Mo (95.00 %). Figure III.25 shows a real sintered pellet and the result of the pellet simulated with MCNP. The simulated $^{100}MoO_3$ target is covered by a thin aluminium film of 625 μm in thickness [111]. The dimensions of the pellet are 10 mm in diameter and 5 mm in thickness, as the realistic $^{100}MoO_3$ samples irradiated by K. Tatenuma *et al.* [112]. In front of the pellet, the neutron source area is plotted with the neutron fluence rate corresponding to 8 cm behind the HFTM (see Figure III.24).

The specific activity of ^{99}Mo has been estimated using different tallies: Tally 4 (F4) with DE & DF card, where the cross-sections have been user-defined and downloaded from ENDF/B VIII.0 and TENDL-2023 databases [63, 113]. Tally 8 (FT8) with CAP card, which allows the analysis of the radioisotopes produced only by (n,γ) capture reactions. And Tally 8 (FT8) with RES card, which allows the study of residual nuclei by energy deposition of the radioisotopes of interest, ^{99}Mo and ^{99}Nb, produced after irradiation regardless of their direct production route. Figure III.26 shows the ^{98}Mo(n,γ), ^{100}Mo(n,2n)

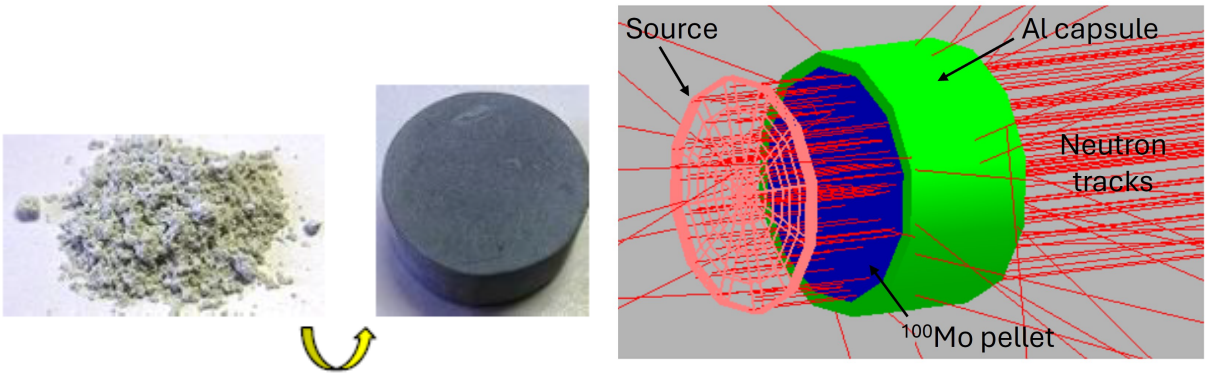

Figure III.25: Left: Realistic $^{100}MoO_3$ powder before and after the spark plasma sintering [110]. Right: MCNP simulation and particle tracks through a $^{100}MoO_3$ target.

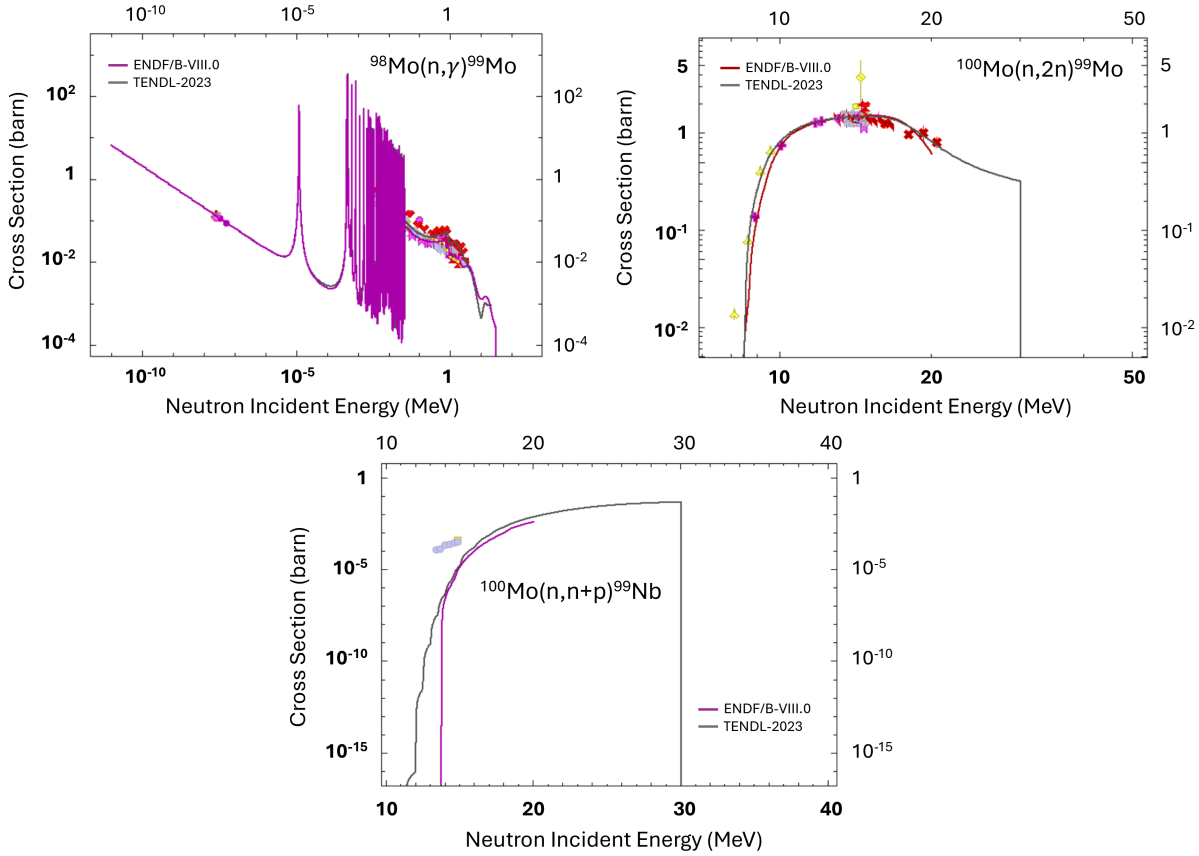

Figure III.26: ^{98}Mo(n,γ)^{99}Mo, ^{100}Mo(n,2n)^{99}Mo and ^{100}Mo(n,n+p)^{99}Nb neutron-induced nuclear reactions cross-section from ENDF/B VIII.0 [113], TENDL-2023 [63] (lines) and EXFOR [62] (dots) databases.

and ^{100}Mo(n,n+p) cross-sections of the ENDF/B VIII.0 library used in MCNP.6.2 simulations by default compared to TENDL-2023 [63] theoretical database up to 30 MeV.

The pellet irradiation position is the cell located 8 cm behind the HFTM as shown in Figure III.24, where the total neutron fluence rate is $3.32{\cdot}10^{13}$ n/cm^2/s. The activities have been determined after 7 days of irradiation and one day of cooling time. As expected and shown in Table III.14, the production via the direct ^{100}Mo(n,2n)^{99}Mo neutron-induced nuclear reaction with fast neutrons is the main production route, higher than the the ^{98}Mo(n,g)^{99}Mo reaction or the indirect route by ^{99}Nb decay. The ^{99}Mo specific activity produced by the indirect ^{100}Mo(n,n+p)^{99}Nb route has been calculated using the Bateman Equation (A.24).

Table III.14 shows the deviation between equivalent counts between different tallies. In the ^{99}Mo production, it should be noted that the interpolation of the cross-section resonances ^{98}Mo(n,γ) is not the same between the user-defined values used for F4 with the DE & DF card calculations, and the internal library from the MCNP.6.2 database used for the FT8 CAP tally. It should be noted that when using a DE & DF card the entries of the cross-section must be monotonically increasing in energy. Therefore, the raw

Sample Mass (g of Mo)	Tally Type, card	^{99}Mo Specific Activity (Bq/g of Mo)		
		^{98}Mo(n,γ)	^{100}Mo(n,2n)	^{100}Mo(n,n+p)^{99}Nb
$\sim$ 1.02	F4, DE & DF card	$5.24{\cdot}10^{7}$ (0.31)	$4.24{\cdot}10^{10}$ (0.01)	$4.34{\cdot}10^{7}$ (0.02)
	FT8, CAP card	$5.00{\cdot}10^{7}$ (0.30)	-	-
	Deviation	5.05 %	-	-
	FT8, RES card	$4.20{\cdot}10^{10}$ (0.18)		$4.31{\cdot}10^{7}$ (0.48)
	Deviation	1.02 %		0.70 %

Table III.14: ^{99}Mo Specific activity estimated by different MCNP.6.2 tallies, after 7 days of irradiation and 1 day of cooling. In brackets, uncertainties of the MCNP.6.2 simulation in percentage. In grey box, the percentage deviation between the different tallies is indicated.

data obtained from the databases must be externally modified to fulfil this requirement and be correctly read. Thus, a deviation of 5.05 % between tally methods is observed. On the other hand, for neutron-induced nuclear reaction at high energy, where no resonances are found, e.g. the (n,2n) or (n,n+p) nuclear reactions, the differences between tallies are lower, around 1 %.

Regarding the impurities production, after 1 day EOB, quantities of ^{101}Mo and of its decay byproduct ^{101}Tc are negligible. The remaining impurities in the sample are only isotopic traces of molybdenum, which do not constitute an issue, as they will be removed chemically in the separation process of ^{99}Mo/^{99m}Tc.

In the following, the estimated values of ^{99}Mo specific activity will be compared to the values obtained by the conventional process with nuclear reactors. Furthermore, we have verified whether the final specific activity obtained is sufficient to be chemically separated in conventional ^{99}Mo/^{99m}Tc generators.

2.1.3 Comparison with other production routes

In this work, the specific activity of ^{99}Mo produced at IFMIF-DONES has been calculated by Monte Carlo simulations using a realistic sample of $^{100}MoO_3$ enriched to 95 %. The specific activity of ^{99}Mo obtained is compared in Table III.15 with other relevant facilities, TRIGA Mark II nuclear reactor in Vienna, Japan Research Reactor (JRR-3) and KURRI-LINAC, a linear electron accelerator where samples are irradiated by Bremsstrahlung photons, producing ^{99}Mo by the ^{100}Mo(γ,n) photoproduction reaction. In these production cases, realistic targets of natural molybdenum oxide or enriched are used [111, 112]. Our results show that production at IFMIF-DONES is comparable to that of other facilities in terms of specific activity.

After the sample irradiation, chemical separation of ^{99}Mo/^{99m}Tc as well as purification of ^{99m}Tc is required. Our estimated production is within the specific activity limits for ^{99}Mo produced by neutron activation, generally in the range of 37-185 GBq/g [105]. The ^{99m}Tc Master Milker (TcMM) process developed by K. Tatenuma *et al.* [112] allows the separation of low specific activity ^{99}Mo and the purification of ^{99m}Tc from ^{99}Mo activities

Sample	Pellet (mm) / Powder (g)	Reaction	Specific Activity ^{99}Mo (Bq/g Mo)	Facility
$^{98}MoO_3$ (98.63 %)	0.06	^{98}Mo(n,γ)	$1.90{\cdot}10^{10}$	TRIGA-II
$^{nat}MoO_3$	$\phi = 20$; $t = 16$	^{98}Mo(n,γ)	$1.48{\cdot}10^{10}$	JRR-3
	$\phi = 10$; $t = 5$	^{100}Mo(γ,n)	$1.37\text{-}3.48{\cdot}10^{6}$	KURRI-LINAC
$^{100}MoO_3$ (95 %)	$\phi = 10$; $t = 5$	^{100}Mo(γ,n)	$1.43\text{-}3.62{\cdot}10^{7}$	
		^{100}Mo(n,2n)	$5.46{\cdot}10^{10}$	This work

Table III.15: ^{99}Mo specific activity for different MoO_3 oxide samples and production routes, after 7 days of irradiation time.

in the $1{\cdot}10^4$ - $2{\cdot}10^{12}$ Bq range, produced by a reactor and/or accelerator. The TcMM process has proven the production of high purity ^{99m}Tc (radiochemical purity > 99.99 %) with an average chemical yield of 90 %. The elution time for ^{99m}Tc is approximately 30 minutes per bath. Radioactive impurities produced in the molybdenum sample, mainly radioactive niobium and traces of stable isotopes of molybdenum, are completely removed from the final eluted product and retained in the generator column as radioactive waste.

Based on estimated results with the average neutron flux 8 cm behind the HFTM, a pellet equivalent to 1.6 g of $^{100}MoO_3$ (1.02 g of Mo) irradiated with neutrons for 7 days, produces a ^{99}Mo activity of 55.7 GBq in total just after irradiation, which corresponds to a specific activity of 54.6 GBq/g of Mo. A conventional hospital radiopharmacy, such as Punta de Europa University Hospital in Spain, requires around 46 GBq of ^{99}Mo per week [114]. Therefore, with only one small enriched sample of $^{100}MoO_3$, the needs of ^{99}Mo/^{99m}Tc of a conventional hospital during 1 week will be covered by reusing neutrons within the TC.

This promising estimate has prompted the study of a larger number of samples, which will produce much larger amounts of ^{99}Mo/^{99m}Tc, for large-scale production at IFMIF-DONES. For this purpose, an adaptation of the TC geometry is necessary to allow the samples to be irradiated weekly and subsequently extracted from the TC, as the neutron flux will be irradiated continuously the samples inside the TC during the whole year.

2.2 RadioIsotope Production Device (RIPD)

The proposed design of the radioisotope production device for radioisotope production by neutron-induced nuclear reaction inside the Test Cell at IFMIF-DONES facility consists of a mechanical side-insertion arm. The proposal aims not to interfere with the main operation at IFMIF-DONES, therefore the insertion and removal of weekly targets is automatic and involves a shielding system to prevent neutron leakage through the duct. The location of the production targets is 8 cm behind the HTFM, where radioisotope production is maximised, as published in a previous study [7]. Figure III.27 shows the

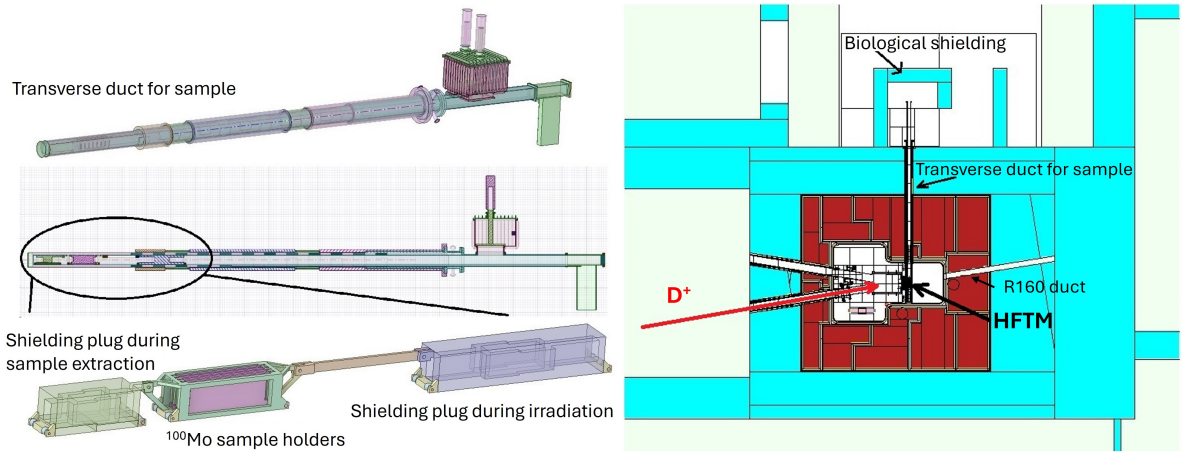

Figure III.27: Left: 3D CAD model of the RIPD. Right: TC horizontal section from the irradiation zone to the vessel outlet.

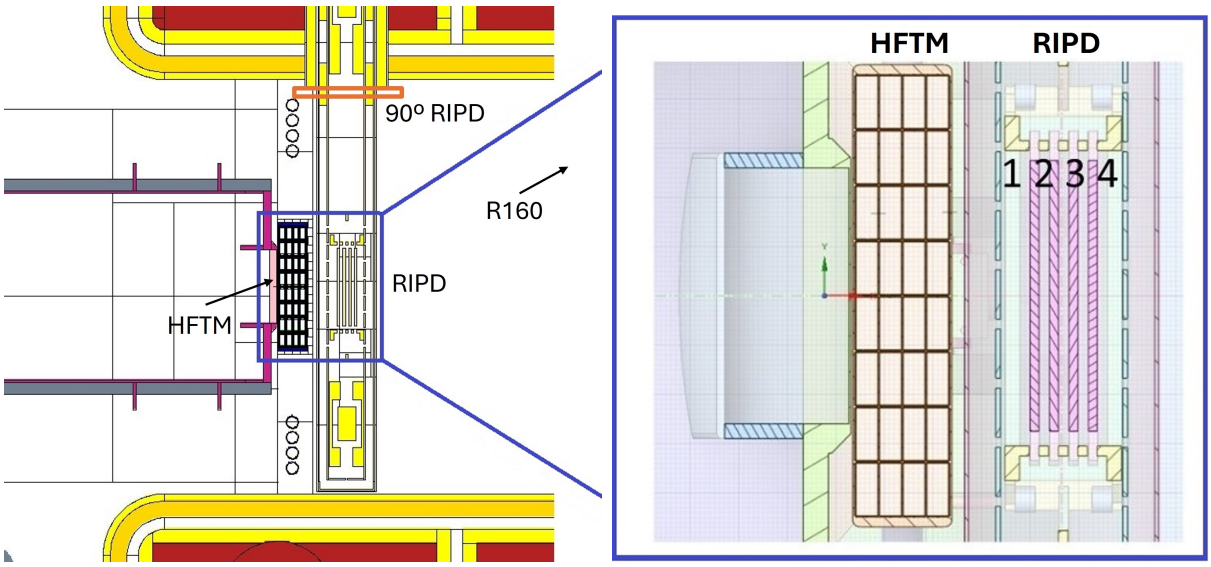

Figure III.28: RIPD horizontal section with the sample holder positioned behind HFTM.

CAD model of the proposed RIPD with four holes for sample carrier plates by means of a lateral insertion. This adaptation to the TC model and the neutron fluence rates within them are provided by F. Mota of the National Fusion Laboratory (CIEMAT). The proposal includes removable shielding plugs that closes the holes of the duct through the vessel to the irradiation zone both at the time of irradiation and at the time of removal of the irradiated plates. The distance between the HFTM and the RIPD is 1.3 cm while the distance between the HFTM and the first $^{100}MoO_3$ sample holder is 8 cm.

For determining the average neutron fluence rate at the sample holder positions shown in Figure III.28, the McDeLicius code (version 17) [115] is employed for the neutron transport calculations. It is an extension to the Monte Carlo code MCNP.6.2 [108] with the capability to simulate the generation of source neutrons and photons based on

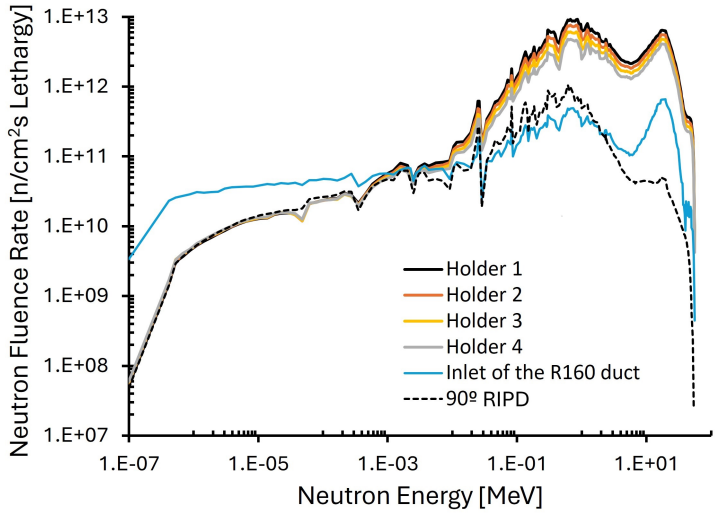

Figure III.29: Average neutron fluence rate [n/(cm^2·s·MeV)] at different positions, in each RIPD sample holder, at the entrance of the R160 duct and at 90° to the RIPD. The indicated positions can be seen in the schematic view in Figure III.28. Private communication by F. Mota.

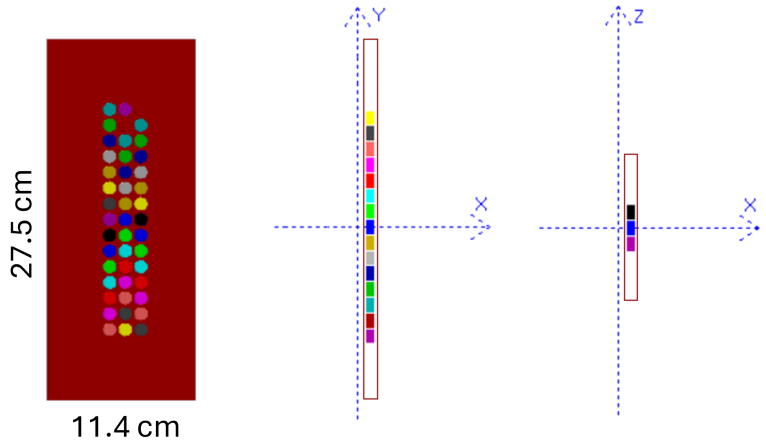

Figure III.30: Carrier plate with 45 enriched $^{100}MoO_3$ pellets, for irradiation in the first holder of the RIPD.

evaluated $D^+ + {}^7Li$ cross-sections [117]. Figure III.29 shows the average neutron fluence rate simulated per each sample holder.

The multiple pellet irradiation shall take place in each of the above mentioned holders. According to their dimensions, 27.5 cm × 11.4 cm × 0.9 cm per holder, the samples are placed on carrier plates inserted in the holders, as shown in Figure III.30, where 45 pellets are located on a carrier plate. Simulated neutron irradiation of 45 enriched $^{100}MoO_3$ pellets (95 %), with a total weight of 72 g (45.9 g of Mo) for 7 days, estimates a total ^{99}Mo production activity of $1.21{\cdot}10^{12}$ Bq EOB, assuming an average specific activity of $2.63{\cdot}10^{10}$ Bq/g Mo. These values have been calculated as an average of the different tally methods calculated. Statistical uncertainty of the MCNP.6.2 simulations is 1.69 %.

Although no specific data are available on the weekly requirement of ^{99}Mo in Spain, this production can be compared with the weekly demand in Japan, one of the most demanding countries in the world. In Japan, this value is equivalent to the amount of ^{99m}Tc needed to cover several days supply [112], so that the Spanish weekly supply could be achieved.

2.2.1 Shielding of the RadioIsotope Production Device pipeline

The proposed lateral insertion of the RadioIsotope Production Device involves a lateral borehole in the Test Cell, the core of the IFMIF-DONES facility and where a high neutron flux is hosted. Therefore, radiation protection considerations are required for the feasibility study of this system.

The structural material of the RIPD is SS316L, a type of austenitic stainless steel of the 316 series, characterised by its low carbon content. It is mainly composed of iron (Fe), chromium (Cr) and nickel (Ni) which gives it a high resistance to corrosion, especially in aggressive environments such as those exposed to high temperatures and extreme conditions. The materials of the plugs incorporated in the RIPD have been studied to guarantee the best radioprotection. A schematic of the geometry and materials of the RIPD is shown in Figure III.31.

In order to study the radiation levels produced in the sample extraction room (R158), located at the end of the RIPD duct, a simulation of neutron transport through the duct has been carried out, starting from the neutron flux at the beginning of the duct, which corresponds to the neutron fluence rate at 90º of the RIPD, shown in Figure III.29. For this purpose, MCNP.6.2 simulations of the neutron flux and dose levels through and around the RIPD have been performed.

Figure III.32 shows the result of the neutron simulation considering concrete plugs to close the duct when the RIPD is closed and the samples are irradiated. The neutron flux in the sample extraction room is higher than 10^7 n/(cm^2·s), corresponding to dose rates

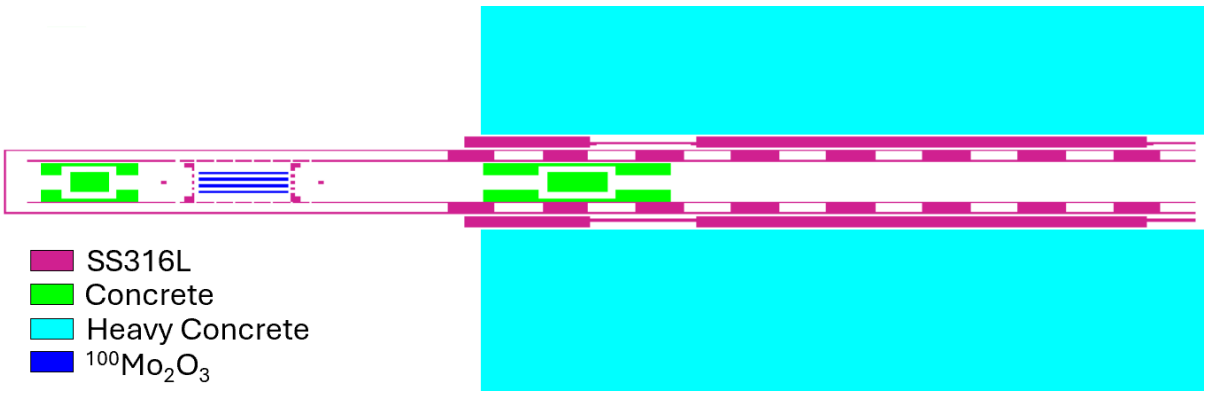

Figure III.31: RIPD geometry and shielding materials. The holes for samples are shown as molybdenum oxide.

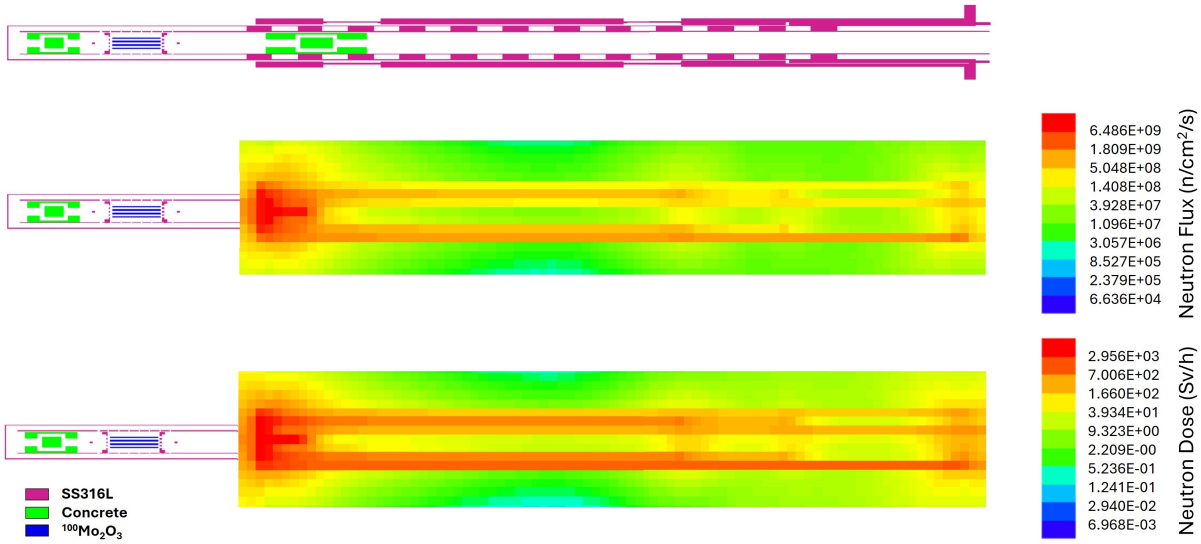

Figure III.32: Simulation of neutron flux and dose around the RIPD, with concrete and polyethylene shielding plugs.

higher than 1 Sv/h, as can be simulated by MCNP.6.2 using the flux to ambient dose equivalent conversion factors recommended in radiation protection by the International Commission on Radiological Protection, ICRP-74 (1996) [116]. The shielding initially foreseen is not sufficient to guarantee safe levels in room R158. Therefore, additional shielding has been considered.

The second proposal studied is a wider duct shielding cap made of various concatenated materials. By testing different materials, the most favourable combination of the study is polyethylene, concrete and lead in different thicknesses, as shown in Figure III.33. This combination reduces the average neutron flux value after shielding by four orders of magnitude. However, the neutron flux and dose rate in room R158 is still high at the exit, because the shielding rails are clearly an escape route for the neutrons, as shown in Figure III.33.

For the time being, this proposal of lateral insertion of the samples to be irradiated inside the Test Cell is in standby until alternative ways of insertion and extraction of the pellets with less impact on the normal operation of the facility can be designed and assessed, since in view of the preliminary and simulated results of the RIPD proposal, this would have a significant impact as a consequence of the leakage of the neutron flux inside the Test Cell.

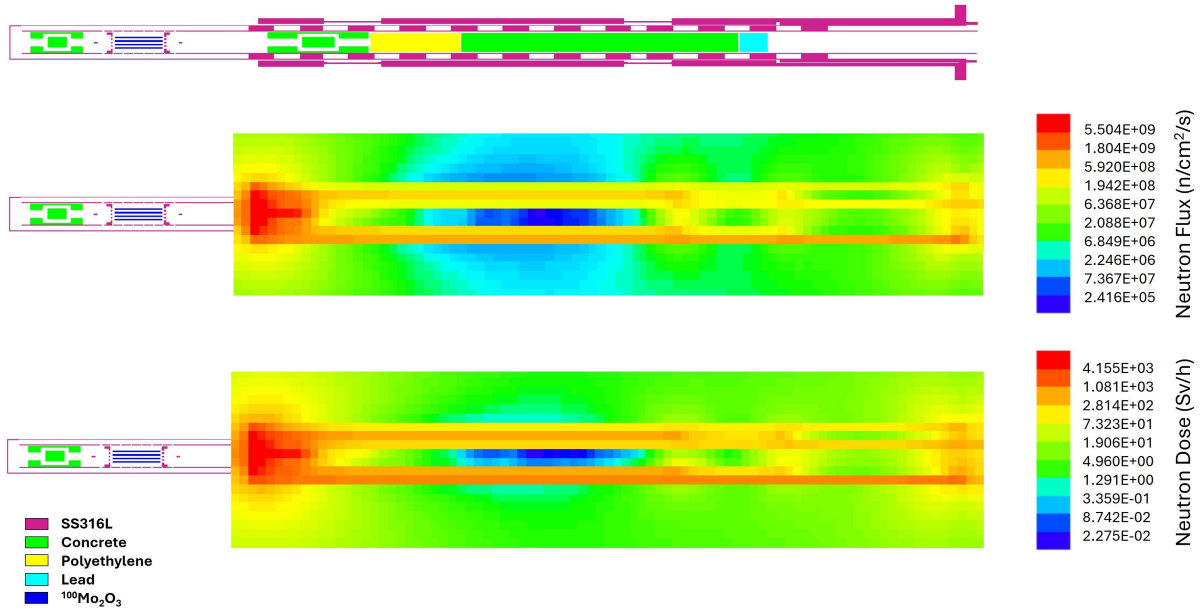

Figure III.33: Geometry of the pipeline with the additional plug inserted and simulation of neutron flux and dose rate around the RIPD.

3 Chapter conclusions

The future International Fusion Materials Irradiation Facility-DEMO Oriented Neutron Source will be a state-of-the-art technology, which will present a unique opportunity in the development of complementary applications, such as the production of radioisotopes for use in Nuclear Medicine.

This chapter has presented realistic studies for the radioisotope production as complementary application in IFMIF-DONES, making use of the two different particle types available. For the case of deuteron beams, it would be necessary to deflect a part of the initial beam into an experimental room and design a setup with cooling system capable of dissipating the high deposited energies. For the production of radionuclides with the residual neutrons inside the Test Cell, it would be necessary to assess a modification of the current design of the Test Cell to guarantee the weekly extraction of the irradiated samples.

The radioisotope studies have been developed in detail, working on the idea of production from different points of view. Firstly, it starts from an improvement in the quality of the nuclear data, increasing the precise and comprehensive physical knowledge of the production cross-sections, used to estimate yields in realistic thick targets accurately. Secondly, the production of these radioisotopes has been estimated following a full and detailed study of all by-products generated after irradiation, aimed at maximizing the isotopic purity, radionuclide purity and specific activity of the radioisotope of interest in the final product, to propose a production route similar to the established one based on nuclear reactors. Finally, from an industrial point of view, feasible mechanical and structural production systems have been studied for their efficient production within the IFMIF-DONES facility.

The results obtained are multiple. In the case of ^{165}Er, the yields and qualities of the final product achieved would allow its application in the clinic. In contrast, in the case of ^{177}Lu, clinical production such as nuclear reactor-based production routes would not be possible. However, the radiophysical qualities of the radioisotope no-carrier-added produced in two-steps would be valid for the development of preclinical research network around the IFMIF-DONES project.

On the other hand, neutron production is indeed efficient, as the ^{99}Mo production studies have been performed using only the first carrier plate of the four designed in the RIPD, leaving possibilities for large-scale production to ensure a statal supply or extending the study to new neutron-induced radioisotopes.

Chapter IV

^{177}Lu as Theranostic Radionuclide

Three fundamental processes can be identified in the preparation of a radiopharmaceutical:

- **Radionuclide:** also called radioactive compound, information vector or radiotracer. This can be obtained directly in nuclear reactors or cyclotrons, or indirectly by radionuclide generators.
- **Conjugation process:** occurs in the majority of radiopharmaceuticals and is the process of binding the vector molecule, which has a high affinity for the organ or tissue to be studied, to a specific bond with chemical properties compatible to the radionuclide.
- **Radiolabelling process:** is the process by which the conjugated vector molecule is bound to the radionuclide. The binding of the two compounds will be achieved by the chemical bond previously conjugated to the vector molecule.

The estimated quantities of ^{177}Lu produced at IFMIF-DONES from the two-step method described in Chapter III Subsection 1.3.4, would be suitable in terms of its quality for the synthesis of radiopharmaceuticals labelled with the theranostic radiotracer ^{177}Lu for the development of preclinical research of new molecular targets, enhancing one of the most selective strategies at cellular level, the Targeted Radionuclide Therapy (TRNT).

Moreover, in a translational perspective, a study of new molecular targets would open the possibility to apply a combination of two selective radiation therapy currently available: TRNT and Boron Neutron Capture Therapy (BNCT).

This chapter presents the preliminary study results of an experimental radiopharmaceutical used to perform preclinical research which aims to combine the two above strategies in xenograft mouse models bearing somatostatin transmembrane receptor (SSRT)-positive neuroendocrine lung tumours (NETs). This study was carried out in collaboration with the Unit of Medical Applications of Ionising Radiation of the Centre for Energy, Environmental and Technological Research (CIEMAT) in Madrid (Spain).

1 Chemical properties of ^{177}Lu

Lutetium (Lu) is a chemical element classified in the Periodic Table as rare-earth metal and the last member of the lanthanide series. In nature, lutetium exists in two isotopic forms, ^{175}Lu stable (97.41 % natural abundance) and ^{176}Lu long-lived β^--emitting radioactive isotope ($3.78{\cdot}10^{10}$ years of half-life and 2.51 % natural abundance) [11]. Besides these two natural isotopes, 56 artificial radioisotopes might be produced including 23 nuclear isomer with mass numbers ranging from 150 to 184. In particular, ^{177}Lu is currently considered as one of the most promising radioisotopes for nuclide therapy of cancer.

The lutetium atom is composed of 71 protons in the nucleus and 71 electrons distributed in different energy levels. The electrons in the higher, external energy levels are involved in its chemical reactivity. Electrons are arranged in the configuration $[\mathrm{Xe}]4f^{14}5d^{1}6s^{2}$, where the integers numbers indicate the different energy levels, the italic letters represent the type of energy level and the superscripts are the number of electrons occupying that level. Upon entering a chemical reaction, a lutetium atom usually loses its two outermost $6s$-electrons and the single $5d$-electron. This leaves 14 electrons in the f-level and results in a 3^+ charged ion.

The f-level with 14 electrons forms a completely filled electron shell, thus forming a closed outer core surrounding the ion. This almost spherical electron shell feels the strong attraction of the high nuclear charge (+71), which forces the electron to move at a speed close to the speed of light. According to the principles of relativity theory, an object moving faster increases its mass concomitantly, and therefore, the outer shell electrons of the Lu^{3+} ion (and, in general, of the entire lanthanide series) are more massive than in other series of the Periodic Table [118]. The increase in mass leads to a significant decrease in electron energy and, consequently, to a greater stabilisation of the outer f-electrons, which are less likely to form chemical bonds with other elements [119].

On the other hand, as a consequence of the increased mass, lutetium has the shortest ionic atomic radius of the lanthanide series. A small radius combined with a 3^+ ionic charge generates a strong electric field that will dominate the Lu^{3+} chemistry. It will form ligands with hard donor atoms, such as negatively charged oxygen (Lu_2O_3), halogenides (LuF_3, $LuCl_3$, $LuBr_3$ or LuI_3) or more complex molecular arrangements. A hard donor is briefly defined as a poorly polarisable coordination atom [120].

In summary, the Lu^{3+} ion allows the formation of robust aggregates with specific ligands that have sufficient stability in aqueous solution, which is the necessary solvent for the preparation of radiopharmaceuticals.

2 Bifunctional chelator (BFC) for ^{177}Lu

Assuming the ionic model discussed for the Lu^{3+} ion, its behaviour can be predicted in aqueous solution. The high electric field of this ion will strongly attract dipolar water molecules, which surround it on the oxygen side. In turn, the high electrostatic attraction might cause one proton to be removed from a water molecule, thus giving rise to a hydroxyl ion OH^-. When there are three OH^- groups around the ion, the resulting neutral aggregate $Lu(OH)_3$ can precipitate as a tiny solid powder, which in water usually takes the form of a colloidal particle. At pH > 6, Lu^{3+} forms insoluble $Lu(OH)_3$. Therefore, the optimum pH for radiolabelling is between 5 and 6 [121]. This is the most common drawback affecting the preparation of ^{177}Lu radiopharmaceuticals.

To avoid this point, the usual strategy is to design a suitable bifunctional chelating agent (BFC) capable of binding the radiometal ion more strongly than the OH^- groups. A bifunctional ligand consists of two parts, as shown in Figure IV.1. A chemical binding site for the radiometal and a pharmacophore that confers biological specificity to the resulting non-radiative compound. Typically, chelators are derivatized with reactive functional groups that can be covalently coupled to biological target vectors (e.g. drugs, peptides, nanoparticles, antibodies, nanobodies).

Identifying the most suitable chelating binding agent for Lu^{3+} ions by seeking to establish a strong ionic interaction with the metal ion and, simultaneously, enveloping it within a cage of coordinating atoms is one of the first steps to be taken. Polydentate ligands, such as polycarboxylates added to a carbon or nitrogen backbone, as DOTA and DTPA illustrated in Figure IV.2, are widely used as chelating systems for ^{177}Lu radiopharmaceuticals [122].

2.1 Thermodynamic and kinetic considerations

The primary considerations for BFCs are the high thermodynamic stability and kinetic inertness of the metal chelate to keep it intact under physiological conditions. The break-

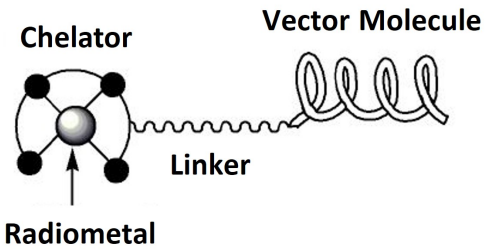

Figure IV.1: Schematic drawing of the structure of a bifunctional chelator (BFC) [122].

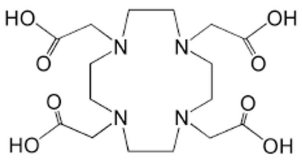

1,4,7,10-tetraanzacyclodecane-1,4,7,10-tetraacetic acid
(DOTA)

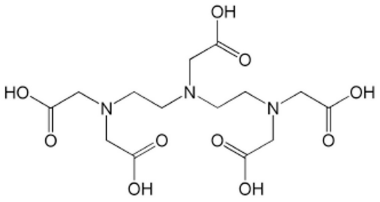

Diethylenetriaminepentaacedic acid
(DTPA)

Figure IV.2: Schematic structure of DOTA and DTPA, BFCs for coordination to ^{177}Lu [122].

down of the metal chelate produces free metal ions, which can deposit in the body and cause toxicity [123] .

The presence of negatively charged oxygen atoms of the polycarboxylate ligands create strong electrostatic interactions with the Lu^{3+} ions. The strength of this interaction should be sufficiently high to compete with the generated OH^- groups. This will be a key factor as it contributes to decrease the enthalpy of formation, which in turn, leads to a decrease in the free energy of the reaction (at constant volume and temperature, a negative free energy indicates a thermodynamically favoured process, $\Delta G=\Delta H-T\cdot\Delta S$). Moreover, the backbone structure of the ligand containing the polycarboxylate groups helps to achieve some preordering of the ligand by bringing all the negatively charged coordination atoms closer to the positively charged ion. This ordering effect causes a decrease of entropy, which has an unfavorable impact on the free energy of the reaction. However, this decrease in entropy is counterbalanced by the removal of water molecules from the hydration cage surrounding the positive ions of the structure.

A favourable thermodynamic situation is empirically reflected in the values of the stability constants of the Lu^{3+} complexes, being the highest for the DOTA complexes [122]. However, high thermodynamic stability is not the only requirement because it reflects the direction, not the rate, of the dissociation reaction. The solution stability of a radiopharmaceutical in the blood is predominantly determined by the kinetic inertness of the metal chelate [123].

The term kinetic inertness refers to the rate of dissociation of the radionuclide from a metal chelate [123]. It is important to note that the choice of the kinetic characteristics of the metal chelate of a BFC also depends on the pharmacokinetics of the vector molecule. For example, antibodies have long biological half-lives in the blood circulation and at the tumour site. Since they are often metabolised in the liver, the radiometallic chelate

must have extremely high thermodynamic stability and kinetic inertness to withstand competition from metal ions and native chelators, such as transferrin, in the blood circulation, and tolerate hepatobiliary metabolism [123].

To sum up, the main requirement when choosing a suitable BFC is to minimise the *in vivo* dissociation of the radionuclide from the chelate and to form a radioconjugate with sufficient stability in aqueous solution and under biological conditions. Polycarboxylate ligands remain the most efficient choice for the development of BFCs radiolabelled with ^{177}Lu as radiotracer.

2.2 DOTA: Structure of a common BFC

The ligand 1,4,7,10-tetraazacyclododecane- 1,4,7,10-tetraacetic acid (DOTA) is one of the most important chelators for radiometal chemistry [124] with a significant impact on the field of diagnostic imaging and therapy [125]. It is widely employed for the preparation of metallic radiopharmaceuticals, including ^{111}In, ^{90}Y, ^{68}Ga and lanthanides such as ^{177}Lu or ^{166}Ho, among others [126]. The backbone of this ligand is an octadentate coordination that binds to the Lu^{3+} ion via the four nitrogen atoms of the macrocyclic ring and the four deprotonated oxygen atoms of the pendant carboxylic groups as shown in Figure IV.3.

For the synthesis of BFCs, some common bifunctional DOTA derivatives use one of the carboxylic acid arms for the conjugation of the vector molecule required for specific targeting properties to the final radiopharmaceutical. As a result, these bifunctional DOTA derivatives retain their maximum potential denticity (octadentate), as well as the same thermodynamic stability and kinetic inertness of the primitive DOTA.

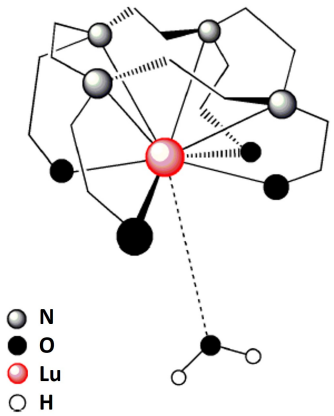

Figure IV.3: Schematic structure of the arrangement of coordinating atoms of DOTA bound to the Lu^{3+} ion as determined by X-ray crystallography [122].

3 ^{177}Lu radiolabelled compounds as therapeutic and imaging agents

^{177}Lu is considered a promising theranostic radioisotope due to its optimal physical characteristics for targeted radionuclide therapy and diagnostic purposes. Its maximum energy β^--emission (100 %) above 496.8 keV with a tissue penetration of up to 1.6 mm, making it suitable for therapeutic uses, while its emission of 112.95 keV (6.23 %) and 208.37 keV (10.41 %) gamma photons [31] makes it detectable with SPECT imaging techniques. Its half-life (6.65 days) is long enough to be radiolabelled with molecular vectors of both short and long biological half-lives, moreover, its physical half-life allows it to be distributed to research centres or hospitals in remote regions.

The use of ^{177}Lu as a theranostic radioisotope in the clinic is already applied with the licensed radiopharmaceuticals Lutatera and Pluvicto, to treat neuroendocrine tumors with DOTA-TATE as a vector molecule [32,127] and in clinical trials for the treatment of metastatic castration-resistant prostate cancer using PSMA [33], respectively. Recently, ^{177}Lu-Anti HER2 appears to be a potential theranostic agent for breast cancer [128]. Moreover, the chemical properties of ^{177}Lu allow it to bind to antibodies opening new possibilities in the development of new radiopharmaceuticals [129].

To date, ^{177}Lu has always been presented as a theranostic agent within the therapies known as Targeted Radionuclide Therapy. TRNT is a powerful cancer treatment strategy that uses high-affinity tumour-targeted vectors, such as peptides or antibodies, to deliver particle-emitting radionuclides to cancer cells, where particles deposit a lethal payload of ionising radiation. TRNT is a highly potent, non-invasive therapy that minimises damage to non-tumorous tissues.

Another of the most promising strategies for the treatment of malignant tumours resistant to conventional methods is Boron Neutron Capture Therapy [130]. BNCT is a radiotherapeutic technique based on the interaction between a low energy neutron beam and boron compounds selectively accumulating in the tumour cells, previously administered to the patient. When neutrons interact with the ^{10}B atoms, a nuclear reaction is generated that releases highly energetic and short-range α-particles and lithium nuclei, selectively destroying tumour cells without damaging surrounding healthy tissues.

This section presents the technique of radiolabelling a borated compound with ^{177}Lu as a radiotracer to preliminarily evaluate the novel objective of combining, TRNT and BNCT, on a tumour model representing clinical cases where conventional treatments are insufficient. To achieve this objective, a peptide radiolabelled with ^{177}Lu will be evaluated as a radiotracer to perform the functions of early diagnosis, staging and SPECT imaging during treatment and as a therapeutic agent by β^--particle and, in the case of optimal and translational results, for α-particle therapy, by external irradiation with an epithermal neutron beam irradiating over the target region.

3.1 [^{10}B]B-DOTA-TATE radiolabelling with ^{177}Lu

Typically, peptides are used as targeting agents or vector molecules in the radiolabelling of lutetium, as they can be chemically modified with cytotoxic payloads while retaining their pharmacokinetic properties and specific binding to target proteins on the surface of target cells. In addition, they have unique features such as metabolic stability, resistance to structural changes, low toxicity, high selectivity, rapid elimination, non-immunogenicity, high tumor penetration, ease of synthesis and different possibilities of conjugation with therapeutic and imaging agents for targeted delivery [131].

Octreotate (TATE) is a peptide analogue with affinity for SSTR. Somatostatin (SS) is a polypeptide hormone that is widely distributed in neural and endocrine tissue. It exists in two biologically active forms, somatostatin-14 and somatostatin-28, the N-terminal extended version, which is produced by different cell types throughout the body. The physiological activities of somatostatin are mediated by high-affinity interactions with a family of G-protein-coupled receptors. Five different somatostatin receptor subtypes (SSTR1, SSTR2, SSTR3, SSTR4, SSTR5) have been cloned [132–134]. They are distinguished by their pharmacological specificity for different analogues, tissue distribution, regulation and intracellular signalling pathways. Inhibition of hormone secretion is thought to be mediated mainly through SSTR2 and SSTR5.

The peptide octreotate interacts preferentially with cell surface SSTR2 that are present in more than 80 % of neuroendocrine tumours (NETs). NETs are a group of epithelial neoplasms arising from neuroendocrine cells. Although they can originate in any location, the most common are gastroenteropancreatic (66 %) and lung (31 %) tumours, being less frequent in skin, adrenal glands, thyroid and urogenital tract. These tumours are complex due to the heterogeneity of their clinical presentation. However, despite their heterogeneity in tissue, NETs share the expression of neuroendocrine immunohistochemical markers that facilitate the secretion of bioactive peptides such as CgA, serotonin, gastrin and insulin. The release of these substances is regulated by SS [135].

In view of the chemistry of Lu^{3+}, polycarboxyl ligands present the most effective option for the development of BFCs suitable for binding ^{177}Lu and forming a radiolabel with sufficient stability in aqueous solution and under biological conditions to avoid dissociation in vivo. DOTA is a chelating agent that exhibit greater kinetic and in vivo thermodynamic stabilities when radiolabelled with ^{177}Lu compared to other metal complexes of chelating agent such as DTPA [136, 137].

Octreotate conjugated with [^{10}B]B-DOTA was obtained from the company LabsinLove S.L. This Spanish company develops studies of different borated vector molecules with potential application in BNCT. One of the most interesting is [^{10}B]B-DOTA-TATE, shown in Figure IV.4. This compound is under study and confidentiality, thus, some of the informa- tion has been omitted, representing only a schematic diagram of its structure.

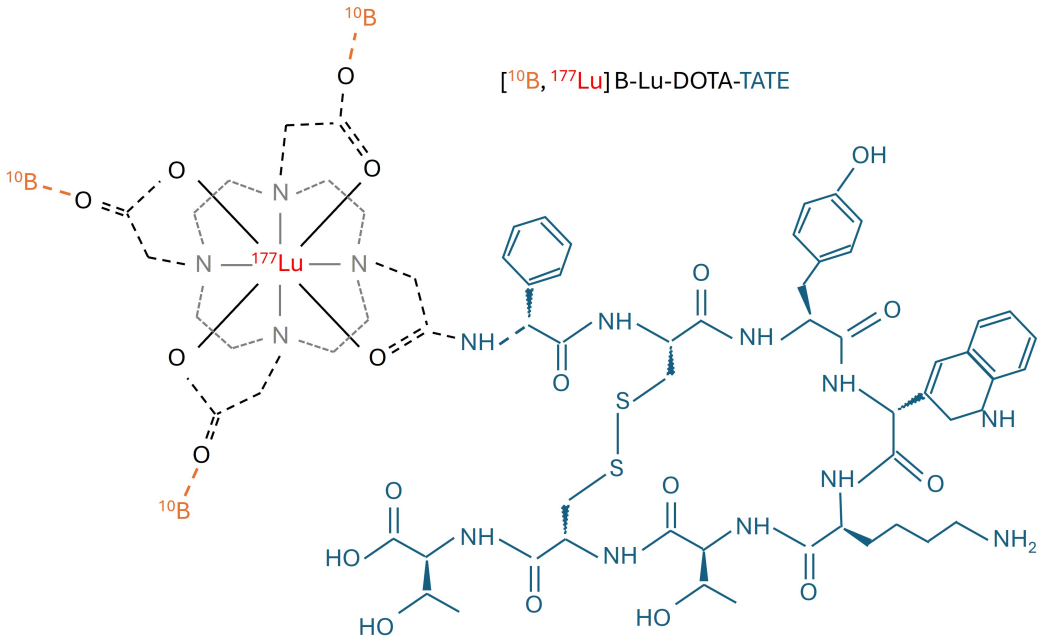

Figure IV.4: Schematic representation of [^{10}B,^{177}Lu]B-Lu-DOTA-TATE structure. Some links have been omitted.

For the radiolabelling process, 500 MBq of $^{177}LuCl_3$ (in 0.04 M HCl) no-carrier-added with high specific activity was obtained from ITM Medical Isotopes GmbH. $^{177}LuCl_3$ was diluted with HCl (0.04 M) to a total volume of 500 μl (500 MBq) and then added to a reaction vial containing 20 μl (1 nmol/μl) of [^{10}B]B-DOTA-TATE conjugated solution and 110 μl of 0.5 M HEPES[1] buffer. The final pH of the solution was around 3.5 – 4.0, remembering that lutetium precipitates above pH 6.0 [121]. The reaction vial was incubated at 90 ^{o}C for 1.5 h and 550 rpm using a Thermomixer (Eppendorf, Hamburg, Germany).

After radiolabelling, the radiopharmaceutical purification step was carried out by eluting the mixture through a C-18 hydrophobicity solid phase extraction cartridge (Sep-Pak C-18 Plus Light Cartridge, Waters) previously conditioned with 2 ml ethanol and equilibrated with 2 ml of water. For the purification process of the labelled peptide, the reaction mixture was passed through the C-18 cartridge. Subsequently, 2 ml of water was passed to remove the free, unreacted ^{177}Lu from the mixture and therefore not bound to [^{10}B]B-DOTA-TATE. Finally, another 2 ml of ethanol was added to remove the radiolabelled peptide and to exchanged the mobile phase of the buffer mixture to ethanol.

Ethanol as a medium is toxic to cells, therefore it was necessary to evaporate it by

[1]HEPES, also known as 2-[4-[4-(2-hydroxyethyl)piperazine-1-yl]ethanesulfonic acid or 4-(2-hydroxyethyl)piperazine-1-ethanesulfonic acid or N-[2-hydroxyethyl]piperazine-N'-[2-ethanesulfonic acid], is an organic soluble compound used as an effective buffer to maintain physiological pH levels. HEPES has negligible metal ion binding capacity and is membrane impermeable.

drying it with N_2. Finally, 122 MBq of [^{10}B,^{177}Lu]B-Lu-DOTA-TATE was obtained in 300 μl of physiological saline solution after 3 h from the start of the radiolabelling process. The efficiency of the radiolabelling process corrected for decay time was 25 % referred to the final activity present in the 300 μl physiological saline solution with respect to the total initial activity.

The efficiency of the radiolabelling process depends on several factors, but mainly on the amount of octreotate to be radiolabelled. Compared to previous studies, the efficiency obtained is lower than the estimated efficiency of ^{177}Lu radiolabelling processes with comparable mass of DOTA-TATE, in the order of 45 % [138]. The reason for the lower yields are presumably due to the presence of boron in the molecule, which would induce steric hindrance. Steric effects arise from the spatial arrangement of atoms. Boron clusters, especially if they are of the carborane or icosahedral type, are bulky and can block the access of Lu^{3+} ion to the chelating site of DOTA.

3.2 Quality control - HPLC

An aliquot of [^{10}B,^{177}Lu]B-Lu-DOTA-TATE was taken to analyse the radiochemical purity (RQP) defined as the percentage fraction of radioactivity of the radionuclide present in the radiopharmaceutical preparation bound to the desired vector molecule in relation to the total radioactivity detected. RQP of the radiolabelled conjugated was determined via High Performance Liquid Chromatography (HPLC) in a Jasco HPLC system equipped with a photodiode array UV-detector MD-4015 (Jasco, Easton, MD) and coupled to a radioactivity monitor (see Figure IV.5). HPLC was performed using a reversed phase column, Jupiter Proteus 90 $\AA$ (Phenomenex), dimensions 5 μm, 250 $\times$ 4.6 mm, as statio-

Figure IV.5: HPLC with UV-detector MD-4015 and radioactivity monitor.

nary phase. As mobile phase, a mixture of 90 % water + 10 % acetonitrile (phase A) and 10 % water + 90 % acetonitrile (phase B), both with 0.1 % aqueous trifluoroacetic acid was prepared. The gradient applied to balance the column with a flow rate 1 ml/min is: $0-5$ min 100 % A; $5-12$ min linear gradient to $0-100$ % B; $12-15$ min 100 % B; $15-17$ min linear gradient to $100-0$ % B; $17-20$ min: 100 % A.

Figure IV.6 shows the radioactivity of the labelled peptide in counts per second (CPS) and the absorbance intensity of the unlabelled peptide as they pass through a reversed-phase column, respectively. Certain molecules are able to emit fluorescence naturally, so if they are illuminated with UV light at the exit of the column, they might absorb the energy and reemit it at a certain wavelength. For the case of peptides, it is in the 220 nm range, as seen in Figure IV.6. The retention time of [^{10}B]B-DOTA-TATE is approximately 11.63 min, corresponds to the retention time of radiopharmaceutical [^{10}B,^{177}Lu]B-Lu-DOTA-TATE since the hydrophobicity of the two compounds is the same.

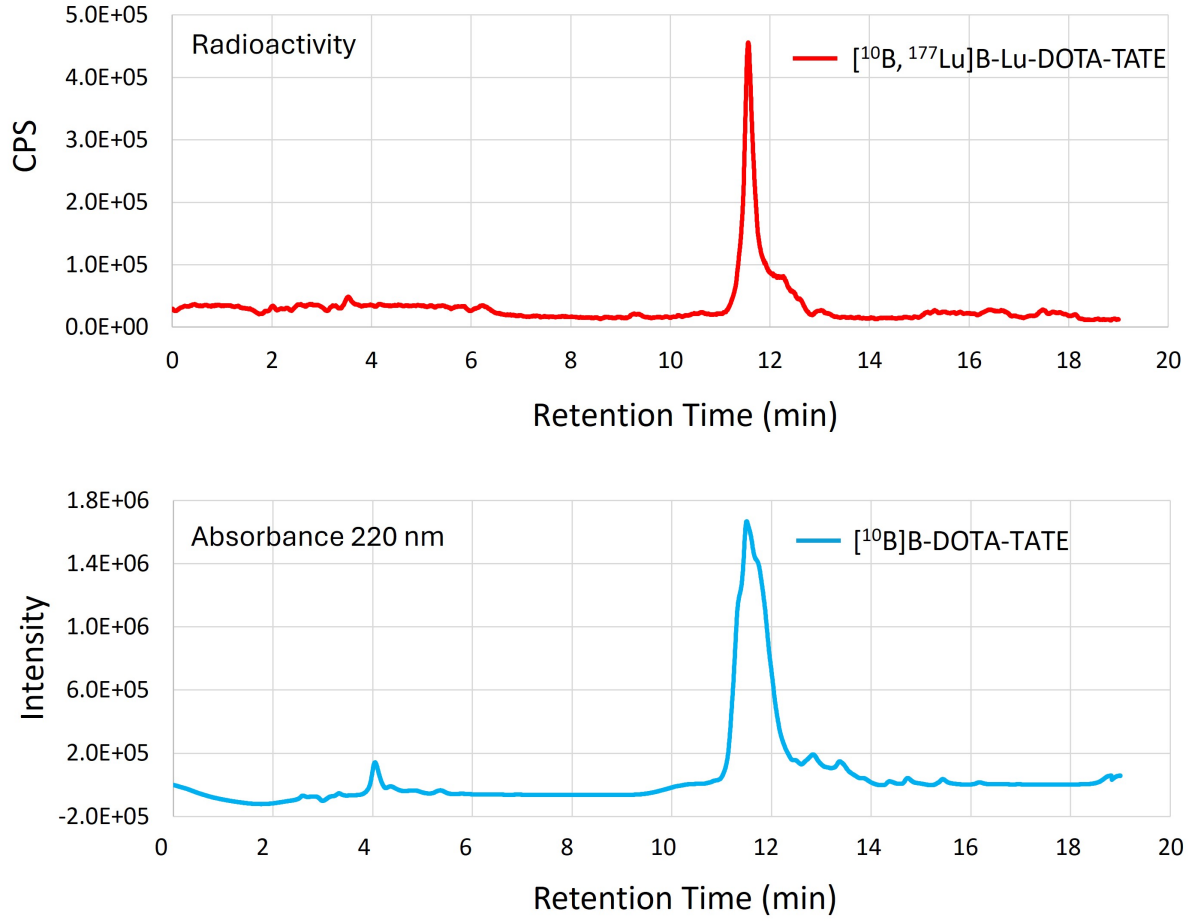

Figure IV.6: [^{10}B,^{177}Lu]B-Lu-DOTA-TATE HPLC profile. The peak at 11.63 min is correlated to ^{177}Lu-radiolabelled peptide. Y-axis represents the count per second detected on the radioactivity monitor for the first case and the intensity of the peptide absorbance at 220 nm wavelength.

[^{10}B,^{177}Lu]B-Lu-DOTA-TATE was prepared with high radiochemical purity, RQP > 95 %, which is determined by HPLC control by the ratio of the area under the peak in CPS to the total area of the HPLC profile. No significant traces of unreacted ^{177}Lu are observed in the final product. If this were the case, a peak prior to 11.63 minutes would be observed in the HPLC radioactivity control and would be correlated with free ^{177}Lu. Hydrophilic, i.e. polar, compounds have less interaction with the stationary phase and are eluted faster with shorter retention time in a reversed-phase column. Finally, the HPLC absorbance results show no significant presence of any other chemical substances.

4 *Ex vivo* studies: [^{10}B,^{177}Lu]B-Lu-DOTA-TATE

Among the different histological subtypes of NET lung cancer, non-small cell lung cancer (NSCLC) is the most frequent and lethal, responsible for $80 - 85$ % of deaths [139]. The non-small cell lung carcinoma cell line NCI-H727 is one of the worst prognostic neuroendocrine tumours, for which conventional therapies are proving insufficient [140].

In the following subsections, the potential of the SSTR2- overexpressing radiopeptide, [^{10}B,^{177}Lu]B-Lu-DOTA-TATE will be studied as a radiotracer in an orthotopic mouse model of NCI-H727 tumour-bearing mice as a model of non-small cell lung cancer.

Biodistribution studies are performed at different post-injection times, 10 minutes, 1, 2, 4 and 24 hours (N=3). The mouse biodistribution data is used to generate time-activity curves, which have been integrated to estimate absorbed doses using a mouse MOBY phantom. Dosimetric assessment of a radiopharmaceutical is essential to ensure its safety and efficacy. The assessment of absorbed dose in small animals is the first step in the development of new radiopharmaceuticals. Then, these data could be used to extrapolate absorbed doses to humans. On the other hand, therapy studies and tumour response results are performed by comparing a group treated with the experimental radiopharmaceutical with a control group, treated only with saline solution (N=3). This animal study was approved by the ethical Committee of CIEMAT (protocol code PROEX 094/15) adhered to the Agreement on Transparency in Animal Experimentation, promoted by the Confederation of Spanish Scientific Societies (COSCE), with the collaboration of European Association for Animal Research (EARA) [141].

4.1 Cell lines and animal model

The non-small cell lung carcinoma cell line NCI-H727 corresponds to a neutroendocrine lung cell line of epithelial morphology that was isolated from the lungs of a 65-year-old white woman with a very aggressive non-small cell carcinoid tumour lacking effective diagnostic and therapeutic options.

The cell line was supplied by the CIC cell bank of the University of Granada. The base medium for this cell line is ATCC-formulated RPMI-1640 Medium. To make the complete growth medium, fetal bovine serum (ATCC 30-2020) to a final concentration of 10 % is needed. The culture is incubated at 37°C in air atmosphere with 5 % CO_2.

Lung cancer subcutaneous xenograft model was generated by injecting $6{\cdot}10^6$ NCI-H727 cells in 100 μl of a mix of PBS[2] with Matrigel[3] (1:1) into the lower right flank of $5 - 6$

[2]Phosphate-buffered saline (PBS) is a buffer solution (pH 7.4) of water-based salt solution containing disodium hydrogen phosphate, sodium chloride and, in some formulations, potassium chloride and potassium dihydrogen phosphate. The buffer helps to maintain a constant pH and has many uses because it is isotonic and non-toxic to most cells. These uses include substance dilution and cell container rinsing.

[3]Solubilized basement membrane preparation extracted from the Engelbreth-Holm-Swarm (EHS) mouse sarcoma, a tumor rich in extracellular matrix proteins. It is ideal for use with in vitro cell growth cultures of a broad range of cell types, including both primary and stem cell applications.

week-old-female athymic Nude-Foxn1^{nu} immunodeficient mice (ENVIGO RMS SPAIN, Barcelona, Spain). Cells were allowed to engraft and tumours were measured twice per week using a calliper. In addition, mice were monitored by measuring body weights. The following equation was used to calculate the tumour volume (TV),

$$TV = \frac{3}{4}\pi \times \frac{D}{2} \times \left(\frac{d}{2}\right)^2 \tag{IV.1}$$

where D and d are the largest and smallest tumour diameters in mm, respectively.

The end-point criterion for animals is considered when the tumour mass reached a maximum size of 1500 mm^3, tumour ulceration was observed, or mice were symptomatic from their tumours, which included signs of lethargy, poor grooming, weight loss ($\geq$ 15 %) and hunching.

4.2 Biodistribution studies

Fifteen female athymic Nude-Foxn1^{nu} immunodeficient mice with non-small cell lung tumour, weighting $20 - 25$ g were divided into 5 groups of 3 mice per group. When tumours reached a mean volume of $50 - 100$ mm^3, 0.57 ± 0.03 MBq in 200 pmol of [^{10}B,^{177}Lu]B-Lu-DOTA-TATE was injected per mouse. Biodistribution studies were carried out at 10 minutes, 1, 2, 4 and 24 hours post-administration. All injections were 120 μl and injected intravenously in a tail vein.

After different time intervals, mice were euthanised by cervical dislocation under anaesthesia (isofluorane in O_2) and blood collection was performed immediately through cardiac puncture. The collected blood samples are centrifuged at 3000 rpm for 10 minutes obtain plasma. Organs and tissues (heart, lung, liver, stomach, small intestine, large intestine, pancreas, spleen, kidneys, fat, muscle, brain, bone, bone marrow and tumour) were excised, washed and wet-weighted for radioactivity measurements using a 2470 Wizard γ-counter (PerkinElmer, Waltam, MA, USA) (see Figure IV.7). An activity standard sample of the injected dose for ^{177}Lu (113 keV and 208 keV γ-photons) was used to calibrate the detector in efficiency by measuring different volume samples, as shown in Figure IV.8. The energy calibration was pre-logged in the detector by default.

Any uptake of the compound radiolabelling is considered relevant and subject to study. The data are background- and decay-corrected. Statistical analysis is performed and the results are presented as percentage of injected dose per gram of organ as % ID/g $\pm$ SEM (N=3). Table IV.1 presents the biodistribution results of 200 pmol [^{10}B,^{177}Lu]B-Lu-DOTA-TATE at 10 minutes, 1, 2, 4, 24 hours. The results of the biodistribution study showed that the radiolabelled peptide is predominantly accumulated in SSTR2-expressing tumour and organs such as pancreas, stomach, small intestine, large intestine and lungs, as well as, in the kidneys, the usual way of peptide excretion. After 24 hours, a generalized clearance of the activity in organs and tissues is observed, however the uptake in the

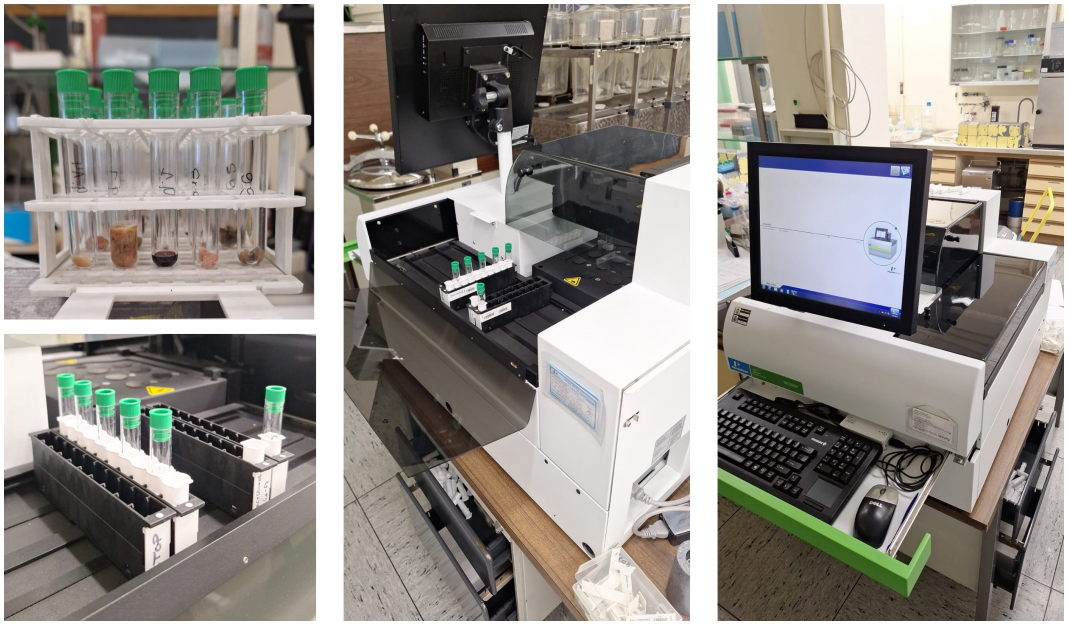

Figure IV.7: Organs and tissues excised, washed and wet-weighted for radioactivity measurements using a 2470 Wizard γ-counter.

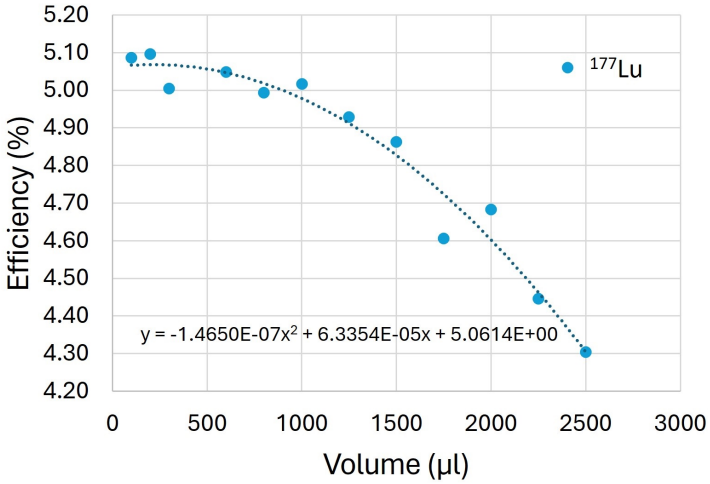

Figure IV.8: Efficiency calibration performed at different volumes of the ^{177}Lu γ-photons for the Wizard γ-counter and semi-empirical polynomial fit of degree 2.

tumour is sustained, obtaining the maximum uptake in the tumour-blood ratio. The annotated biodistribution is shown in Figure IV.9.

The preliminary biodistribution results of 200 pmol [^{10}B,^{177}Lu]B-Lu-DOTA-TATE presented in Table IV.1 can be compared with a previous study of [^{177}Lu]Lu-DOTA-TATE in nude mice bearing HEK-hsst2 tumor xenografts by Nicolas *et al.* [142]. This study shows the biodistribution of [^{177}Lu]Lu-DOTA-TATE at different times as a function of the peptide mass injected. Comparing the same amount, 200 pmol of [^{177}Lu]Lu-DOTA-TATE,

Organ/Tissue	10 min	1 h	2 h	4 h	24 h
Blood	14.02 ± 0.36	1.03 ± 0.14	0.34 ± 0.03	0.14 ± 0.01	0.026 ± 0.002
Plasma	25.54 ± 0.80	1.83 ± 0.30	0.61 ± 0.05	0.26 ± 0.02	0.043 ± 0.003
Heart	6.70 ± 0.80	1.83 ± 0.30	0.74 ± 0.17	0.36 ± 0.02	0.18 ± 0.03
Lung	13.50 ± 0.15	18.15 ± 2.87	15.16 ± 4.18	11.10 ± 3.72	5.66 ± 2.13
Liver	5.91 ± 1.15	1.23 ± 0.16	1.52 ± 0.28	1.05 ± 0.04	0.57 ± 0.11
Stomach	12.09 ± 0.57	5.87 ± 1.05	5.79 ± 0.69	5.00 ± 0.31	3.42 ± 0.34
Small intestine	8.59 ± 1.79	5.32 ± 0.27	10.24 ± 0.82	3.01 ± 0.56	1.18 ± 0.08
Large intestine	8.17 ± 0.89	5.08 ± 0.59	6.62 ± 0.69	22.50 ± 1.65	3.57 ± 0.31
Pancreas	64.41 ± 6.14	52.87 ± 5.03	36.03 ± 3.41	15.71 ± 0.62	6.48 ± 0.97
Spleen	5.36 ± 0.47	2.79 ± 0.06	5.24 ± 1.51	1.69 ± 0.16	0.90 ± 0.09
Kidney	81.04 ± 14.38	22.70 ± 2.16	23.60 ± 0.52	20.29 ± 2.24	10.47 ± 1.11
Fat	6.80 ± 0.92	2.36 ± 0.65	0.48 ± 0.15	2.05 ± 1.53	0.73 ± 0.26
Muscle	4.22 ± 0.98	0.56 ± 0.19	1.17 ± 0.82	0.09 ± 0.02	0.05 ± 0.02
Brain	0.64 ± 0.07	0.08 ± 0.01	0.058 ± 0.004	0.06 ± 0.01	0.04 ± 0.01
Bone	7.02 ± 0.51	2.06 ± 0.09	1.89 ± 0.09	1.74 ± 0.18	1.46 ± 0.17
Bone Marrow	3.72 ± 0.19	1.71 ± 0.16	1.08 ± 0.3	0.92 ± 0.10	0.60 ± 0.10
Tumour	8.52 ± 2.33	4.00 ± 0.34	3.85 ± 0.26	2.81 ± 0.61	2.39 ± 0.50

Table IV.1: Biodistribution results (% ID/g ± SEM (N=3)) at different times after injection of 200 pmol [^{10}B,^{177}Lu]B-Lu-DOTA-TATE in nude mice bearing NCI-H727 tumour xenografts.

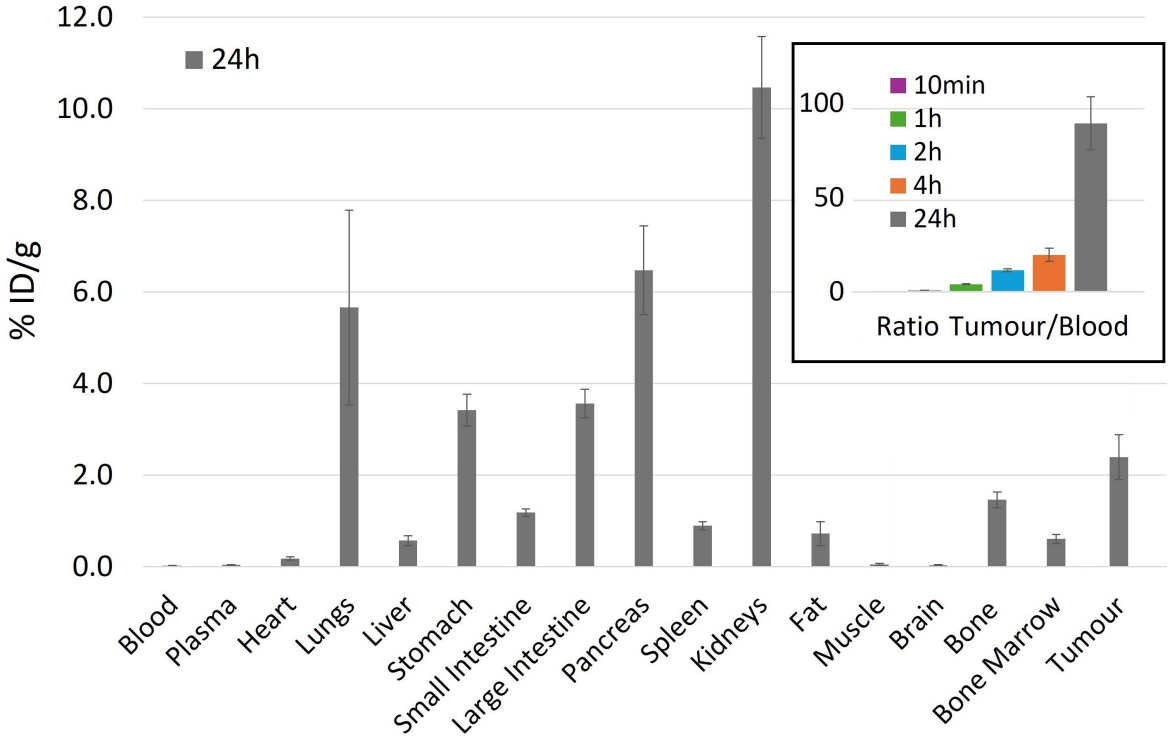

Figure IV.9: Biodistribution results of 200 pmol [^{10}B,^{177}Lu]B-Lu-DOTA-TATE at 24 hours after injection in NCI-H727 tumour-bearing mice.

the biodistribution profile is compatible with our results in terms of high uptake in organs expressing SSTR2 receptors, such as lungs, pancreas, stomach and intestines.

However, Nicolas *et al.* [142] presents a relevant study of the "mass effect" to reduce uptake in SSTR2 receptors, improving tumour-to-normal tissue ratios. To achieve this, an excess of unlabelled DOTA-TATE (20 nmol) is administered prior to the injection of [^{177}Lu]Lu-DOTA-TATE. The goal is to suppress radiotracer uptake in all SSTR2-expressing organs and tissues, thereby increasing the tumour-to-background ratio. Therefore, this mass effect on the saturation of organs SSTR2-expressing is a technique to be study more in detail to improve the pharmacokinetics.

4.2.1 Boron concentration estimations

Based on the biodistribution results of the experimental radiopharmaceutical, it is possible to assess an estimation of the amount of boron present in both the tumour and the organs exhibiting uptake. Each molecule of DOTA-TATE contains 54 atoms of ^{10}B and the molecular mass of the compound [^{10}B]B-DOTA-TATE is 2807.49 Da. The mass quantity injected per mouse is 200 pmol of [^{10}B,^{177}Lu]B-Lu-DOTA-TATE.

The boron concentration required to consider translational research of this experimental radiopharmaceutical to BNCT would be one that provides at least a tumour-to-normal tissue boron concentration ratio greater than 3:1, as well as, a significant amount of ^{10}B mass ppm in the tumour. Table IV.2 shows the ^{10}B tumour-to-normal tissue concentration ratios and the absolute values.

Tumour-to-normal tissue	Ratio	^{10}B (ppm)
Blood	92:1	$3.0{\cdot}10^{-5}$
Plasma	55:1	$5.0{\cdot}10^{-5}$
Heart	13:1	$2.1{\cdot}10^{-4}$
Lungs	2:5	$6.6{\cdot}10^{-3}$
Liver	4:1	$6.7{\cdot}10^{-4}$
Stomach	2:3	$4.0{\cdot}10^{-3}$
Small Intestine	2:1	$1.4{\cdot}10^{-3}$
Large Intestine	2:3	$4.2{\cdot}10^{-3}$
Pancreas	1:3	$7.6{\cdot}10^{-3}$
Spleen	3:1	$1.1{\cdot}10^{-3}$
Kidneys	1:5	$1.22{\cdot}10^{-2}$
Fat	3:1	$8.5{\cdot}10^{-4}$
Muscle	48:1	$5.8{\cdot}10^{-5}$
Brain	60:1	$4.7{\cdot}10^{-5}$
Bone	5:3	$1.7{\cdot}10^{-3}$
Bone Marrow	4:1	$7.08{\cdot}10^{-4}$
Tumour	1:1	$2.8{\cdot}10^{-3}$

Table IV.2: Assessment of ^{10}B uptake in tumour, organs and tissues of interest.

The minimum 3:1 tumour-to-normal tissue boron concentration ratio is not achieved in SSTR2-expressing organs, where compound uptake is higher. However, considering the mass effect proposed by Nicolas *et al.* [142], these preliminary results may change significantly, suggesting that there is still potential to improve the technique.

On the other hand, the boron concentration (in ppm) in different tissues and tumour is directly related to the administered mass of the borated compound. In this study, the amount given to mice was equivalent to 200 pmol of [^{10}B,^{177}Lu]B-Lu-DOTA-TATE. To reach a concentration of at least 20 ppm in tumours, it would be necessary to administer around 1.4 μmol of the borated compound in humans. This value corresponds to 4 mg of [^{10}B,^{177}Lu]B-Lu-DOTA-TATE, which is still well below the typical administered amounts of $170-900$ mg/kg of boronophenylalanine (BPA), a commonly used radiopharmaceutical in BNCT [143, 144]. This suggests that there is potential to increase the administered amount in future applications.

4.3 Dosimetry studies

The dosimetry evaluation of a radiopharmaceutical is essential to ensure its safety and efficacy, especially in the context of Nuclear Medicine and preclinical targeted therapies. Small animal absorbed dose assessment is a preponderant step when it comes to developing new radiopharmaceuticals or establishing a relationship between absorbed dose and biological effects.

The process consists of estimating the amount of radiation absorbed by the organs and tissues of the body post-radiopharmaceutical administration. The Absorbed Dose (D) is defined as the mean energy imparted (or expectation value of the energy imparted) ($\bar{\varepsilon}$) per unit mass to an infinitesimal volume [16]. In the International System the absorbed dose unit is J/kg, known as Gray [Gy] is defined as,

$$D = \frac{1}{\rho} \lim_{V \to 0} \frac{\bar{\varepsilon}}{V} \tag{IV.2}$$

where ρ is the density of the medium in volume V.

The absorbed dose is the fundamental quantity on which current radiation protection recommendations are based, but it is not sufficient to quantify the real risk, as the LET of the incident particle must be taken into consideration. For this reason, the quantity of Equivalent Dose (H) is defined to consider the biological effectiveness of the different types of ionising radiation (photons, electrons, neutrons, heavy particles, etc).

The equivalent dose in an organ or tissue due to the radiation expressed in units of J/kg (IS), known as Sievert [Sv] is defined as:

$$H_T = \sum_R w_R \cdot D_{T,R} \tag{IV.3}$$

where, $D_{T,R}$ is the average absorbed dose for radiation, R, in an organ or tissue, T, and

Radiation Type	Energy	w_R
Photons	-	1
Electrons Positrons Muons	-	1
Protons Charged-pions	-	2
Alpha particles Fission fragments Heavy ions	-	20
Neutrons	< 1 MeV $1 - 50$ MeV > 50 MeV	$2.5 + 18.2\ e^{-ln(E)^2/6}$ $5.0 + 17.0\ e^{-ln(2\cdot E)^2/6}$ $2.5 + 3.25\ e^{-ln(0.04\cdot E)^2/6}$

Table IV.3: Radiation weighting factors (w_R) according to the ICRP-103 report (2007) [145] and currently in force in Spanish regulations.

w_R is the weighting factor for the radiation. The weighting factors are dimensionless. Table IV.3 presents the values of the radiation weighting factors, w_R, recommended in the ICRP-103 report (2007) [145].

In this study, the dosimetric assessment for radionuclides of diagnostic and therapeutic interest is based on the Medical Internal Radiation Dose (MIRD) formalism [146] which expresses the calculation of absorbed dose $D(r_T, T_D)$ [Gy] as the mean energy imparted [J] to a target region, r_T, per unit tissue mass [kg], where the region is irradiated over a dose integration period, T_D [s] [147]. The absorbed dose coefficient $d(r_T, T_D)$ is the absorbed dose normalized to the administered activity A_0 [Gy/Bq]. If the subject's anatomy does not change with time, the absorbed dose coefficient can be calculated as:

$$d(r_T, T_D) = \sum_{r_S} \tilde{a}(r_S, T_D) \cdot S_{(r_T \leftarrow r_S)} \tag{IV.4}$$

where $\tilde{a}(r_S, T_D)$ [s] is the Time-Integrated Activity Coefficient (TIAC) and $S_{(r_T \leftarrow r_S)}$ [Gy/Bq·s] is the absorbed dose rate to target region, r_T, per unit activity in source region, r_S, known as the "S-value" (or S-coefficient). Source regions and target regions refer to the areas of the body where nuclear transformations take place, and, where radiation energy is imparted, respectively. These may include whole organs, organ substructures, or groups of organs. The TIAC represents the number of nuclear transformations occurring in a source region over the dose integration period T_D [s] normalized to the administered activity and can be computed as:

$$\tilde{a}(r_S, T_D) = \int_0^{T_D} a(r_S, t)\ dt \tag{IV.5}$$

where $a(r_S, t)$ is the administered activity-normalized activity in r_S at time t post-administration, know as "time-activity curve". For radiopharmaceutical dosimetry, the dose integration period is usually taken to be infinity (i.e., to complete decay of the administered activity).

Following this scheme, TIAC-coefficients and S-values can be independently determined to obtain an organ-level dosimetry.

4.3.1 TIAC-coefficients

An organ-level dosimetry estimation starts from animal biodistribution data obtained from different groups of mice sacrificed at different time periods. Biodistribution data previously obtained at 10 minutes, 1, 2, 4 and 24 hours is used to generate time-activity curves for each organ, identified as the source region where the radiopharmaceutical is concentrated.

Biodistribution data have been quantified as a percentage of the administered dose per gram [% ID/g]. To determine time-activity curves it is necessary to express the biodistribution data as the Standard Uptake Value (SUV). SUV is the measure of activity concentration in an organ or tissue region, which is decay-corrected to the time of administration and normalised to total body mass:

$$\overline{SUV}(r_S^{AN})_i = \overline{[\%ID/g]}(r_S^{AN})_i \cdot \frac{\overline{M}}{100} \tag{IV.6}$$

where index i represents a i^{th} time point.

Standard deviations of the mean values of the respective activity concentration parameters at each time point should be recorded, not only as an indicator of the "quality" of the time-activity curve but also because curve-fitting weights the data points by their respective standard deviations [147].

The reference mouse phantom model used in this study corresponds to the MOBY model, a realistic hybrid model developed by Segars *et al.* [148], which is widely used in preclinical absorbed dose calculation applications. The first-order approach assumes that the body mass-normalized SUV is equivalent among species and phantoms used to approximate them:

$$\overline{SUV}(r_S^{AN})_i = \overline{SUV}(r_S^{PH})_i \rightarrow \overline{SUV}(r_S)_i$$

The fraction of administered activity in the phantom source regions, $a(r_S, t)$, must be computed by scaling the SUV for source region, r_S, with its corresponding mass in the phantom, corrected for the decay of the injected activity dose,

$$a(r_S, t_i) = \overline{SUV}(r_S)_i \cdot \frac{m(r_S^{PH})}{M^{PH}} \cdot e^{-\lambda \cdot t_i} \tag{IV.7}$$

where $m(r_S^{PH})$ is the mass of r_S defined in the phantom, M^{PH} is the total body mass

Organ/Tissue	Density (g/cm^3)	Mass (g)
Blood Cardiorespiratory	1.06	0.112
Heart	1.03	0.207
Lungs	0.30	0.167
Liver	1.06	2.230
Stomach	1.04	0.506
Small Intestine	1.04	2.110
Large Intestine	1.04	0.725
Pancreas	1.05	0.314
Spleen	1.06	0.106
Kidneys	1.05	0.388
Muscle	0.98	25.20
Brain	1.03	0.590
Bone	1.80	2.730
Bone Marrow	1.10	0.350
Tumour	1.00	0.154
Total Mass		37.148

Table IV.4: Organ densities and masses of the MOBY phantom for dosimetry.

of the MOBY phantom, λ the decay constant of the radionuclide [s^{-1}] and t_i is the time post-administration of the ith point [s]. The organ masses of the MOBY mouse reference phantom are listed in Table IV.4.

At this point, we can establish the time-activity curves from the discrete data of the fractions of activity administered in the phantom source regions. To integrate the time-activity curves and estimate the absorbed doses using the MOBY phantom, it is necessary to fit the calculated time-activity curves. The bicompartmental functions are the mathematical model that best describes the time evolution of the distribution of the radiopharmaceutical between blood, organs and tissues. This model considers two intercommunicating compartments. The central compartment is the one offering fast access to the radiopharmaceutical and the peripheral compartment is the one where the radiopharmaceutical enters more slowly. These compartments cannot be assimilated to specific anatomophysiological zones, although it could be assumed that well irrigated organs and tissues are part of the central compartment, while tissues with lower blood flow are part of the peripheral compartment where the arrival of the radiopharmaceutical is delayed.

In this work, bicompartmental fitting of the time-activity curves is carried out using Origin v8.0 software, by means of the following user-defined function:

$$a(r_S, t) = a_1 \cdot e^{-b_1 \cdot t} + a_2 \cdot e^{-b_2 \cdot t} \tag{IV.8}$$

However, not all organs fit a bicompartmental model well because each organ has unique physiological properties and the kinetics of the radiopharmaceutical are different.

In these cases, a trapezoidal function is used for adjustment and integration. The time-activity curves are approximated as a piecewise linear function passing through each measured point. The area under these functions (AUC) are calculated using the trapezoid rule, where the area is divided into trapezoids with vertices defined by the measured points and their projections on the time axis.

With this method, to avoid overestimation error the following consideration should be taken for rapidly excreted molecules compared to the half-life of the radiotracer. To extrapolate the shape of the function from the last point of our biodistribution to infinity a monoexponential function is defined. The decay constant corresponding to the effective biological elimination constant of the peptide, which can be assumed to be the slope of the last measurement points.

Figure IV.10 shows the time-activity curves in tumour, blood cardiorespiratory and lungs for [^{10}B,^{177}Lu]B- Lu-DOTA-TATE from independent biodistribution experiments performed at 10 minutes, 1, 2, 4 and 24 hours post-administration in nude mice bearing

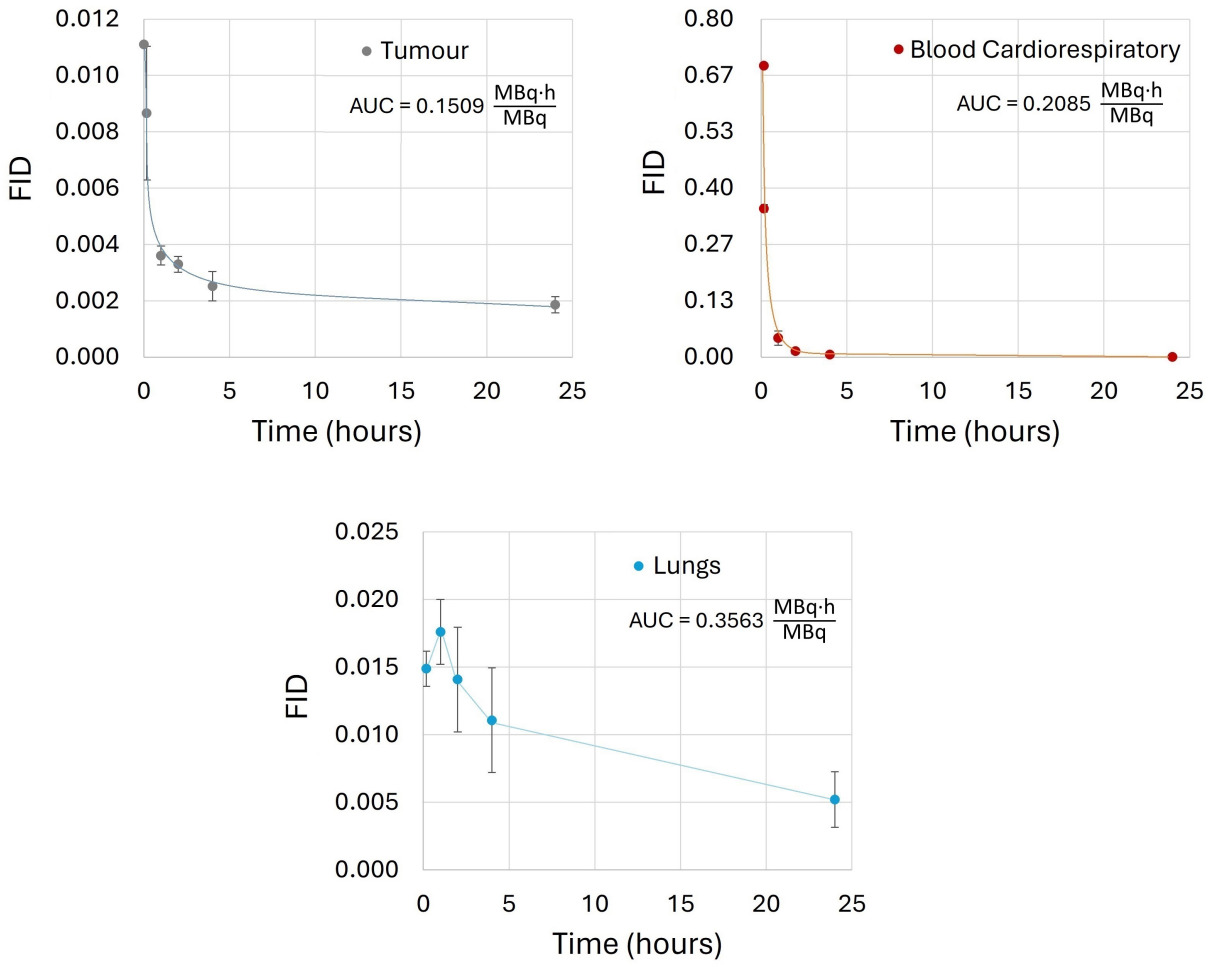

Figure IV.10: Fraction injected dose (FID) as time–activity curves in tumour, blood cardio respiratory and lungs.

Organ/Tissue	Fit	TIAC $\left(\frac{MBq \cdot h}{MBq}\right)$
Blood Cardio.	Bi	0.2085
Heart	Bi	0.0162
Lungs	Tr	0.3563
Liver	Tr	0.4704
Stomach	Bi	0.5315
Small Intestine	Tr	1.0780
Large Intestine	Tr	1.3978
Pancreas	Bi	0.3058

Organ/Tissue	Fit	TIAC $\left(\frac{MBq \cdot h}{MBq}\right)$
Spleen	Tr	0.0381
Kidneys	Bi	1.5812
Muscle	Tr	1.0707
Brain	Bi	0.0085
Bone	Bi	2.047
Bone Marrow	Bi	0.0831
Tumour	Bi	0.1509

Table IV.5: TIAC-coefficients calculated from the different methods of fitting for the main visceral organs. (Bi: Bicompartmental or Tr: Trapezoid rule).

NCI-H727 tumour. TIAC-coefficients for the different organs are listed in Table IV.5, as well as the type of adjustment implemented.

4.3.2 Organ-level dosimetry software

Numerous software tools are available to facilitate organ-level dosimetric calculations in animal or human phantoms. Most calculate absorbed dose by Equation (IV.4), using stored databases of S-values combined with user input of the TIAC for each source region of a computational reference phantom. In this study, the internal dosimetry software used to perform dosimetric calculations is PARaDIM [149]. A flowchart describing the PARaDIM function for organ level dose calculation is described in Figure IV.11.

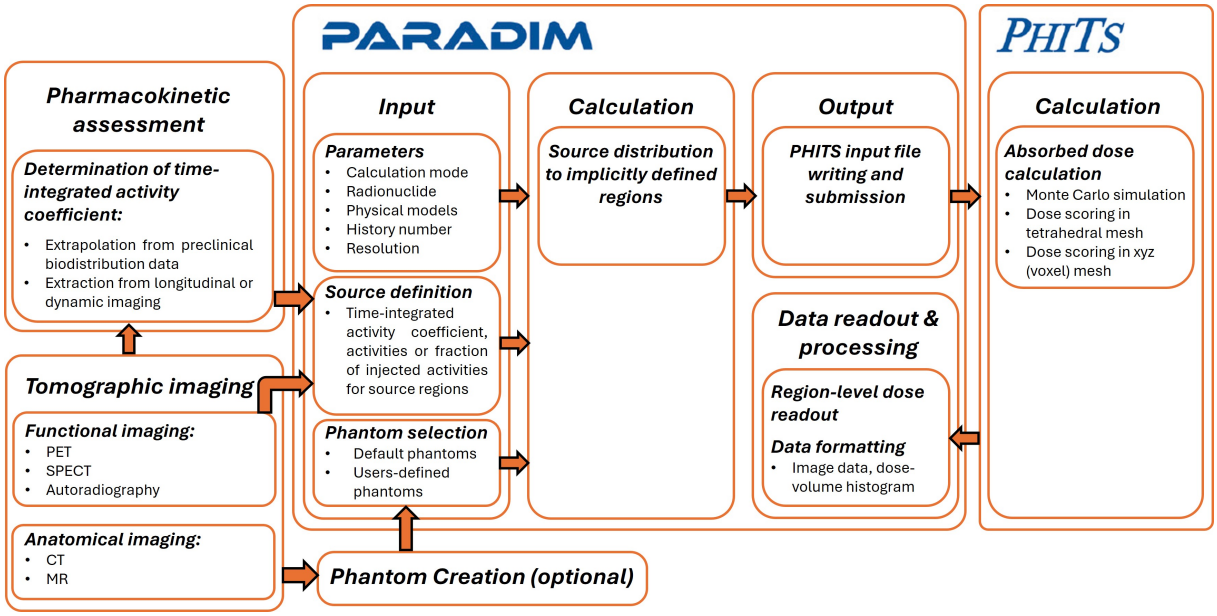

Figure IV.11: Flowchart describing the PARaDIM function for organ-level and 3D dose calculation and the relationships to relevant techniques [149].

Particle and Heavy Ion Transport Code System (PHITS)-Based Application for Radionuclide Dosimetry in Meshes (PARaDIM) is an easy-to-use graphical user interface tool for input of time-integrated activity coefficients and generation of organ-level absorbed doses under the assumption that the activity is uniformly distributed throughout each source region. No knowledge of the PHITS source code, input file format, or parameter syntax is required for its use.

PARaDIM assembles the user-specified phantom geometry, source definition, and simulation parameters into a PHITS-compatible input file for execution. After submission of a PARaDIM simulation, PHITS initiates and transports the various particle emissions (α, β, γ, positrons, and Auger/conversion electrons) into the phantom geometry and tallies the energy deposition within phantom regions or in a voxel grid. Finally the simulation values are reported to PARaDIM software which prints an output with the absorbed and effective dose values of the dosimetry study.

The estimated mean absorbed dose to mouse visceral organs and tumour after injection of 200 pmol of [^{10}B,^{177}Lu]B-Lu-DOTA-TATE is summarised in Table IV.6. The results obtained are part of a preliminary study of the evaluation of a new radiopharmaceutical at preclinical level in animals. From these results it is possible to extrapolate absorbed doses in humans, which should guarantee dosimetric safety. In view of the preliminary dosimetric results, where the highest doses received correspond to vital organs such as lungs, pancreas, stomach, intestines and kidneys, the study of the experimental radiopharmaceutical has been completed to this point.

Organ/Tissue	Absorbed Dose (mGy/MBq)
Blood	11.5 ± 0.2
Heart	17.9 ± 0.2
Lungs	146.9 ± 0.6
Liver	18.62 ± 0.06
Stomach	199.5 ± 0.6
Small Intestine	86.18 ± 0.13
Large Intestine	310.7 ± 0.4
Pancreas	79.7 ± 0.4
Spleen	30.6 ± 0.4
Kidneys	333.0 ± 0.6
Muscle	13.08 ± 0.02
Brain	4.17 ± 0.06
Bone	57.8 ± 0.1
Bone Marrow	26.8 ± 0.2
Tumour	80.6 ± 0.5
Total Body	987 ± 28

Table IV.6: [^{10}B,^{177}Lu]B-Lu-DOTA-TATE radiation absorbed dose estimation from mouse biodistribution data.

4.4 Therapy studies and tumour response

Finally, the preliminary therapeutic efficacy of [^{10}B,^{177}Lu]B-Lu-DOTA-TATE β^--particles was evaluated in six female athymic Nude-Foxn1^{nu} immunodeficient mice with non-small cell lung tumour, which were divided into two groups (N=3). Group 1 was injected with a single dose of [^{10}B,^{177}Lu]B-Lu-DOTA-TATE (8.78 $\pm$ 0.04 MBq). Group 2 was injected with a single dose of normal saline. All injections were 120 μL volume and intravenous into a tail vein. The mouse weights and tumour sizes were measured twice per week.

Figure IV.12.A shows the weight monitoring of the mice over time, where no significant weight loss is observed in any of the groups. Figure IV.12.B evaluates the therapeutic efficacy of β^--particles compared to control group from day 13 post tumour cells inocula-

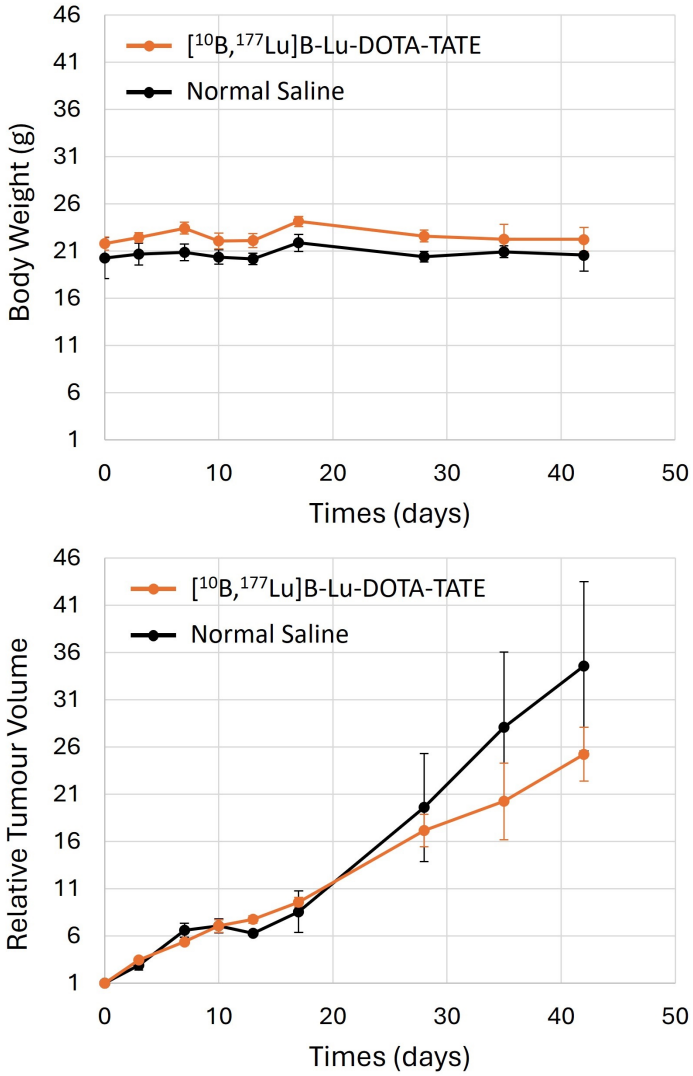

Figure IV.12: A. Body weight of mice in treatment or normal saline groups. B. Relative tumour volume of mice in treatment or normal saline groups.

tion. The results are presented as mean relative tumour volume as a function of time post-administration up to 6 weeks after treatment. Treatment with the radiopharmaceutical [^{10}B,^{177}Lu]B-Lu-DOTA-TATE reduced tumour growth compared to the control group. It should be noted that these results are preliminary. Furthermore, it would be necessary to evaluate the tumour growth of unlabelled [^{10}B]B-DOTA-TATE, as well as, to evaluate a therapeutic effect of repeated doses (3 doses), as is done in clinical and preclinical animal studies with ^{177}Lu as a radiotracer [129].

5 Chapter conclusions

^{177}Lu is considered one of the most promising theranostic radioisotopes of the coming decades. The concept of theranostics is already implemented in the clinic in NETs and prostate cancer, allowing a more comprehensive approach to disease treatment, through its diagnostic and therapeutic effect, owing to the combination of the gamma emission for imaging and the high cytotoxic potency of β^--particles together with the specificity of vector molecules targeting molecular markers. Targeted Radionuclide Therapy offers a promising therapeutic option for cases where other treatments have failed.

Within this framework of innovation, another of the most promising strategies for the treatment of malignant tumours resistant to conventional methods is the Boron Neutron Capture Therapy. A radiotherapeutic strategy that takes advantage of the interaction between thermal neutrons and boron compounds, previously administered to the patient and selective with the tumour cells. When neutrons strike ^{10}B nuclei, a nuclear reaction is generated that releases highly energetic α-particles and lithium nuclei, destroying tumour cells and selectively sparing surrounding healthy tissues away from the irradiation field.

At IFMIF-DONES, the quantities of ^{177}Lu produced would allow the development of a research network to promote the study of new molecular targets, as well as allowing synergy studies between therapies, thus enhancing preclinical research.

In this chapter, a practical approach has been given as a final point of the thesis, using a quantity of the theranostic radioisotope ^{177}Lu of high specific activity, no-carrier-added and with high isotopic and radionuclide purities that could be produced at IFMIF-DONES to perform a translational research between Targeted Radionuclide and Boron Neutron Capture Therapies. For this purpose, a labelled somatostatin analogue, [^{10}B,^{177}Lu]B-Lu-DOTA-TATE has been preclinically evaluated as a dual therapeutic agent by TRNT and BNCT therapies in mice bearing NCI-H727 non-small cell lung carcinoma, a poorly prognostic tumour line with no efficient clinical possibilities.

Biodistribution, dosimetry and therapeutic studies have been carried out to study the selective uptake in different organs and tissues of this experimental radiopharmaceutical. Accurate dosimetry is a requirement both for significant risk projection of low-dose imaging procedures, as well as for reliable dose planning prior to radionuclide therapy, response assessment and characterisation of potential toxicities. Therefore, in preclinical setting, animal studies are essential and the first step to be evaluated clinical uses.

The preliminary results of this study show significant uptake of [^{10}B,^{177}Lu]B-Lu-DOTA-TATE in tumour, but also in non-target organs SSTR2-overexpressing receptors, such as lung, stomach, intestines and pancreas. Therefore, the main conclusion is the need to consider strategies to minimise uptake in non-target organ SSTR2. Among these strategies, the study of the mass effect proposed by Nicolas *et al.* [142], would open new perspectives for future work and improvements of this translational research concept developed as a practical application in the context of the thesis.

Chapter V

Summary and outlook

Nuclear Medicine encompasses an important part of the medical applications of ionizing radiation, based on the use of radioisotopes as radiation sources and allowing the diagnosis and medical treatment of the main diseases with the greatest social impact [15].

In recent years, Nuclear Medicine has presented great advances thanks to the research of new molecular targets allowing a more personalized and precision medicine, in which the doses administered are safe and effective, with minimal toxicity in the surrounding healthy tissue, cost-effective and mild side effects. Research and development in Nuclear Medicine represents a particularly significant change in the treatment of earlier stages of oncological diseases.

Today, more than 50 million Nuclear Medicine procedures are performed worldwide every year, and this number is constantly increasing. More than 10000 hospitals worldwide use radioisotopes, and about 90 % of the procedures are for diagnostic imaging. The most widely used radionuclide in SPECT diagnostics is ^{99m}Tc. It is estimated to be used in almost 85 % of SPECT imaging, corresponding to about 40 million patient studies per year [21].

Other radioisotopes of high clinical interest are the so-called emerging radioisotopes, defined by the International Atomic Energy Agency (IAEA) as those whose capacity to improve medical applications has been demonstrated, but whose use has not yet been standardized, e.g. the Auger electron-emitting radioisotope, ^{165}Er, or the so-called theranostic radioisotopes, used for simultaneous diagnostic imaging and therapeutic procedures using a single radiopharmaceutical. The novel ^{177}Lu radioisotope, a gamma photon emitter detectable by SPECT and β^--particle emitter for therapy, is one of the most relevant and promising theranostic radioisotopes to date.

Currently the concept of theranostics is already being implemented in the clinic [32,33], allowing a more comprehensive approach to disease management, as imaging can offer several simultaneous functions: disease assessment, monitoring and treatment selection in a more efficient way, selecting patients who would benefit most from certain therapeutic interventions, while reducing unnecessary treatments. In addition, this therapy combines

the high cytotoxicity of the β-particles with the high specificity of the vector molecule for target cells, offering a promising therapeutic option for cases where other treatments have failed.

However, the consolidation of this medical strategy requires a solid radioisotope production network to ensure a worldwide supply of theranostic, emerging or conventional agents to cover the growing demand for therapeutic and diagnostic radionuclides in our hospitals.

Radioisotopes used in Nuclear Medicine are produced by bombarding stable nuclides with charged-particles, photons or neutrons, to produce nuclear reactions, either in nuclear reactors or in particle accelerators (linacs, synchrotrons, cyclotrons, etc.). These two technologies are the main ways of medical radionuclide production at present, and should be considered complementary and non-competitive.

Within this framework, the future International Fusion Materials Irradiation Facility - Demo Oriented NEutron Source (IFMIF-DONES) will be a unique scientific infrastructure where the materials to be used in future nuclear fusion reactors will be tested, validated and qualified. In addition to its relevance for the development of fusion as an energy source, it will also be very important in other areas of research and knowledge that will benefit from its infrastructure, such as medicine, particle physics, industry, etc. In December 2017, Fusion for Energy (F4E) welcomed the joint proposal by Spain and Croatia to locate IFMIF-DONES in Escúzar (Granada) [1].

The state-of-the-art, high-intensity linear accelerator, IFMIF-DONES, will be able to accelerate deuterons up to an energy of 40 MeV and a current of 125 mA. These charged particles will strike a liquid lithium target producing neutrons through the $D^+ + {}^7Li$ production nuclear reaction contained inside the Test Cell [4]. It is expected to generate a fast neutron flux of 10^{14} n/cm^2/s with a broad peak between $14-20$ MeV in its neutron spectrum.

The unique characteristics of the facility will allow the development of complementary applications for fundamental and applied physics with minimal impact on the normal operation of the facility [5–8]. In the field of radioisotope production, IFMIF-DONES would facilitate both deuteron beam and residual neutron flux production possibilities within the Test Cell. For this purpose, the feasibility of production of some of the most relevant radioisotopes in the current clinic will be studied exhaustively, as well as their realistic production adaptation, considering some improvements in the design of the accelerator for the correct implementation of this complementary application relevant to the field of Nuclear Medicine.

Experimental measurements of charged-particle cross-sections

As a fundamental step, prior to the study of new alternative production routes for emerging and/or conventional radioisotopes, a thorough knowledge of the nuclear data of the nuclear reactions involved in these alternative production routes is essential for a correct assessment of the feasibility of the project.

In the second chapter, the stacked-foil activation technique for the measurement of the cross-sections of nuclear reactions induced by charged-particle beams, mainly deuterons, has been developed in detail. In addition, the experience and results obtained during two visiting periods in international centres for the measurement of experimental nuclear data for the deuteron production of two emerging radioisotopes of high clinical interest, ^{165}Er and ^{177}Lu, are presented. The first collaboration took place at the cyclotron of the *Centre Conditions Extrêmes et Matériaux: Haute Température et Irradiation* (CEMHTI) (Orleans, France) [44] and involved the measurement of the cross-section of the nuclear reaction ^{nat}Ho(d,2n)^{165}Er and its main impurities ^{nat}Ho(d,p)^{166g,166m}Ho up to a deuteron energy of 17.5 MeV. The second collaboration consisted in the measurement of the nuclear reaction ^{nat}Yb(d,x)^{177cum}Lu, plus numerous impurities, as well as, the upper limit of its isotopic impurity ^{177m}Lu, and took place at the cyclotron of the GIP ARRONAX laboratory (Saint-Herblain, France) [45] up to 33 MeV deuteron energy.

Stacked-foil technique

The stacked-foil technique is an activation method that consists of stacking a series of thin foils, one after the other, to perform several measurements of the cross-section of a nuclear reaction at different energies [49]. The method is convenient for several reasons. Firstly, cross-sections are energy-dependent functions of the charged-particles, whose kinetic energy is reduced as it penetrates the material. The use of thin foils means that the energy loss of the charged-particles due to their interaction with matter is negligible in the thickness of the foil, so the particle flux per target depth remains almost constant within the foil. Secondly, also because a particular radioisotope can be formed as a result of different simultaneous nuclear reactions characterised by different cross-sections and threshold energies, the total excitation function of a nuclear reaction can be well defined by using stacked thin foils.

The stack will be defined as a set of several identical patterns, each consisting of a target foil and several monitoring foils, separated by a thick foil, which acts as a degrader, allowing us to study sets of differentiated energies between the different foil patterns in the stack. Each pattern provides a cross-section measurement.

The stacked-foil technique by the activation method involves a relative calculation method. This relative method for calculating the cross-sections of the nuclear reactions of interest consists of a prior determination of the particle beam flux through the control foils. These foils, strategically placed within the stack, produce several nuclear reactions whose cross-sections are well known. The IAEA provides reference nuclear reaction cross-sections for different projectiles over a wide range of energies [51]. One of the main advantages of this relative method for beam flux calculation is its ease of application during irradiation and the versatility in the location or number of monitoring foils within the stack. Finally, the activity of the foils was measured by HPGe.

Main relevant results of the experimental measurements of the ^{nat}Ho(d,x) reactions at CEMHTI laboratory

The experimental results obtained for the cross-section of the ^{nat}Ho(d,2n)^{165}Er reaction reaction using the ^{nat}Ho stacked-foil technique are in the energy range of $8 - 17.5$ MeV, which includes the maximum cross-section peak, now defined more precisely.

The obtained results have been compared with results from previous studies by F. Tárkányi *et al.* [57] up to 20 MeV and A. Hermanne *et al.* [61] up to 42 MeV, showing high consistency in the near peak energy region and reducing the uncertainties described so far. On the other hand, and in comparison with the theoretical estimates obtained from the TENDL-2023 database [63], for energies higher than the peak energy of 12 MeV, the estimated trend curve does not fully reproduce the behaviour observed by the different experimental data. Thus, the acquisition of new experimental nuclear results might help to improve the theoretical estimates.

Another relevant result obtained in this study is the contribution of new experimental data not available in databases until now. Specifically, it is the reaction corresponding to the production of the metastable state ^{165}Ho(d,p)^{166m}Ho. The knowledge of the cross-section of the ^{166m}Ho metastable state is relevant for two main reasons. The first is a consequence of the β-decay of ^{166m}Ho into the stable radioisotope ^{166}Er, whose production by this additive route would reduce the gross value of the specific activity of the final product of interest, ^{165}Er. To avoid this drawback, an early chemical separation of the two elements would be necessary. On the other hand, the present work allowed us to study the excitation function of ^{nat}Ho(d,p)^{166g}Ho, another emerging β-therapeutic agent. Typically, ^{166g}Ho is produced in nuclear reactors by ^{nat}Ho(n,γ) capture reaction, resulting in a high yield product. Being aware that the ^{165}Ho(d,p) route investigated here cannot compete with the reactor method in terms of yield, a preclinical production of ^{166g}Ho by this complementary route could be considered as a final by-product of our reaction of interest. For this, the estimation of its isotopic impurity ^{166m}Ho is essential, as it would only contribute unwanted dose.

Finally, the measured ratio between the activities of ^{166m}Ho/^{166g}Ho is less than $1/10^6$, therefore, the contamination by ^{166m}Ho state is negligible.

Main relevant results of the experimental measurements of the ^{nat}Yb(d,x) reactions at GIP ARRONAX cyclotron

Experimental measurements of the cross-sections of the deuteron-induced nuclear reactions for the production of ^{177cum}Lu, ^{177}Yb and the other radionuclides studied by the ^{nat}Yb stacked-foil technique have been performed in the high energy range of $19 - 33$ MeV.

The novel theranostic radioisotope ^{177g}Lu ($7/2^+$) can be produced by direct deuteron-induced nuclear reaction ^{176}Yb(d,n)$^{177(g+m)}$Lu or indirectly by decay of its parent nucleus ^{177}Yb ($9/2^+$), where the production of metastable ^{177m}Lu ($23/2^-$) is forbidden due to

parity and angular momentum selection rules.

The obtained results have been compared with previous experimental measurements performed by A. Hermanne *et al.* [71], S. Manenti *et al.* [72], F. Tárkányi *et al.* [74] and M. Khandaker *et al.* [73], available in the EXFOR database [62]. This experimental data set for the radioisotope of interest ^{177cum}Lu, correctly defines its excitation function up to 24 MeV energy. At higher energies, only one data set is available, which shows discrepancies with respect to the rest of the nuclear data. This thesis provides new experimental data that allow to correctly discern the experimental trends and to define the excitation functions more precisely. Finally, in view of the experimental results obtained, it can be affirmed that the estimates evaluated from the TENDL-2023 database [63] do not accurately reproduce the experimental results, concluding that the acquisition of new experimental measurements will allow improving the estimates evaluated from these nuclear databases.

In this study, numerous excitation functions of all isotopic and non-isotopic impurities detected by the activation measurement technique of irradiated natural ytterbium samples have been redefined. In addition, an upper limit has been estimated for the yield achieved by the metastable impurity of ^{177m}Lu, produced directly by the nuclear reaction ^{176}Yb(d,n), which is relevant in the study due to its long half-life. This upper limit has been estimated according to the Currie's criterion [79], by remeasuring the foils after a cooling time of six months. The yield ratio between the ^{177m}Lu detection limit and the ^{177g}Lu yield at the end of the irradiation, for an irradiation energy around 20 MeV, is estimated to be 0.0005 %. A lower value than the percentages obtained by conventional reactor production routes of 0.010 - 0.015 % [81] or 0.02 % [82].

Comprehensive study of radioisotope production and industrial implementation at IFMIF-DONES

Within the framework of the future international IFMIF-DONES facility, numerous complementary applications have emerged around its innovative technology. The state-of-the-art, high-intensity linear deuteron accelerator will be capable of accelerating deuterons up to 40 MeV energy and 125 mA current. This deuteron beam will produce by a spallation reaction on a lithium liquid target a high neutron flux (10^{14} n/cm^2/s) inside the IFMIF-DONES Test Cell. Therefore, the future facility will have exceptional particle flux characteristics, which has led numerous studies to postulate the complementary application of radioisotope production for Nuclear Medicine as one of the complementary applications with the greatest social impact within the facility [5–8].

Some improvements in the Linac design have been studied specifically for these complementary applications. In particular, for the alternative use of part of the initial deuteron beam, the possibility has been considered of diverting 1 pulse per 1000 of the beam, which would mean a 0.1 % current intensity of the initial deuteron beam, to an experimental

room (R026) under the Linac hall. This would make a deuteron beam of 40 MeV energy and 125 μA current intensity available for complementary deuteron applications. Simultaneously, the feasibility of the complementary application of production of different radioisotopes by neutron-induced nuclear reactions have been studied, taking into account the residual neutron flux available inside the Test Cell after the High Flux Test Module. For this purpose, the design of a mechanised lateral insertion Radioisotope Production Device coupled to the geometry of the Test Cell design drawings has been developed and studied.

Based on these considerations, an exhaustive and realistic study of the production of the emerging and conventional radioisotopes ^{165}Er, ^{177}Lu and ^{99}Mo/^{99m}Tc has been carried out, with special emphasis on the study of the isotopic and non-isotopic impurities generated in the final product, on the radionuclide qualities and purity, as well as on the production yields achieved. All this in comparison and taking as a reference the conventional methods of radioisotope production based on nuclear reactors or proton accelerators. Finally, the production devices have been analysed structurally, thermally and mechanically using industrial design software such as SolidWorks [86], and also using Monte Carlo codes for the transport of particles and their estimated energies deposited in matter, such as SRIM 2003 [50] for charged-particles and MCNP6.2 [108] for neutrons.

Results of ^{165}Er production by deuteron-induced reaction

The alternative production route of ^{165}Er by deuteron-induced nuclear reactions has an estimated thick target yield three times higher than that described by conventional production methods using proton-induced nuclear reactions [55]. In addition, the nuclear production reaction, ^{165}Ho(d,2n)^{165}Er, has several advantages that facilitate its production in Linacs, such as its maximum cross-section peak below 18 MeV energy, 100 % natural abundance of ^{165}Ho target, elimination of costs arising from the enrichment of targets and the possibility of irradiating at lower energies, achieving comparable yields and reducing the co-production of impurities.

The production of ^{165}Er at IFMIF-DONES would cover clinical needs, guaranteeing high isotopic purity and radionuclide purity qualities, as well as a high specific activity of the final product, with only 30 hours of irradiation and 10 hours of cooling.

Results of ^{177}Lu production by deuteron-induced reaction

The second radioisotope of clinical interest studied in the context of this thesis has been the theranostic radioisotope ^{177}Lu. So far, its production has been dependent on the availability of nuclear reactors and the use of highly enriched $^{176}Lu_2O_3$ or $^{176}Yb_2O_3$ targets. Thermal neutron-induced nuclear capture reactions (n,γ), characteristic of fission reactors, allow the production of ^{177}Lu in its two versions, carrier-added with the metastable carrier impurity ^{177m}Lu or no-carrier-added, free of it. Both production routes are efficient and

economical [101], predominantly the c.a. route.

The complementary production route proposed by deuteron-induced nuclear reactions has certain limitations as a consequence of the isotopic impurities generated simultaneously in the final product. Although the radionuclide purity of the final product is not affected and is very high, the presence of stable or very long half-life atoms, such as ^{175}Lu or ^{176g}Lu, considerably decreases its isotopic purity. These atoms would compete chemically with the ^{177}Lu atoms in their radiolabelling, decreasing their efficacy for clinical use as a theranostic agent.

In terms of isotopic purity, this production route by deuterons would be equivalent to the current carrier-added routes of nuclear reactors with 7 day of irradiation and 2 day of cooling time. Whereas, the yield achieved is lower, as a consequence of the significant difference in cross-section production. In order to maximise isotopic purity, a two-step production has been studied. In this case, the yield achieved would still be lower due to the elimination of the contribution from the direct production route by the first Yb/Lu chemical separation, although the final product presents high specific activity, isotopic purity and radionuclide purity, making it suitable for preclinical use. Its production requires irradiations of 6 hours and cooling times of 12 hours of $^{176}Yb_2O_3$ enriched samples.

Despite all this, the relevance of studying and promoting new alternative production routes induced by deuterons has an added value in our study, as we continuously observe supply shortages of radioisotopes from nuclear reactors, due to their ageing and limited use, and considering that new reactors will not be constructed, the need to find alternative routes is becoming a priority.

Results of ^{99}Mo production by neutron-induced reaction

Finally, the last radioisotope analysed in detail and with great perspectives for its large-scale production in IFMIF-DONES, is ^{99}Mo, the parent nucleus of the most widely used radioisotope in Nuclear Medicine procedures for SPECT imaging, ^{99m}Tc.

In view of the efficient results comparable to conventional production in nuclear reactors by irradiation of individual pellets [7], multiple irradiation in carrier plates consisting of 45 pellets with a total mass of 72 g (45.9 g molybdenum) has been proposed. The results show a competitive and clinical level supply for the regional and/or state health system, producing weekly $1.21 \cdot 10^{12}$ Bq of ^{99}Mo per irradiation, with an average specific activity of $2.63 \cdot 10^{10}$ Bq/g molybdenum. For this, it is necessary to adapt this complementary application to the current Test Cell designs, allowing the insertion of a device that guarantees the weekly recovery of the irradiated samples.

Finally, thanks to the high active volume behind the High Flux Test Module, the possibility of producing other radioisotopes by neutron-induced nuclear reactions would remain open and subject to the availability of the mechanised sample extraction model.

^{177}Lu as theranostic radioisotope

In recent years, Nuclear Medicine has made great advances thanks to research into new molecular targets, allowing for more personalised and precision medicine. The term theranostics, already implemented in clinical practice, refers to a strategy that combines diagnosis and therapy of diseases using molecules labelled with radioisotopes. The vector molecule is able to identify specific targets in organs and tissues of interest, while the radioisotope or radioisotopes to which it is linked perform the functions of evaluation and treatment. For this reason, recent years have seen an increase in demand for theranostic radioisotopes, one of the most promising candidates being ^{177}Lu, thanks to its optimal physical characteristics, which allow both functions in a single radiopharmaceutical. The ^{177}Lu is a particle-emitting radioisotope (100 %) with maximum energies of 496.8 keV, which also emits low-energy gamma photons 112.95 keV (6.23 %) and 208.37 keV (10.41 %), which allows its detection by the SPECT imaging technique [31]. Finally, another relevant advantage is its half-life of 6.65 days, which makes it possible to produce and transfer it to hospitals efficiently.

Considering the chemical properties of lutetium, the Lu^{3+} ion allows the formation of robust aggregates with specific ligands that have sufficient stability in aqueous solution. For this, the best option is the use of a bifunctional chelating agent (BFC) able to confine the radiometallic ion, while conferring biological specificity to be bound to a non-radioactive compound that would act as a vector molecule able to identify the desired molecular targets [122]. A common BFC in the radiometallic chemistry of lutetium is DOTA and its derivatives, which have an octadentate structure that binds to the Lu^{3+} ion via the four nitrogen atoms of the macrocyclic ring and the four deprotonated oxygen atoms of the pendant carboxylic groups.

Currently, ^{177}Lu has always been presented as a theranostic agent within the therapies known as Targeted Radionuclide Therapies. However, another strategy for the treatment of malignant tumours resistant to conventional methods is Boron Neutron Capture Therapy [130]. BNCT is a radiotherapeutic technique based on the interaction between a thermal neutron beam and boron compounds, previously administered to the patient and selective for tumour cells. When the neutrons interact with the ^{10}B nuclei, a nuclear reaction is generated that releases highly energetic α-particles (high LET) and lithium nuclei, selectively destroying tumour cells without damaging surrounding healthy tissues.

Within this biomedical setting, the fourth chapter has described a "translational research" involving an experimental radiopharmaceutical radiolabelling with ^{177}Lu to address the novel goal of combining TRNT and BNCT. The study has been performed at the preclinical level in xenotransplanted somatostatin transmembrane receptor-positive mouse models bearing neuroendocrine lung tumours. The experimental pharmaceutical studied was [^{10}B,^{177}Lu]B-Lu-DOTA-TATE in collaboration with the Unit of Medical Applications of Ionising Radiation of the Centre for Energy, Environmental and Technological Research (CIEMAT) in Madrid (Spain). The animal study was approved by the

CIEMAT Ethics Committee (protocol code PROEX094/15) adhering to the Agreement on Transparency in Animal Experimentation, promoted by the Confederation of Spanish Scientific Societies (COSCE), with the collaboration of the European Association for Animal Research [141].

[^{10}B,^{177}Lu]B-Lu-DOTA-TATE

The octreotate (TATE) is a peptide analogue with affinity for transmembrane somatostatin receptors. Somatostatin is a polypeptide hormone widely distributed in neuroendocrine system tissues. The physiological activities of somatostatin are mediated by high-affinity interactions with a family of G-protein-coupled receptors. Five different somatostatin receptor subtypes (SSTR1, SSTR2, SSTR3, SSTR4, SSTR5) are currently known [132–134]. Inhibition of hormone secretion is mediated mainly through SSTR2 and SSTR5 receptors.

The octreotate interacts with the cell surface SSTR2, which is present in more than 80 % of neuroendocrine tumours. Neuroendocrine tumours are a group of epithelial neoplasms arising from neuroendocrine cells. Although they can originate in any location, the most frequent are gastroenteropancreatic (66 %) and pulmonary (31 %) tumours, being less frequent in skin, adrenal glands, thyroid and urogenital tract. These tumours are complex due to the heterogeneity of their clinical presentation. However, despite their tissue heterogeneity, neuroendocrine tumours share the expression of neuroendocrine immunohistochemical markers that facilitate the secretion of bioactive peptides such as CgA, serotonin, gastrin and insulin. The release of these substances is regulated by somatostatin [135].

The octreotate conjugated with [^{10}B]B-DOTA has been provided by the Spanish company LabsinLove S.L, while the high specific activity $^{177}LuCl_3$ (n.c.a.) produced in nuclear fission reactor from enriched $^{176}Yb_2O_3$ targets, has been purchased from ITM Medical Isotopes GmbH.

Results of HPLC quality control of the radiopharmaceutical

After the radiolabelling process, the final product obtained has been evaluated by HPLC quality control, taking as a sample an aliquot of the experimental radiopharmaceutical [^{10}B,^{177}Lu]B-Lu-DOTA-TATE prepared. The results show a yield efficiency of 25 % in the radiolabelling process, as well as a radiochemical purity of more than 95 % of the final eluted product. No significant traces of free ^{177}Lu or other chemicals were observed.

The yield efficiency of the process is below the typical yield value for radiolabelling processes of somatostatin analogues with ^{177}Lu. This may be due to steric hindrance effects, influenced by the high bulk functional group of the molecule, which contains 54 boron atoms, and which would somewhat hinder the binding of lutetium to the molecule.

Ex vivo study: Preliminary results on biodistribution, dosimetry studies and therapeutic effect of the radiopharmaceutical

Among the different histological subtypes of neuroendocrine lung cancer, non-small cell lung cancer is the most frequent and lethal, responsible for 80-85 % of deaths [139]. The non-small cell lung carcinoma cell line NCI-H727 is one of the worst prognostic neuroendocrine tumours, for which conventional therapies are proving insufficient [140].

Working with this cell line, a subcutaneous xenotransplanted model of mouse bearing non-samll cell lung carcinoma has been developed, generated from $6{\cdot}10^6$ NCI-H727 cells inoculated into the flanks of $5-6$ week old immunodeficient female Nude-Foxn1^{nu} mice. The potential experimental radiopharmaceutical, [^{10}B,^{177}Lu]B-Lu-DOTA-TATE, has been evaluated in this model.

Biodistribution and dosimetry studies of experimental radiopharmaceuticals are crucial for the assessment of their effectiveness and safety. Absorption, distribution, metabolism and excretion profiles must be well understood to minimise risks to patients. Preclinical studies in animal models are always the first step to be assessed. *Ex vivo* biodistribution studies have been performed at different intravenous post-administration times of the labelled compound, namely 10 minutes, 1, 2, 4 and 24 hours (N=3). The biodistribution results in mice have been used to generate time-activity curves, which have been integrated to estimate the absorbed doses in the different vital organs, using a MOBY mouse model available in the internal dosimetric software PARaDIM.

Preliminary results of the biodistribution study show that the experimental radiopharmaceutical accumulates satisfactorily in the tumour, but also significantly in organs overexpressing SSTR2 receptors, such as the lungs, stomach, small intestine, large intestine and pancreas, as well as in the kidneys, the usual route of peptide excretion. In view of the results obtained, the main conclusion would be the need to find and consider strategies to minimise the uptake of the compound in healthy non-target organs. Among these strategies, we can highlight the relevant study proposed by Nicolas *et al.* [142], where the influence of the prior administration of an excess of unlabelled octreotate on the pharmacokinetic results of the administered radiocompounds is analysed. This strategy would represent a "mass effect" to require thorough investigation within our model.

Finally, preliminary results from the therapeutic evaluation indicate that treatment with the radiopharmaceutical [^{10}B,^{177}Lu]B-Lu-DOTA-TATE reduces tumour growth compared to the control group. However, it is also necessary to evaluate tumour growth following the administration of unlabelled [^{10}B]B-DOTA-TATE and to carry out a more detailed study in this regard.

Estimation of boron concentration

As a direct translational consequence of these results, estimates of ^{10}B concentration expressed as the ratio of parts per million (ppm) of boron atoms in tumour-to-normal

tissue are unfavourable for SSTR2 receptor-overexpressing organs with high radiopharmaceutical uptake, such as lungs. Consequently, current conditions do not support an ideal synergy between the two therapeutic strategies.

However, regarding the absolute value of boron concentration in tumour (in ppm), this is optimal. The measured boron concentration is directly related to the amount of borated compound administered, which in this study was 200 pmol of [^{10}B,^{177}Lu]B-Lu-DOTA-TATE. Equivalent concentrations of 20 ppm boron in tumour could be achieved by administering 4 mg of borated compound, which is considerably lower than the amounts typically administered with boronophenylalanine (BPA) in BNCT [143, 144].

On the other hand, it is important to note that the presence of the radioisotope in the molecule does not limit the amount of compound that can be administered, since only a fraction of the [^{10}B]B-DOTA-TATE is radiolabelled. Moreover, the radiolabelling efficiency may vary when larger amounts of the compound are used, potentially being lower than the value reported in this thesis. Nevertheless, the final activity of the radiopharmaceutical can be adjusted according to the specific requirements of the study, provided that the radiolabelling efficiency is known.

Finally, the concept of translational research developed between TRNT and BNCT therapies does not necessarily imply the exclusive use of therapeutic radioisotopes. This approach can be extended to include radioisotopes used in imaging techniques, such as PET or SPECT, which would allow for monitoring of compound uptake prior to neutron beam irradiation. In this context, some radioisotopes that have already demonstrated affinity for the DOTA chelator and could be considered for evaluation include ^{89}Zr ($T_{1/2}$ = 78.41 h) and ^{68}Ga ($T_{1/2}$ = 67.71 min) [152, 153].

Perspectives

Unique characteristics presented by the future IFMIF-DONES facility for the production of radionuclides have not gone unnoticed among the proposals for secondary applications within the framework of the facility. Numerous efforts and collaborations are trying to push forward the feasibility of the proposal with some important issues remaining to be improved.

Large-scale radionuclide production within the Test Cell would be one of them. A viable sample extraction system is the most immediate problem to be solved, as it must be contemplated in the pre-design phase of the Test Cell before its construction phase. Therefore, one of the main objectives to be promoted and worked on will be the optimisation of a reliable system for the insertion and extraction of irradiated ^{99}Mo pellets in order to guarantee, at least, a regional supply of ^{99m}Tc.

On the other hand, the possibility of exploring new radioisotopes compatible with their production in IFMIF-DONES by deuteron-induced nuclear reactions up to 40 MeV energy or by residual neutron flux within the Test Cell remains always open in this complementary application.

Another future line of work is related to the possibility of producing ^{177}Lu at a preclinical level, due to its high interest as a theranostic radioisotope. This perspective would mean enhancing the development of a possible preclinical research network for applications in radionuclide therapies and their synergy with other clinical strategies such as Boron Neutron Capture Therapy.

After the preliminary study and the results obtained for the experimental radiopharmaceutical evaluated, a not-too-distant work perspective would be to study the "mass effect" mentioned above by injecting different amounts of radiopharmaceutical, the assessment of their possible changes in biodistribution data and to extrapolate the dosimetry results to humans. In addition, these new scenarios would allow re-evaluation of the quantification of boron concentrations in different tissues, organs and tumours by more precise methods of measurement.

Finally, in a positive case, it would be possible to extend the study to new experimental radiopharmaceuticals or tumour lines with higher receptor expression, leaving open a wide range of possibilities and new challenges.

Appendix A

Radioisotope Production Equations

This appendix describes the formalism for calculating the number of radioactive atoms produced as a result of nuclear reactions during an irradiation process. Mathematically, it is modeled by combining the concepts of production and decay of radioactive nuclei.

Firstly, recall some basic concepts of radioactive nuclei, such as the natural exponential decay law, which describes how the amount of radioactive atoms decreases over time due to its spontaneous decay. The general mathematical formula is as follows:

$$\frac{dN(t)}{dt} = -\lambda N(t) \tag{A.1}$$

where the term $-\lambda N(t)$, is the decay rate of the radioisotope. Solving the homogeneous differential equation, it is obtained:

$$N(t) = N(0)e^{-\lambda t} \tag{A.2}$$

where $N(t)$, is the amount of atoms remaining in time, $N(0)$, is the initial amount of atoms, λ, is the decay constant, which depends on the radioactive nucleus and is related to its half-life ($T_{1/2}$) and t, the elapsed time.

The half-life is the time required to decay half of the nuclei of an initial sample of a radioisotope and is related to the decay constant by the formula:

$$\lambda = \frac{ln(2)}{T_{1/2}} \tag{A.3}$$

Finally, remember the law of radioactive activity, which relates the concepts of activity and number of radioactive atoms by means of the decay rate for a given time as,

$$A(t) = \lambda N(t) \tag{A.4}$$

Therefore,

$$A(t) = A(0)e^{-\lambda t} \tag{A.5}$$

1 Radioisotope direct production: During irradiation

During an irradiation process, a radioactive nucleus can be produced by a direct nuclear reaction, $A(x, y)B$, whose target, A, is a stable nucleus.

The basic differential equation that describes the net balance of the radioactive number of atoms produced, $\mathrm{N}_B(\mathrm{t})$, during an irradiation process is given by the following equation,

$$\frac{dN_B(t)}{dt} = R_B - \lambda_B N_B(t) \tag{A.6}$$

where the first term, R_B, is the production rate (assuming a constant particle flux and a stable target), while the second term, $-\lambda_B N_B(t)$, is the decay rate of the radioisotope.

This is a first order linear differential equation. To solve it, we use an integrating factor, so we multiply both sides by the factor, $e^{\lambda_B t}$, and rearrange to separate dependent terms:

$$\frac{dN_B(t)}{dt}e^{\lambda_B t} = R_B e^{\lambda_B t} - \lambda_B N_B(t) e^{\lambda_B t} \tag{A.7}$$

$$\frac{dN_B(t)}{dt}e^{\lambda_B t} + \lambda_B N_B(t) e^{\lambda_B t} = R_B e^{\lambda_B t} \tag{A.8}$$

This converts the left-hand side into the derivative of the product:

$$\frac{d[N_B(t)e^{\lambda_B t}]}{dt} = R_B e^{\lambda_B t} \tag{A.9}$$

Integrating both sides of the equation with respect to time:

$$\int_0^t \frac{d[N_B(t)e^{\lambda_B t}]}{dt}dt = R_B \int_0^t e^{\lambda_B t}\, dt \tag{A.10}$$

$$N_B(t)e^{\lambda_B t} = R_B \frac{(e^{\lambda_B t} - 1)}{\lambda_B} \tag{A.11}$$

$$N_B(t) = R_B \frac{(1 - e^{\lambda_B t})}{\lambda_B} \tag{A.12}$$

2 Radioisotope indirect production: The Bateman equation

On the other hand, during an irradiation process, a radioactive nucleus can be produced indirectly by the decay of another radioactive nucleus produced by a direct nuclear reaction.

In nuclear physics, the Bateman equation is a mathematical model that describes the time evolution of the number of atoms of radioactive nuclei in a radioactive decay chain. This equation generalises the behaviour of several radionuclides which decay sequentially following the scheme:

$$N_1 \xrightarrow{\lambda_1} N_2 \xrightarrow{\lambda_2} N_3 \xrightarrow{\lambda_3} ... \xrightarrow{\lambda_{k-1}} N_k \tag{A.13}$$

Daughter nuclei, N_n, with $n = 2, 3, ..., k$, are generated by the decay of the parent nuclei. The Bateman equation assumes that initially there is only population of the first parent radionuclide. Therefore the boundary conditions would be, $N_1(t = 0) \neq 0$ and $N_n(t = 0) = 0$.

The general formula for the number of atoms formed in time, $N_n(t)$, of a radionuclide A_n, is given by:

$$N_n(t) = N_1(0) \cdot \left(\prod_{i=1}^{n-1} \lambda_i \right) \cdot \sum_{i=1}^{n} \left(\frac{e^{-\lambda_i t}}{\prod_{j=1, j\neq i}^{n} (\lambda_j - \lambda_i)} \right) \tag{A.14}$$

2.1 Two-radionuclides chain

For a chain of two radionuclides ($n = 2$),

$$N_1 \xrightarrow{\lambda_1} N_2 \tag{A.15}$$

The differential equations that describe the decay of a chain of two radionuclides A_1 and A_2, are obtained by solving the nuclear decay equations:

For A_1 describing the exponential decay of the parent radionuclide:

$$\frac{dN_1(t)}{dt} = -\lambda_1 N_1(t) \tag{A.16}$$

Whose solution is:

$$N_1(t) = N_1(0) e^{-\lambda_1 t} \tag{A.17}$$

For A_2 describing its increase due to the decay of the parent nucleus and its decrease due to its own decay.

$$\frac{dN_2(t)}{dt} = \lambda_1 N_1(t) - \lambda_2 N_2(t) \tag{A.18}$$

$$\frac{dN_2(t)}{dt} + \lambda_2 N_2(t) = \lambda_1 N_1(0) e^{-\lambda_1 t} \tag{A.19}$$

To solve it, we use an integrating factor, so we multiply both sides by the factor, $e^{\lambda_2 t}$:

$$\frac{dN_2(t)}{dt} e^{\lambda_2 t} + \lambda_2 N_2(t) e^{\lambda_2 t} = \lambda_1 N_1(0) e^{-\lambda_1 t} e^{\lambda_2 t} \tag{A.20}$$

This converts the left-hand side into the derivative of the product:

$$\frac{d[N_2(t) e^{\lambda_2 t}]}{dt} = \lambda_1 N_1(0) e^{(\lambda_2 - \lambda_1) t} \tag{A.21}$$

Integrating both sides of the equation with respect to time:

$$\int_0^t \frac{d[N_2(t) e^{\lambda_2 t}]}{dt} dt = \lambda_1 N_1(0) \int_0^t e^{(\lambda_2 - \lambda_1) t} \, dt \tag{A.22}$$

$$N_2(t) e^{\lambda_2 t} = \lambda_1 N_1(0) \frac{(e^{(\lambda_2 - \lambda_1) t} - 1)}{(\lambda_2 - \lambda_1)} \tag{A.23}$$

$$N_2(t) = \frac{\lambda_1}{(\lambda_2 - \lambda_1)} N_1(0) (e^{-\lambda_1 t} - e^{-\lambda_2 t}) \tag{A.24}$$

Appendix B

HPGe Detector Calibrations

In this appendix we will detail the calibrations performed for the detectors used in the experiment to measure the cross-sections of the nuclear reactions ^{nat}Yb(d,x) carried out at the cyclotron of the GIP ARRONAX facility (Saint-Herblain, France).

In order to analyse the data acquired with the γ-ray spectrometer, it is necessary to perform an energy and efficiency calibration of HPGe detectors. For this purpose, data were acquired using a reference source such as ^{152}Eu and ^{241}Am (LEA-CERCA, France).

Regarding the ^{152}Eu source, its half-life is 13.537 years and the source activity was 3.437 kBq on 26 November 2008 at 12 h GMT. Regarding the ^{241}Am source, its half-life is 432.6 years and the source activity was 42.8 kBq on 9 December 2021 at 12 h GMT.

Figure B.1: View of the HPGe Detector called Recherche. The samples were placed at a distance of 19 cm from the detector head.

1 HPGe Recherche detector at GIP ARRONAX

The HPGe detector, called Recherche, used for the measurement is a n-type model manufactured by the company CANBERRA. The HPGe Recherche detector is shown in Figure B.1. The calibration spectrum of ^{152}Eu was acquired for 322353 s, while the ^{241}Am spectrum for 251990 s, both in the geometry used in this thesis, i.e. 19 cm from the detection head.

1.1 Energy calibration

β-emitting radionuclides are often accompanied by the emission of gamma photons in their decay. Therefore, the gamma photon energies are the parameters used to identify the radionuclides present in the source.

The energy calibration was performed by fitting γ-peak energies to each detection channel of the acquisition system. Using the energy and channels presented in Table B.1, a linear fit of the form:

$$E(c) = a_1 + a_2 \cdot c \tag{B.1}$$

was performed, as shown in Figure B.2. The correlation obtained is a R^2 value of 0.9999.

Isotope	Energy, E_γ (keV)	Intensity, I_γ (%)	Channel
^{152}Eu	121.8	28.6	1010
	244.7	7.6	1982
	344.3	26.5	2810
	411.1	2.2	3415
	778.9	12.9	6473
	867.4	4.2	7151
	964.0	14.6	8012
	1085.8	10.2	9025
	1112.1	13.6	9243
	1212.9	1.4	10082
	1299.1	1.6	10752
	1408.0	21.0	11649
^{241}Am	59.5	35.9	493

Table B.1: Energies, intensities and corresponding channels associated with the most intense γ-peaks of the ^{154}Eu and ^{241}Am radioactive sources for Recherche detector.

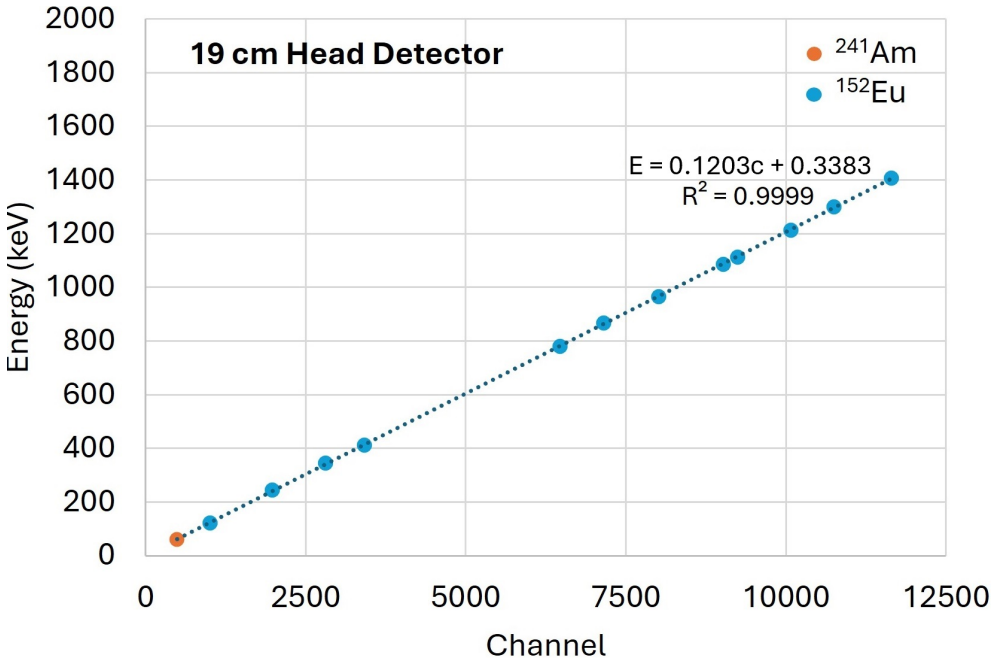

Figure B.2: Energy calibration performed with the ^{152}Eu and ^{241}Am radioactive sources for Recherche detector.

1.2 Efficiency calibration

After the energy fitting, the next step was to perform the HPGe detector efficiency calibration. The definition of efficiency is the area of the detected peaks in counts between the total gamma emissions made by the sample (as the product between the activity of the sample and the relative intensity of each γ-line detected) during the measured time. The formula is described in Chapter II Section 1.3

$$\varepsilon(E_\gamma) = \frac{C_{peak}(E_\gamma)}{LT \cdot A_0 \cdot I_\gamma(E_\gamma)} e^{\lambda t_c} \frac{\lambda \cdot RT}{(1 - e^{-\lambda RT})} \tag{B.2}$$

The semi-empirical formula between efficiency and energy can be approximated to a typical relationship of the type form:

$$\varepsilon(E) = \sum_{i=0}^{5} b_i \cdot ln(E)^i \tag{B.3}$$

The efficiency has been calculated from Equation (B.2) for each peak and is shown in Table B.2. In addition, the empirical calibration curve is shown in Figure B.3.

Isotope	Energy, E_γ (keV)	Efficiency, $\varepsilon(E_\gamma)$ (%)
^{152}Eu	121.8	0.26510
	244.7	0.16900
	344.3	0.12160
	411.1	0.10410
	778.9	0.05541
	867.4	0.04999
	964.0	0.04727
	1085.8	0.04161
	1112.1	0.04038
	1212.9	0.03845
	1299.1	0.03503
	1408.0	0.03332
^{241}Am	59.5	0.30530

Table B.2: Efficiency at 19 cm from the head detector of the most intense γ-peaks of the ^{154}Eu and ^{241}Am radioactive sources for Recherche detector.

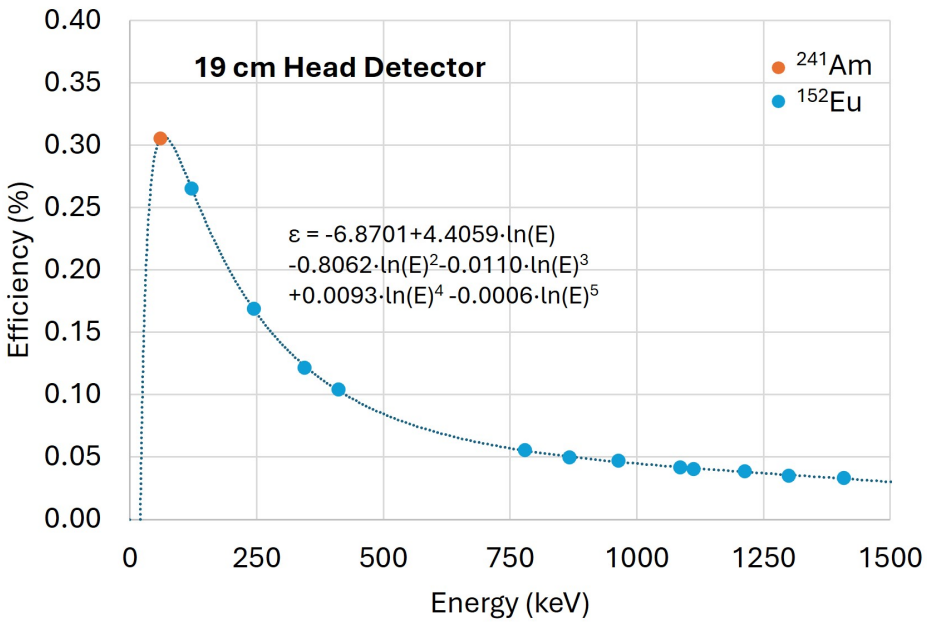

Figure B.3: Efficiency calibration performed with the ^{152}Eu and ^{241}Am radioactive sources for Recherche detector.

2 HPGe Passeur detector at GIP ARRONAX

The HPGe detector, called Passeur, is a n-type model manufactured by the company CANBERRA. The HPGe Passeur detector is shown in Figure B.4. The calibration spectrum of ^{152}Eu was acquired for 256127 s, while the ^{241}Am spectrum for 223783 s, both in the geometry used in this thesis, i.e. 20 cm from the detection head.

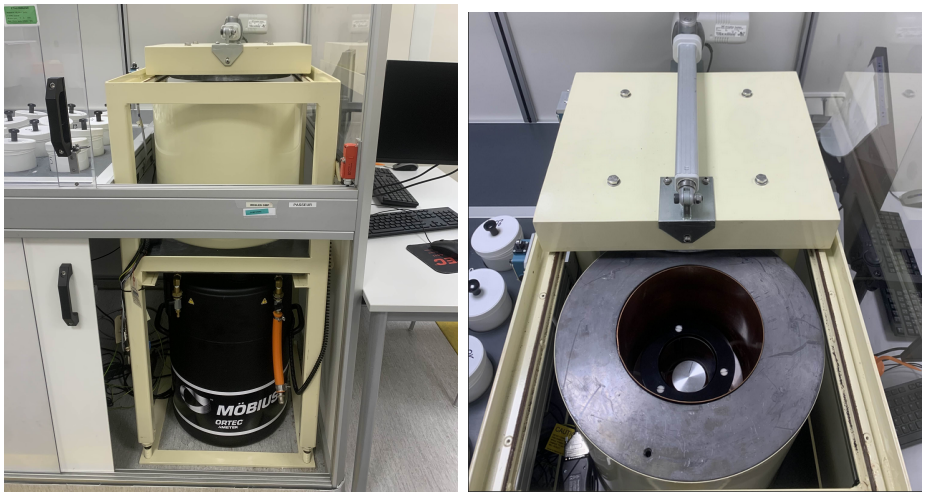

Figure B.4: View of the HPGe Detector called Passeur. The samples were placed at a distance of 20 cm from the detector head.

2.1 Energy calibration

The energy calibration was performed by fitting γ-peak energies to each detection channel of the acquisition system. Using the energy and channels presented in Table B.3, a linear fit of the form $E(c) = a_1 + a_2 \cdot c$ was performed, as shown in Figure B.5. The correlation obtained is a R^2 value of 0.9999.

2.2 Efficiency calibration

The efficiency has been calculated for each gamma energy peak of the calibration sources and is shown in Table B.4. While the obtained values together with the empirical fit between efficiency and energy can be seen in Figure B.6.

Energy and efficiency calibration is a key point to properly assess radioisotopes in our samples. Energy calibration has helped to understand at what energy photopeaks originate and efficiency calibration is necessary to identify possible overlaps between different contaminants and to distinguish them in.

Isotope	Energy, E_γ (keV)	Intensity, I_γ (%)	Channel
^{152}Eu	121.8	28.6	845
	244.7	7.6	1697
	344.3	26.5	2389
	411.1	2.2	2854
	778.9	12.9	5409
	867.4	4.2	6024
	964.0	14.6	6696
	1085.8	10.2	7542
	1112.1	13.6	7725
	1212.9	1.4	8426
	1299.1	1.6	9025
	1408.0	21.0	9781
^{241}Am	59.5	35.9	344

Table B.3: Energies, intensities and corresponding channels associated with the most intense γ-peaks of the ^{154}Eu and ^{241}Am radioactive sources for Passeur detector.

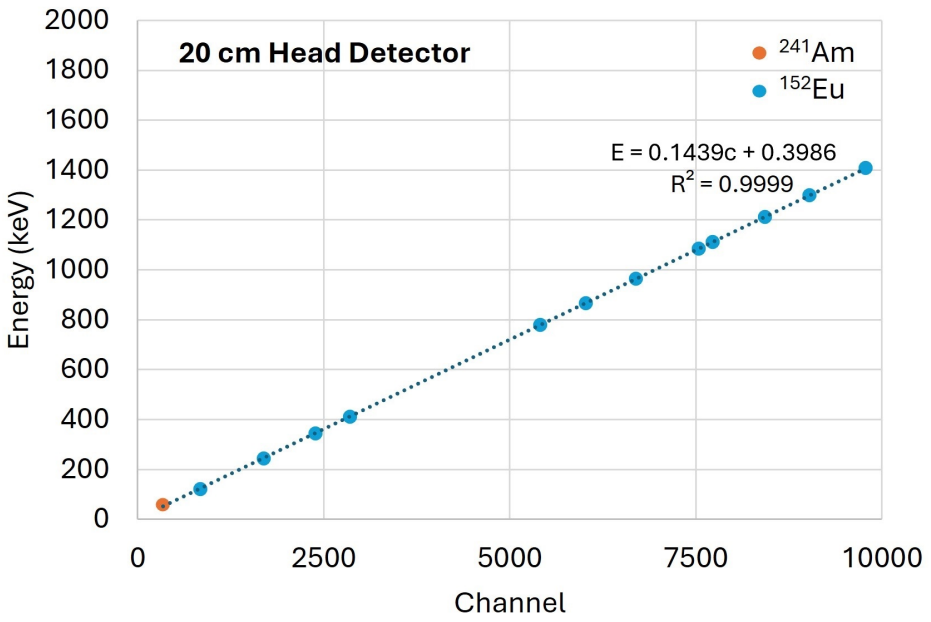

Figure B.5: Energy calibration performed with the ^{152}Eu and ^{241}Am radioactive sources for Passeur detector.

Isotope	Energy, E_γ (keV)	Efficiency, $\varepsilon(E_\gamma)$ (%)
^{152}Eu	121.8	0.26150
	244.7	0.17020
	344.3	0.12420
	411.1	0.10420
	778.9	0.05855
	867.4	0.05151
	964.0	0.04899
	1085.8	0.04347
	1112.1	0.04211
	1212.9	0.03811
	1299.1	0.03759
	1408.0	0.03469
^{241}Am	59.5	0.29130

Table B.4: Efficiency at 20 cm from the head detector of the most intense γ-peaks of the ^{154}Eu and ^{241}Am radioactive sources for Passeur detector.

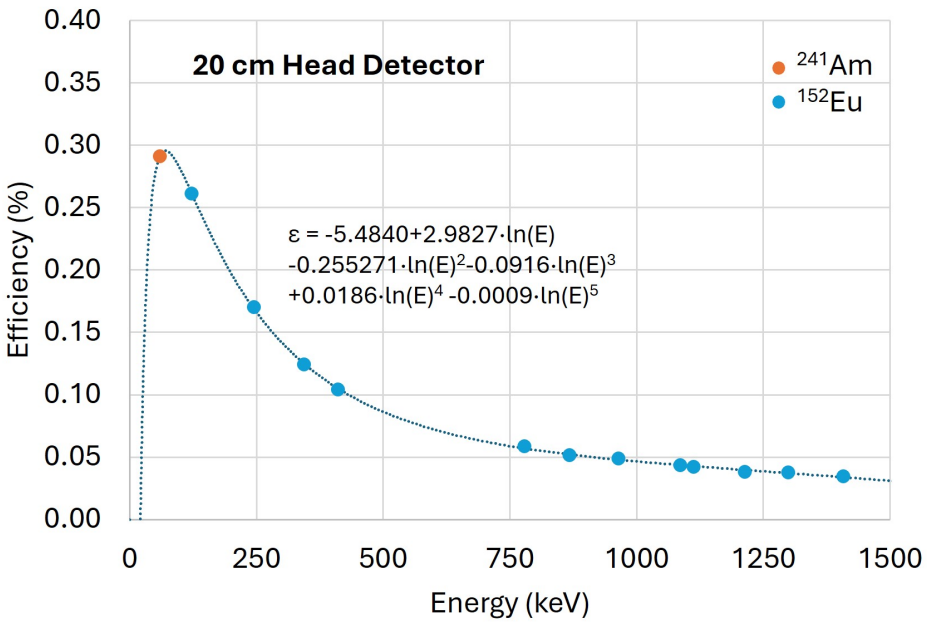

Figure B.6: Efficiency calibration performed with the ^{152}Eu and ^{241}Am radioactive sources for Passeur detector.

Appendix C

Radionuclide Yield Calculator (v2.0)

Radionuclide Yield Calculator (RYC) developed by Mateusz Sitarz is a GUI program that calculates the production yield and activity of radioisotopes based on radiation parameters (for protons, deuterons and alpha particles) and an excitation function stemming from experimental measures or databases, such as TENDL. This software is made available free of charge for use and distribution under certain conditions [54].

Part of this Appendix is taken from the RYC Manual, Copyright (c) 2018, GIP ARRONAX.

1 Main features

Radionuclide Yield Calculator is a programme dedicated to the production of radioisotopes using the cyclotron. It calculates the yield, activity and number of nuclei of any isotope for different production conditions.

The main functions that can be performed by the presented tool are:

- Fitting different experimental functions to the cross-section data.
- Import estimated cross-sections from the TENDL database.
- Calculate the Thick Target Yield (production yield).
- Calculate the activity and the number of nuclei produced at EOB.
- Search for radioactive impurities.

2 Layout and use

To illustrate the use of the program, we will simulate the calculation of the Thick Target Yield and the irradiation plan for the calculation of the production of ^{177g}Lu by ^{176}Yb(d,x)^{177cum}Lu in a realistic $^{176}Yb_2O_3$ target (99.43% of ^{176}Yb enriched).

2.1 Cross-section inputs and plot

There are three fields dedicated to the user-defined cross-section and one more for TENDL. You can select which data sets are to be taken into account in the subsequent analysis by checking the corresponding checkboxes.

For user-defined data, enter or modify the cross-section data by typing one energy value [MeV] and the corresponding cross-section value [mb] (separated by space or tab)

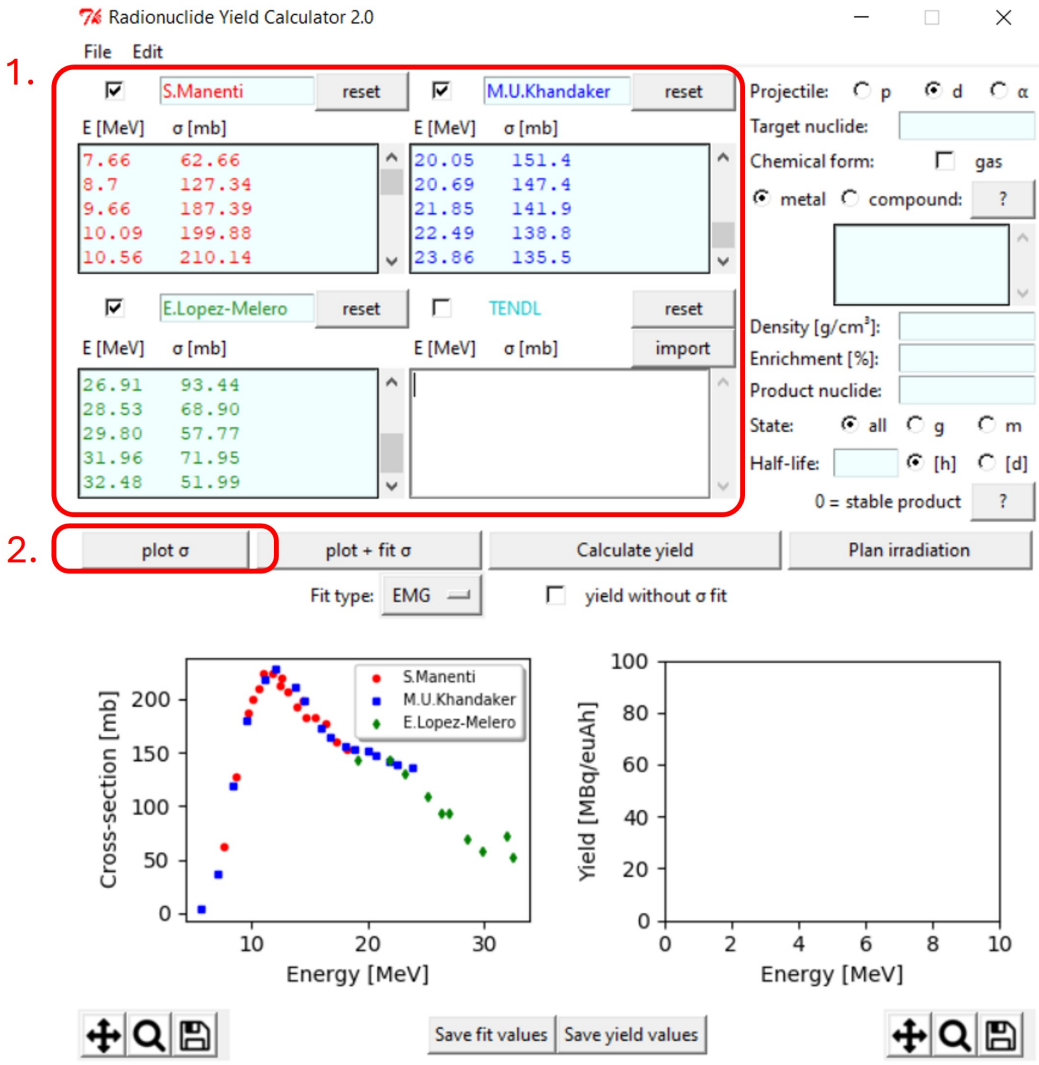

Figure C.1: User-defined cross-section ^{176}Yb(d,x)^{177cum}Lu plot, measured by different authors.

per row in the text box. You may use scientific notation. Use the dot "." as the decimal separator. Do not use any other symbols and do not add empty rows. You can name each dataset above the text box (the name will serve as a label on the graph).

2.1.1 Import TENDL database

The "import" command imports the cross-section from TENDL (TALYS-based evaluated nuclear data library) and inserts it into the text box. For this, it is necessary to specify projectile, target nuclide, product nuclide and its state (in the parameter entries).

By default, RYC only imports nuclear data from the TENDL-2017 database. You can add a new, more up-to-date entry by copying and pasting the nuclear data directly into the text box. In our case we are going to use TENDL-2023 downloaded from the website: `https://tendl.web.psi.ch/tendl_2023/deuteron_html/deuteron.html`.

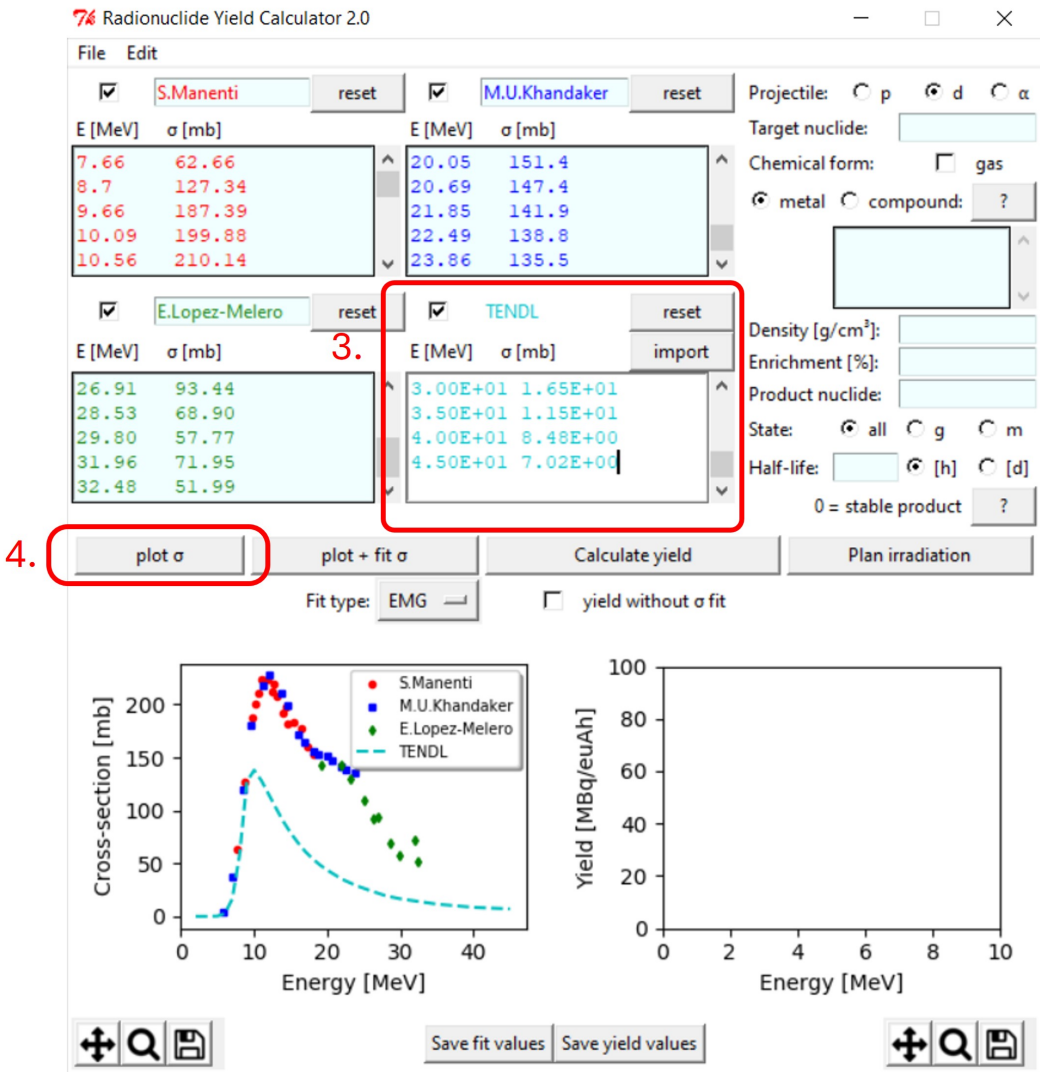

Figure C.2: Replot of the used-defined cross-section ^{176}Yb(d,x)^{177cum}Lu from TENDL database.

The "plot σ" command plots the cross-section data on the cross-section plot. Only selected data sets will be used. Do not select empty data sets.

2.1.2 Fit cross-section inputs

The command "plot + fit σ" additionally also fits the function to the data using the least squares method. Deselect TENDL database so that the fitted values are only the experimental ones. You can select the fitting function from the Fit Type list:

- ◇ EMG (Experimentally Modified Gaussian distribution).
- ◇ GGD (Generalised Gaussian Distribution)
- ◇ q-W (modified q-Weibull distribution)
- ◇ pol-n (polynomial of degree n)

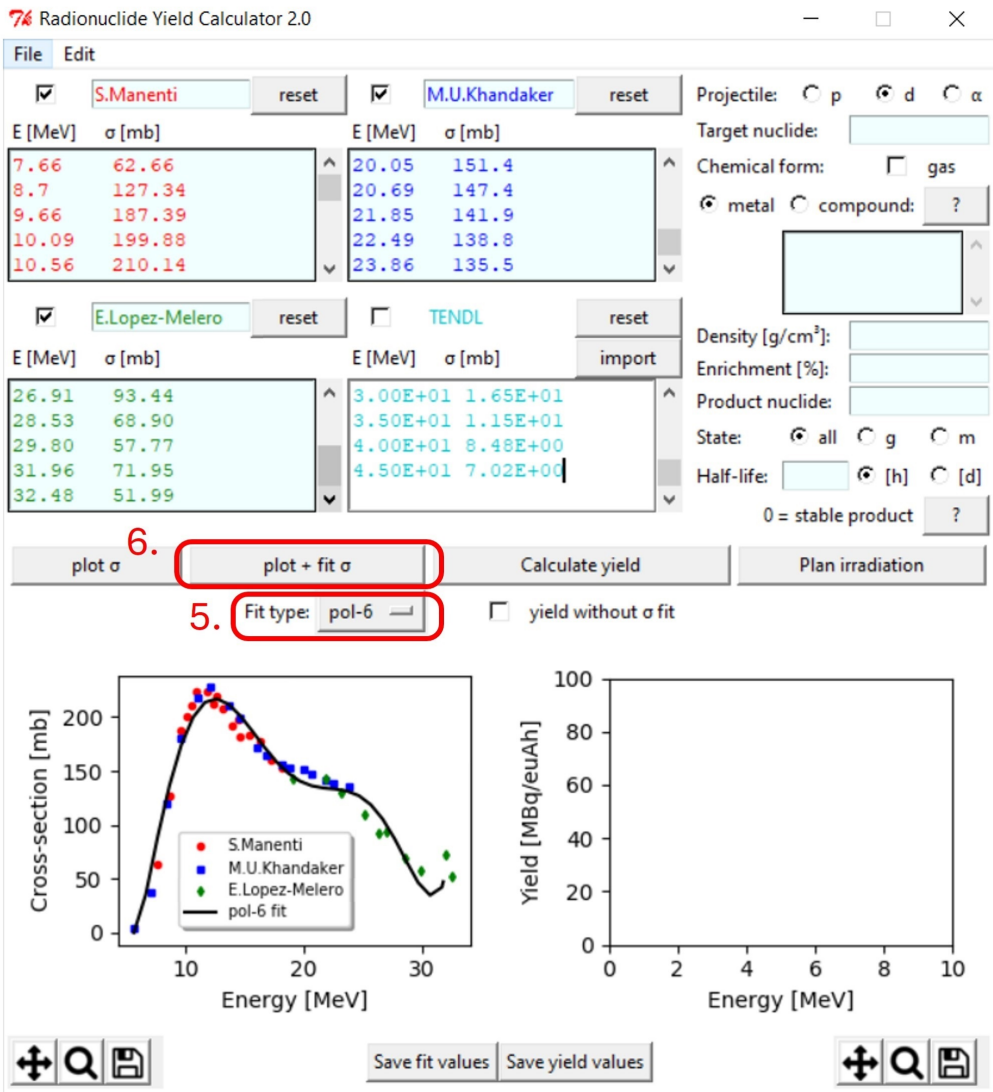

Figure C.3: Fit type pol-6 of the used-defined cross-section ^{176}Yb(d,x)^{177cum}Lu.

2.2 Parameter inputs

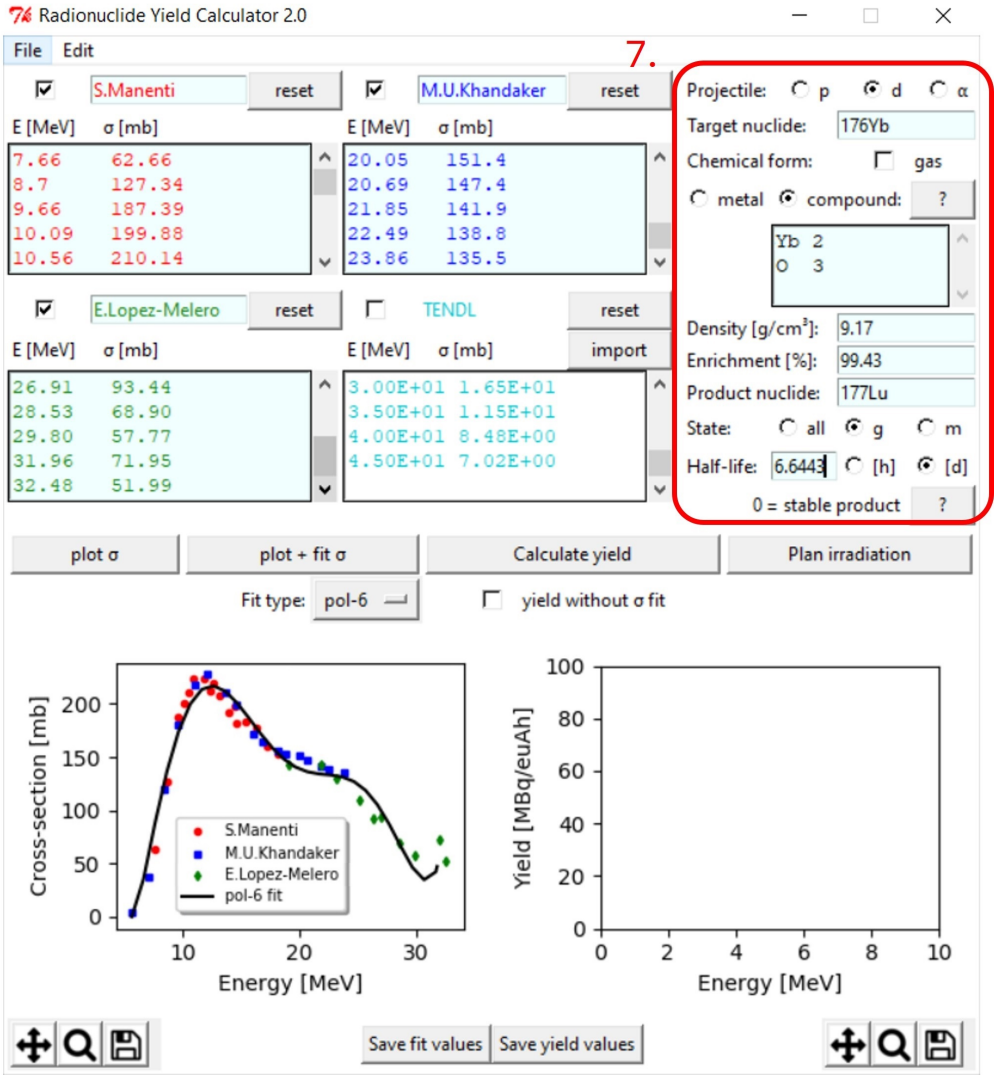

Figure C.4: Parameter inputs of the deuteron-induced nuclear reaction ^{176}Yb(d,x)^{177g}Lu on a enriched target $^{176}Yb_2O_3$ (99.43 %)

- Projectile striking the target: choose p (proton), d (deuteron) or α (alpha particle).
- Target nuclide: atomic mass followed by the symbol of the element in which the nuclear reaction of interest occurs. If only the element symbol is given, e.g. "Yb", the programme will assume the mass of the natural element.
- Chemical form: select the metallic or compound target (and check if gaseous). In the latter case, list all elements in the text box: symbol of each element and its stoichiometry per row (separated by space or tab; do not use empty rows). The atom specified in target nuclide must be present.

- Density of the chemical form of the target to calculate the stopping power.
- Enrichment: abundance of the target nuclide in the target material. Enter 100 if using the values of the cross-section in the natural target.
- Product nuclide: atomic mass followed by the element symbol, e.g. "177Lu", which is the desired product of the nuclear reaction.
- Product nuclide state: g (ground), m (metastable), all (sum of all states).
- Product nuclide half-life: the value in hours [h] or days [d]. Half-life = 0 in the case of stable product.

2.3 Calculate yield

The "Calculate yield" command performs the following operations:

1. Updates the cross-section plot and fit (if necessary).
2. Starts the SRIM module (SRModule.exe) in the background to calculate the stopping power at the target (for this it is not necessary to install the SRIM software separately).
3. Integrates the cross-section and stopping power with Simpson's algorithm to calculate the Thick Target Yield (TTY), i.e. production yield.
4. Plots the yield on the yield plot.

You can also perform this procedure without the cross-section fit. To do so, select the command "yield without σ fit" check box and select only one data set to be used. The selected data set must consist of at least three non-zero single values. Wait up to 2 seconds for this command to be executed.

The following formula is used for the TTY calculation:

$$TTY(E) = \frac{\chi \cdot \lambda}{Ze} \int_{E_{out}}^{E_{in}} \left(-\frac{1}{\rho} \frac{dE}{dx} \right)^{-1} \sigma(E)\, dE \left[\frac{MBq}{\mu A \cdot h} \right] \tag{C.1}$$

where χ is the isotopic and chemical purity of the target, λ is the decay constant [s^{-1}], Z the charge number ($Z = 1$ for protons and deuterons), e the charge of the projectile [C], E_{in} and E_{out} is the beam energy at the entrance and exit of the sample, respectively [MeV], $(-1/\rho\ dE/dx)$ is the stopping power for the target material [eV/(10^{15}atm/cm^2)] and $\sigma(E)$ the cross-section as a function of the charged-particle kinetic energy [cm^2].

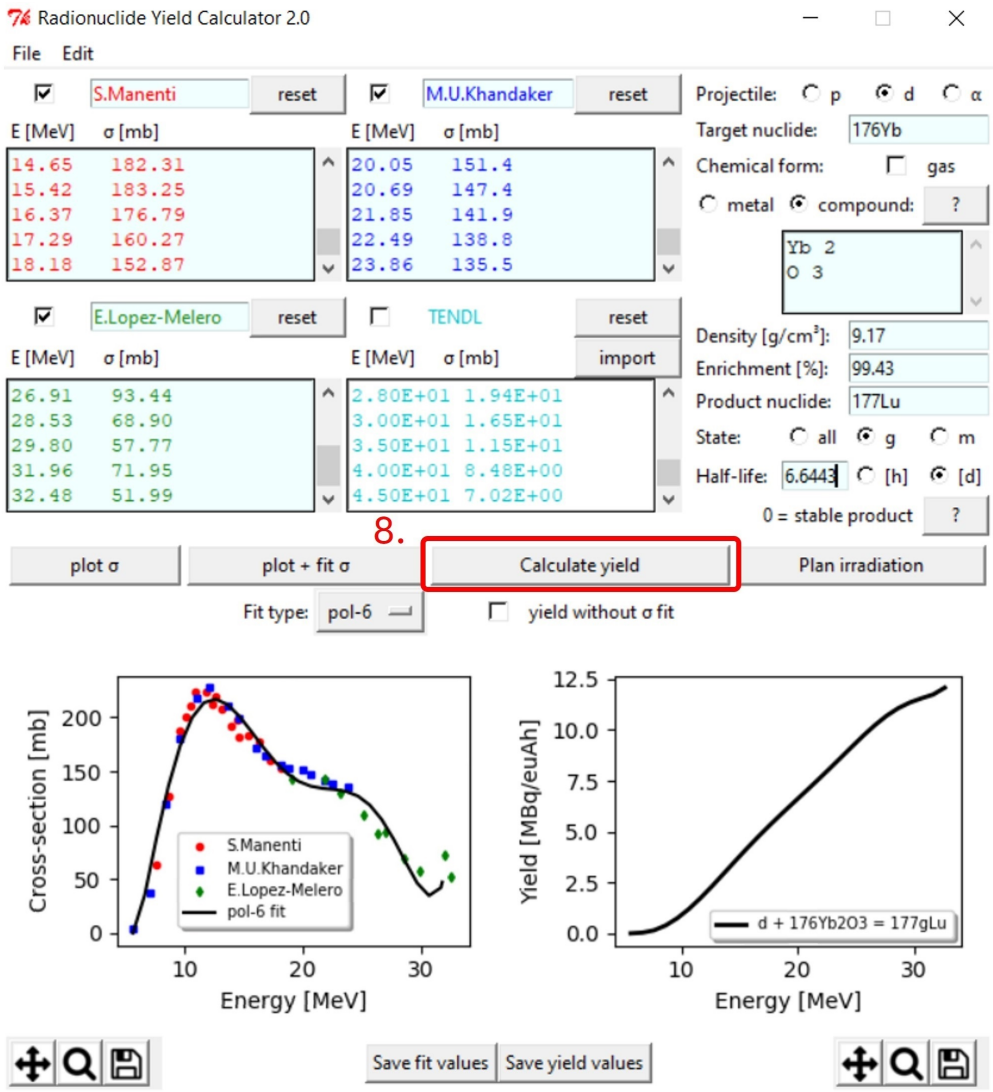

Figure C.5: Calculate Thick Target Yield (TTY) of the radionuclide ^{177g}Lu.

2.4 Plan irradiation and check impurities

The "Plan irradiation" command creates a separate window for specifying irradiation conditions:

- Beam current, I [eμA].
- Irradiation time, t [h].
- The energy range [MeV] of the projectile within the target (from E_{max}=E_{in} to E_{min}=E_{out}).

The "Calculate" command prints the result of such irradiation, also based on the current yield (must be pre-calculated for the energy range selected with Calculate Yield).

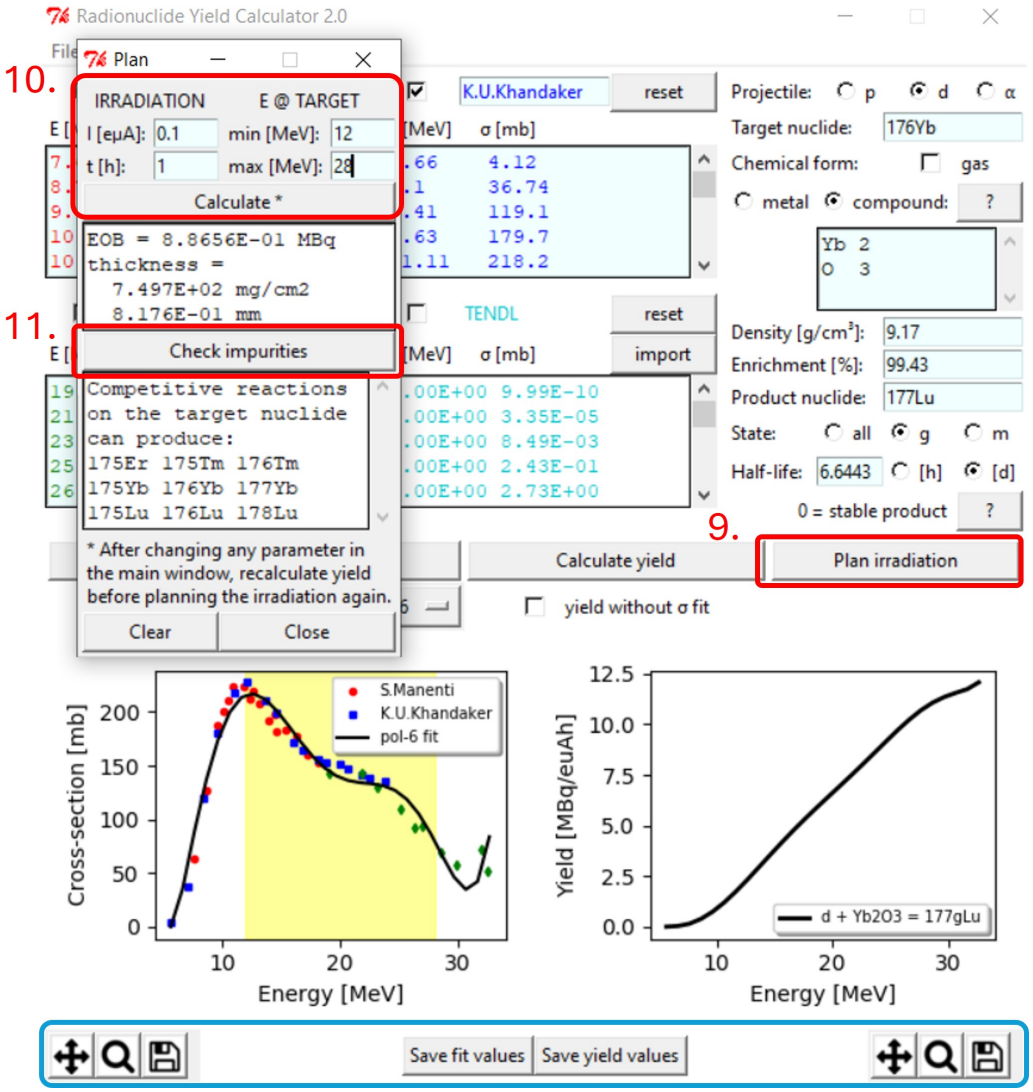

Figure C.6: Irradiation plan of the radionuclide ^{177g}Lu and export cross-section fit and yield data.

It prints the EOB activity and the required target thickness. The selected energy range will be visible in the cross-section plot.

The following formula is used to calculate the EOB:

$$A(EOB) = TTY(E_{max} \rightarrow E_{min}) \cdot \frac{I}{\lambda} \cdot (1 - e^{-\lambda \cdot t}) \ [MBq] \tag{C.2}$$

Finally "Check impurities" command uses the input E_{max} and compares it with the energy thresholds of other TENDL nuclear reactions to estimate possible radioactive contaminants produced in the element specified in target nuclide.

2.5 Export data

Two graphs, cross-section plot and yield plot, are updated automatically by the program. Each has its own command panel in which you can select a tool to edit the graph with:

- Panning tool allows to move the graph by clicking and holding left mouse button on it, or change the scale with the right mouse button,
- Zooming tool allows to create a rectangle on the graph by clicking, holding and moving left/right mouse button and zoom in/out the graph upon the release.
- Disc tool creates ".png" image of the corresponding graph on your computer.

Save fit/yield values create a ".txt" file with the values of the fit/yield from the graph.

2.6 Stable product case

It is possible to calculate the production of stable isotopes. To do that, proceed exactly as in radioactive product case described above but use 0 as half-life in Parameters inputs. All outputs are given in number of produced nuclei instead of activity. The yield is calculated using the following formula:

$$TTY_{stable}(E) = \frac{\chi}{Ze}\int_{E_{out}}^{E_{in}}\left(-\frac{1}{\rho}\frac{dE}{dx}\right)^{-1}\sigma(E)\ dE\ \left[\frac{nuclei}{\mu A\cdot h}\right] \tag{C.3}$$

The calculated number of nuclei assumes no decay of the product during the irradiation, estimating the number of produced nuclei as:

$$N(EOB) = TTY_{stable}(E_{max}\rightarrow E_{min})\cdot I\cdot t\ \ [nuclei] \tag{C.4}$$

This tool has been used to estimate the Thick Target Yield of the studies in this thesis. However, the equations of this tool can be solved analogously by means of a numerical integral. An integrative method, as described in detail in Appendix D, requires a prior parameterisation of the experimental cross-section and the mass stopping power for a given particle and its energy, which pass through a certain material.

The main difference between the two tools is the possibility to know the uncertainties of the cross-section fit. In the RYC method, there are default settings, which cannot be changed and for which the uncertainty of the fitting and therefore the uncertainty of the activity value estimated by the calculator is unknown. Whereas, the integrative method allows to control all the parameters of the equation, as well as, their uncertainties. Simpson's compound rule has been used to solve it and the corresponding theory is detailed in the next section, Appendix D.

Appendix D

Numerical integration method

In this work, it has been necessary to solve numerically a definite integral of the type,

$$I = \int_a^b f(x)\ dx \tag{D.1}$$

According to the theory [150], numerical integration techniques are required for their solution in those cases where:

- Known analytically $f(x)$, it is impossible to calculate its primitive $F(x)$, such that $F'(x) = f(x)$.
- $f(x)$ is not known analytically and only its values $f(x_j)$ at $n+1$ points are known, $\{x_j\}_{j=0,\ldots,n}$

Based on the concept of the Riemann integral, the simplest formulas for approximating an integral appear, which are the so-called Riemann sums. By means of this approximation, the error associated with the integration is considerable. However, the error can be minimised by considering small sum intervals $(x_{i+1} - x_i)$, using integration formulas based on interpolation theory.

1 Newton-Cotes quadrature rules

Given a function $f(x)$, interpolation theory allows us to approximate it by another function $g(x)$, so that,

$$f(x) = g(x) + R(x) \tag{D.2}$$

where $R(x)$ is the interpolation error.

Using Lagrange interpolation [150], the function $g(x)$ is a polynomial of degree n which is called $L_n(x)$,

$$L_n(x) = \sum_{i=0}^{n} f(x_i) l_i(x) \quad with \quad l_i(x) = \prod_{j=0;\ j\neq i}^{n} \frac{x - x_j}{x_i - x_j} \tag{D.3}$$

where $l_i(x)$ are the Lagrange polynomials.

The function $f(x)$ can now be expressed in the following form:

$$f(x) = \sum_{i=0}^{n} f(x_i) l_i(x) + R(x) \tag{D.4}$$

Adding this approach to Equation (D.1), the integral can be evaluated as

$$I = \int_a^b \left[\sum_{i=0}^{n} f(x_i) l_i(x) + R(x) \right] dx = \sum_{i=0}^{n} f(x_i) \int_a^b l_i(x)\ dx + \int_a^b R(x)\ dx$$

$$I = \sum_{i=0}^{n} A_i f(x_i) + r \tag{D.5}$$

where $A_i = \int_a^b l_i(x)\ dx$, are the Lagrange interpolation polynomial and $r = \int_a^b R(x)\ dx$, the integration error.

In this way, we have changed the problem of evaluating an integral for that of calculating the coefficients A_i, for which we also have to carry out an integral, but now the functions of the integrand are simpler. Specifically, the integral we have to solve will be:

$$A_i = \int_{a=x_0}^{b=x_n} l_i(x)\ dx$$

$$A_i = \int_{a=x_0}^{b=x_n} \prod_{j=0;\ j\neq i}^{n} \frac{x - x_j}{x_i - x_j}\ dx = \int_{x_0}^{x_n} \frac{\prod_{j=0;\ j\neq i}^{n} (x - x_j)}{\prod_{j=0;\ j\neq i}^{n} (x_i - x_j)}\ dx \tag{D.6}$$

Using the assumption that the points x_j are equidistance, i.e. $h = x_{i+1} - x_i$, and making the change of variable:

$$\left\{ \begin{matrix} x = x_0 + th \\ x_j = x_0 + jh \end{matrix} \right\} \Rightarrow \left\{ \begin{matrix} x - x_j = (t-j)h \\ x_i - x_j = (i-j)h \end{matrix} \right\} \;\; ; \;\; dx = hdt$$

where the new limits of integration are,

$$\left\{ \begin{matrix} x = x_0 \\ x = x_n \end{matrix} \right\} \Rightarrow \left\{ \begin{matrix} t = 0 \\ t = n \end{matrix} \right\}$$

Applying these changes of variable to the expression in Equation (D.6),

$$A_i = \int_0^n \frac{\prod_{j=0;\ j\neq i}^{n} (t-j)}{\prod_{j=0;\ j\neq i}^{n} (i-j)}\ hdt =$$

$$= \int_0^n \frac{\prod_{j=0;\ j\neq i}^{n} (t-j)}{i\cdot(i-1)\cdot(i-2)\cdots(i-(i-1))\cdot(i-(i+1))\cdots(i-n)}\ hdt \Rightarrow$$

$$A_i = \frac{(-1)^{n-i}h}{i!(n-1)!} \int_0^n \prod_{j=0;\ j\neq i}^{n} (t-j)\ hdt \tag{D.7}$$

Finally, an expression for the coefficients A_i is obtained which depend in each case on the interval length between successive abscissas, $h = (b-a)/n$. In addition, the above expression can also be expressed in terms of totally general coefficients, which are independent of the particular case of integration being carried out, which are defined as the coefficients of Cotes H_i, as follows

$$H_i = \frac{1}{n}\frac{(-1)^{n-i}h}{i!(n-1)!} \int_0^n \prod_{j=0;\ j\neq i}^{n} (t-j)\ hdt \tag{D.8}$$

In this way, the integral calculation of our expression (D.1) is converted into a sum of coefficients H_i whose values are tabulated [150], multiplied in turn by the values of the function of the integrand, of the form:

$$I = \int_a^b f(x)\ dx = (b-a)\sum_{i=0}^{n} H_i f(x_i) + r \tag{D.9}$$

1.1 Residual of integration

As for the error of integration, it will be determined by the interpolation error, which in the case of Lagrange interpolation [150] takes the form:

$$r = \int_a^b R(x)\ dx = \int_a^b \frac{\varpi_{n+1}(x) f^{n+1)}(\xi)}{(n+1)!}\ dx \tag{D.10}$$

where $\varpi_{n+1}(x) = \prod_{j=0}^{n}(x - x_j)$ and $\xi\ \epsilon\ [a, b]$.

Applying the above change of variable to the latter definition, it is obtained:

$$r = \frac{h^{n+2}}{(n+1)!} \int_0^n f^{n+1)} \left[\prod_{j=0}^{n}(t-j)\right]\ dt \tag{D.11}$$

The dependence $\xi = \xi(x)$ is not known so we cannot carry out the above integral strictly, although an estimate of the error can be made by relating it to the step size, $\mathcal{O}(h)$.

2 Simpson's rule

In the work of this thesis, the numerical integrals have been carried out using the Simpson's rule characterised by its precision and simplicity, and which is obtained by particularising the general Newton-Cotes quadrature expression for $n = 2$.

$$I = \int_a^b f(x)\ dx \approx (b-a)\sum_{i=0}^{2} H_i f(x_i) = (b-a)[H_0 f(x_0) + H_1 f(x_1) + H_2 f(x_2)] \quad \text{(D.12)}$$

Using the Cotes coefficient tables [150], for $n = 2$, an approximate integral is obtained,

$$I \approx \frac{h}{3}\left[f(x_0) + 4f(x_1) + f(x_2)\right] \quad \text{(D.13)}$$

Equation called **Simpson's rule** or parabola rule, where $h = (b-a)/2$.

If the interval [a,b] is not small enough, the error in calculating the integral can be large. For this purpose, Simpson's composite formula is used, from which a further interpolation can be developed by making n subintervals of the total array and regrouping them. In this way, the last point of the first subinterval is also the first point of the next subinterval, with the subintervals of even subscripts (except x_0 and x_n) intervening twice. The subintervals will be of the form: $[x_0, x_2]$, $[x_2, x_4]$, $[x_4, x_6]$, ..., $[x_{n-2}, x_n]$.

$$I = \int_a^b f(x)\ dx \approx \tfrac{h}{3}\left[f(x_0) + 4f(x_1) + f(x_2)\right] + \tfrac{h}{3}\left[f(x_2) + 4f(x_3) + f(x_4)\right] +$$

$$\tfrac{h}{3}\left[f(x_4) + 4f(x_5) + f(x_6)\right] + ... + \tfrac{h}{3}\left[f(x_{n-2}) + 4f(x_{n-1}) + f(x_n)\right]$$

$$I = \int_a^b f(x)\ dx \approx \tfrac{h}{3}\left[f(x_0) \ + \ 4\sum_{i\ impares} f(x_i) \ + \ 2\sum_{i\ pares;\ i\neq 0,n} f(x_i) \ + \ f(x_n)\right] \quad \text{(D.14)}$$

Equation called **Simpson's composite rule**, where $h = (b-a)/2$.

2.1 Residual of integration

Finally, as for the error estimation, as we know that for the interpolated Simpson's rule comes from the Newton-Cotes approximation for $n = 2$ subintervals, the residual is given by the expression,

$$r_i = \frac{h^5}{90}\sum_{i=1}^{n/2} f^{IV}(\xi_i) \quad \text{(D.15)}$$

Since we cannot carry out this integral strictly, the most we can estimate the error in the numerical integral is that it will be of the order of $\mathcal{O}(h^5)$.

3 Numerical integral radioisotope production

In the work of this thesis, the numerical integral to be solved is a quotient of two functions dependent on the energy of the charged-particle as it moves in matter,

$$I = \int_{E_{out}}^{E_{in}} \frac{\sigma_{(d,x)}(E)}{S_d(E)}\, dE \tag{D.16}$$

Both functions must be correctly parameterised in order to be able to carry out the numerical calculation of the integral and, in turn, to obtain the final uncertainty of the integral as the root of the sum quadratically of the uncertainties of the independent variables of our study, which would be: the uncertainties of the cross-section fit parameters, the uncertainties of the stopping power fits for the deuterons in the different targets studied, and the uncertainty in the integration step used in the method.

In the following subsections, both the stopping power and cross-section fit parameters are grouped together with their uncertainties for the different studies carried out in the Chapter III of this thesis.

3.1 Stopping power functions

At high energies (above 1 MeV/amu) the Bethe's stopping power predicts the energy loss by charged-particles accurately with two physical parameters (ionisation potentials and shell corrections) for different stopping materials. The semi-empirical expression developed by Andersen and Ziegler [151] for protons describes such behaviour at high energies, according to the following expression dependent on the energy,

$$S_p(E) = \frac{A_6}{\beta^2}\left[ln\left(\frac{A_7\beta^2}{1-\beta^2}\right) - \sum_{i=0}^{4} A_{i+8} ln(E)^i\right] \tag{D.17}$$

where, $\beta^2 = 1 - (1/(1 + E/m_p))^2$, E is the proton energy per unit atomic mass in [keV/amu], m_p is the proton mass [keV/c^2] and A_i are Bethe's stopping coefficients characteristic of the material. The stopping power is given in unit of eV/(10^{15} atom·cm^2).

Recall that the stopping power depends on the type of particle in terms of mass and charge and on the material medium. Therefore, the relation between the expression for the stopping power of deuterons and protons is:

$$S_d(E) = S_p\left(\frac{m_p}{m_d}E\right) \tag{D.18}$$

where m_p and m_d are the mass of a proton and deuteron in the units keV/c^2, respectively.

The table D.1 shows the Bethe's stopping coefficients A_i of the semi-empirical expression developed by Andersen and Ziegler [151] for the different materials used in this thesis.

Target	Bethe's stopping coefficients						
	A_6	A_7	A_8	A_9	A_{10}	A_{11}	A_{12}
^{165}Ho	0.03416	1640	-14.74	5.051	-0.6117	0.03141	-0.0005801
$^{176}Yb_2O_3$	0.08898	1494	-14.05	5.272	-0.8058	0.06527	-0.0019935

Table D.1: Bethe's stopping coefficients A_i of the semi-empirical expression developed by Andersen and Ziegler [151] for the different materials. Coefficients are dimensionless with the exception of the A_6 expressed in eV/(10^{15} atom·cm^2). These coefficients lack uncertainty, as it is not provided by SRIM 2003 software [50].

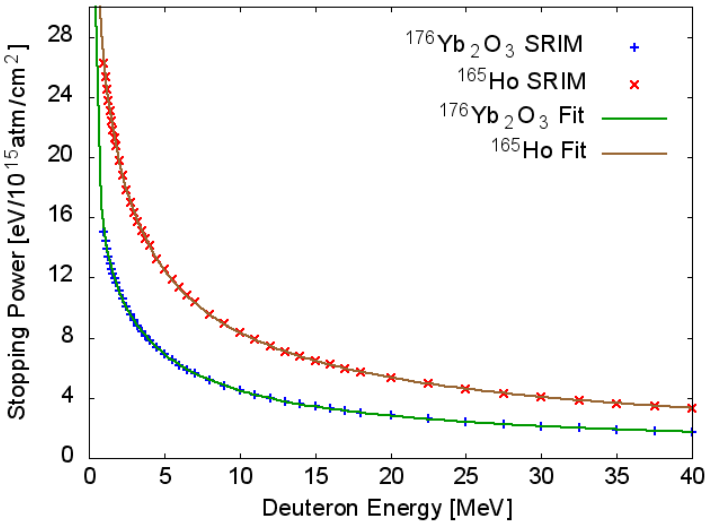

Figure D.1: Stopping power estimated using SRIM and semi-empirical fit using Andersen and Ziegler's formula, for the different material.

The function has been obtained by fitting the stopping power values simulated by SRIM 2003 code [50] up to 40 MeV deuteron energies.

3.2 Excitation functions

The excitation functions have been defined by fitting the experimental cross-sections available in the EXFOR database [62] and our own measurements described in Chapter II. In view of the possible absence of some experimental values, we have also worked with the TENDL evaluated database [63] for these cases.

The following is a summary, according to the nuclear reactions studied, the fit type performed for the cross-section values, the values of fit parameters and the associated uncertainties.

3.2.1 ^{165}Ho(d,x):

The type of adjustment implemented has been:

$$\sigma_{(d,x)}(E) = \begin{cases} a_1 e^{-a_2(E-a_3)^2} & , \quad E < a_3 \\ a_1 e^{-b_1(E-a_3)} & , \quad E > a_3 \end{cases} \tag{D.19}$$

Nuclear Reaction	Fit parameters			
	a_1 (mbarn)	a_2 (MeV^{-2})	a_3 (MeV)	b_1 (MeV^{-1})
^{165}Ho(d,2n)^{165}Er	680 (0.79 %)	0.129 (3.54 %)	12.16 (0.03 %)	0.115 (1.34 %)
^{165}Ho(d,n)^{166}Er	29.2 (2.51 %)	0.109 (10.75 %)	11.10 (1.09 %)	0.058 (1.51 %)
^{165}Ho(d,γ)^{167}Er	0.0025 (1.50 %)	0.130 (7.52 %)	11.90 (0.63 %)	0.169 (7.42 %)
^{165}Ho(d,p)^{166g}Ho	160.3 (2.98 %)	0.090 (12.1 %)	11.15 (1.25 %)	0.073 (0.29 %)
^{165}Ho(d,p)^{166m}Ho	64.7 (0.81 %)	0.126 (4.27 %)	12.70 (0.42 %)	0.073 (2.84 %)

Table D.2: Fit parameters of the ^{165}Ho(d,x) excitation functions from the cross-section values available in the databases and our new measurements. Uncertainties of the fit parameters are included.

3.2.2 ^{173}Yb(d,x):

The type of adjustment implemented has been:

$$\sigma_{(d,x)}(E) = \begin{cases} a_1 e^{-a_2(E-a_3)^2} & , \quad E < E_{sw_1} \;\; or \;\; a_3 \\ \frac{c_1}{E-c_2} \;\; or \;\; a_1 e^{-c_3(E-a_3)} & , \quad E > E_{sw_1} \;\; or \;\; a_3 \end{cases} \tag{D.20}$$

where E_{sw_1} and a_3 are the switching energy connected to the two functional shapes.

Fit Parameters	Nuclear Reaction	
	^{173}Yb(d,n)^{174m}Lu	^{173}Yb(d,2n)^{173}Lu
a_1 (mbarn)	4.4 (0.15 %)	120 (0.55 %)
a_2 (MeV^{-2})	0.120 (0.85 %)	0.104 (3.10 %)
a_3 (MeV)	8.9 (0.08 %)	13.1 (0.38 %)
c_1 (mbarn·MeV)	-31 (5.89 %)	
c_2 (MeV)	1.85 (36.06 %)	
c_3 (MeV^{-1})		0.164 (2.71 %)
E_{sw_1} (MeV)	9.0	a_3

Table D.3: Fit parameters of the ^{173}Yb(d,x) excitation functions from the cross-section values available in the databases and our new measurements. Uncertainties of the fit parameters are included. Grey cells indicate that this type of fit does not apply.

3.2.3 ^{174}Yb(d,x):

The type of adjustment implemented has been:

$$\sigma_{(d,x)}(E) = \begin{cases} a_1 e^{-a_2(E-a_3)^2} & , \quad E < E_{sw_1} \\ b_0 + b_1 x + b_2 x^2 + b_3 x^3 & , \quad E_{sw_1} < E < E_{sw_2} \\ \frac{c_1}{E-c_2} \quad or \quad a_1 e^{-c_3(E-a_3)} & , \quad E > E_{sw_2} \end{cases} \tag{D.21}$$

where E_{sw_1} and E_{sw_2} are the switching energy connected to the two functional shapes.

Fit Parameters	Nuclear Reaction		
	^{174}Yb(d,γ)^{176g}Lu	^{174}Yb(d,n)^{175}Lu	^{174}Yb(d,2n)^{174g}Lu
a_1 (mbarn)	0.0026 (1.44 %)	33 (1.64 %)	163 (2.42 %)
a_2 (MeV^{-2})	0.117 (5.62 %)	0.174 (6.08 %)	0.075 (17.15 %)
a_3 (MeV)	12.78 (0.44 %)	9.96 (0.49 %)	12.9 (2.07 %)
b_0 (mbarn)			
b_1 (mbarn/MeV)			
b_2 (mbarn/MeV^2)			
b_3 (mbarn/MeV^3)			
c_1 (mbarn·MeV)		-212 (3.27 %)	
c_2 (MeV)		3.47 (8.55 %)	
c_3 (MeV^{-1})	0.146 (2.40 %)		0.206 (10.83 %)
E_{sw_1} (MeV)	a_3	10.2	a_3
E_{sw_2} (MeV)			

Fit Parameters	Nuclear Reaction		
	^{174}Yb(d,2n)^{174m}Lu	^{174}Yb(d,3n)^{173}Lu	^{174}Yb(d,p)^{175}Yb
a_1 (mbarn)	37 (2.39 %)		72 (1.37 %)
a_2 (MeV^{-2})	0.141 (9.32 %)	0	0.086 (6.70 %)
a_3 (MeV)	13.7 (1.17 %)		11.4 (0.81 %)
b_0 (mbarn)		1307.06 (15.8 %)	
b_1 (mbarn/MeV)		-331.428 (14.97 %)	
b_2 (mbarn/MeV^2)		24.9124 (14.60 %)	
b_3 (mbarn/MeV^3)		-0.53497 (15.02 %)	
c_1 (mbarn·MeV)		-2835 (57.89 %)	
c_2 (MeV)		14.98 (26.33 %)	
c_3 (MeV^{-1})	0.180 (14.3 %)		0.062 (13.4 %)
E_{sw_1} (MeV)	a_3	11.3	a_3
E_{sw_2} (MeV)		23.0	

Table D.4: Fit parameters of the ^{174}Yb(d,x) excitation functions from the cross-section values available in the databases and our new measurements. Uncertainties of the fit parameters are included. Grey cells indicate that this type of fit does not apply.

3.2.4 ^{176}Yb(d,x):

The type of adjustment implemented has been:

$$\sigma_{(d,x)}(E) = \begin{cases} a_1 e^{-a_2(E-a_3)^2} & , \quad E < E_{sw_1} \\ b_0 + b_1 x + b_2 x^2 + b_3 x^3 + b_4 x^4 + b_5 x^5 & , \quad E_{sw_1} < E < E_{sw_2} \\ \frac{c_1}{E-c_2} \quad or \quad a_1 e^{-c_3(E-a_3)} & , \quad E > E_{sw_2} \end{cases} \tag{D.22}$$

where E_{sw_1} and E_{sw_2} are the switching energy connected to the two functional shapes.

Fit Parameters	Nuclear Reaction		
	^{176}Yb(d,x)^{177cum}Lu	^{176}Yb(d,2n)^{176g}Lu	^{176}Yb(d,2n)^{176m}Lu
a_1 (mbarn)	222 (5.06 %)	300 (0.45 %)	293 (3.62 %)
a_2 (MeV^{-2})	0.078 (9.37 %)	0.124 (2.40 %)	0.128 (8.72 %)
a_3 (MeV)	11.1 (2.80 %)	11.8 (0.27 %)	11.6 (1.26 %)
b_0 (mbarn)	-3363.17 (1.58 %)		
b_1 (mbarn/MeV)	1002.87 (1.70 %)		
b_2 (mbarn/MeV^2)	-107.502 (1.93 %)		
b_3 (mbarn/MeV^3)	5.52334 (2.18 %)		
b_4 (mbarn/MeV^4)	-0.137338 (2.43 %)		
b_5 (mbarn/MeV^5)	0.0013252 (2.70 %)		
c_1 (mbarn·MeV)	-582 (8.71 %)		-703 (4.93 %)
c_2 (MeV)	20.36 (2.72 %)		9.91 (9.27 %)
c_3 (MeV^{-1})		0.102 (3.97 %)	
E_{sw_1} (MeV)	9.7	a_3	12.7
E_{sw_2} (MeV)	26.0		

Table D.5: Fit parameters of the ^{176}Yb(d,x) excitation functions from the cross-section values available in the databases and our new measurements. Uncertainties of the fit parameters are included. Grey cells indicate that this type of fit does not apply.

Fit Parameters	Nuclear Reaction		
	^{176}Yb(d,3n)^{175}Lu	^{176}Yb(d,4n)^{174g}Lu	^{176}Yb(d,4n)^{174m}Lu
a_1 (mbarn)	1228 (1.40 %)	118 (2.96 %)	43 (3.69 %)
a_2 (MeV^{-2})	0.036 (6.53 %)	0.045 (14.33 %)	0.034 (14.72 %)
a_3 (MeV)	18.4 (0.73 %)	27.2 (1.20 %)	28.0 (1.04 %)
b_0 (mbarn)			
b_1 (mbarn/MeV)			
b_2 (mbarn/MeV^2)			
b_3 (mbarn/MeV^3)			
b_4 (mbarn/MeV^4)			
b_5 (mbarn/MeV^5)			
c_1 (mbarn·MeV)	-5794 (6.85 %)	-2430 (14.16 %)	-430 (12.89 %)
c_2 (MeV)	14.97 (2.99 %)	6.90 (55.51 %)	18.69 (9.22 %)
c_3 (MeV^{-1})			
E_{sw_1} (MeV)	20.7	27.5	29.4
E_{sw_2} (MeV)			

Fit Parameters	Nuclear Reaction		
	^{176}Yb(d,5n)^{173}Lu	^{176}Yb(d,p)^{177}Yb	^{176}Yb(d,x)^{175}Yb
a_1 (mbarn)	76 (1.26 %)	227 (1.97 %)	53 (1.22 %)
a_2 (MeV^{-2})	0.027 (6.04 %)	0.101 (11.79 %)	0.007 (4.45 %)
a_3 (MeV)	38.8 (0.42 %)	11.06 (1.24 %)	36.95 (0.66 %)
b_0 (mbarn)			
b_1 (mbarn/MeV)			
b_2 (mbarn/MeV^2)			
b_3 (mbarn/MeV^3)			
b_4 (mbarn/MeV^4)			
b_5 (mbarn/MeV^5)			
c_1 (mbarn·MeV)	-1841 (13.1 %)		
c_2 (MeV)	14.11 (16.25 %)		
c_3 (MeV^{-1})		0.079 (1.86 %)	
E_{sw_1} (MeV)	38.3	a_3	-
E_{sw_2} (MeV)			

Table D.6: Fit parameters of the ^{176}Yb(d,x) excitation functions from the cross-section values available in the databases and our new measurements. Uncertainties of the fit parameters are included. Grey cells indicate that this type of fit does not apply.

Appendix E

MCNP6.2 Tallies

MCNP tallies are standard summary information that gives users a better insight into the physics of the studied problem and the adequacy of the Monte Carlo simulation.

MCNP code offers an array of standard tallies such us, particle current, particle flux or energy deposition, among others. Currents can be tallied as a function of direction across any set of surfaces, surface segments, or sum of surfaces in the problem. Charge can be tallied for charged-particles. Fluxes across any set of surfaces, cells, segments or sum of bodies are also available. All these MCNP tallies are normalised to be per source particle unless a different normalisation has been specified.

The seven standard tally quantities actually scored in the MCNP code before the final normalization are presented in Table E.1. The variables used are:

W	Particle weight.
μ	Ω·n, cosine of angle between surface normal n and particle direction vector Ω.
A,V	Surface area (cm^2) and volume (cm^3), calculated by the code or input by user.
T_l	Track length (cm), even transit time multiplied by the particle velocity.
$p(\Omega_P)$	Probability density function for scattering in the direction p towards the point detector.
λ	Total number of mean free paths from particle location to detector.

Tally	Description	Score	Units
F1	surface current	W	particles
F2	surface flux	$\frac{W}{\lvert\mu\rvert A}$	particles/cm^2
F4	cell flux	W $\frac{T_l}{V}$	particles/cm^2
F5	detector flux	$\frac{W\ p(\Omega_P)\ e^{-\lambda}}{L^2}$	particles/cm^2
F6	energy deposition	W T_l σ_t(E) H(E) $\frac{\rho_a}{m}$	MeV/g
F7	fission-energy deposition	W T_l σ_f(E) Q $\frac{\rho_a}{m}$	MeV/g
F8	pulse-height tally	W_C put in bin E_D	pulses

Table E.1: Tally quantities scored [108, 109].

L	Distance to detector from the source or collision event (cm).
σ_t(E)	Microscopic total cross-section (barns).
σ_f(E)	Macroscopic fission cross-section (barns).
H(E)	Heating number (MeV/collision).
Q	Total prompt energy release per fission (MeV).
ρ_a	Atom density (atom/barn·cm).
m	Cell mass (g).
W_C	Collective weight from a history for pulse-height tally.
E_D	Total energy deposited by a history in a detector (MeV).

The units of each tally are derived from the units of the source. When the source has particle units, the current tallies have particle units and flux tallies actually represent fluences with units of particles per unit area. If the source has units of particles per unit time, current tallies are particles per unit time and flux tallies are particles per unit time per unit area.

By using the indicated tallies, any quantity of the form,

$$q = \int_E \phi(E) \cdot f(E)\ dE \tag{E.1}$$

can be tallied, where $\phi(E)$ is the neutron energy-dependent flux source and $f(E)$ is any product or summation of the quantities in the cross-section libraries or a response function provided by the user.

In the case under study, the quantity to be analysed is the radionuclide production rate (R_B) in order to calculated the specific activity produced (SA_B) of a radioisotope by a neutron-induced nuclear reaction of the form $A(n, y)B$:

$$SA_B(t) = \frac{A_B(t)}{m} = \frac{R_B}{m} \cdot (1 - e^{-\lambda_B \cdot t}) = C \cdot I \cdot q \cdot (1 - e^{-\lambda_B \cdot t}) \tag{E.2}$$

where C is a scalar mass quantity [g^{-1}], I is the total particle current [s^{-1}] (MCNP tallies are normalised to be per source particle) and q is the resulting tally value of activated nuclei. C- & q-factors are conditioned by the tally used as the method of calculation, where the production rate term, R_B, is defined differently.

MCNP code allows to calculate the amount of activity of each nuclide produced in a cell using four different tallies, which will be described below.

1 F4 Tally

The physical quantity of Tally F4, is defined as the average particle flux in a cell:

$$F4 = \overline{\phi_V} = \frac{1}{V} \int dE \int dt \int dV \int d\Omega \; \psi(r, \Omega, E, t) \tag{E.3}$$

Defining the angular flux as typically defined in nuclear reactor theory $\psi(r, \Omega, E, t) = v \cdot \rho(r, \Omega, E, t)$, where ρ is the particle density (particles/cm^3/MeV/steradian) and v is the velocity (cm/sh), the average particle flux in a cell can be calculated as,

$$\overline{\phi_V} = \frac{1}{V} \int dE \int dV \int dt \int d\Omega \; v \cdot \rho(r, E, t) = \frac{1}{V} \int dE \int dV \int dt \; v \cdot N(r, E, t) \tag{E.4}$$

where $N(r, E, t) = \int d\Omega \; \rho(r, \Omega, E, t)$ is the density of particles, regardless of their trajectories, at a point. Defining ds to be the differential unit track length and nothing that $ds = v \cdot dt$ yields,

$$\overline{\phi_V} = \frac{1}{V} \int dE \int dV \int ds \; N(r, E, t) \tag{E.5}$$

The quantity $N(r, E, t) \cdot ds$ may be thought of as a track-length density; thus, the average flux can be estimated by summing track lengths. The MCNP code estimate $\overline{\phi_V}$ by summing, $W \cdot T_l / V$, for all particle tracks in the cell, so the units of this tally are particles·cm/cm^3 or equivalently, particles/cm^2.

Time- and energy-dependent subdivisions of $\overline{\phi_V}$ are made by binning the track lengths in appropriate time and energy bins. The track length estimator is generally quite reliable because there are frequently many tracks in a cell (compared to the number of collisions), leading to many contributions to this tally.

1.1 F4 Tally with FM4 card

The FM4 card is a multiplicative operation that converts a flux tally (F4) into a production rate taking into account a cross-section of a given nuclear reaction. That is, the FM4 card is used in this study to calculate the activation rate quantity of the form,

$$R_B = \int_E \phi(E) \cdot R_m(E) \; dE \tag{E.6}$$

where $\phi(E)$ is the neutron energy-dependent flux source (s^{-1}) and R_m(E) is an operator of additive and/or multiplicative response functions from MCNP6 cross-section ENDF/B VIII.0 library that takes into account the atom density of the cell where the tally is applied. Therefore, in the definition syntax of the tally it is necessary to indicate the aforementioned information, according to the exemplified form.

Example:

(Fn:par	cell)		F4:N	10		
(FMn	c	m	r_i)	FM4	-1	92238	102
				FM4	10E-24		

With the input parameters:

c = -1	Normalization factor (indicating macroscopic cross-sections (barn) multipled by the atom density of the cell (atoms/cm^3)).
m = 92238	Material number for ^{238}U defined on the material card.
r_i = 102	Reaction number for radiative capture cross-section (102 = (n,γ)) ENDF/B-VIII.0 database. Other reaction numbers are available in the MCNP.6.2 handbook.

In this example, the F4 card is used to calculate the flux in a cell, and the FM4 card is used to convert that flux into a production rates in cell 10 with the material ^{238}U (atomic fraction of 100 %). The average fluence is multiplied by the microscopic (n,γ) cross-section of ^{238}U (with atomic fraction of $\chi = 1$), but as the normalization factor is c < 0 (c = -1) the tally FM4 printout will indicate the number of ^{239}U atoms/cm^3 produced as a result of (n,γ) capture with ^{238}U. The conversion factor 1 barn = 10^{-24} cm^2 should be indicated by an additional FM4 multiplicative factor.

It is important to note that if a monoisotopic material is considered (χ=1), this FM4 tally function calculates the production rate for the only possible reaction channel (r_i) available. On the other hand, if a non-monoisotopic material or a composite material is considered, this type of tally 4 calculates a total production rate for all energetically possible channels for the different radioisotopes that come into play for the reaction (r_i) indicated. By not separating the different contributions. It is therefore only recommended for monoisotopic materials.

1.2 F4 Tally with DE4 & DF4 card

This feature allows you to enter a point wise response function (such as cross-section) as a function of energy to modify a regular tally, or apply a built-in conversion/response function. The production rate quantity is expressed in the form,

$$R_B = \chi \cdot n_A \cdot \int_E \phi(E) \cdot \sigma(E)\, dE \tag{E.7}$$

The syntax used in order to insert the response function as a tally modifier is using a table with the following correlation between an energy card (DE) and the excitation function card (DF) such as cross-section. When both DE and DF cards are present to provide a user-specified quantity table, they must have the same number of numerical

entries and they must be monotonically increasing in energy. Particle energies outside the energy range defined on these cards use either the highest or lowest value.

In order to calculate the production rate quantity of the Equation (E.7) it is necessary to choose the cross-section of the reaction of interest. The nuclear reaction cross-section can be download from different experimental or evaluated databases, such as EXFOR or ENDF databases [62, 113]. For this reason, any cross-section available in databases can be tallied.

Example:

(Fn:part	cell)	F4:N	8
(# DEn (MeV)	DFn (barn))	# DE4	DF4
e_1	f_1	9.99949E-12	10.0119
e_2	f_2	1.10304E-11	9.53283
...	...	...	...
e_k	f_k	2.00000E+2	0.00001
		FM4 10E-24	

With the input parameters:

- n Tally number (type tally 4).
- e_i The eth energy value (in MeV).
- f_i The value of the function corresponding to e_i.

In this example, the neutron capture reaction (n,γ) on ^{100}Mo in cell 8 for the production of ^{101}Mo is tallied. As can be seen, there is no information on the material or density of cell 8.

In this case, the average fluence is multiplied by a microscopic cross-section (whose units are barns), therefore, the conversion factor 1 barn = 10^{-24} cm^2 should be indicated by an additional FM4 multiplicative factor. The tally printout indicates the number of activated nuclei produced independent of the atom density of the cell. For this reason, an integrated mass correction must be made to the C-factor, taking into account the target atoms and their atomic mass density in the cell (see Section 3).

2 F8 Tally

The physical quantity of Tally F8 is defined as pulse-height tally which is a radical departure from other MCNP6 tallies. Normally, it provides the energy distribution of pulses created in a cell that models a physical detector. Moreover, it also can provide the energy deposition in a cell. Although the entries on the F8 card are cells, this is not a track length cell tally. Thus, the pulse-height tally records the energy or charge deposited in a cell by each source particle and its secondary particles per history.

In this kind of tally, cell, user, and energy bin cards are allowed whereas flagging and multiplier bins are not allowed. Use of the dose energy (DE) and dose function (DF) cards is also disallowed.

However, with the FT8 special tally treatments card the F8 tally can become an anti-coincidence pulse-height tally or a different kind of tally altogether. For example, FT8 CAP is a neutron coincidence capture tally and FT8 RES tallies the residual nuclides from physics-model evaporation and fission models. These kind of tallies are useful to estimated activation rate in units of activated nuclei, expressed in the form,

$$R_B = \int_E \phi(E) \cdot \sum \sigma_{(n,x)}(E)\ dE \tag{E.8}$$

where neutron-induced cross-sections used by MCNP6 are from ENDF/B VIII.0 library.

2.1 FT8 CAP card

The FT8 CAP is a special treatment option which converts the pulse-height tally to a neutron capture tally, which means only nuclear reactions (n,γ). It scores the number of captures in specified combinations of nuclides at the end of each history, thus, its units are activated nuclei accumulated for the entire geometry or for specific cells listed, normalised per incident neutron. The syntax and an example of the tally are shown below.

Example:

```
(Fn:par  cell)        F8:N      2
(FTn  CAP  m)         FT8 CAP 3006

                      F18:N     7
                      FT18 CAP 5010
```

In this example, the neutron capture reaction (n,γ) for the nuclides ^{6}Li and ^{10}B are tallied in cells 2 and 7, respectively.

2.2 FT8 RES card

The interactions of high-energy particles with target nuclei causes the production of many residual nuclei. The generated residual nuclei can be recorded in an F8 tally if used with a special treatment option such as FT8 RES. The residuals are recorded at each physics model interaction as well as each neutron library interaction. The residual data can be accumulated for the entire geometry or for specific cells listed.

When used with the F8 tally, the FT8 RES card yields a list of residual nuclides produced by all neutron-induced reactions and model reactions of all incident particle types (photon and proton library reactions do not yet produce residuals).

The F8 tally with an FT8 RES special tally treatment is then simply the distribution of nuclides resulting from a single collision. Its units are activated nuclei normalised per incident neutron. The syntax and an example of the tally are shown below.

Example:

```
(Fn:par  cell)        F8:N      6
(FTn  RES  m)         FT8 RES 8016

                      F18:N     6
                      FT18 RES 20040

                      F28:N     6
                      FT28 RES 26000

                      F38:N     6
                      FT38 RES 92238
```

In this example, the combination of tally cards creates a charge deposited tally in cell 6 and then creates four user bins for the isotopes ^{16}O, ^{40}Ca, all iron isotopes and ^{238}U.

3 C- & q-factors for different tallies

Tally & card - Description	C-factor	q-factor
FM4 card is only available for the reactions: (n,γ)=102, (n,p)=103, (n,α)=107, (n,2n)=16, (n,3n)=17 or (n,n+p)=28.	$\mathrm{n}_A^{-1} \left[\frac{atm}{cm^3}\right] \cdot \frac{N_A[mol^{-1}]}{M_{at}[g/mol]}$	FM4 $\left[\frac{nuclei}{cm^2} \cdot \frac{atm}{cm^3}\right] \cdot$ FM4 $\left[\frac{cm^2}{barn}\right] \cdot XS\,[barn]$
DE4 & DF4 card is available for all reactions due to the fact that the cross-section is included by hand for the user.	$\chi \cdot \frac{N_A}{M_{at}} \left[\frac{mol^{-1}}{g/mol}\right]$	F4 $\left[\frac{nuclei}{cm^2}\right] \cdot XS\,[barn] \cdot$ FM4 $\left[\frac{cm^2}{barn}\right]$
FT8 CAP refers exclusively to capture reaction (n,γ).	$\chi \cdot \frac{1}{m} \left[\frac{1}{g}\right]$	FT8 $[nuclei]$
FT8 RES refers exclusively to residual nuclei, which can be obtained by different energetic route: (n,γ), (n,p) (n,α), (n,2n), (n,3n), (n,n+p).	$\chi \cdot \frac{1}{m} \left[\frac{1}{g}\right]$	FT8 $[nuclei]$

Table E.2: C-factors for mass normalisation of the different q-factors tallies results in the production rate calculation by different methods. Remember that all results of the tallies, q-factors, are normalised per incident particle, thus it must be multiplied by the total particle current, I [s^{-1}].

Resumen extenso en español

Introducción

La Medicina Nuclear engloba una parte importante de las aplicaciones médicas de las radiaciones ionizantes, basándose en el uso de radioisótopos como fuentes de radiación y permitiendo el diagnóstico y tratamiento médico de las principales enfermedades con mayor impacto social [15].

En los últimos años, la Medicina Nuclear ha presentado grandes avances gracias a la investigación de nuevas dianas moleculares que permiten una medicina más personalizada y de precisión, en las que las dosis administradas son seguras y efectivas, con toxicidad mínima en el tejido sano circundante, coste rentable y efectos secundarios leves. La investigación y el desarrollo de la Medicina Nuclear supone un cambio muy significativo en el tratamiento de estadios más precoces de enfermedades oncológicas.

Hoy en día se realizan más de 50 millones de procedimientos de Medicina Nuclear al año en todo el mundo, y esta cifra aumenta constantemente. Más de 10000 hospitales utilizan radioisótopos, y alrededor del 90 % de los procedimientos son para diagnóstico por imagen. El radionucleido más utilizado en diagnóstico SPECT es el ^{99m}Tc. Se calcula que se utiliza en casi el 85 % de los diagnósticos por imagen SPECT, lo que corresponde a unos 40 millones de estudios de pacientes al año [21].

Otros radioisótopos de alto interés clínico son los denominados como radioisótopos emergentes, definidos así por el Organismo Internacional de Energía Atómica (OIEA) como aquellos cuyas capacidades para mejorar las aplicaciones médicas han quedado demostradas, pero cuyo uso aún no se ha estandarizado. Uno de ellos es el radioisótopo emisor de electrones Auger, ^{165}Er. Otros radioisótopos de alto interés son los llamandos "teragnósticos", utilizados para procesos simultáneos de pruebas diagnósticas por imagen y terapia con radionucleidos haciendo uso del mínimo número de procedimientos. El novedoso radioisótopo ^{177}Lu, emisor de fotones gamma detectable mediante técnica SPECT y, a su vez, emisor de partículas beta para terapia, es hasta el momento uno de los radioisótopos teragnósticos más relevantes y prometedores.

En la actualidad el concepto de "teragnosis" ya se está implementado en clínica [32,33], permitiendo un enfoque más completo de la gestión de la enfermedad, dado que el diagnóstico mediante imágenes puede ofrecer varias funciones simultáneas: valoración de

la enfermedad, monitorización y selección del tratamiento de forma más eficaz, seleccionando a los pacientes que más se beneficiarían de ciertas intervenciones terapéuticas, al tiempo que se reducen o eliminan tratamientos innecesarios. Además, esta terapia combina la alta potencia citotóxica de las partículas beta con la especificidad de moléculas dirigidas a dianas moleculares, ofreciendo una opción terapéutica prometedora para casos donde otros tratamientos han fallado.

Sin embargo, la consolidación de esta estrategia clínica requiere de una red de producción de radioisótopos sólida y constante que garantice el suministro mundial de agentes teranósticos, emergentes o convencionales para satisfacer la creciente demanda de radionucleidos terapéuticos y de diagnóstico en nuestros hospitales.

Los radioisótopos utilizados en Medicina Nuclear son producidos artificialmente bombardeando isotopos estables con partículas cargadas, fotones o neutrones, para producir reacciones nucleares, ya sea en reactores nucleares o en aceleradores de partículas (linacs, sincrotrones, ciclotrones, etc.). Estas dos tecnologías, junto con el uso de generadores de radionucleidos, son las principales formas de abastecimiento de radioisótopos médicos en los hospitales, y deben considerarse como rutas de producción complementarias y no competitivas.

Dentro de este marco tecnológico, la futura instalación International Fusion Materials Irradiation Facility - Demo Oriented NEutron Source (IFMIF-DONES) será una infraestructura científica única en el mundo donde se ensayarán, validarán y cualificarán los materiales que se utilizarán en los futuros reactores nucleares de fusión. Además de su relevancia para el desarrollo de la fusión como fuente de energía, también será muy importante en otras áreas de investigación y conocimiento, las cuales se beneficiarán de su infraestructura, como la medicina, la física de partículas o la industria, entre otras. En diciembre de 2017, Fusion for Energy (F4E) valoró positivamente la propuesta conjunta de España y Croacia para ubicar IFMIF-DONES en Escúzar (Granada) [1].

El acelerador lineal de alta intensidad y última generación, IFMIF-DONES, podrá acelerar deuterones hasta una energía de 40 MeV y una corriente de 125 mA. Estas partículas cargadas golpearán un blanco de litio líquido produciendo neutrones a través de la reacción nuclear de producción $D^+ + {}^7Li$, contenida dentro de la celda de prueba (*Test Cell*) [4]. Se espera generar un flujo de neutrones rápidos de 10^{14} n/cm^2/s con un pico amplio entre $14 - 20$ MeV en su espectro neutrónico.

Las características únicas de la instalación permitirán desarrollar aplicaciones complementarias para la física fundamental y aplicada con un impacto mínimo en el normal funcionamiento de la instalación [5–8]. En el campo de la producción de radioisótopos, IFMIF-DONES facilitaría tanto las posibilidades de producción con haces de deuterones como con el flujo residual de neutrones localizado dentro de la celda de prueba. Para este fin, se estudiará de forma exhaustiva la viabilidad de producción de algunos de los radioisótopos más relevantes en la clínica actual, así como su adaptación realista de producción, considerándose algunas actualizaciones en el diseño del acelerador.

Medidas experimentales de secciones eficaces con partículas cargadas

Como paso fundamental y previo al estudio de nuevas vías alternativas de producción de radioisótopos emergentes y/o convencionales, es esencial un conocimiento profundo de los datos nucleares de las reacciones implicas en estas vías de producción, para la correcta evaluación de la viabilidad del proyecto.

En el capítulo segundo de este documento, se ha desarrollado en detalle la técnica de activación por láminas apiladas para la medición de las secciones eficaces de reacciones nucleares inducidas por haces de partículas cargadas, principalmente deuterones. Además, se presenta la experiencia y los resultados obtenidos durante dos colaboraciones internacionales para la medida de datos nucleares experimentales de la producción con deuterones de dos radioisótopos con alto interés clínico, ^{165}Er y ^{177}Lu. La primera tuvo lugar en el ciclotrón del centro de investigación *Conditions Extrêmes et Matériaux: Haute Température et Irradiation* (CEMHTI) (Orleans, Francia) [44] e implicó la medida de la sección eficaz de la reacción nuclear ^{nat}Ho(d,2n)^{165}Er y sus principales impurezas ^{nat}Ho(d,p)^{166g,166m}Ho hasta una energía máxima de deuterones de 17.5 MeV. La segunda colaboración consistió en la medición de la reacción nuclear ^{nat}Yb(d,x)^{177cum}Lu, además de numerosas impurezas, así como, el límite superior de su impureza isotópica ^{177m}Lu, y tuvo lugar en el ciclotrón del laboratorio GIP ARRONAX (Saint-Herblain, Francia) [45] hasta 33 MeV de energía máxima de deuterones.

Técnica de activación por láminas apiladas

La técnica de activación por láminas apiladas es un método de activación que consiste en apilar una serie de láminas delgadas, una detrás de otra, para realizar varias mediciones de la sección eficaz de una reacción nuclear a diferentes energías [49]. El método es conveniente por varias razones. En primer lugar, las secciones eficaces son funciones dependientes de la energía de las partículas cargadas, que ven reducida su energía cinética a medida que penetran en el material. El uso de láminas delgadas significa que la pérdida de energía de las partículas cargadas debido a su interacción con la materia es insignificante en el espesor de la lámina, por lo tanto, el flujo de partículas por profundidad del blanco permanece casi constante dentro de la lámina. En segundo lugar, debido también a que un radioisótopo concreto se puede formar como resultado de diferentes reacciones nucleares simultáneas caracterizadas por diferentes secciones eficaces y energías umbrales, la función de excitación de una reacción nuclear puede definirse perfectamente a una energía determinada mediante el uso de láminas finas apiladas.

La pila se definirá como un conjunto de varios patrones idénticos, cada uno formado por una lámina objetivo y varias láminas de monitoreo, separadas por una lámina gruesa, que actúa como degradador, lo que nos permite estudiar conjuntos de energías diferenciadas entre los distintos patrones de las láminas que conforman la pila.

La técnica de láminas apiladas por el método de activación conlleva un método de cálculo relativo. Este método relativo para el cálculo de las secciones eficaces de las reacciones nucleares de interés consiste en una determinación previa del flujo del haz de partículas a través de las láminas de control. Estas láminas, situadas estratégicamente dentro de la pila, producirán varias reacciones nucleares, cuyas secciones eficaces son bien conocidas. El OIEA proporciona secciones eficaces de reacción nuclear de referencia para diferentes proyectiles en una amplia gama de energías [51]. Una de las principales ventajas de este método relativo para el cálculo del flujo del haz es su fácil aplicación durante los experimentos de irradiación. Así como, su versatilidad en la localización o número de láminas de monitoreo insertadas en la pila.

Finalmente, la determinación de la actividad de las láminas activadas tras la irradiación, para la correcta implementación del método, se puede realizar experimentalmente haciendo uso de detectores de Germanio de Alta Pureza (HPGe), previamente calibrados en energía y eficiencia.

Principales resultados de las medidas experimentales de la reacciones nucleares ^{nat}Ho(d,x) hasta 17.5 MeV en el laboratorio CEMHTI

Los resultados experimentales obtenidos para la medida de la sección eficaz de la reacción ^{165}Ho(d,2n)^{165}Er mediante la técnica de láminas apiladas de ^{nat}Ho, se realiza en el rango de energías entre $8 - 17.5$ MeV, el cual comprende el pico de máxima probabilidad, que pretende ser redefinido con mayor precisión. El radioisótopo ^{165}Er es un emisor de electrones Auger, los cuales depositan toda su energía en un rango nanométrico una vez internalizados en los blancos diana. Esto supone una alta deposición de energía por unidad de longitud, es decir, son partículas con alta LET, muy relevantes para la terapia de enfermedades con radionucleidos.

Los resultados obtenidos de sección eficaz han sido comparados con resultados de estudios anteriores realizados por F. Tárkányi *et al.* [57] hasta 20 MeV y A. Hermanne *et al.* [61] hasta 42 MeV, mostrando una gran consonancia en la región de energías próximas al pico y reduciendo las incertidumbres descritas hasta el momento. Por el contrario, y en comparación con las estimaciones teóricas obtenidas en la base de datos TENDL-2023 [63], para energías superiores al pico de energía, aproximadamente 12 MeV, la curva de tendencia estimada no reproduce correctamente el comportamiento observado por los diferentes datos experimentales. Por este motivo, la adquisición de nuevos resultados nucleares experimentales puede ayudar a mejorar las estimaciones teóricas.

Otro resultado relevante obtenido en este estudio es la aportación de nuevos datos nucleares, hasta el momento, no dispones en bases de datos. Concretamente, de la reacción correspondiente a la producción del estado metaestable ^{165}Ho(d,p)^{166m}Ho. El conocimiento de la sección eficaz del estado metaestable ^{166m}Ho es relevante por dos razones principalmente. La primera se debe a la consecuencia de la desintegración β^- del radioisótopo ^{166m}Ho en el isótopo estable ^{166}Er, cuya producción por esta vía aditiva

reduciría el valor bruto de la actividad específica del producto final de interés, ^{165}Er. Para evitar este inconveniente, sería necesaria una separación química temprana de los dos elementos.

Por otro lado, el presente trabajo permite estudiar la función de excitación de la reacción nuclear ^{165}Ho (d,p)^{166g}Ho. El ^{166g}Ho es un agente terapéutico emisor β^- utilizado en clínica y que habitualmente se produce en reactores nucleares por captura gamma ^{165}Ho(n,γ), dando lugar a un producto con alto rendimiento. Siendo conscientes de que la ruta ^{165}Ho(d,p) investigada aquí no puede competir con el método de producción en reactor en cuanto a rendimiento, sí se podría plantear la producción preclinica del ^{166g}Ho por una ruta complementaria como subproducto final de nuestra reacción de interés. Para ello, la estimación de su impureza isotópica ^{166m}Ho es esencial, ya que sólo aportaría dosis no deseada.

Finalmente, la relación medida entre las actividades detectadas de ^{166m}Ho y ^{166g}Ho es inferior al $1/10^6$, siendo la contaminación por el estado ^{166m}Ho despreciable.

Principales resultados de las medidas experimentales de la reacciones nucleares ^{nat}Yb(d,x) hasta 33 MeV en el ciclotrón de GIP ARRONAX

Las medidas experimentales de las secciones eficaces de las reacciones nucleares inducidas por deuterones para la producción del ^{177cum}Lu e ^{177}Yb, así como, para el resto de radionucleidos estudiados en esta sección, se ha realizado mediante la técnica de láminas apiladas de ^{nat}Yb en el rango de altas energías comprendidas entre $19 - 33$ MeV. El principal interés de este estudio ha sido la medida del radioisótopo teragnóstico ^{177}Lu, considerado uno de los radioisótopos más prometedores para el diagnóstico y terapia de enfermedades oncológicas, gracias a su emisión de partículas β^- y fotones gamma de baja energía de forma simultánea.

El novedoso radioisótopo teranóstico ^{177g}Lu ($7/2^+$) puede producirse mediante la reacción nuclear directa inducida por deuterones ^{176}Yb(d,n)$^{177(g+m)}$Lu o indirectamente por desintegración de su núcleo padre ^{177}Yb ($9/2^+$), donde la producción del estado metaestable ^{177m}Lu ($23/2^-$) está prohibida debido a las reglas de selección de paridad y momento angular.

Los resultados obtenidos de la sección eficaz de interés han sido comparados con medidas experimentales anteriores realizadas por A. Hermanne *et al.* [71], S. Manenti *et al.* [72], F. Tárkányi *et al.* [74] y M.U Khandaker *et al.* [73], disponibles en la base de datos EXFOR [62]. Este conjunto de datos experimentales para el radioisótopo de interés ^{177cum}Lu, definen correctamente su función excitación hasta 24 MeV de energía. A energías más altas, solo se dispone de un conjunto de datos, el cual muestra discrepancias con respecto al resto de datos nucleares. Nuestras medidas proporcionan nuevos valores que permiten discernir correctamente las tendencias experimentales y definir una función de excitación más precisa.

Por otro lado, en vista a los resultados experimentales obtenidos se puede afirmar

que las estimaciones evaluadas de la base de datos TENDL-2023 [63] no terminan de reproducir con exactitud los resultados experimentales, reafirmandose la idea de que la adquisición y publicación de nuevas medidas experimentales va a permitir mejorar las estimaciones evaluadas en las bases de datos teóricas.

Finalmente, en este estudio se han redefinido numerosas funciones de excitación de todas las impurezas isotópicas y no isotópicas detectadas mediante la técnica de medida de activación de las muestras naturales de ytterbio irradiadas. Además, se ha estimado un límite máximo superior del rendimiento alcanzado por la impureza metaestable del ^{177m}Lu, producida directamente por la reacción nuclear ^{176}Yb(d,n), permitiendo cuantificar la contaminación del producto final por esta impureza isotópica, relevante en el estudio debido a su larga vida media. Este límite superior ha sido estimado de acuerdo con el criterio de Currie [79], mediante una nueva medición de las láminas tras un tiempo de enfriamiento de seis meses. El coeficiente de rendimiento entre el límite de detección del ^{177m}Lu y el ^{177g}Lu, al final de la irradiación, para una energía en torno a 20 MeV se estima en 0.0005 %. Un valor inferior a los porcentajes obtenidos mediante las rutas convencionales de producción en reactores, del $0.010 - 0.015$ % [81] o 0.02 % [82].

Estudio exhaustivo para la producción de radioisótopos y su implementación industrial en IFMIF-DONES

Dentro del marco de trabajo de la futura instalación internacional IFMIF-DONES, han surgido numerosas aplicaciones complementarias en torno a su tecnología innovadora. El acelerador lineal de deuterones de alta intensidad y última generación será capaz de acelerar deuterones hasta 40 MeV de energía y 125 mA de corriente. Este haz de deuterones incidirá sobre un blanco de litio produciendo un elevado flujo de neutrones (10^{14} n/cm^2/s) dentro de la celda de pruebas. Es, por tanto, que la futura instalación presentará unas características excepcionales en cuanto a lo que refiere flujo de partículas, lo que ha llevado a que numerosos estudios postulen la aplicación comple- mentaria de producción de radioisótopos para Medicina Nuclear como una de las aplicaciones complementarias con mayor impacto social dentro de la instalación [5–8].

Algunas actualizaciones en el diseño del acelerador han sido estudiadas para la correcta implementación de esta aplicación complementaria. En caso concreto de la producción de radioisótopos con deuterones, se ha barajado la posibilidad de desviar 1 pulso por 1000 del haz, lo que supondría un 0.1 % de intensidad de corriente del haz de deuterones inicial, hacia una sala experimental (R026) bajo la planta del Linac. Esto supondría la posibilidad de disponer de un haz de deuterones de 40 MeV de energía y 125 μA de intensidad de corriente para aplicaciones complementarias con deuterones. De forma simultánea, se ha estudiado la viabilidad de la aplicación complementaria de producción de diferentes radioisótopos mediante reacciones nucleares inducidas por neutrones, teniendo en cuenta su elevado flujo residual disponible dentro de la celda de pruebas tras el módulo de alto

flujo (*High Flux Test Module*). Para ello, se ha desarrollado y estudiado el diseño de un dispositivo de producción de radioisótopos mecanizado de inserción lateral acoplado a la geometría de los planos de diseño de la sala de pruebas.

Partiendo de estas consideraciones, en el tercer capítulo se ha llevado a cabo un estudio exhaustivo de producción de algunos radioisótopos emergentes y convencionales más relevantes en la clínica, ^{165}Er, ^{177}Lu y ^{99}Mo/^{99m}Tc, realizando especial énfasis en el estudio de las impurezas isotópicas y no isotópicas generadas en el producto final, en las calidades radioquímicas y de pureza, así como, en los rendimientos de producción alcanzados. Todo ello en comparación y tomando como referencia los métodos convencionales de producción de radioisótopos basados en reactores nucleares y/o aceleradores de protones. Finalmente, los dispositivos de producción han sido analizados estructural, térmica y mecánicamente mediante el uso de programas de diseño industrial como SolidWorks [86], y también, haciendo uso de códigos de Monte Carlo para el transporte de las partículas en la materia y la estimación de energía depositada en el medio, como SRIM 2003 [50] para partículas cargadas y MCNP6.2 [108] para neutrones.

Producción de ^{165}Er mediante reacciones inducidas por deuterones

La ruta de producción alternativa de ^{165}Er mediante reacciones nucleares inducidas por deuterones presenta un rendimiento estimado para muestras gruesas tres veces superior al descrito por los métodos convencionales de producción mediante reacciones nucleares inducidas por protones [55]. Además, la reacción nuclear de producción ^{165}Ho(d,2n)^{165}Er presenta numerosas ventajas que facilitan su producción en aceleradores de deuterones, como son su pico máximo de sección eficaz por debajo de los 18 MeV de energía, la abundancia natural del 100 % de la muestra (^{165}Ho), reducción de los costes derivados del enriquecimiento de la muestra, o la posibilidad de irradiar a energías inferiores, alcanzando rendimientos equiparables y reduciendo la coproducción de impurezas.

La producción de ^{165}Er en IFMIF-DONES cubriría necesidades clínicas garantizando altas calidades de pureza isotópica y pureza radionucleida, así como una alta actividad específica del producto final, con tan solo 30 horas de irradiación y 10 horas de enfriamiento.

Producción de ^{177}Lu mediante reacciones inducidas por deuterones

El segundo radioisótopo de interés clínico estudiado en el contexto de esta tesis ha sido el radioisótopo teragnóstico ^{177}Lu. Hasta el momento, su producción ha quedado supeditada a la disponibilidad de reactores nucleares y el uso de blancos enriquecidos de $^{176}Lu_2O_3$ o $^{176}Yb_2O_3$. A través de las reacciones nucleares de captura inducidas por neutrones térmicos (n,γ), características de los reactores de fisión, se permite la producción de ^{177}Lu en sus dos versiones, *carrier-added* de la impureza metaestable ^{177m}Lu o, *no-carrier-added*, libre de ella. Ambas rutas de producción son eficientes y económicas, predominantemente la ruta *carrier-added* [101].

La nueva ruta de producción planteada mediante reacciones nucleares inducidas por deuterones presenta ciertas limitaciones como consecuencia de las impurezas isotópicas generadas simultáneamente, en el producto final. Aunque la pureza radionucleida del producto final no se ve afectada y es muy alta, la presencia de átomos estables o de vida media muy larga como el ^{175}Lu o ^{176g}Lu, disminuyen considerablemente su pureza isotópica. Estos átomos competirían químicamente con los átomos de ^{177}Lu durante el proceso de marcaje del radiofármaco, disminuyendo su eficacia para uso clínico como agente teragnóstico.

En términos de pureza isotópica, la ruta alternativa de producción mediante deuterones sería equivalente a las actuales rutas *carrier-added* de los reactores nucleares, mediante irradiaciones de 7 días y 2 día de enfriamiento. Sin embargo, el rendimiento final sería mucho menor, como consecuencia de la diferencia significativa en la sección eficaz de producción. En búsqueda de una maximización de la pureza isotópica, una producción en dos pasos ha sido estudiada. Sin embargo, el rendimiento alcanzado sería aún inferior, debido a la eliminación de la contribución por la ruta de producción directa mediante la primera separación química Yb/Lu. A pesar de ello, el producto final presentaría alta actividad específica, pureza isotópica y radionucleida permitiendo su uso a nivel preclínico. La producción en dos pasos implicaría irradiaciones de 6 horas y tiempos de enfriamiento de 12 horas de muestras altamente enriquecidas de $^{176}Yb_2O_3$.

La relevancia de estudiar y potenciar rutas alternativas de producción inducidas por deuterones tiene un valor añadido en nuestro estudio, ya que continuamente observamos cortes de suministro de los radioisótopos procedentes de reactores nucleares, debido a su envejecimiento y limitación de uso, y en vista a la no construcción de nuevos reactores la necesidad de encontrar rutas alternativas se está convirtiendo en una prioridad.

Producción de ^{99}Mo/^{99m}Tc mediante reacciones inducidas por neutrones

Finalmente, el último radioisótopo analizado en detalle y con grandes perspectivas para su producción a gran escala en IFMIF-DONES, es el ^{99}Mo, núcleo padre del radioisótopo más utilizado en procedimientos de Medicina Nuclear para el diagnóstico SPECT por imagen, ^{99m}Tc.

En vista a los resultados eficientes y equiparables a la producción convencional en reactores nucleares mediante la irradiaciones de pellets individuales [7], se ha propuesto la irradiación múltiple en placas portadoras constituidas por 45 pellets con masa total de 72 g (45.9 g de molibdeno), que permitiría un suministro competitivo y a nivel clínico para el sistema regional y/o estatal de salud, produciendo semanalmente $1.21{\cdot}10^{12}$ Bq de ^{99}Mo por irradiación, con una actividad específica media de $2.63{\cdot}10^{10}$ Bq/g de molibdeno. Para ello, es necesario la adaptación de esta aplicación complementaria a los actuales diseños de la celda de pruebas, permitiendo la inserción de un dispositivo que garantice la recuperación semanal de las muestras irradiadas.

Por otro lado, gracias al elevado volumen activo tras le módulo de alto flujo, la

posibilidad de producción de otros radioisótopos mediante reacciones nucleares inducidas por neutrones quedaría abierta y supeditada a la disponibilidad del modelo mecanizado de extracción de muestras.

^{177}Lu como radioisótopo teragnóstico

En los últimos años, la Medicina Nuclear ha presentado grandes avances gracias a la investigación de nuevas dianas moleculares permitiendo una medicina más personalizada y de precisión. El término teragnosis, ya implementado en clínica, hace referencia a la estrategia que combina el diagnóstico y la terapia de enfermedades usando moléculas marcadas con isótopos radiactivos. La molécula vectora es capaz de identificar blancos específicos en órganos y tejidos de interés, mientras que el radioisótopo o los radioisótopos a los que va ligada realizan las funciones de evaluación y tratamiento. Por ello, en los últimos años se ha observado un incremento en la demanda de radioisótopos teragnósticos, siendo uno de los candidatos más prometedores el ^{177}Lu, gracias a sus óptimas características físicas, que le permiten realizar ambas funciones en un único radiofármaco. El ^{177}Lu es un radioisótopo emisor de partículas β^- (100 %) con energías máximas de 496.8 keV, que además es emisor de fotones gamma de baja energía 112.95 keV (6.23 %) y 208.37 keV (10.41 %), lo cual permite su detección mediante la técnica de diagnóstico por imagen SPECT [31]. Finalmente, otra ventaja relevante es su vida media de 6.65 días, que hace posible su producción y traslado a hospitales de forma eficiente.

Teniendo en cuenta las propiedades químicas del lutecio, el ion Lu^{3+} permite la formación de agregados robustos con ligandos específicos que tienen suficiente estabilidad en solución acuosa. Para ello, la mejor opción es el uso de un agente quelante bifuncional (BFC) capaz de confinar al ion radiometálico, al mismo tiempo que le confiere especificidad biológica para ser unido a un compuesto no radiactivo que actuaría como molécula vectora capaz de identificar las dianas moleculares deseadas [122]. Un BFC común en la química radiometálica del lutecio es el DOTA[1] y sus derivados, que presentan una estructura octadentada que se une al ion Lu^{3+} a través de los cuatro átomos de nitrógeno del anillo macrocíclico y los cuatro átomos de oxígeno desprotonados de los grupos carboxílicos colgantes.

Actualmente, el ^{177}Lu se ha presentado siempre como un agente teragnóstico dentro de las terapias conocidas como terapias dirigidas con radionucleidos (TRNTs). Sin embargo, otra de las estrategias más prometedoras para el tratamiento de tumores malignos resistentes a los métodos convencionales es la terapia con neutrones por captura de boro (BNCT) [130]. La BNCT es una técnica radioterapéutica basada en la interacción entre un haz de neutrones térmicos y compuestos de boro, previamente administrados al paciente y selectivos con las células tumorales. Cuando los neutrones interactúan con los átomos de ^{10}B, se genera una reacción nuclear que libera partículas alfas altamente energéticas (alto

[1] Ácido 1,4,7,10 - tetraazaciclododecano - N,N',N",N"' - tetraacético.

LET) y núcleos de litio, destruyendo selectivamente las células tumorales sin dañar los tejidos sanos circundantes.

Dentro de este entorno biomédico, en el capítulo cuarto se ha desarrollado una "investigación traslacional" que implica el radiomarcaje con ^{177}Lu de un radiofármaco experimental para abordar el novedoso objetivo de combinar las dos estrategias que actualmente se consideran como las más selectivas a nivel celular, la TRNT y la BNCT. El estudio se ha llevado a cabo a nivel preclínico en modelos de ratones xenotransplantados con receptores transmembrana de somatostatina positivos en tumores neuroendocrinos de pulmón. El radiofármaco experimental estudiado ha sido [^{10}B,^{177}Lu]B-Lu-DOTA-TATE en colaboración con la Unidad de Aplicaciones Médicas y de las Radiaciones Ionizantes del Centro de Investigaciones Energéticas, Medioambientales y Tecnológicas (CIEMAT) en España. El estudio con animales fue aprobado por el Comité ético del CIEMAT (código de protocolo PROEX094/15) adherido al Acuerdo sobre Transparencia en la Experimentación Animal, promovido por la Confederación de Sociedades Científicas de España (COSCE), con la colaboración de la Asociación Europea para la Investigación Animal (EARA) [141].

[^{10}B,^{177}Lu]B-Lu-DOTA-TATE

La octreotida (TATE) es un péptido análogo con afinidad por los receptores transmembrana de somatostatina. La somatostatina es una hormona polipeptídica ampliamente distribuida en los tejidos del sistema nervioso y endocrino. Las actividades fisiológicas de la somatostatina están mediadas por interacciones de alta afinidad con una familia de receptores acoplados a proteínas G. Actualmente, se conocen cinco subtipos diferentes de receptores de somatostatina (SSTR1, SSTR2, SSTR3, SSTR4, SSTR5) [132–134]. La inhibición de la secreción hormonal está mediada principalmente a través de los receptores SSTR2 y SSTR5.

La octreotida interactúa con la superficie celular SSTR2, presente en más del 80 % de los tumores neuroendocrinos. Los tumores neuroendocrinos son un grupo de neoplasias epiteliales que surgen de células neuroendocrinas. Aunque pueden originarse en cualquier localización, los más frecuentes son los tumores gastroenteropancreáticos (66 %) y pulmonares (31 %), siendo menos frecuentes en piel, glándulas suprarrenales, tiroides y tracto urogenital. Estos tumores son complejos debido a la heterogeneidad de su presentación clínica. Sin embargo, a pesar de su heterogeneidad tisular, los tumores neuroendocrinos comparten la expresión de marcadores inmunohistoquímicos neuroendocrinos que facilitan la secreción de péptidos bioactivos como CgA, serotonina, gastrina e insulina. La liberación de estas sustancias está regulada por la somatostatina [135].

La octreotida conjugada con [^{10}B]B-DOTA ha sido proporcionado por la empresa española LabsinLove S.L, mientras que el $^{177}LuCl_3$ (*n.c.a.*) de alta actividad específica producido en reactor nuclear de fisión a partir de blancos enriquecidos de $^{176}Yb_2O_3$, ha sido comprado a ITM Medical Isotopes GmbH.

Resultados del control de calidad del radiofármaco por HPLC

Tras el proceso de radiomarcaje, se ha evaluado mediante control de calidad HPLC el producto final obtenido, tomando como muestra una alícuota del radiofármaco experimental [^{10}B,^{177}Lu]B-Lu-DOTA-TATE preparado. Los resultados muestran una eficiencia de rendimiento del 25 % en el proceso de radiomarcaje, así como una pureza radioquímica superior al 95 % del producto final eluido. No observándose trazas significativas de ^{177}Lu libre ni otras sustancias químicas en el mismo.

La eficiencia de rendimiento del proceso se encuentra por debajo del valor típico de rendimiento de los procesos de radiomarcaje de análogos de somatostatina con ^{177}Lu. Este hecho puede deberse a efectos de impedimento estérico, influenciados por el elevado volumen del grupo funcional de la molécula, que contiene 54 átomos de boro, y que en cierta forma dificultaría la unión del lutecio a la molécula.

Estudio *ex vivo*: Resultados preliminares de los estudios de biodistribución, dosimetría y del efecto terapéutico del radiofármaco

Entre los diferentes subtipos histológicos de cáncer de pulmón neuroendocrino, el cáncer de pulmón de células no pequeñas (NSCLC) es el más frecuente y letal, responsable del $80-85$ % de las muertes [139]. La línea celular de carcinoma pulmonar no microcítico NCI-H727 es uno de los tumores neuroendocrinos de peor pronóstico, para el que las terapias convencionales están resultando insuficientes [140].

Trabajando con esta línea celular, se ha establecido un modelo xenotransplantado subcutáneo de cáncer de pulmón en ratón, generado a partir de $6{\cdot}10^6$ células NCI-H727 inoculadas en los flancos de ratones hembras inmunodeficientes Nude-Foxn1^{nu} de 5-6 semanas de edad. En este modelo se ha evaluado el potencial radiofármaco experimental, [^{10}B,^{177}Lu]B-Lu-DOTA-TATE.

La biodistribución y dosimetría de los radiofármacos experimentales es crucial para el estudio de su efectividad y seguridad. Los perfiles de absorción, distribución, metabolismo y excreción deben ser bien entendidos para minimizar los riesgos para los pacientes. Los estudios preclínicos en modelo animal siempre son el primer paso por definir. Los estudios de biodistribución *ex vivo* han sido realizados a diferentes tiempos de post-administración intravenosa del compuesto marcado, concretamente 10 minutos, 1, 2, 4 y 24 horas (N=3). Los resultados de biodistribución en ratones han sido utilizados para generar curvas de tiempo-actividad, que se han sido integradas para estimar las dosis absorbidas en los diferentes órganos vitales, utilizando para ello, un modelo de ratón MOBY disponible en el software PARaDIM.

Los resultados preliminares del estudio de biodistribución muestran que el péptido radiomarcado se acumula de forma satisfactoria en el tumor, pero también, de forma muy relevante en órganos sobreexpresantes de receptores SSTR2, como son el páncreas, estómago, intestino delgado, intestino grueso y los pulmones, así como, los riñones, vía

habitual de excreción de los péptidos.

En vista de los resultados obtenidos, la principal conclusión sería la necesidad de encontrar y considerar estrategias para minimizar la captación del compuesto en los órganos sanos no diana. Entre estas estrategias, se puede destacar el relevante estudio propuesto por Nicolas *et al.* [142], donde se analiza la influencia de la administración previa de un exceso de octreotida no radiomarcada en los resultados de la farmacocinética de los radiocompuestos administrados. Esta estrategia supondría un "efecto de masa" significativo que merece un estudio detallado en nuestro modelo.

Finalmente, los resultados preliminares de la evaluación terapéutica muestran que el tratamiento con el radiofármaco [^{10}B,^{177}Lu]B-Lu-DOTA-TATE reduce el crecimiento tumoral en comparación con el grupo control. Sin embargo, es necesario evaluar también el crecimiento tumoral tras la administración de [^{10}B]B-DOTA-TATE sin marcar y realizar un estudio más detallado al respecto.

Estimación de la concentración de boro

Como consecuencia directa y traslacional de los resultados farmacocinéticos, las estimaciones de concentración de ^{10}B medidas como la relación entre la cantidad de partes por millón (ppm) de átomos de boro en tumor-tejidos sanos resulta desfavorable para aquellos que sobreexpresan receptores SSTR2, como son entre otros, los pulmones. No permitiendo, de momento, las condiciones idóneas de sinergia entre ambas estrategias terapéuticas.

Sin embargo, en cuanto al valor absoluto de concentración de boro en tumor (en ppm), sí resulta óptimo. La concentración de boro medida está directamente relacionada con la cantidad de compuesto borado administrado en ratón, que en este estudio fue de 200 pmol de [^{10}B,^{177}Lu]B-Lu-DOTA-TATE. Concentraciones equivalentes a 20 ppm de boro en tumor podrían alcanzarse mediante la administración de 4 mg de compuesto borado en paciente, una cantidad considerablemente inferior a las administradas por el compuesto típicamente utilizado en BNCT, la boronofenilalanina (BPA) [143, 144].

Por otra parte, es importante destacar que la presencia del radioisótopo en la molécula no es un limitante para la cantidad de compuesto administrable, ya que solo una fracción del [^{10}B]B-DOTA-TATE se encuentra radiomarcada. Además, la eficiencia del proceso de radiomarcaje puede variar cuando se emplean cantidades elevadas de compuesto, pudiendo ser inferior a la reportada en esta tesis. No obstante, la actividad final del radiofármaco puede ajustarse en función de los requerimientos específicos del estudio, siempre que se conozca el valor de dicha eficiencia.

Finalmente, el concepto de investigación translacional desarrollado entre las terapias TRNT y BNCT no implica necesariamente el uso exclusivo de radioisótopos con finalidad terapéutica. Este enfoque puede ampliarse al empleo de radioisótopos utilizados en técnicas de imagen, como PET o SPECT, lo que permitiría monitorizar la captación del compuesto antes de la irradiación con un haz de neutrones. Para este caso, algunos

radioisótopos que ya han demostrado afinidad por el quelante DOTA y que podrían ser evaluados son el ^{89}Zr ($T_{1/2}$ = 78.41 h) y el ^{68}Ga ($T_{1/2}$ = 67.71 min) [152, 153].

Bibliography

[1] International Fusion Materials Irradiation Facility-DEMO Oriented Neutron Source, IFMIF-DONES, https://ifmif-dones.es/es/ (Accessed 17 Nov 2024)

[2] Mota, F. *et al.* (2015). Sensitivity of IFMIF-DONES irradiation characteristics to different design parameters. Nuclear Fusion, 55(12), 123024, https://iopscience.iop.org/article/10.1088/0029-5515/55/12/123024/pdf

[3] Community Research and Development Information Service. IFMIF-DONES Preparatory Phase. https://cordis.europa.eu/project/id/870186 (Accessed 25 October 2021).

[4] Królas, W. *et al.* (2021). The IFMIF-DONES fusion oriented neutron source: evolution of the design. Nuclear Fusion, 61(12), 125002, https://iopscience.iop.org/article/10.1088/1741-4326/ac318f/pdf

[5] Maj A., Lewitowicz M. and Królas W. (2016). White book on the complementary scientific programme at IFMIF-DONES, https://rifj.ifj.edu.pl/handle/item/78

[6] Praena J., *et al.* (2020). Feasibility study of the use of DONES for Radioisotope Production. Electronics Irradiation and Neutron Scattering, ENS-7.2.3.1-T13-06-N1. EUROfusion Internal Report.

[7] López-Melero, E., *et al.* (2024). Production of ^{99}Mo at IFMIF-DONES reusing the flux of neutrons. Nuclear Materials and Energy, 38, 101575, https://doi.org/10.1016/j.nme.2023.101575

[8] López-Melero, E., *et al.* (2024). Study of the production of radioisotopes at IFMIF-DONES: ^{177}Lu with deuterons. Radiation Physics and Chemistry, 220, 111687, https://doi.org/10.1016/j.radphyschem.2024.111687

[9] López-Melero, E., *et al.* (2024). Production of ^{165}Er with deuterons at IFMIF-DONES. Nuclear Materials and Energy, 39, 101659, https://doi.org/10.1016/j.nme.2024.101659

[10] Spanish Nuclear Industry Forum, About Nuclear Physics, https://www.foronuclear.org/descubre-la-energia-nuclear/preguntas-y-respuestas/sobre-fisica-nuclear/que-son-los-radioisotopos/ (Accesses 15 Nov 2024)

[11] Live Chart of Nuclides, IAEA Nuclear Data Section, https://www-nds.iaea.org/relnsd/vcharthtml/VChartHTML.html (Accesses 15 Nov 2024)

[12] Tavernier, S. (2010). Experimental techniques in nuclear and particle physics. Springer Nature, 306, https://library.oapen.org/handle/20.500.12657/56972

[13] Auger, P. (1975). The auger effect. Surface Science, 48(1), 1-8, https://doi.org/10.1016/0039-6028(75)90306-4

[14] National Institute of Biomedical Imaging and Bioengineering, Nuclear Medicine, https://www.nibib.nih.gov/science-education/science-topics/nuclear-medicine (Updated 3 Jan 2021; accesses 15 Nov 2024)

[15] World Health Organization, The top 10 causes of death, https://www.who.int/news-room/fact-sheets/detail/the-top-10-causes-of-death (Updated 7 Aug 2024; accessed 15 Nov 2024)

[16] International Commission on Radiation Units and Measurements ICRU (1980). Radiation Quantities and Units. ICRU Report 33. Washington, D.C.

[17] Carlsson, G.A. *et al.* (1999). Use of the concept of energy imparted in diagnostic radiology. Applied radiation and isotopes, 50(1), 39-62, https://doi.org/10.1016/S0969-8043(98)00087-6

[18] International Atomic Energy Agency, What are Radiopharmaceuticals?, https://www.iaea.org/newscenter/news/what-are-radiopharmaceuticals (Updated 12 Aug 2024; accessed 15 Nov 2024)

[19] de Lima, J.J.P. (1998). Radioisotopes in medicine. European Journal of Physics, 19(6), 485, https://iopscience.iop.org/article/10.1088/0143-0807/19/6/003/pdf

[20] Losilevsky, G. *et al.* (1989). A practical SPECT technique for quantitation of drug delivery to human tumors and organ absorbed radiation dose. In Seminars in nuclear Medicine, 19 (1), 33-46, https://doi.org/10.1016/S0001-2998(89)80034-0

[21] World Nuclear Association, Radioisotopes in Medicine, https://world-nuclear.org/information-library/non-power-nuclear-applications/radioisotopes-research/radioisotopes-in-medicine (Updated 30 Apr 2024; accessed 15 Nov 2024)

[22] National Nuclear Data Center, NuDat (3.0), ^{99m}Tc Radioisotope, https://www.nndc.bnl.gov/nudat3/decaysearchdirect.jsp?nuc=99Tc&unc=NDS (Accessed 18 Jan 2024).

[23] Kapoor, V., McCook, B.M. and Torok, F.S. (2004). An introduction to PET-CT imaging. Radiographics, 24(2), 523-543, https://doi.org/10.1148/rg.242025724

[24] Mattsson, S. and Söderberg, M. (2011). Radiation dose management in CT, SPECT/CT and PET/CT techniques. Radiation Protection Dosimetry, 147(1-2), 13-21, https://doi.org/10.1093/rpd/ncr261

[25] Wilkens, J.J. and Oelfke, U. (2003). Analytical linear energy transfer calculations for proton therapy. Medical Physics, 30(5), 806-815, https://doi.org/10.1118/1.1567852

[26] National Nuclear Data Center, NuDat (3.0), ^{165}Er Radioisotope, https://www.nndc.bnl.gov/nudat3/decaysearchdirect.jsp?nuc=165Er&unc=NDS (Accessed 14 Dec 2024).

[27] Bolcaen, J. *et al.* (2023). Marshalling the potential of Auger electron radiopharmaceutical therapy. Journal of Nuclear Medicine, 64(9), 1344-1351, https://jnm.snmjournals.org/content/jnumed/64/9/1344.full.pdf

[28] Da Silva, I., *et al.* (2021). A high separation factor for ^{165}Er from Ho for targeted radionuclide therapy. Molecules, 26(24), 7513, https://doi.org/10.3390/molecules26247513

[29] Saeedi Saghez, B., *et al.* (2024). First preclinical SPECT/CT imaging and biodistribution of [^{165}Er]$ErCl_3$ and [^{165}Er]Er-PSMA-617. EJNMMI Radiopharmacy and Chemistry, 9(1), 90, https://link.springer.com/article/10.1186/s41181-024-00312-9

[30] Naskar, N. and Lahiri, S. (2021). Theranostic terbium radioisotopes: challenges in production for clinical application. Frontiers in Medicine, 8, 675014, https://doi.org/10.3389/fmed.2021.675014

[31] National Nuclear Data Center, NuDat (3.0), ^{177}Lu Radioisotope, https://www.nndc.bnl.gov/nudat3/decaysearchdirect.jsp?nuc=177Lu&unc=NDS (Accessed 18 Dec 2024)

[32] Bodei, L. *et al.* (2011). Peptide receptor radionuclide therapy with ^{177}Lu-DOTATATE: the IEO phase I-II study. European journal of nuclear medicine and molecular imaging, 38, 2125-2135, https://link.springer.com/article/10.1007/s00259-011-1902-1

[33] Kratochwil, C. *et al.* (2019). EANM procedure guidelines for radionuclide therapy with ^{177}Lu-labelled PSMA-ligands (^{177}Lu-PSMA-RLT). European journal of nuclear medicine and molecular imaging, 46, 2536-2544, https://doi.org/10.1007/s00259-019-04485-3

[34] World Nuclear Association, Research Reactors, https://world-nuclear.org/information-library/non-power-nuclear-applications/radioisotopes-research/research-reactors?utm_source=chatgpt.com (Updated 21 May 2024; accessed 15 Nov 2024)

[35] IAEA. Cyclotrons used for Radionuclide Production, https://nucleus.iaea.org/sites/accelerators/Pages/Cyclotron.aspx (Updated 2024; accessed 15 Nov 2024)

[36] Zotkin, A. (2012) Frecuencia de resonancia del ciclotrón, sistemas caóticos y teoría de la relatividad. Website (Accessed 15 Nov 2024)

[37] Mirzadeh, S. and Knapp, F.F. (1996). Biomedical radioisotope generator systems. Journal of Radioanalytical and Nuclear Chemistry, 203, 471-488, https://link.springer.com/article/10.1007/BF02041524

[38] Cummins, P.M., Rochfort, K.D. and O'Connor, B.F. (2017). Ion-exchange chromatography: basic principles and application. Protein Chromatography: Methods and Protocols, 209-223, https://link.springer.com/protocol/10.1007/978-1-4939-6412-3_11

[39] Charisopoulos, S. and Picot, W. (2022). What are Particle Accelerators?. IAEA Bulletin (Online), 63(2), 4-5, https://inis.iaea.org/records/xak8p-tw143

[40] Brookhaven National Laboratory, U.S. Radioisotopes for nuclear medicine and industry, https://www.bnl.gov/mirp/index.php (Accessed 17 Nov 2024)

[41] PULSAR-7 PET Isotope Production System Report, https://www.accsys.com/pdf/pulsar_brochure.pdf (Updated 2004; accessed 17 Nov 2024)

[42] International Atomic Energy Agency (2009). Medical Isotopes Shortage Reveals Larger Issue, https://www.iaea.org/newscenter/news/medical-isotopes-shortage-reveals-larger-issue (Accessed 17 Nov 2024)

[43] CERN MEDICIS Facility. PRISMAP - The European medical isotope programme, https://medicis.cern/prismap-european-medical-isotope-programme (Accessed 25 October 2021).

[44] Conditions Extrêmes et Matériaux: Haute Température et Irradiation CEMHTI - UPR3079 CNRS, Orleans, France. Website: https://www.cemhti.cnrs-orleans.fr/

[45] GIP ARRONAX Cyclotron, Saint-Herblain, Nantes, France. Website: https://www.arronax-nantes.fr/en/gip-arronax/

[46] Lane, A.M. (1957). Nuclear Reactions. Reviews of Modern Physics, 29(2), 191, https://doi.org/10.1103/RevModPhys.29.191

[47] International Atomic Energy Agency, Nuclear Medicine Physics: A Handbook for Teachers and Students, 2014, https://www-pub.iaea.org/MTCD/Publications/PDF/Pub1617web-1294055.pdf (Accessed 14 May 2024)

[48] de Saavedra, F.A., Porras, I. and Praena, J. (2018). Routes for the production of isotopes for PET with high intensity deuteron accelerators. Nuclear Instruments and Methods in Physics Research Section A: Accelerators, Spectrometers, Detectors and Associated Equipment, 887, 50-53, https://doi.org/10.1016/j.nima.2018.01.048

[49] Nigron, E., Guertin, A. and Haddad, F. (2018). Radioactive isotopes produced for medical applications: setting up an accurate measurement method for production cross section. In Journée de l'école doctorale" Matière, Molécules et Matériaux" Rennes 2018, https://hal.science/hal-02414720/

[50] Ziegler J.F. (2003). SRIM - The Stopping and Range of Ions in Matter, http://www.srim.org/ (Accessed 14 May 2024)

[51] Hermanne, A., Ignatyuk, A.V. and Capote, R. (2017). Reference Cross Sections for Charged-particle Monitor Reactions. Nuclear Data Sheet, 148, 338-382, https://www-nds.iaea.org/medical/monitor_reactions.html

[52] National Nuclear Data Center, NuDat (3.0), https://www.nndc.bnl.gov/nudat3/ (Accessed 14 May 2024)

[53] Otuka, N. and Takács, S. (2015). Definitions of radioisotope thick target yields. Radiochimica Acta, 103, 1-6, https://www.degruyter.com/document/doi/10.1515/ract-2013-2234/html

[54] Sitarz, M. Tool-Radionuclide Yield Calculator. ARRONAX Nantes, Tool Download, https://www.arronax-nantes.fr/en/outil-telechargement/tool-radionuclide-yield-calculator/ (Update Dec 2018)

[55] Gracheva, N., *et al.* (2020). ^{165}Er: a new candidate for Auger electron therapy and its possible cyclotron production from natural holmium targets. Applied Radiation and Isotopes, 159, 109079, https://doi.org/10.1016/j.apradiso.2020.109079

[56] Kassis, A.I. (2011). Molecular and cellular radiobiological effects of Auger emitting radionuclides. Radiation Protection Dosimetry, 143(2-4), 241-247, https://doi.org/10.1093/rpd/ncq385

[57] Tárkányi, F., *et al.* (2008). Experimental study of the ^{165}Ho(d,2n) and ^{165}Ho(d,p) nuclear reactions up to 20 MeV for production of the therapeutic radioisotopes ^{165}Er and ^{166g}Ho. Nuclear Instruments and Methods in Physics Research Section B: Beam Interactions with Materials and Atoms, 266(16), 3529-3534, https://doi.org/10.1016/j.nimb.2008.05.123

[58] Sadeghi, M., Enferadi, M. and Tenreiro, C. (2010). Nuclear model calculations on the production of Auger emitter ^{165}Er for targeted radionuclide therapy. Journal of Modern Physics, 1(04), 217, https://www.scirp.org/pdf/JMP20100400004_98921653.pdf

[59] Goodfellow, Holmium, https://www.goodfellow.com/eu/ytterbium-foil

[60] Genie 2000 Gamma Analysis Software. Mirion Technologies, https://mirionprodstorage.blob.core.windows.net/prod-20220822/cms4_mirion/files/pdf/spec-sheets/c47691_genie-2000_gamma_analysis_software_spec_sheet_1.pdf

[61] Hermanne, A., *et al.* (2013). Deuteron induced reactions on Ho and La: Experimental excitation functions and comparison with code results. Nuclear Instruments and Methods in Physics Research Section B: Beam Interactions with Materials and Atoms, 311, 102-111, https://doi.org/10.1016/j.nimb.2013.06.014

[62] Experimental Nuclear Reaction Data (EXFOR), https://www-nds.iaea.org/exfor/ (Accessed 17 Dec 2024).

[63] TALYS-Based Evaluated Nuclear Data Library 2023 (TENDL-2023), https://tendl.web.psi.ch/tendl_2023/tendl2023.html (Accessed 17 Dec 2024).

[64] National Nuclear Data Center, NuDat (3.0), ^{166}Ho Radioisotope, https://www.nndc.bnl.gov/nudat3/decaysearchdirect.jsp?nuc=166Ho&unc=NDS (Accessed 17 Dec 2024).

[65] Roosen, J., *et al.* (2021). Development of an MRI-guided approach to selective internal radiation therapy using holmium-166 microspheres. Cancers, 13(21), 5462, https://doi.org/10.3390/cancers13215462

[66] Kim, T., *et al.* (2024). Systematic analysis for the thermal stability assessment of ^{166}Ho production using HANARO: An in silico study. Nuclear Engineering and Technology, 56(11), 4914-4920, https://doi.org/10.1016/j.net.2024.07.001

[67] Beyer, G.J., Zeisler, S.K. and Becker, D.W. (2004). The Auger-electron emitter ^{165}Er: excitation function of the ^{165}Ho(p,n)^{165}Er process. Radiochimica Acta, 92(4-6), 219-222, https://doi.org/10.1524/ract.92.4.219.35608

[68] Dmitriev, P.P., Krasnov, N.N. and Molin, G.A. (1982). Radioactive nuclide yields for thick target at 22 MeV deuterons energy. Yadernie Konstanti, 34(4), 38.

[69] Dash, A., Pillai, M.R.A. and Knapp, F.F. (2015). Production of ^{177}Lu for targeted radionuclide therapy: available options. Nuclear Medicine and Molecular Imaging, 49, 85-107, https://doi.org/10.1007/s13139-014-0315-z

[70] Advancing Nuclear Medicine (2023). Lutetium-177 no carrier added, https://www.advancingnuclearmedicine.com/articles (Accessed 18 Dec 2024).

[71] Hermanne A., Takacs S. and Goldberg M.B. (2006). Deuteron-induced reactions on Yb: Measured cross sections and rationale for production pathways of carrier-free, medically relevant radionuclides. Nuclear Instruments and Methods in Physics Research Section B: Beam Interactions with Materials and Atoms, 247(2), 223-231, https://doi.org/10.1016/j.nimb.2006.03.008

[72] Manenti S., Groppi F. and Gandini A. (2011). Excitation function for deuteron induced nuclear reactions on natural ytterbium for production of high specific activity ^{177g}Lu in no carrier added form for metabolic radiotherapy. Applied Radiation and Isotopes, 69, 37–45, https://doi.org/10.1016/j.apradiso.2010.08.008

[73] Khandaker M.U., Haba H. and Otuka N. (2014). Investigation of (d,x) nuclear reactions on natural ytterbium up to 24 MeV. Nuclear Instruments and Methods in Physics Research Section B: Beam Interactions with Materials and Atoms, 335, 8-18, https://doi.org/10.1016/j.nimb.2014.05.020

[74] Tárkányi F., Ditrói F. and Takács S. (2013). Activation cross-sections of longer lived products of deuteron induced nuclear reactions on ytterbium up to 40 MeV. Nuclear Instruments and Methods in Physics Research Section B: Beam Interactions with Materials and Atoms, 304, 36-48, https://doi.org/10.1016/j.nimb.2013.03.056

[75] Nigron, E., *et al.* (2021). Is ^{70}Zn(d,x)^{67}Cu the best way to produce ^{67}Cu for medical applications?. Frontiers in Medicine, 8, 674617, https://doi.org/10.3389/fmed.2021.674617

[76] García-Infantes, F., *et al.* (2024). Measurement of the ^{176}Yb(n,γ) cross section at the n_TOF facility at CERN. Physical Review C, 110, 064619, https://doi.org/10.1103/PhysRevC.110.064619

[77] Goodfellow, Ytterbium, https://www.goodfellow.com/eu/ytterbium-foil

[78] Fitzgerald, J. and Servives's, J.C. Software Fitzpeaks Gamma Analysis Software, Software version 3.66. Oxfordshire.

[79] Currie, L.A. (1968). Limits for qualitative detection and quantitative determination. Application to radiochemistry. Analytical Chemistry, 40(3), 586-593, https://pubs.acs.org/doi/pdf/10.1021/ac60259a007?casa_token=26kMSiEaXJIAAAAA:DOXQi2c9VGPU-m_GyhZSoae2E76dwjDTPpBFEGZsTLcrr5_isgNeN06LJUqzT9qSuKyigTErSXXod5c

[80] Nagai, Y., *et al.* (2022). Estimated isotopic compositions of Yb in enriched ^{176}Yb for producing ^{177}Lu with high radionuclide purity by ^{176}Yb(d,x)^{177}Lu. Journal of the Physical Society of Japan, 91(4), 044201, https://journals.jps.jp/doi/full/10.7566/JPSJ.91.044201

[81] Pillai, M.R.A., *et al.* (2003). Production logistics of ^{177}Lu for radionuclide therapy. Applied Radiation and Isotopes, 59(2-3), 109-118, https://doi.org/10.1016/S0969-8043(03)00158-1

[82] Canella, L., *et al.* (2008). Accurate determination of half-life and radionuclidic purity of reactor produced ^{177g}Lu (^{177m}Lu) for metabolic radiotherapy. Journal of Radioanalytical and Nuclear Chemistry, 276(3), 813-818, https://doi.org/10.1007/s10967-008-0637-3

[83] Praena J., *et al.* (2020). Radioisotope production at the IFMIF-DONES facility. EPJ Web of Conferences 239, 23001, https://doi.org/10.1051/epjconf/202023923001

[84] Mastinu, P., *et al.* (2012). Status of the LEgnaro NeutrOn Source facility (LENOS). Physics Procedia, 26, 261-273, https://doi.org/10.1016/j.phpro.2012.03.034

[85] Mastinu, P., *et al.* (2015). Micro-channel-based high specific power lithium target. Il Nuovo Cimento C, 38, 1-7, https://inspirehep.net/files/01722abdb4291cddfe43798050f64e5d

[86] Vidal, C.R. (2016). Diseño mecánico con SolidWorks 2015. Ra-Ma Editorial.

[87] Ideal Vacuum Products. KF Fittings and Flanges, https://www.idealvac.com/en-us/KF-Fittings-and-Flanges/ct/2-90

[88] Matsson, J.E. (2023). An Introduction to SOLIDWORKS Flow Simulation 2023. SDC publications.

[89] Tárkányi, F., *et al.* (2008). Experimental study of the ^{165}Ho(p,n) nuclear reaction for production of the therapeutic radioisotope ^{165}Er. Nuclear Instruments and Methods in Physics Research Section B: Beam Interactions with Materials and Atoms, 266(15), 3346-3352, https://doi.org/10.1016/j.nimb.2008.05.005

[90] Gracheva, N., *et al.* (2020). ^{165}Er: a new candidate for Auger electron therapy and its possible cyclotron production from natural holmium targets. Applied Radiation and Isotopes, 159, 109079, https://doi.org/10.1016/j.apradiso.2020.109079

[91] Tarkanyi, F., *et al.* (2009). Investigation of production of the therapeutic radioisotope ^{165}Er by proton induced reactions on erbium in comparison with other production routes. Applied Radiation and Isotopes, 67(2), 243-247, https://doi.org/10.1016/j.apradiso.2008.10.006

[92] Luurtsema, G., *et al.* (2021). EANM guideline for harmonisation on molar activity or specific activity of radiopharmaceuticals: impact on safety and imaging quality. EJNMMI Radiopharmacy and Chemistry, 6, 1-16, https://link.springer.com/article/10.1186/s41181-021-00149-6

[93] Berenguer, L.R., Lozano, M.L. and Alonso, J.C. (2016). Terapia metabólica mediante radiofármacos en Medicina nuclear. Nuclear España: Revista de la Sociedad Nuclear española, (369), 28-31, https://www.revistanuclear.es/wp-content/uploads/hemeroteca/369/NE369-04.pdf

[94] Orain, S., *et al.* (2001). Use of genetic algorithms for the simultaneous estimation of thin films thermal conductivity and contact resistances. International journal of heat and mass transfer, 44(20), 3973-3984, https://doi.org/10.1016/S0017-9310(01)00025-4

[95] Isotopes for Science, Medicine and Industry (ISOFLEX USA), https://www.isoflex.com/component/search/?searchword=176Yb&searchphrase=all&Itemid=144 (Accessed 10 Jan 2025)

[96] Shao, L. (2023). Optimization of deuteron irradiation of ^{176}Yb for producing ^{177}Lu of high specific activity exceeding 3000 GBq/mg. Molecules, 28(16), 6053, https://doi.org/10.3390/molecules28166053

[97] European Directorate for the Quality of Medicines & HealthCare, https://www.edqm.eu/en/ (Accessed 13 Jan 2025)

[98] European 9.3, Radiopharmaceutical preparations and starting materials for radiopharmaceutical preparations, Lutetium (^{177}Lu) solution for radiolabelling, 2798.

[99] Balasubramanian, P.S. (1994). Separation of carrier-free lutetium-177 from neutron irradiated natural ytterbium target. Journal of Radioanalytical and Nuclear Chemistry, 185, 305-310, https://link.springer.com/article/10.1007/BF02041303

[100] Hashimoto, K., Matsuoka, H. and Uchida, S. (2003). Production of no-carrier-added 177 Lu via the ^{176}Yb(n,γ)^{177}Yb $\rightarrow$ ^{177}Lu process. Journal of Radioanalytical and Nuclear Chemistry, 255, 575-579, https://link.springer.com/article/10.1023/A:1022557121351

[101] Henkelmann, R., *et al.* (2013). Production of ^{177}Lu n.c.a. in high-flux reactors. Isotope Technologies Garching GmbH, https://indico.frm2.tum.de/event/0/attachments/4/14/Henkelmann_177Lu_gek.pdf

[102] International Atomic Energy Agency, 2013. Non-HEU Production Technologies for Molybdenum-99 and Technetium-99m, https://www-pub.iaea.org/MTCD/Publications/PDF/Pub1589_web.pdf

[103] Ruth T.J. (2020). The Shortage of Technetium-99m and Possible Solutions. Annual Review of Nuclear and Particle Science, 70, 77-94, https://doi.org/10.1146/annurev-nucl-032020-021829

[104] Bernardi, D., *et al.* (2022). The IFMIF-DONES project: design status and main achievements within the EUROfusion FP8 work programme. Journal of Fusion Energy, 41(2), 24, https://link.springer.com/article/10.1007/s10894-022-00337-5

[105] Blaauw, M., *et al.* (2017). Estimation of ^{99}Mo production rates from natural molybdenum in research reactors. Journal of Radioanalytical and Nuclear Chemistry, 311, 409-418, https://link.springer.com/article/10.1007/s10967-016-5036-6

[106] Matsubayashi, M., *et al.* (2000). Design and characteristics of the JRR-3M thermal neutron radiography facility and its imaging systems. Nuclear Technology, 132(2), 309-324, https://doi.org/10.13182/NT00-A3146

[107] The MCNP Code, Los Alamos National Laboratory, https://mcnp.lanl.gov/

[108] Werner, C.J., *et al.* (2017). MCNP Users Manual- Code Version 6.2. Los Alamos National Laboratory, Tech. Rep. LA-UR-17-29981, https://mcnp.lanl.gov/pdf_files/TechReport_2018_LANL_LA-UR-18-20808_WernerBullEtAl.pdf

[109] Kulesza, J.A, *et al.* (2022). MCNP® Code Version 6.3.0 Theory & User Manual, Los Alamos National Laboratory Tech. Rep. LA-UR-22-30006, https://www.osti.gov/servlets/purl/1889957

[110] Jang, J., *et al.* (2017). Mo-99 Topical Meeting, Montréal, Canada, https://mo99.ne.anl.gov/2017/pdfs/presentations/S9-P3%20Jang%20Presentation.pdf (Accessed 20 Jan 2024)

[111] Matyskin, A.V., *et al.* (2013). Feasibility study for production of ^{99m}Tc by neutron irradiation of MoO_3 in a 250 kW TRIGA Mark II reactor. Journal of Radioanalytical and Nuclear Chemistry, 298, 413-418, https://link.springer.com/article/10.1007/s10967-012-2381-y

[112] Tatenuma, K., *et al.* (2016). Generator of Highly Concentrated Pure ^{99m}Tc from Low Specific Activity ^{99}Mo Produced by Reactor and/or Electron Linear Accelerator. In part at Mo-99 Topical Meeting, Missouri, USA, https://kakenlabo.co.jp/06english/Mo_Tc_Article.pdf

[113] Evaluated Nuclear Data File (ENDF), Database Version of 2024-11-28; Software Version of 2024-10-08, https://www-nds.iaea.org/exfor/endf.htm

[114] Fernández-Maza, L. Radiopharmaceutical of the Punta de Europa University Hospital, Algeciras, Cádiz, Spain. Private communication.

[115] Simakov, S.P., *et al.* (2012). Status of the McDeLicious approach for the D-Li neutron source term modeling in IFMIF neutronics calculations. Fusion Science and Technology, 62(1), 233-239, https://doi.org/10.13182/FST11-444

[116] International Commission on Radiological Protection (1996). ICRP Publication 74: Conversion coefficients for use in radiological protection against external radiation (No. 74). Elsevier Health Sciences.

[117] Fischer, U., *et al.* (2007). Evaluation and validation of d–Li cross section data for the IFMIF neutron source term simulation. Journal of Nuclear Materials, 367, 1531-1536, https://doi.org/10.1016/j.jnucmat.2007.04.038

[118] Seth, M., *et al.* (1995). Lanthanide and actinide contractions: relativistic and shell structure effects. Journal of the American Chemical Society, 117(24), 6597-6598, https://pubs.acs.org/doi/pdf/10.1021/ja00129a026

[119] Pitzer, K.S. (1979). Relativistic effects on chemical properties. Accounts of Chemical Research, 12(8), 271-276, https://pubs.acs.org/doi/pdf/10.1021/ar50140a001

[120] Pearson, R.G. (2005). Chemical hardness and density functional theory. Journal of Chemical Sciences, 117, 369-377, https://www.ias.ac.in/article/fulltext/jcsc/117/05/0369-0377

[121] Chakravarty, R. and Chakraborty, S. (2021). A review of advances in the last decade on targeted cancer therapy using ^{177}Lu: Focusing on ^{177}Lu produced by the direct neutron activation route. American Journal of Nuclear Medicine and Molecular Imaging, 11(6), 443, https://pmc.ncbi.nlm.nih.gov/articles/PMC8727880/

[122] Parus, L.J., *et al.* (2015). Chemistry and bifunctional chelating agents for binding ^{177}Lu. Current radiopharmaceuticals, 8(2), 86-94, https://sfera.unife.it/bitstream/11392/2370900/3/CR_Lu-Chemistry.postprint.pdf

[123] Liu, S. (2008). Bifunctional coupling agents for radiolabeling of biomolecules and target-specific delivery of metallic radionuclides. Advanced drug delivery reviews, 60(12), 1347-1370, https://doi.org/10.1016/j.addr.2008.04.006

[124] Viola-Villegas, N. and Doyle, R.P. (2009). The coordination chemistry of 1,4,7,10-tetraazacyclododecane-N, N',N",N"-tetraacetic acid (H_4DOTA): Structural overview and analyses on structure–stability relationships. Coordination Chemistry Reviews, 253(13-14), 1906-1925, https://doi.org/10.1016/j.ccr.2009.03.013

[125] Stasiuk, G.J. and Long, N.J. (2013). The ubiquitous DOTA and its derivatives: the impact of 1,4,7,10-tetraazacyclododecane-1,4,7,10-tetraacetic acid on biomedical imaging. Chemical Communications, 49(27), 2732-2746, https://pubs.rsc.org/en/content/articlehtml/2013/cc/c3cc38507h

[126] Cutler, C.S., *et al.* (2013). Radiometals for combined imaging and therapy. Chemical reviews, 113(2), 858-883, https://pubs.acs.org/doi/full/10.1021/cr3003104

[127] Zidan, L., *et al.* (2022). Efficacy and safety of ^{177}Lu-DOTATATE in lung neuroendocrine tumors: a bicenter study. Journal of Nuclear Medicine, 63(2), 218-225, https://doi.org/10.2967/jnumed.120.260760

[128] Camargo-Miranda A.C., *et al.* (2021). Radioimmuno-theranostic Pair Based on the Anti-HER2 Monocolnal Antibody: Influence of Chelating Agents and Radionuclides on Biological Properties. Pharmaceutics 13, 971. https://doi.org/10.3390/pharmaceutics13070971

[129] Magro, N., *et al.* (2024). Target engagement of an anti-MT1-MMP antibody for triple-negative breast cancer PET imaging and beta therapy. Nuclear Medicine and Biology, 136, 108930, https://doi.org/10.1016/j.nucmedbio.2024.108930

[130] Suzuki, M. (2020). Boron neutron capture therapy (BNCT): A unique role in radiotherapy with a view to entering the accelerator-based BNCT era. International journal of clinical oncology, 25(1), 43-50, https://link.springer.com/article/10.1007/s10147-019-01480-4

[131] Pirooznia, N., *et al.* (2020). ^{177}Lu-labeled cyclic RGD peptide as an imaging and targeted radionuclide therapeutic agent in non-small cell lung cancer: biological evaluation and preclinical study. Bioorganic Chemistry, 102, 104100, https://doi.org/10.1016/j.bioorg.2020.104100

[132] Yamada, Y., *et al.* (1992). Cloning and functional characterization of a family of human and mouse somatostatin receptors expressed in brain, gastrointestinal tract, and kidney. Proceedings of the National Academy of Sciences, 89(1), 251-255, https://doi.org/10.1073/pnas.89.1.251

[133] Yamada, Y., *et al.* (1992). Somatostatin receptors, an expanding gene family: cloning and functional characterization of human SSTR3, a protein coupled to adenylyl cyclase. Molecular Endocrinology, 6(12), 2136-2142, https://doi.org/10.1210/mend.6.12.1337145

[134] Yamada, Y., *et al.* (1993). Cloning, functional expression and pharmacological characterization of a fourth (hSSTR4) and a fifth (hSSTR5) human somatostatin receptor subtype. Biochemical and biophysical research communications, 195(2), 844-852, https://doi.org/10.1006/bbrc.1993.2122

[135] Prado-Wohlwend, S., *et al.* (2022). Terapia con péptidos radiomarcados con [^{177}Lu]Lu-DOTA-TATE, Revista Española de Medicina Nuclear e Imagen Molecular, 41(1), 55-65, https://doi.org/10.1016/j.remn.2021.11.001

[136] Weinera, R.E. and Thakurb, M.L. (2003). Chemistry of gallium and indium radiopharmaceuticals. Handbook of radiopharmaceuticals: radiochemistry and applications, 363.

[137] Mier, W., *et al.* (2005). Conjugation of DOTA using isolated phenolic active esters: the labeling and biodistribution of albumin as blood pool marker. Bioconjugate chemistry, 16(1), 237-240.

[138] Liu, F., *et al.* (2017). ^{68}Ga/^{177}Lu-labeled DOTA-TATE shows similar imaging and biodistribution in neuroendocrine tumor model. Tumor Biology, 39(6), https://doi.org/10.1177/1010428317705519

[139] de Groot, P.M., *et al.* (2018). The epidemiology of lung cancer. Translational Lung Cancer Research, 7(3), 220, https://tlcr.amegroups.org/article/view/21996/pdf

[140] Mijatovic, T., *et al.* (2006). Cardenolide-induced lysosomal membrane permeabilization demonstrates therapeutic benefits in experimental human non-small cell lung cancers. Neoplasia, 8(5), 402-412, https://doi.org/10.1593/neo.05850

[141] Engaging, Informing, Supporting. European Animal Research Association, https://www.eara.eu/spain (Accessed 6 Mar 2025).

[142] Nicolas, G.P., *et al.* (2017). Biodistribution, pharmacokinetics, and dosimetry of ^{177}Lu-, ^{90}Y-, and ^{111}In-labeled somatostatin receptor antagonist OPS201 in comparison to the agonist ^{177}Lu-DOTATATE: the mass effect. Journal of Nuclear Medicine, 58(9), 1435-1441, https://doi.org/10.2967/jnumed.117.191684

[143] Fukuda, H. (2021). Response of normal tissues to boron neutron capture therapy (BNCT) with ^{10}B-borocaptate sodium (BSH) and ^{10}B-paraboronophenylalanine (BPA). Cells, 10(11), 2883, https://doi.org/10.3390/cells10112883

[144] Bergenheim, A.T., *et al.* (2005). Distribution of BPA and metabolic assessment in glioblastoma patients during BNCT treatment: a microdialysis study. Journal of neuro-oncology, 71, 287-293, https://link.springer.com/article/10.1007/s11060-004-1724-0

[145] International Commission on Radiological Protection (2007). ICRP Publication 103, https://www.icrp.org/docs/icrp_publication_103-annals_of_the_icrp_37(2-4)-free_extract.pdf

[146] Loevinger, R., Budinger, T.F. and Watson, E.E. (1988). MIRD primer for absorbed dose calculations, Society of Nuclear Medicine, New York, 1988

[147] Carter, L.M. and Zanzonico, P.B. (2024). MIB Guides: Preclinical radiopharmaceutical dosimetry. Molecular Imaging and Biology, 26(1), 17-28, https://pmc.ncbi.nlm.nih.gov/articles/PMC10462246/pdf/nihpp-rs3225362v1.pdf

[148] Segars, W.P., *et al.* (2004). Development of a 4-D digital mouse phantom for molecular imaging research. Molecular Imaging & Biology, 6(3), 149-159, https://doi.org/10.1016/j.mibio.2004.03.002

[149] Carter, L.M., *et al.* (2019). PARaDIM: a PHITS-based Monte Carlo tool for internal dosimetry with tetrahedral mesh computational phantoms. Journal of Nuclear Medicine, 60(12), 1802-1811, https://doi.org/10.2967/jnumed.119.229013

[150] Davis, P.J. and Rabinowitz, P. (2007). Methods of numerical integration. Courier Corporation. Dover Publication, ING. Mineola, New York.

[151] Andersen, H.H. and Ziegler, J.F. (1977). Hydrogen. Stopping powers and ranges in all elements. Stopping Powers and Ranges of Ions in Matter. Vol. 3. Pergamon Press. New York. ISBN 0-08-021605-6.

[152] Pandya, D.N., *et al.* (2017). Zirconium tetraazamacrocycle complexes display extraordinary stability and provide a new strategy for zirconium-89-based radiopharmaceutical development. Chemical Science, 8(3), 2309-2314, https://pubs.rsc.org/en/content/articlepdf/2017/sc/c6sc04128k

[153] Moradi, F., *et al.* (2016). Spectrum of ^{68}Ga-DOTA TATE uptake in patients with neuroendocrine tumors. Clinical nuclear medicine, 41(6), 281-287, https://mirt.tsnmjournals.org/articles/doi/mirt.galenos.2021.37268